Design and Optimization of Next-Generation Broad Energy Pinhole PET/SPECT

Valerio Cosmi

Design and Optimization of Next-Generation Broad Energy Pinhole PET/SPECT

Dissertation

for the purpose of obtaining the degree of doctor

at Delft University of Technology

by the authority of the Rector Magnificus, Prof. dr. ir. H. Bijl,

chair of the Board for Doctorates

to be defended publicly on

Monday 2 March 2026 at 15:00

by

Valerio COSMI

This dissertation has been approved by the promotors.

Composition of the doctoral committee:

Rector Magnificus,	chairperson
Prof. dr. F.J. Beekman,	Delft University of Technology, *promotor*
Dr.ir. M.C. Goorden,	Delft University of Technology, *copromotor*
Independent members:	
Prof. dr. B. Rieger	Delft University of Technology
Prof. dr. ir. C. Tsoumpas	University Medical Center Groningen / University of Groningen
Dr. B. Vastenhouw	MILabs B.V.
Prof. dr. F. A. Verburg	Erasmus Medical Center
Prof. dr. ir. H. H. Weinans	Delft University of Technology

The research leading to this thesis was financed by the Dutch Research Council (NWO) under the research grant QUARAT: Quantitative Universal Radiotracer Tomography (TTW16885).

Keywords: preclinical, SPECT, PET, collimator, pinhole, gamma camera, image reconstruction, molecular imaging, Monte Carlo simulation

Printed by: Proefschriftenprinten

Cover by: Foreground: Schematic image of a Super-Cluster collimator. Background: Microsoft designer.

ISBN 978-90-836415-8-4

An electronic copy of this dissertation is available at `https://repository.tudelft.nl/`.

Contents

Summary

Imaging the biodistribution of radioisotopes in living organisms enables non-invasive visualization, characterization, and quantification of biological processes at the molecular and cellular levels. This capability plays a critical role in both clinical and preclinical settings. In clinical practice, radioisotope imaging is applied across various fields such as cardiology, neurology, and oncology. It supports early disease detection, diagnosis, staging, and treatment monitoring, while also guiding personalized, disease-specific therapies. In preclinical research, it is widely used in small-animal studies (e.g., mice and rats) to investigate disease mechanisms and assess therapeutic interventions. This facilitates drug discovery and validation, ultimately accelerating the development of new diagnostic and therapeutic strategies. The imaging techniques that visualize these radiolabeled tracer distributions are single photon emission computed tomography (SPECT) and positron emission tomography (PET). This thesis focuses on their instrumentation in preclinical imaging applications.

SPECT and PET differ in the types of radioactively labeled molecules (radiotracers or radiopharmaceuticals) they image, resulting in distinct design and operational characteristics for each modality's scanner. SPECT systems image single-gamma emitting isotopes using mechanical collimators that selectively transmit photons based on their direction. These transmitted gamma photons are then detected by a gamma camera, typically consisting of a large continuous scintillation crystal coupled to an array of photomultiplier tubes (PMTs). The crystal converts each gamma photon into thousands of visible light photons, which are subsequently detected by the PMTs to estimate the position of the original gamma interaction. PET systems, on the other hand, image positron-emitting isotopes. The emitted positron quickly annihilates with an electron, producing a pair of 511 keV photons emitted in nearly opposite directions. PET scanners commonly use block detectors (arrays of segmented scintillation crystals arranged in rings) to enable coincidence detection of these photon pairs, a process known as electronic collimation. Although electronic collimation is the standard in PET, some systems have adopted mechanical collimation similar to SPECT, and are referred to as mechanically collimated PET systems. This configuration has facilitated the development of systems that combine mechanically collimated PET and SPECT into a single platform, allowing for truly simultaneous dual-modality imaging. One such system is VECTor (MILabs B.V.), the imaging platform employed in this study.

Thanks to its advanced collimation strategy, VECTor enables sub-mm resolution imaging across an extended energy range (30 keV to 1 MeV), significantly broader than that of conventional SPECT systems (30 keV to 350 keV). This expanded range enables the

imaging of several radionuclides that emit high-energy gamma photons (> 350 keV) and are increasingly being investigated for therapeutic and theranostic applications. These radionuclides were previously overlooked due to the difficulty of producing high-quality images of their distributions, caused by factors such as excessive photon penetration and reduced detection sensitivity, both of which degrade spatial resolution and quantitative accuracy. The current VECTor configuration can overcome such limitations and already delivers strong performance in this domain, yet further improvements remain both feasible and desirable.

Enhancing performance in such systems, however, presents significant challenges due to the complex interplay of physical effects and technical limitations. These can be addressed through both software and hardware advancements, for instance, by exploring alternative image reconstruction techniques or by optimizing key components such as the detector or collimator. In this context, the present thesis offers a simulation-based investigation of the preclinical PET/SPECT system VECTor, focusing on strategies to improve image quality in high-energy imaging scenarios.

First, we assessed the system's capability to handle radionuclides that emit prompt gammas across a broad energy range (603 keV to 2.2 MeV), for which achieving high resolution with conventional PET systems is challenging. This evaluation included the radionuclides ^{52}Mn, ^{94}Tc, ^{89}Zr, ^{44}Sc, ^{86}Y, ^{72}As, ^{124}I, ^{38}K, and ^{66}Ga. The results demonstrate that sub-millimeter resolution is achievable for most isotopes up to 1.4 MeV with the current collimator configuration. These findings highlight the robustness of clustered pinhole (CP) collimation and may open new avenues for tracer development and therapeutic applications using these PET isotopes.

To improve image quality, particularly under low-activity conditions, we proposed and evaluated alternative reconstruction methods based on multi-photopeak joint reconstruction for isotopes that emit gammas at different energies (captured in different photopeaks), as opposed to relying on a single photopeak. Three reconstruction strategies were compared, each differing in how information from multiple gamma peaks was combined and retained. These methods were tested in simulations using resolution phantoms containing rods of various diameters filled with either ^{225}Ac, ^{226}Ac, or ^{89}Zr. The joint reconstruction approach consistently outperformed the single-photopeak method, particularly by enhancing the contrast-to-noise ratio in the smallest distinguishable rods. These results demonstrate the potential of joint multi-photopeak reconstruction to enhance both image quality and quantitative accuracy in SPECT, PET, and PET/SPECT, particularly in low-count scans.

After evaluating reconstruction methods, we turned our attention to hardware-based strategies for enhancing system performance, starting with the gamma detector. Conventional SPECT gamma detectors typically use 9.5 mm thick NaI(Tl) scintillation crystals, which offer excellent sensitivity at standard SPECT energies (e.g., about 90% photopeak efficiency for ^{99m}Tc at 140 keV) but perform poorly with higher-energy gamma photons (e.g., roughly 12% photopeak efficiency for ^{18}F at 511 keV). This reduced sensitivity at higher energies limits overall system performance and degrades image quality when

imaging radionuclides emitting high-energy gamma rays. To overcome this, we analyzed gamma camera configurations optimized for high-energy imaging by varying scintillation crystal and light guide thicknesses, as well as PMT shapes and arrangements. Performance was evaluated at both conventional (140 keV) and high (511 keV) gamma energies. The results demonstrated that thicker crystals can substantially improve sensitivity, with only modest spatial resolution loss when paired with cost-effective PMTs, whereas using smaller, more expensive PMTs offers spatial performance improvements.

Following the evaluation of the gamma camera, we next directed our efforts toward the collimator design. Building on the characteristics of the currently used advanced clustered pinhole (CP) collimation geometry, a new Twisted Clustered Pinhole (TCP) collimator was proposed to improve performance in high-energy gamma imaging. The TCP collimator features a novel pinhole arrangement wherein individual pinholes are twisted around their cluster central axis. This allows to preserve the same field of view (FOV) as with CP while enabling the use of narrower pinhole opening angles to further reduce the degrading effects of pinhole edge penetration by high-energy gammas. A comparative study between the two collimators was conducted to assess sensitivity at matched system resolution and system resolution at matched sensitivity, using both low and high activity levels for ^{18}F and ^{89}Zr. The results show that the TCP collimator provides improved sensitivity and enhanced system resolution compared to the CP collimator. This study suggests that TCP collimation has potential to improve high-energy gamma imaging.

A limitation of both CP and TCP collimators is that the close proximity of pinholes within each cluster restricts simple geometric modifications, such as increasing the pinhole diameter, since this could lead to overlap between adjacent pinholes. To address this constraint, an alternative Super-Cluster (SC) collimator design was explored. The SC design features a more uniform pinhole distribution across the collimator surface, allowing straightforward adjustment of pinhole diameter to modulate the resolution-sensitivity trade-off. This level of flexibility, not available in CP or TCP collimation, is achieved while preserving the FOV size and the narrow opening angles required for high-energy applications. The performance of the SC collimator was evaluated using ^{18}F and ^{89}Zr at different activity concentrations. Compared to CP, SC increased sensitivity approximately threefold for ^{18}F and twofold for ^{89}Zr without introducing visible artifacts, confirming adequate angular sampling. This sensitivity gain proved to be particularly beneficial at low activity concentrations of ^{18}F and ^{89}Zr, resulting in improved image quality and greater quantitative accuracy. These results demonstrate that the added flexibility of the SC design can lead to significant improvements in both image quality and quantitative performance, particularly at low activity levels, highlighting its strong potential for sensitivity-limited applications.

The studies presented in this thesis provide deeper insight into the performance of the VECTor preclinical scanner and introduce several software and hardware approaches to enhance image quality, particularly for high-energy imaging. These findings are especially relevant given the growing interest in high-energy SPECT for imaging radionuclides with complex spectra and high-energy gamma emissions, which remain challenging for other modalities.

Samenvatting

Het in beeld brengen van de biodistributie van radio-isotopen in levende organismen maakt niet-invasieve visualisatie, karakterisering en kwantificering van biologische processen op moleculair en cellulair niveau mogelijk. Deze mogelijkheid speelt een cruciale rol in zowel klinische als preklinische toepassingen. In de klinische praktijk wordt radio-isotopenbeeldvorming toegepast in uiteenlopende vakgebieden zoals cardiologie, neurologie en oncologie. Het ondersteunt vroege ziektedetectie, diagnose, stadiëring en behandelingsmonitoring, en draagt tevens bij aan gepersonaliseerde, ziekte-specifieke therapieën. In preklinisch onderzoek wordt deze techniek veelvuldig toegepast in kleinedierenstudies (bijvoorbeeld muizen en ratten) om ziekte-mechanismen te onderzoeken en therapeutische interventies te evalueren. Dit versnelt het proces van geneesmiddelontwikkeling en validatie, en bevordert de ontwikkeling van nieuwe diagnostische en therapeutische strategieën. De beeldvormingstechnieken die de verdeling van deze radioactief gelabelde tracers zichtbaar maken, zijn single photon emission computed tomography (SPECT) en positron emission tomography (PET). Dit proefschrift richt zich op de instrumentatie van deze technieken binnen preklinische beeldvorming.

SPECT en PET verschillen in de soorten radioactief gelabelde moleculen (radiotracers of radiopharmaca) die zij in beeld brengen, wat resulteert in uiteenlopende ontwerp- en gebruikskenmerken van de scanners. SPECT-systemen beelden isotopen af die enkelvoudige gammastraling uitzenden, waarbij mechanische collimatoren worden gebruikt die fotonen selectief doorlaten afhankelijk van hun richting. Deze doorgelaten gammaphotonen worden vervolgens gedetecteerd door een gammacamera, doorgaans bestaande uit een groot continu scintillatiekristal gekoppeld aan een array van fotomultiplierbuizen (PMT's). Het kristal zet elk gammaphoton om in duizenden zichtbare lichtfotonen, die vervolgens door de PMT's worden gedetecteerd om de positie van de oorspronkelijke gamma-interactie te schatten. PET-systemen daarentegen beelden positron-emitterende isotopen af. Het uitgezonden positron annihileert vrijwel direct met een elektron, waarbij een paar fotonen van 511 keV in bijna tegengestelde richtingen worden uitgezonden. PET-scanners gebruiken doorgaans blokdetectoren (arrays van gesegmenteerde scintillatiekristallen die in ringen zijn geplaatst) om gelijktijdige detectie van deze fotonenparen mogelijk te maken, een proces dat elektronische collimatie wordt genoemd. Hoewel elektronische collimatie de standaard is in PET, zijn er systemen die mechanische collimatie toepassen, vergelijkbaar met SPECT. Deze worden mechanisch gecollimeerde PET-systemen genoemd. Deze configuratie heeft geleid tot de ontwikkeling van systemen die mechanisch gecollimeerde PET en SPECT combineren in één platform, waardoor werkelijk simultane dual-modality beeldvorming mogelijk is. Een dergelijk systeem is VECTor (MILabs B.V.), het beeldvormingsplatform dat in dit onderzoek wordt gebruikt.

Dankzij zijn geavanceerde collimatiestrategie maakt VECTor beeldvorming met submillimeterresolutie mogelijk over een uitgebreid energiebereik (30 keV tot 1 MeV), aanzienlijk breder dan dat van conventionele SPECT-systemen (30 keV tot 350 keV). Dit vergrote bereik maakt de beeldvorming van verschillende radionucliden mogelijk die hoog-energetische gammaphotonen (> 350 keV) uitzenden en die steeds vaker worden onderzocht voor therapeutische en theranostische toepassingen. Deze radionucliden werden voorheen vaak genegeerd vanwege de moeilijkheid om beelden van hoge kwaliteit te verkrijgen van hun verdelingen, veroorzaakt door factoren zoals excessieve fotonpenetratie en verminderde detectiegevoeligheid, die beide leiden tot een lagere ruimtelijke resolutie en kwantitatieve nauwkeurigheid. De huidige VECTor-configuratie kan dergelijke beperkingen grotendeels overwinnen en levert al sterke prestaties op dit gebied, hoewel verdere verbeteringen zowel mogelijk als wenselijk blijven.

Het verbeteren van de prestaties van dergelijke systemen brengt aanzienlijke uitdagingen met zich mee, vanwege de complexe wisselwerking tussen fysieke effecten en technische beperkingen. Deze uitdagingen kunnen worden aangepakt door middel van zowel software- als hardwareontwikkelingen, bijvoorbeeld door het verkennen van alternatieve beeldreconstructietechnieken of door het optimaliseren van cruciale componenten zoals de detector of de collimator. In dit kader presenteert dit proefschrift een simulatiegebaseerd onderzoek naar het preklinische PET/SPECT-systeem VECTor, met als doel strategieën te ontwikkelen ter verbetering van de beeldkwaliteit bij hoog-energetische beeldvorming.

Ten eerste hebben wij het vermogen van het systeem beoordeeld om radionucliden af te beelden die prompt gammas uitstralen over een breed energiebereik (603 keV tot 2.2 MeV), waarvoor het bereiken van hoge resolutie met conventionele PET-systemen een uitdaging vormt. Deze evaluatie omvatte de radionucliden ^{52}Mn, ^{94}Tc, ^{89}Zr, ^{44}Sc, ^{86}Y, ^{72}As, ^{124}I, ^{38}K en ^{66}Ga. De resultaten tonen aan dat submillimeterresolutie haalbaar is voor de meeste isotopen tot 1,4 MeV met de huidige collimatorconfiguratie. Deze bevindingen onderstrepen de robuustheid van clustered pinhole (CP) collimatie en kunnen nieuwe mogelijkheden openen voor tracerontwikkeling en therapeutische toepassingen met deze PET-isotopen.

Om de beeldkwaliteit te verbeteren, met name bij lage activiteit, hebben wij alternatieve reconstructiemethoden voorgesteld en geëvalueerd op basis van multi-photopeak joint reconstruction voor isotopen die gammas uitzenden op verschillende energieën (gedetecteerd in verschillende photopeaks), in plaats van te vertrouwen op één enkele photopeak. Drie reconstructiestrategieën zijn vergeleken, die elk verschilden in de manier waarop informatie van meerdere gammapieken werd gecombineerd en behouden. Deze methoden zijn getest in simulaties met resolutiefantomen die staafjes van verschillende diameters bevatten, gevuld met ^{225}Ac, ^{226}Ac of ^{89}Zr. De gezamenlijke reconstructiebenadering presteerde consequent beter dan de single-photopeak methode, met name door de contrast-ruisverhouding in de kleinste onderscheidbare staafjes te verbeteren. Deze resultaten tonen het potentieel van gezamenlijke multi-photopeak reconstructie om zowel de beeldkwaliteit als de kwantitatieve nauwkeurigheid te verbeteren in SPECT, PET en PET/SPECT, vooral bij low-count scans.

Na de reconstructiemethoden te hebben geëvalueerd, richtten we ons op hardwarematige strategieën ter verbetering van de systeemprestaties, te beginnen met de gammadetector. Conventionele SPECT-gammacamera's gebruiken doorgaans 9,5 mm dikke NaI(Tl)-scintillatiekristallen, die een uitstekende gevoeligheid bieden bij standaard SPECT-energieën (bijv. ongeveer 90% photopeak-efficiëntie voor ^{99m}Tc bij 140 keV), maar slecht presteren bij hoogenergetische gammaphotonen (bijv. ongeveer 12% photopeak-efficiëntie voor ^{18}F bij 511 keV). Deze verminderde gevoeligheid bij hogere energieën beperkt de systeemprestaties en verslechtert de beeldkwaliteit bij het afbeelden van radionucliden die hoog-energetische gammas uitzenden. Om dit te verhelpen hebben we gammacamera-configuraties geanalyseerd die geoptimaliseerd zijn voor hoog-energetische beeldvorming, door variaties in scintillatiekristaldiktes en lichtgeleiders, evenals PMT-vormen en -opstellingen. De prestaties zijn geëvalueerd bij zowel conventionele (140 keV) als hoge (511 keV) gamma-energieën. De resultaten toonden aan dat dikkere kristallen de gevoeligheid aanzienlijk kunnen verbeteren, met slechts een bescheiden verlies in ruimtelijke resolutie wanneer ze worden gecombineerd met kosteneffectieve PMT's, terwijl kleinere, duurdere PMT's verbeteringen in ruimtelijke prestaties bieden.

Na de analyse van de gammacamera hebben we ons vervolgens gericht op het ontwerp van de collimator. Op basis van de kenmerken van de huidige geavanceerde clustered pinhole (CP) collimatiegeometrie werd een nieuwe Twisted Clustered Pinhole (TCP) collimator voorgesteld om de prestaties bij hoog-energetische gamma-beeldvorming te verbeteren. De TCP-collimator introduceert een nieuw ontwerp waarin individuele pinholes rond hun cluster-centrale as worden gedraaid. Dit maakt het mogelijk hetzelfde field of view (FOV) te behouden als bij CP, terwijl nauwere pinhole-hoeken gebruikt kunnen worden om de verstorende effecten van pinhole-randpenetratie door hoogenergetische gammas verder te verminderen. Een vergelijkende studie tussen beide collimatoren werd uitgevoerd om de gevoeligheid bij gelijke systeemresolutie en de systeemresolutie bij gelijke gevoeligheid te beoordelen, met gebruik van zowel lage als hoge activiteitsniveaus voor ^{18}F en ^{89}Zr. De resultaten laten zien dat de TCP-collimator verbeterde gevoeligheid en hogere systeemresolutie biedt vergeleken met de CP-collimator. Deze studie suggereert dat TCP-collimatie potentieel heeft om de beeldvorming van hoogenergetische gammas te verbeteren.

Een beperking van zowel CP- als TCP-collimatoren is dat de nauwe nabijheid van pinholes binnen een cluster eenvoudige geometrische aanpassingen belemmert, zoals het vergroten van de pinhole-diameter, aangezien dit zou kunnen leiden tot overlapping tussen aangrenzende pinholes. Om dit probleem te omzeilen is een alternatief Super-Cluster (SC) collimatorontwerp onderzocht. Het SC-ontwerp kenmerkt zich door een meer uniforme pinhole-verdeling over het collimatoroppervlak, waardoor het eenvoudig wordt om de pinhole-diameter aan te passen en zo de resolutie-gevoeligheidsafweging te moduleren. Dit niveau van flexibiliteit, niet aanwezig in CP- of TCP-collimatie, wordt bereikt met behoud van FOV-grootte en de nauwe openingshoeken die vereist zijn voor hoog-energetische toepassingen. De prestaties van de SC-collimator zijn geëvalueerd met ^{18}F en ^{89}Zr bij verschillende activiteitconcentraties. Vergeleken met CP verhoogde SC de gevoeligheid ongeveer driemaal voor ^{18}F en tweemaal voor ^{89}Zr, zonder zichtbare artefacten te introduceren, wat een adequate hoekbemonstering bevestigt. Deze gevoe-

ligheidswinst bleek bijzonder waardevol bij lage activiteitconcentraties van ^{18}F en ^{89}Zr, wat resulteerde in verbeterde beeldkwaliteit en grotere kwantitatieve nauwkeurigheid. Deze resultaten tonen aan dat de extra flexibiliteit van het SC-ontwerp kan leiden tot aanzienlijke verbeteringen in zowel beeldkwaliteit als kwantitatieve prestaties, vooral bij lage activiteitsniveaus, en benadrukken het sterke potentieel voor toepassingen die beperkt worden door gevoeligheid.

De studies die in dit proefschrift worden gepresenteerd bieden diepere inzichten in de prestaties van de VECTor-preklinische scanner en introduceren verschillende software- en hardwarebenaderingen om de beeldkwaliteit te verbeteren, met name voor hoog-energetische beeldvorming. Deze bevindingen zijn bijzonder relevant gezien de groeiende belangstelling voor hoog-energetische SPECT bij de beeldvorming van radionucliden met complexe spectra en hoog-energetische gamma-emissies, die voor andere modaliteiten een blijvende uitdaging vormen.

1

Introduction

1.1. Nuclear medicine and the role of molecular imaging

Nuclear medicine stands at the forefront of biomedical innovation, driving advances in diagnostic tools and therapeutic strategies across preclinical, translational, and clinical research. These developments play a central role in molecular medicine, a field that emerged from the integration of biology and medicine. In this context, molecular imaging with radioisotopes has provided unprecedented insights into biological processes [1].

Molecular imaging encompasses nuclear imaging methods such as positron emission tomography (PET) [2, 3], single-photon emission computed tomography (SPECT) [4, 5], and planar gamma camera imaging, which use radioactively labeled molecules (radiotracers or radiopharmaceuticals). It also includes optical imaging modalities (OI or OPT), such as bioluminescence and fluorescence imaging, which rely on light-based signals. These techniques distinguish themselves from other imaging modalities by enabling the visualization, characterization, and quantification of a wide range of cellular and subcellular types of activity in living subjects [6, 7]. This capability allows for the detection of disease-related molecular and cellular mechanisms in vivo, providing functional information that complements the anatomical detail offered by imaging techniques such as X-ray radiography, computed tomography (CT), magnetic resonance imaging (MRI), and ultrasound.

This functional perspective has greatly advanced our understanding of disease pathophysiology, e.g., by clarifying how molecular alterations drive disease onset and progression. Such insights, along with the direct applications of nuclear imaging, support key clinical objectives including early disease detection, refinement of targeted therapies, monitoring of therapeutic response, and identification of disease recurrence. Clinical applications of molecular imaging now span across a broad spectrum of conditions, including cancer [8], bone and cardiovascular diseases [9, 10], neurological and psychiatric disorders [11, 12], as well as infections and inflammatory conditions [13, 14], thereby contributing to improved patient care worldwide.

Nowadays, molecular imaging also plays an essential role in preclinical research (Fig. 1.1) [15, 16], which often relies on small animal models such as mice and rats. These animals are widely used due to their genetic and physiological similarities to humans, ease of handling, and short reproductive cycles. Such models facilitate the investigation of disease mechanisms and enhance drug discovery and validation efforts, thereby accelerating the development of effective diagnostics and therapeutics [17].

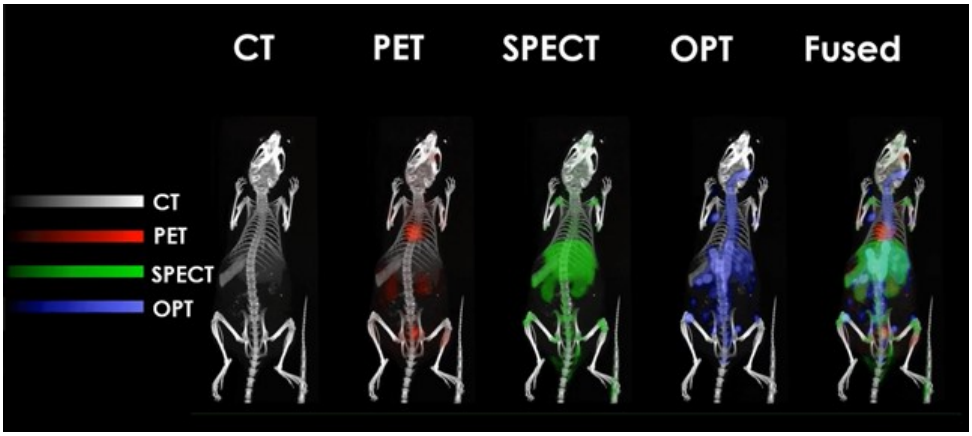

Figure 1.1: Complementary imaging information obtained in a single multi-modal scan of a mouse. Image courtesy of MILabs (*Utrecht, The Netherlands).* Reproduced with permission.

These advantages establish the significance of preclinical imaging in research, and this thesis addresses this by focusing on preclinical PET and SPECT instrumentation. The following sections describe the fundamental principles of both modalities, as well as the characteristics of their respective instrumentation.

1.2. PET and SPECT: mechanisms, strengths, and limitations

PET and SPECT both utilize radiotracers, which are most commonly administered by injection into the subject, enter the bloodstream, circulate, and gradually accumulate in specific target regions. These radiotracers continuously undergo radioactive decay, emitting radiation from wherever they are present. This radiation is detected externally by one or multiple arrays of detectors that may be stationary or rotate around the subject, producing images known as projections. By acquiring projection data from multiple angles, three-dimensional (3D) images can be computed, providing an estimate of the 3D radiotracer distribution within the subject, a process called image reconstruction. The resulting images can reveal, for example, tracer accumulation in tumors (known as 'hot spots'), as well as tracer uptake in the heart, which may indicate blood flow, innervation, or tissue viability, and in the brain, which may suggest neurodegenerative diseases or tumors.

Although PET and SPECT share a similar imaging workflow, they differ in the radionuclides employed and the range of available tracers (Fig. 1.2).

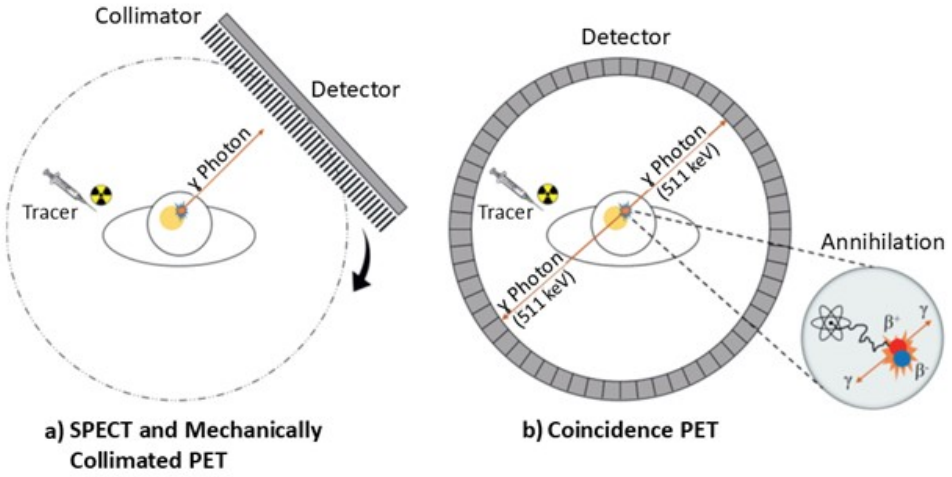

Figure 1.2: Working principle of a) SPECT or PET using mechanical collimation and b) traditional PET based on coincidence detection. The figure is adapted from [18], reproduced with permission.

PET uses radiotracers labeled with positron-emitting radionuclides. The emitted positrons typically annihilate with electrons within one or a few millimeters from their point of emission, producing pairs of high-energy (511 keV) annihilation photons that travel in nearly opposite directions. Clinical PET systems detect these photons in near coincidence, that is when the two photons are detected almost simultaneously by opposing detectors. This allows the system to localize the line where the annihilation occurred, known as the line of response (LOR), which connects the two detectors that registered the photon pair. This technique, called coincidence detection, forms the basis of clinical PET as well as a large fraction of preclinical PET scanners. While this is the dominant approach, some preclinical PET systems, such as those investigated in this thesis, take a different route by incorporating mechanical collimators [19], and are referred to as mechanically collimated PET systems.

By comparison, SPECT employs radiotracers labeled with gamma-emitting radionuclides. SPECT systems typically use a mechanical collimator, which permits only photons traveling along specific directions to reach the detector while blocking those on other paths. This selective filtering enables the collimator to acquire a two-dimensional (2D) projection image of the radiotracer distribution, which is effectively a large set of LORs.

The fundamental differences in detection mechanisms lead to distinct strengths and limitations. For large subjects (e.g. clinical applications), PET offers significantly higher sensitivity, by two to three orders of magnitude, thanks to coincidence detection, which eliminates the need for physical collimators. Clinical PET scanners also provide better spatial resolution, typically ~3 mm [20–22], whereas general-purpose clinical SPECT

systems generally achieve resolutions of 8-10 mm [23–26]. For preclinical PET scanners, however, spatial resolution typically ranges from 0.6 to 4 mm [27] and is ultimately constrained by intrinsic physical factors. These include positron range, which is the distance a positron travels before annihilating with an electron; photon non-collinearity; random coincidences; and detector-related effects such as intrinsic resolution and variations in depth of interaction (DOI). Preclinical SPECT, in contrast, by detecting single photons directly, avoids or significantly reduces many of these limitations. It is not affected by positron range, photon non-collinearity, or random coincidences. This reduction in degrading effects, combined with carefully optimized system design choices that will be discussed later, can result in substantially higher spatial resolution, down to 0.25 mm in *vivo* [28], which further improves to 120 μm *ex vivo* [29].

One of SPECT's key advantages over PET is its capacity to easily perform simultaneous multi-tracer imaging. In PET, this capability is highly limited as all positron-emitting isotopes produce gamma-photons of the same energy (511 keV), preventing energy-based discrimination. In contrast, different SPECT isotopes often emit gamma-photons at distinct energies, allowing for energy discrimination between tracers. These emissions may originate directly from the primary decay process, from prompt gamma emissions that occur immediately as the daughter nucleus transitions from an excited to a stable state, or from delayed gamma emissions produced by subsequent decay products. Each emission type usually generates photons at characteristic energies, giving rise to photopeaks, which are distinct peaks visible in the energy spectrum (Fig. 1.3). By selecting tracers with non-overlapping energy spectra, it becomes possible to differentiate and quantify multiple physiological or pathological processes within a single scan, as projection images corresponding to different tracers can be acquired and stored separately. However, this approach introduces technical challenges. A critical factor to consider is downscatter: high-energy photons can undergo Compton scattering before reaching the detector, losing energy and deviating from their original path. These scattered photons may then fall within the energy acceptance windows of tracers with lower-energy emissions and be unintentionally registered, resulting in image haziness and quantification errors. Addressing these effects requires careful energy window selection and correction algorithms to preserve the integrity of multi-tracer imaging. Beyond its technical advantages, SPECT also offers important practical benefits, being generally more accessible and cost-effective than PET.

Despite their differences in detection mechanisms and imaging capabilities, both PET and SPECT systems fundamentally rely on gamma detectors to convert incoming photon interactions into measurable signals. These detectors are central to image formation and play a critical role in determining system performance, including spatial resolution, sensitivity, and energy discrimination. Therefore, a deep understanding of gamma detector design and limitations is essential for guiding the technological improvements that drive progress in PET and SPECT imaging.

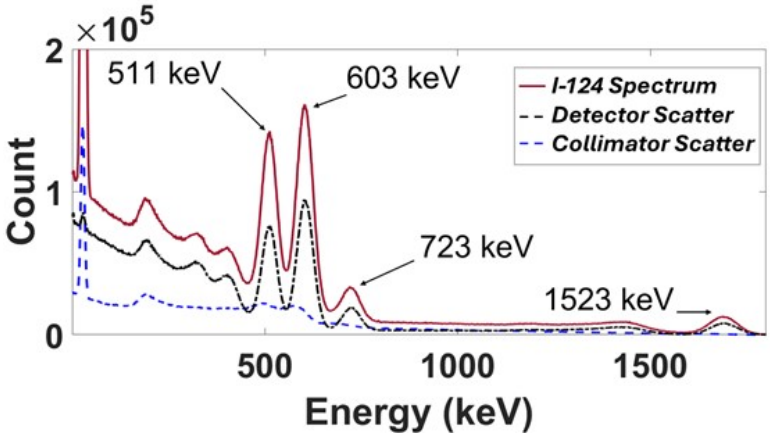

Figure 1.3: Energy spectrum for ^{124}I where the main emissions are shown. Collimator and detector downscatter spectra are also shown. The figure is adapted from [30], licensed under CC BY 4.0.

1.3. Basic principles of gamma detectors

Gamma detectors are systems designed to detect gamma photons and convert their deposited energy into electrical signals, which can then be processed to generate images or perform quantitative analysis. Gamma photons can interact with matter through several physical mechanisms, each with distinct consequences for energy deposition. The most relevant interactions include the photoelectric effect, Compton scattering, and, at higher energies, pair production. In the photoelectric effect, the photon is entirely absorbed and its energy is transferred to an electron. In Compton scattering, the photon is deflected and part of its energy is transferred to an electron, while the scattered photon continues with reduced energy. At high energies (> 1 MeV), pair production can occur, where the photon disappears and its energy is used to create an electron-positron pair.

The effectiveness of a gamma detector in capturing these interactions depends on its characteristics. The majority of gamma detectors are composed of a scintillation crystal, such as sodium iodide doped with thallium (NaI(Tl)), lutetium-yttrium oxyorthosilicate (LYSO), or bismuth germanate (BGO), which converts the deposited gamma energy into visible light. This light is then detected by photodetectors, such as photomultiplier tubes (PMTs) or silicon photomultipliers (SiPMs), which convert the light into an electrical signal proportional to the original deposited energy. Finally, dedicated electronics process these signals to extract essential information such as energy, spatial gamma interaction location, and timing, enabling accurate detection and image reconstruction.

Although the basic structure of gamma detectors remains consistent, their configuration is tailored to meet the needs of different imaging modalities. In PET, this often results in block detectors composed of segmented scintillation crystals coupled to arrays of photodetectors. In SPECT, the most widely adopted configuration is the Anger camera, which typically employs a large continuous scintillation crystal read out by an array of

photodetectors.

The Anger camera, or gamma camera, was first introduced by Hal Anger in 1953 and has since undergone significant refinement [31, 32]. While other nuclear imaging technologies have emerged over the years, the gamma camera remains unparalleled in its balance of image quality, detection efficiency, and practical utility. Traditionally, it comprises a collimator, a large-area scintillation crystal, a light guide, and an array of photomultiplier tubes (PMTs), though certain designs have since been developed that exclude the collimator altogether. In preclinical applications, the scintillation crystal is often made of NaI(Tl) and typically has a thickness of 9.5 mm, though thicker (e.g. ~14 or ~20 mm) crystals are also available. The thinner crystals are well suited for detecting gamma photons within the energy range typically encountered in SPECT imaging (30−350 keV), offering an effective compromise between sensitivity and spatial resolution. The thicker crystals are generally employed in theranostic or PET/SPECT applications, where photon energies are significantly higher (e.g. 511 keV for annihilation photons, or even higher in certain scenarios) than in conventional SPECT and require greater detection capability to maintain high image quality.

Beyond the individual physical components, understanding how they interact during the imaging process is essential to appreciate the functionality of the gamma camera as a whole. The fundamental principles of image formation with a gamma camera are illustrated in Figure 1.4.

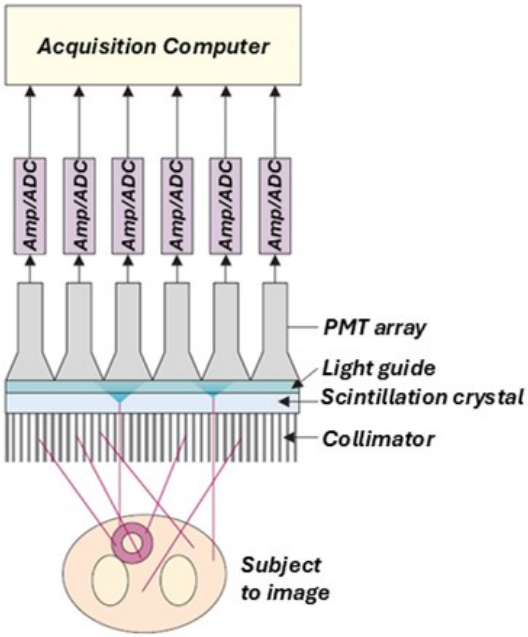

Figure 1.4: Basic principles and components of a gamma camera. Image adapted from [33], © 2012 Elsevier.

The imaging process begins with the emission of gamma photons from a radiotracer distributed within the subject. These photons travel towards the collimator, which selectively allows those traveling in specific directions to reach the scintillation crystal, providing 2D spatial information that reflects the 3D distribution of the tracer. Upon interaction with the crystal, the radiation produces scintillation photons that are transmitted through the light guide to the PMTs. The resulting signals are amplified, digitized, and processed by the acquisition system to determine the energy and spatial coordinates of each detected event.

While this process forms the backbone of gamma imaging, translating it into high-quality images is not without challenges. Image quality is not determined by a single factor, but rather by the interplay of multiple parameters, including spatial resolution and sensitivity. In SPECT, these are shaped by the detector's intrinsic characteristics and, even more critically, by the collimator, which plays a central role in defining the overall system's performance [34].

1.4. Collimators in preclinical SPECT

The collimator controls how gamma photons from the radiotracer distribution are directionally filtered and projected onto the detector. It is typically constructed from dense, highly attenuating materials such as lead, tungsten, or specialized alloys. It may contain one or multiple holes, whose shape and arrangement determine the collimator type, such as pinhole, parallel hole, diverging, or converging (Fig. 1.5).

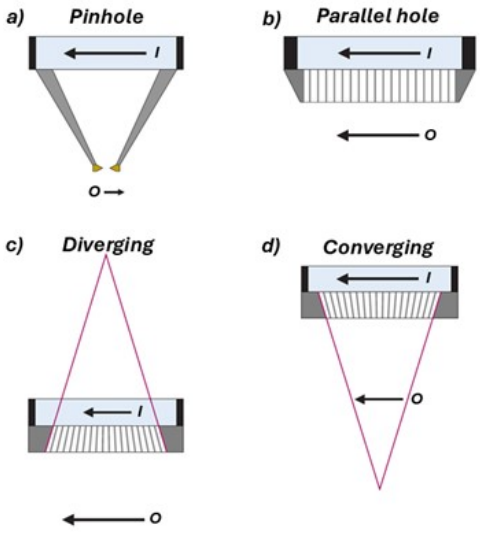

Figure 1.5: Schematic representation of different collimator types. 'O' denotes the object being imaged, and 'I' indicates its projected image on the detector. Image adapted from [33], © 2012 Elsevier.

In preclinical applications, where objects are typically small and fine spatial detail is essential, pinhole collimators have become the most widely used design [34].

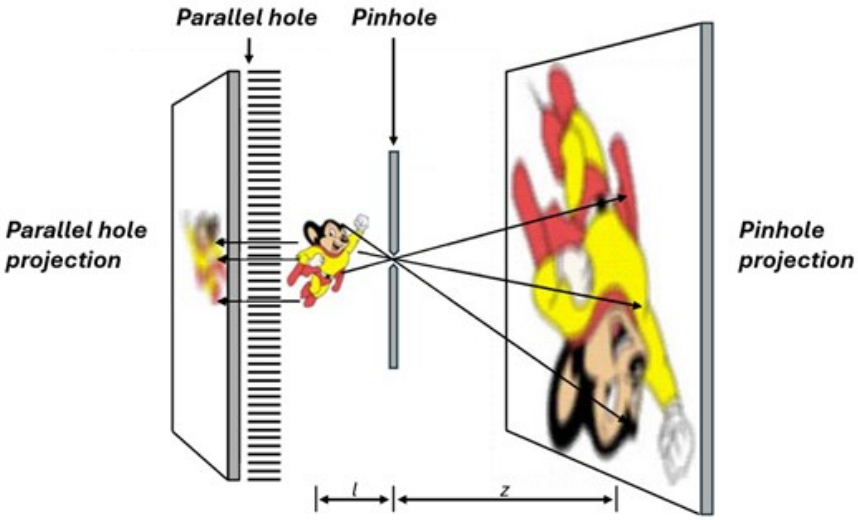

Figure 1.6: Projections using a parallel-hole collimator and a pinhole collimator. With parallel-hole collimation (left), intrinsic camera blurring significantly degrades resolution. Pinhole imaging (right) reduces this blurring effect by magnifying the object onto the projection. The figure is adapted from [35], © Springer Nature 2007, reproduced with permission.

This preference stems from their ability to mitigate image degradation associated with the detector's intrinsic limitations. These limitations arise from several physical characteristics, including the spread of scintillation light within the crystal, the limited number of photons generated per gamma interaction (which introduces positional uncertainty), and the finite spatial resolution of position-sensitive photodetectors. Together, these factors define the detector's intrinsic spatial resolution, typically around 3.5 mm in most clinical and preclinical NaI detectors, which significantly constrains the overall achievable image resolution. Pinhole collimators overcome this limitation by magnifying the object's projection onto the detector. The degree of magnification depends on the system geometry, in particular the relative distances between the object, the pinhole, and the detector surface, and directly influences how effectively the intrinsic resolution is compensated. Specifically, since the image is first magnified and then scaled back to its original size, the final blurring applied is not determined by the intrinsic resolution itself, but rather by that value divided by the magnification factor (e.g., with a magnification of 14 times, a resolution of 0.25 mm can be reached), resulting in sharper images.

To further enhance pinhole collimators' performance, modern designs often incorporate multiple pinholes [36]. This multi-pinhole approach improves both axial and angular sampling by capturing multiple projections simultaneously, allowing the use of stationary detectors [37–39]. The combination of improved sampling and increased system

sensitivity, resulting from the greater number of pinholes being used, contributes to superior overall image quality, reduced acquisition times, and lower radiotracer doses.

Due to the significant impact collimators have on imaging performance, preclinical systems incorporate specialized designs tailored to the unique demands of small-animal imaging. One such system is the Versatile Emission Computed Tomography (VECTor) platform [40], developed by MILabs B.V. (Utrecht, The Netherlands), which was modeled and simulated in this thesis.

1.5. VECTor: a preclinical PET and SPECT system

VECTor is a unique integrated PET/SPECT system that uses pinhole imaging for both modalities, enabling simultaneous SPECT and PET acquisitions that produce perfectly aligned images in space and time. This allows for direct correlation of different tissue functions, leveraging the complementary strengths of SPECT and PET to provide more comprehensive insights into biological processes, especially when appropriate radiolabeled tracers are employed. Integrated systems like VECTor also offer practical advantages, including reduced operating costs, shorter imaging and training times, minimized floor space requirements, and the ability to conduct dual-modality imaging under a single dose of anesthesia.

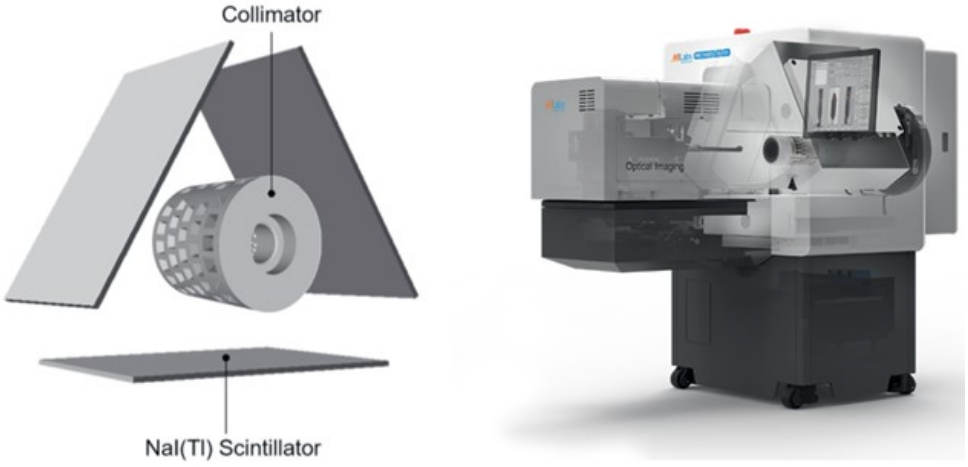

Figure 1.7: Schematic representation of the VECTor system's triangular detector setup alongside a realistic see-through rendering of the complete system. Image courtesy of MILabs (*Utrecht, The Netherlands)*. Reproduced with permission.

The system features three PMT-based, large-area monolithic NaI(Tl) scintillation detectors, each measuring 590×470 mm and available in thicknesses of 9.5 mm or 19 mm, arranged in a stationary triangular configuration (Fig. 1.7). Combined with advanced collimation strategies, this detector configuration enables sub-mm resolution

imaging over a broad energy range, from 30 keV to 1 MeV [41–45]. As a result, VECTor supports a wide variety of advanced imaging applications, including simultaneous SPECT and PET, multi-isotope PET, therapeutic radionuclide imaging, and positron-range-free PET. The system's performance has been extensively validated in these applications. For example, VECTor has demonstrated excellent results in simultaneous imaging of ^{99m}Tc (140 keV) and ^{18}F (511 keV), already achieving spatial resolutions of 0.50 mm and 0.80 mm, respectively, with its prototype [40], and currently reaching 0.40 mm SPECT resolution and 0.60 mm PET resolution with the same collimator. It has also proven capable of imaging therapeutically relevant radionuclides that are challenging due to their high-energy emissions. Notably, gamma rays from radionuclides such as ^{131}I (364 keV) and ^{213}Bi (440 keV) were successfully imaged, yielding resolutions down to 0.55 mm and 0.70 mm, respectively [46, 47]. Furthermore, the system supports prompt gamma imaging, which avoids degradation from positron range and enables positron-range-free and energy-discriminated multi-isotope PET. Prompt gamma imaging with ^{89}Zr (909 keV) and ^{124}I (603 keV) achieved resolutions of 0.75 mm [45], while simultaneous PET imaging with ^{18}F and ^{124}I was likewise performed at the same resolution [45].

These imaging capabilities are made possible by the system's advanced high-energy collimation technology. The design of advanced collimators involves careful optimization of numerous interdependent parameters. These include the number of pinholes, their diameter, their opening angle, their spatial arrangement, the material of the collimator, distances from the pinholes to both the object and the detector, and the extent of overlap between pinhole projections onto the detector. These parameters create a complex design space with many inherent trade-offs, particularly between spatial resolution and sensitivity, as improving one often comes at the expense of the other. For this reason, collimator design often starts by fixing one parameter (e.g., desired resolution) and optimizing the others accordingly.

Given the complexity of collimator design, the next section delves into how these principles were applied to develop VECTor's high-performance collimation system.

1.6. Clustered pinhole technology

At the core of VECTor capabilities is the clustered pinhole (CP) collimator [48, 49] (Fig. 1.8). The CP collimator is constructed from a tungsten alloy and is characterized by a cylindrical shape with significant wall thickness, allowing for efficient collimation of high-energy photons. It features pinholes with small diameters of 0.70 mm and narrow opening angles of 18° or 16°, arranged in 2×2 clusters. This clustered design enables the use of smaller opening angles than those typically used in traditional multi-pinhole configurations, while maintaining the same field-of-view (FOV). The use of these reduced angles helps mitigate the likelihood of pinhole edge penetration, a phenomenon where gamma photons pass through the edges of the pinholes instead of being properly collimated. This effect is a major limitation of conventional designs, particularly at high energies, as it reduces image quality. By narrowing the pinhole opening angles, the CP

collimator increases the material thickness that photons must traverse near the pinhole edges, improving the rejection of off-angle photons and thus enhancing image quality.

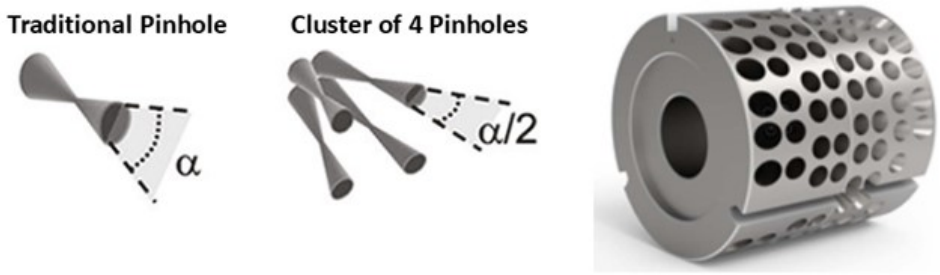

Figure 1.8: Images of the clustered pinhole collimator and schematic representation of its geometry. The figures are adapted from [45, 48]; [45] licensed under CC BY 4.0, [48] © 2010 IOP Publishing, reproduced with permission.

Despite the strong performance of the current system with CP collimators, further improvements in image quality remain both desirable and feasible as shown in this thesis.

1.7. Improving image quality

Improving the image quality of an imaging system is inherently complex, as various physical effects and technical limitations can degrade performance. Notably, effects such as photon downscatter and positron range blurring, introduced earlier, are important contributors to image degradation. In the context of high-energy imaging, additional challenges emerge. One major limitation is the reduced sensitivity of conventional gamma cameras, typically equipped with 9.5 mm thick crystals, for detecting high-energy photons (> 511 keV). These photons are more likely to penetrate through the crystal and escape detection (~70% for 511 keV), resulting in lower counting efficiency and reduced quantitative accuracy. To compensate, thicker scintillation crystals are often used. However, this increases the uncertainty in determining the DOI, negligible in 9.5 mm thick crystals, because gamma photons can interact over a wider range of depths within the crystal. DOI uncertainty refers to the discrepancy between the apparent and true interaction positions, caused by the detector's limited ability to accurately determine the depth at which the interaction occurred. This lack of DOI information leads to parallax errors that ultimately degrade spatial resolution.

These effects often interact in non-trivial ways, making it clear that addressing them in isolation is insufficient. Instead, improving performance requires a system-level approach, where key factors such as spatial resolution and sensitivity must be carefully balanced. To be effective, such solutions must also consider technical feasibility and practical constraints, ensuring performance gains without adding excessive complexity

or sacrificing usability and adaptability.

Strategies to achieve this can be implemented at both the software and hardware levels [50]. In software, advances in image reconstruction methods have been shown to significantly improve performance [51–54]. For example, accurately modeling high-energy annihilation photon transport and accounting for variable DOI within the detector contributed to such improvements [55]. Similarly, in hardware, various strategies can be applied depending on the targeted component [56–60]. For instance, increasing sensitivity by enlarging pinhole apertures has been shown to enhance image quality for standard SPECT and PET isotopes such as ^{99m}Tc and ^{18}F, particularly under low-activity conditions. When combined with a 19 mm thick scintillation crystal, this approach resulted in peak sensitivities of 12.4% and 17.0%, respectively [61].

These findings motivate further investigation into how software and hardware strategies can be applied to specific imaging systems to address practical challenges and enhance performance.

1.8. Research aims and thesis outline

This thesis aims to enhance the effective detection sensitivity and imaging performance of the preclinical PET/SPECT scanner VECTor, with a particular focus on high-energy imaging. This is achieved through optimized image reconstruction techniques and targeted modifications to the detector and collimator design. The study is based on simulation-driven investigations evaluating both software and hardware adaptations tailored to this context.

Chapter 2 explores the performance of the current VECTor system across an extended energy range from 600 keV to 2.2 MeV, evaluating how the system handles increasingly higher gamma energies and whether sub-mm resolution can be maintained at these elevated energies. To this end, a selection of PET isotopes was investigated, each with promising applications but also challenging imaging characteristics, such as long positron ranges, low positron emission probabilities, and significant downscatter. For each isotope, both annihilation photons and prompt gammas were used for image reconstruction, enabling a comparison of image resolution and uniformity to determine which emission type yielded superior image quality. **Chapter 3** presents the results of implementing advanced reconstruction techniques, specifically joint reconstruction methods, within the current image reconstruction workflow of the system. This approach provides a software-based solution to the challenge of low count data, which is often encountered when imaging theranostic isotopes. By simultaneously utilizing multiple gamma emissions from the same isotope, these methods leverage additional information to enhance image quality. A selection of isotopes was tested, and the performance of different joint reconstruction methods was evaluated using both visual inspection and quantitative analysis of resolution phantom images. **Chapter 4** analyzes a NaI(Tl) gamma camera by assessing how changes in crystal thickness, photomultiplier tube geometry, and light guide thickness influence the system's imaging performance. The

study quantifies the resolution–sensitivity trade-off to evaluate whether sensitivity can be enhanced without substantially compromising resolution. This analysis was conducted using photon energies typical of SPECT and PET imaging applications. **Chapter 5** introduces a novel collimator geometry designed to further enhance the performance of clustered pinhole (CP) technology by employing even narrower pinhole opening angles (POAs). This work highlights the geometric challenges of integrating such narrow POAs into a cluster configuration and presents a solution involving the rotation of pinholes around the cluster's central axis. The resulting design, referred to as twisted clustered pinholes (TCP), is proposed and characterized in this study, with its performance compared against that of conventional CP designs through full system simulations using specifically designed phantoms. **Chapter 6** presents an alternative collimator concept to that of **Chapter 5**, called the Super-Cluster (SC), aimed at simplifying the CP and TCP designs while still delivering excellent performance for high-energy imaging. The proposed geometry adopts a layout in which the pinholes within each ring are arranged in a fan-like pattern, forming what is known as a supercluster. This configuration yields a more uniform pinhole distribution across the collimator surface compared to the CP approach, while also enhancing design flexibility by allowing straightforward modulation of the resolution–sensitivity trade-off using pinhole diameters not feasible in CP or TCP configurations. Furthermore, it maintains the narrow POAs required for high-energy applications, while also preserving the FOV size. The performance of this novel design was assessed in comparison to the CP approach through comprehensive system simulations with dedicated phantoms. **Chapter 7** presents a synthesis of the main outcomes of this work, expands on the interpretation of the results, and outlines directions for future investigations in the field.

2

Ultra-high energy spectral prompt PET

This chapter is adapted from: Satyajit Ghosh, Valerio Cosmi, Ruud M. Ramakers, Freek J. Beekman and Marlies C. Goorden, Ultra-high energy spectral prompt PET. *Physics in Medicine & Biology*, 2025. 70(7).

Utilizing prompt gammas in preclinical pinhole-collimated positron emission tomography (PET) avoids image degradation due to positron range blurring and photon down scatter, enables multi-isotope PET and can improve counting statistics for low-abundance positron emitters. This was earlier reported for ^{124}I, ^{89}Zr and simultaneous ^{124}I - ^{18}F PET using the VECTor scanner (MILabs, The Netherlands), demonstrating sub-mm resolution despite long positron ranges. The aim of the present study is to investigate if such sub-mm PET imaging is also feasible for a large variety of other isotopes including those with extremely high energy prompt gammas (>1 MeV) or with complex emission spectra of prompt gammas.

We use Monte Carlo simulations to assess achievable image resolutions and uniformity across a broad range of spectrum types and emitted prompt gamma energies (603 keV-2.2 MeV), using ^{52}Mn, ^{94}Tc, ^{89}Zr, ^{44}Sc, ^{86}Y, ^{72}As, ^{124}I, ^{38}K, and ^{66}Ga.

Our results indicate that sub-mm resolution imaging may be feasible for almost all isotopes investigated, with the currently used cluster pinhole collimators. At prompt gamma energies of 603 keV of ^{124}I, an image resolution of ~0.65 mm was achieved, while for emissions at 703, 744, 834, and 909 keV of ^{94}Tc, ^{52}Mn, ^{72}As, and ^{89}Zr, respectively, ~0.70 mm resolution was obtained. Finally, at ultra-high energies of 1.2 (^{44}Sc) and 1.4 MeV (^{52}Mn) resolutions of ~0.75 mm and ~0.80 mm could still be achieved although ring artifacts were observed at the highest energies (1.4 MeV). For ^{38}K (2.2 MeV), an image resolution of 1.2 mm was achieved utilizing its 2.2 MeV prompt emission.

This work shows that current cluster pinhole collimators are suitable for sub-mm resolution prompt PET up till at least 1.4 MeV. This may open up new avenues to developing new tracer applications and therapies utilizing these PET isotopes.

2.1. Introduction

Among the numerous modalities employed in small animal imaging, dedicated Positron Emission Tomography (PET) and Single Photon Emission Computed Tomography (SPECT) scanners are widely utilized. Many different radioisotopes have been employed and investigated with these scanners, facilitating the studies of various diseases, tracer molecules and therapies [62]. Most often PET imaging operates by detecting pairs of annihilation photons (coincidence PET), whereas SPECT and some recently developed preclinical PET devices rely on the detection of single gammas, including prompts.

The image quality of coincidence PET is isotope-dependent and relies on factors such as positron range and the emission spectrum. The range over which a positron travels before the generation of 511 keV annihilation photons occurs (positron ranges: table 2.1) imposes a fundamental limit on the achievable image resolution [63]. This is particularly problematic in preclinical PET, where resolution requirements are stringent due to the small size of anatomical structures in mice and images get easily compromised, both quantitatively and visually. While using information on the positron range kernel and accurate tissue boundaries during image reconstruction can partially mitigate image degradation, it remains a challenge in many instances e.g., due to the long tail of the positron range kernel (table 2.1). Another image degrading effect may occur for PET

isotopes that co-emit one or more high energy prompt gammas of sufficient intensities, the probability of which can exceed the positron emission probability by more than an order of magnitude (table 2.1). These prompt gammas can contaminate the 511 keV photopeak through down scatter, complicating the use of 511 keV gammas for imaging [64–66]. Although various scatter correction methods have been proposed, such as uniform background subtraction [67], sinogram tail fitting [68], and scaled randoms sinogram subtraction, further efforts are necessary to resolve the issue fully [69].

Preclinical SPECT systems primarily employ pinhole collimation to benefit from high magnification effects that can be obtained in small animals. Significant advancements have been made to adapt pinhole collimation for high energy imaging [49, 70] which made these systems also suitable for PET and simultaneous PET/SPECT imaging. This was demonstrated for the VECTor (Versatile Emission Computed Tomography) PET/SPECT scanner equipped with proprietary high energy cluster pinhole collimation technology [40] in which pinholes are organized into clusters of pinholes with small opening angles to reduce blurring due to edge penetration. In a recent experimental study [45], VECTor demonstrated imaging of ^{124}I and ^{89}Zr in phantoms and mice by utilizing their prompt gammas of 603 keV and 909 keV, respectively, resulting in positron-range free images without down scatter contamination. The scanner achieved a conservative estimate of image resolution of 0.75 mm for both ^{89}Zr and ^{124}I. Additionally, simultaneous ^{124}I-^{18}F PET with excellent separation of isotopes and high quantitative accuracy was demonstrated.

One of the aims of this simulation-based work is to investigate if this concept can be extended to a much wider range of PET isotopes by investigating a series of PET isotopes that have interesting applications but that face challenges when imaging their distributions because they suffer from long positron ranges, low probability of positron range emissions and/or down scatter (table 2.1). For all isotopes, we utilized both annihilation and prompt gammas for imaging to determine which emission provided the optimal image resolution and uniformity for each isotope. Furthermore we assess the deterioration in image quality associated with increasing gamma energy (>1 MeV). The following PET isotopes ^{52}Mn, ^{94}Tc, ^{89}Zr, ^{44}Sc, ^{86}Y, ^{72}As, ^{124}I, ^{38}K, and ^{66}Ga were selected for this study to address the aforementioned objectives, with ^{18}F included for comparison. Both image resolution and uniformity were studied for relevant gamma emissions of the isotopes.

Isotope	$T_{1/2}$ [*h*]	*Mean Positron range [mm]*	*Max Positron range [mm]*	*Positron emi. probability*	*Prompt gamma energy [keV]*	*Application*
^{18}F	1.83	0.64	2.27	96.73%	n.a.	FDG-PET [71]
^{52}Mn	134.16	0.58	1.99	29.4%	744 (90%), 936 (94.5%), 1434 (100%)	immunoPET [72], bone scanning [73]
^{94}Tc	4.88	0.85	3.15	10.5%	703 (99.6%), 850+871 (195.6%)	
^{89}Zr	78.41	0.96	3.61	22.74%	909 (99.04%)	immunoPET [74]
^{44}Sc	3.97	1.68	6.64	94.28%	1157 (99.89%)	prostate cancer [75]
^{86}Y	14.74	1.73	6.86	31.9%	1077+1153 (113%)	theranostic pair of ^{90}Y [76]
^{72}As	26.00	3.24	12.8	87.8%	834 (81%)	immunoPET [77]
^{124}I	100.32	3.28	12.9	22.7%	603 (62.9%)	thyroid cancer [78]
^{38}K	0.13	3.39	13.4	99.53%	2167 (99.85%)	myocardial perfusion [79]
^{66}Ga	9.49	5.16	19.8	57%	1039 (37%)	prostate cancer [80]

Table 2.1: Half-lives, positron ranges, positron emission probabilities, prompt gamma energies (with emission probabilities), and medical applications of studied PET isotopes.

2.2. Materials and methods

2.2.1. Scanner description

The VECTor scanner simulated in the present study is equipped with a triangular set up of PMT-based monolithic NaI(Tl) scintillator detectors, each with an area of 590×470 mm^2 and standardly a crystal thickness of 9.5 mm. The tungsten collimator comprises 162 pinholes, each with a diameter of 0.7 mm. The original design of the cluster collimator for the VECTor scanner included 192 pinholes; however, only 162 pinholes were utilized for image reconstruction. This is due to some of the pinholes not projecting onto the detector, owing to gaps between the three triangular detectors. The pinholes are arranged in 2×2 clusters [49]. These clusters are grouped into four side-by-side rings in the cylindrical collimator [40]. The full opening angle for the pinholes in the inner two rings populated with clusters is 18°, while for the outer two rings, it is 16°, ensuring uniform coverage of pinhole projections on the detector surfaces. The collimator has an inner diameter of 48 mm, a length of 190 mm, and a wall thickness of 43 mm. The centers of all pinholes are defined at a diameter of 64 mm. A specific portion of the field-of-view (FOV), referred to as the central field of view (CFOV), is sampled collectively by all pinhole clusters. It has an approximate diameter of 12 mm and a longitudinal length of 9 mm. The CFOV experiences complete data sampling (satisfies Tuy's conditions [81]) in a single bed position and this area is readily increased up to the entire body when the bed is

translated through the collimator. Data is then acquired from all bed positions (Scanning Focus Method [82]) after which all data is utilized jointly in image reconstruction (as detailed in "Image Reconstruction" section of [82]).

2.2.2. Monte Carlo simulations

Monte Carlo (MC) simulations were conducted using GATE v9.0 [83–85], which is based on Geant4 v10.05 [86]. The simulations were executed on a CentOS 7.0 cluster utilizing 216 processors concurrently. All relevant physics processes were included in the simulation using the '*emstandard*' physics list builder, as described in the GATE documentation. The events in which gamma photons lose energy due to multiple interactions within the detector were processed using GATE's '*adder*' digitizer module. In this module, the energies from different interactions are summed, and the position is determined as the energy-weighted centroid of the interaction points. The light guides and PMTs of the detector were not directly simulated; instead, their effects were implicitly simulated as a post-processing step. This was done by assuming an energy resolution of 9% at 511 keV and an intrinsic spatial resolution of 3.5 mm, in accordance with the specifications provided by the manufacturer. The energy resolution at other energies was scaled using a $\frac{1}{\sqrt{E}}$ proportionality relation, which approximates the experimentally determined energy resolution values at various gamma energies (table 2.2, [87]). These resolutions were implemented by sampling from Gaussian distributions. All post-processing tasks were performed using in-house MATLAB scripts. The detector electronics of the current VECTor scanner are optimized for gamma acquisition up to 1.2 MeV. For this simulation-based study, we assumed that the scanner can be accurately calibrated to a maximum energy of 2.3 MeV (2.2 MeV being the highest energy in our study). MC simulations were both done for a single pinhole and for a full VECTor scanner as detailed below.

Source	***Energy*** [keV]	***Exp.*** E_{res} ***(%)***	***Sim.*** E_{res} ***(%)***
^{22}Na	511	9.7%	9.0%
^{124}I	603	8.1%	8.3%
^{89}Zr	909	7.2%	6.8%

Table 2.2: Experimental (Exp.) and simulated (Sim.) energy resolution for different radionuclide sources.

Single pinhole simulation

To assess the extent of edge penetration for different energies, we conducted MC simulations to obtain the Point Spread Function (PSF) of a single pinhole. PSFs were generated for a point source placed both on the pinhole axis and 5 mm off-axis (figure 2.1). The geometrical parameters of the simulation were chosen to be conform to those of the VECTor scanner: the distance between the point source and the inner wall of the collimator was 24 mm, while the pinhole-to-detector distance was 178 mm.

The pinhole, with a diameter of 0.7 mm, was positioned at the center of a tungsten rectangular slab with a thickness of 43 mm. Depending on photon travel paths, photon interaction positions in the detector plane can be classified into three regions: the direct beam, edge penetration, and wall penetration, depicted in green, blue, and red, respectively, in figure 2.1. Direct beam photons are considered to be those that pass through the hole, while edge penetration photons traverse the pinhole edges. In instances of wall penetration, photons pass through the full thickness of the collimator wall. In practice, the boundaries between these regions are not completely distinct due to the intrinsic spatial resolution of the detector and Compton scattering from pinhole edges. Additionally, in the actual VECTor scanner, the relative positions and orientations of pinholes and the detector are different for different pinholes. Despite this complexity, we believe that our simplified simulated experiment captures the major variations of the PSFs.

For computational efficiency, a gamma pencil beam with an angular width of 40° was directed towards the line connecting source position and pinhole center. Various gamma energies were tested: 140 keV, 511 keV, 603 keV, 744 keV, 834 keV, 909 keV, 1.0 MeV, 1.2 MeV, 1.4 MeV, 2.2 MeV. These energies correspond to those of the annihilation and prompt gamma energies emitted by the isotopes considered in this work except for 140 keV, which is the standard energy for SPECT imaging and therefore chosen for comparison. The photopeak energy windows used for these gamma energies are the same as those used in the phantom simulations (table 2.3). In each simulation, a total of 10^{10} emitted gammas was simulated.

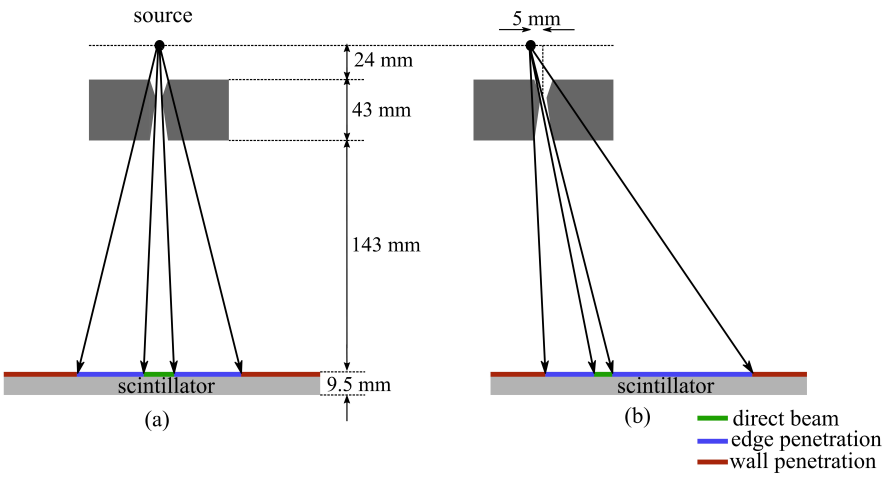

Figure 2.1: Geometry of the single pinhole simulation for a point source placed (a) on the pinhole axis and (b) 5 mm from the pinhole axis. Gamma photon paths are classified into three categories: the direct beam (photons passing through the hole), edge penetration (photons penetrating the pinhole edges), and wall penetration (photons traversing the full thickness of the collimator wall). Diagram not to scale.

Scanner simulation and data acquisition

Additional to single pinhole simulations, a MC simulation of the full VECTor scanner was conducted. Among the three detectors, the first detector was oriented perpendicular to the y-axis and translated to coordinates (0, -215 mm, 0). The second and third detectors were rotated by ±120° around the z-axis and translated to (-186 mm, -107 mm, 0) and (186 mm, -107 mm, 0), respectively, to accurately represent the triangular geometry of the VECTor scanner. The multi-pinhole cluster collimator was defined in the simulation based on the geometry parameters provided by the manufacturer. The materials used in the collimator were tungsten (97%), iron (1.5%), and nickel (1.5%). The pinholes were modeled as two conical cylinders facing each other.

A total of nine PET isotopes, ^{52}Mn, ^{94}Tc, ^{89}Zr, ^{44}Sc, ^{86}Y, ^{72}As, ^{124}I, ^{38}K, ^{66}Ga, were considered (see table 2.1). The selection of isotopes was based on factors such as possible biomedical applications, prompt gamma emission energies (up to 2.2 MeV for scanner characterization), and their relevance to studying down scatter issues unique to certain isotopes, e.g., ^{66}Ga, ^{89}Zr. The standard PET isotope ^{18}F was included for comparison. The isotopes were defined as 'ion sources' to simulate all possible emissions with their correct intensities. Three-dimensional photon interaction locations in the NaI(Tl) crystal were then used to generate detector projections, which were sampled on a 1.072×1.072 mm^2 pixel grid, matching the pixel size of the detector used in the VECTor scanner. Projections from both annihilation gamma and available prompt gamma emission(s) of sufficient intensity were acquired for each isotope based on the photopeak windows provided in table 2.3.

Digital phantoms

A Derenzo resolution phantom containing rods with diameters of 0.60 mm, 0.65 mm, 0.70 mm, 0.75 mm, 0.80 mm, and 0.85 mm, each with a height of 10 mm, was employed in this study. The phantom was assumed to be made of PMMA cylinder of diameter 20 mm and height 12 mm. The activity concentration was set to 250 MBq/ml for all isotopes, and the scan duration was set to one hour. All possible types of emissions from the isotopes were simulated. Due to the phantom's dimensions exceeding the CFOV of the scanner, data acquisition was performed using a multiplanar trajectory (MPT) [88] over 9 bed positions. The MPT scheme was selected to guarantee sufficient sampling of the object, achieved by employing a conservatively high number of bed positions per plane. For ^{38}K, in addition to the first Derenzo resolution phantom, a second phantom with rod diameters of 0.90 mm, 1.0 mm, 1.1 mm, 1.2 mm, 1.3 mm, and 1.4 mm was employed to assess resolution. This was necessary because no rod sectors were resolved in the first Derenzo phantom for this isotope.

For uniformity studies, a cylindrical water phantom with a diameter of 20 mm and a height of 15 mm, containing a uniform activity concentration of 5 MBq/ml, was used. The scan duration was kept at the same value as for the Derenzo phantom (one hour). The scan was conducted using a spiral trajectory [88] over 17 bed positions. The use

of a spiral trajectory reduces scan time compared to a multiplanar trajectory, without compromising image quality [88].

Uniformity phantom analysis

Uniformity was calculated using six circular ROIs with a radius of 1.5 mm, measured across five axial slices with a slice thickness of two voxels each, where voxel size was 0.4 mm. Percentage uniformity was defined as the ratio of the standard deviation (σ_U) to the mean ($\bar{U}$), averaged over all six ROIs and the five axial slices.

$$Uniformity\,[\%] = 100 \times \frac{\sigma_U}{\bar{U}} \tag{2.1}$$

Positron range simulations

Positron annihilation point distributions for the PET isotopes under study were generated through MC simulations; a point source was placed at the center of a 20 cm water sphere and five million annihilation point coordinates were recorded for each isotope. The probability of annihilation within each voxel of a $31 \times 31 \times 31$ voxel grid was stored, with the center of the central voxel in the grid corresponding to the point source position. The voxel size was set to 0.4 mm, matching the reconstructed image voxel size.

The use of an effectively infinite water medium to generate positron range kernels is an approximation. A more accurate model would involve using the actual three-dimensional distribution of the different materials present in the phantom.

2.2.3. Image reconstruction

Image reconstruction was conducted utilizing the dual-matrix dual-voxel similarity regulated ordered-subset expectation maximization (DM-DV-SROSEM) algorithm [89] which was also used in experimental studies. SROSEM [90] resembles OSEM but dynamically adapts the number of subsets used based on the similarity of update terms across different subsets. In our implementation, a maximum of 128 pixel-based subsets [91] was employed, with a similarity threshold set at 40%. A cutoff of 1% was applied to the forward projectors, meaning that gammas traveling paths with a probability of less than 1% of penetrating the collimator were not included [55]. Following the dual-matrix framework, unmatched backprojectors were employed with a higher cutoff value of 20%, facilitating faster convergence without compromising image quality. To further accelerate reconstruction, the dual-voxel approach was adopted [92]. In this approach, forward matrices were divided into a central part with fine voxel binning and a slowly varying tail part with rougher binning (twice the voxel size). Positron range correction (PRC) was implemented by iteratively convolving the activity distribution with the positron range kernel during the forward projection step of the reconstruction process. Comparisons

were made between the 511 keV reconstructions with and without PRC. Notably, image reconstruction from prompt emissions does not require PRC, as prompt gammas are emitted directly from the isotope.

Energy-dependent system matrices were computed for all necessary energies using a ray-tracing software [55, 93]. This ray-tracing code accounts for attenuation through the collimator and detector but does not include scatter. However, the scatter component of the projection, captured using the triple energy window technique [94], was incorporated in image reconstruction to compensate for the absence of a scatter contribution in the matrices. In the 1.4 and 2.2 MeV reconstructions, instead of 1%, 3% and 5% cutoff forward matrices were used, respectively, to reduce ring artifacts (more in sections 2.2.4 and 2.3.6). Additionally, multi-photopeak imaging of closely spaced prompt gamma pairs, 850+871 keV for ^{94}Tc and 1077+1153 keV for ^{86}Y, was performed using system matrices at intensity-weighted gamma energies. For ^{94}Tc, the intensity-weighted gamma energy of the 850+871 keV photopeak is 861 keV, whereas for ^{86}Y, the corresponding energy of the 1077+1153 keV photopeak is 1096 keV.

The original reconstructed images have dimensions of 76×76×26, with a voxel size of 0.4 mm. For improved visualization, ten central layers along the transaxial dimension were summed, and the obtained 76×76 images were redefined on a finer 256×256 grid using MATLAB's 'resize' function which applies bicubic interpolation. All images were subsequently smoothed using a 0.5 mm FWHM Gaussian kernel. For comparison, all isotope images were scaled to activity concentration units (MBq/ml). Both positron range-corrected and uncorrected 511 keV images from each isotope were obtained for comparative analysis. All prompt gamma emissions with adequate intensities were utilized individually for image reconstruction. The maximum achievable resolution for each isotope was determined through a visual comparison of all Derenzo resolution phantom images.

2.2.4. Effect of different tail cut off in ultra-high energy imaging

In [55] it was demonstrated that using the same tail cutoff for the forward projections (20%), as employed in 140 keV reconstructions for the same system, does not yield high-quality images for 511 keV. This is attributed to the fact that gamma photon paths with a probability of less than 20% of penetrating the collimator edges, which belong to the tail part of the PSF, constitute a significant portion of the photon flux at gamma energies of 511 keV ([55]). Hence, simulating this tail in system matrix calculation is essential for high energy imaging. It was found that a cutoff of 1% provided a good trade-off between image quality and reconstruction time [55]. Given that we are imaging ultra-high energy gamma emissions (>1 MeV) for the first time, it is crucial to investigate the effect of cutoff on imaging performance. To this end, we generated system matrices with cutoffs ranging from 1% to 7% for ultra-high energies of 1.4 and 2.2 MeV. The reconstructed resolution images using these different matrices were then analyzed. To minimize computation time, only the 1% and 3% matrices were utilized for the analysis of uniformity phantom images.

2.3. Results

2.3.1. PSFs for a single pinhole

The line profiles of PSFs for the single pinhole are presented in figure 2.2. The plot is segmented into three distinct regions: a segment consisting of direct photons, a segment with photons that penetrated through the pinhole edges, and a part containing photons that penetrated through the collimator wall, as defined in section 2.2.2. As anticipated, the amount of pinhole edge penetration increases with higher gamma energies. Notably, at ultra-high energies (>1 MeV), significant penetration through the entire 43 mm thickness of the collimator (wall penetration) was observed at considerable distances from the pinhole axis. Both edge and wall penetrations are more pronounced for the off-axis source position (figure 2.2b). It is suggested that wall penetration from adjacent pinholes can accumulate and significantly contribute to system matrices. These effects undoubtedly broaden PSFs at ultra-high energies, thereby probably making the image reconstruction problem more underdetermined. The percentage of photons passing through the 43 mm collimator wall without any interaction was calculated using the Beer-Lambert law [95] for the gamma energies of interest (table A.3).

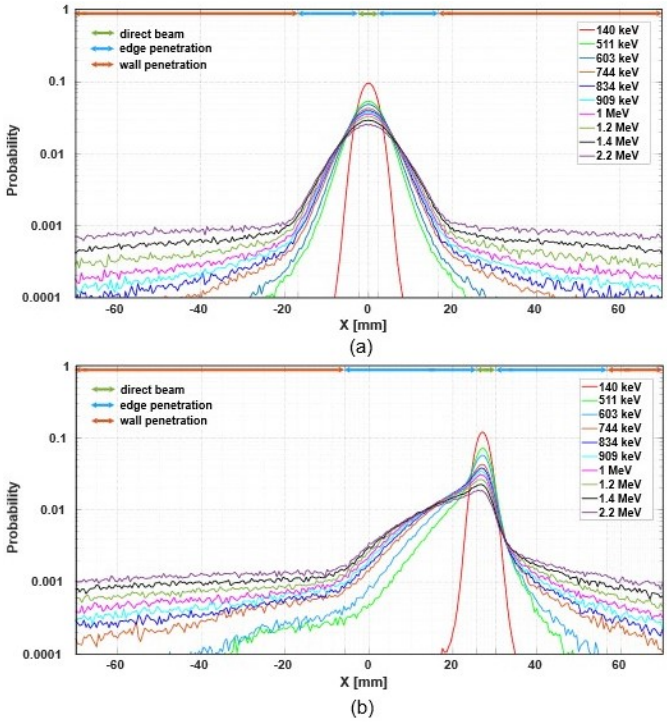

Figure 2.2: Single pinhole response to a point source, placed on the pinhole axis (a) and 5 mm away from the pinhole axis (b), for gamma energies relevant to this study. The x-axis is divided into three regions: direct beam, edge penetration, and wall penetration (see top of figures).

2.3.2. Phantom simulation

The energy spectra of all ten PET isotopes under study, derived from the first 1 minute of acquisition data from resolution phantom simulations, are presented in figure 2.3. Collimator and detector scatter contributions are also included. Here, the detector scatter contribution refers to events involving at least one Compton scatter event within the detector, while none occurs in the collimator. For some isotopes, higher energy gamma emissions may be detected into the photopeak windows of lower energy gamma emissions due to Compton scattering within the phantom, collimator edges, or detector crystal, a phenomenon denoted by down scatter.

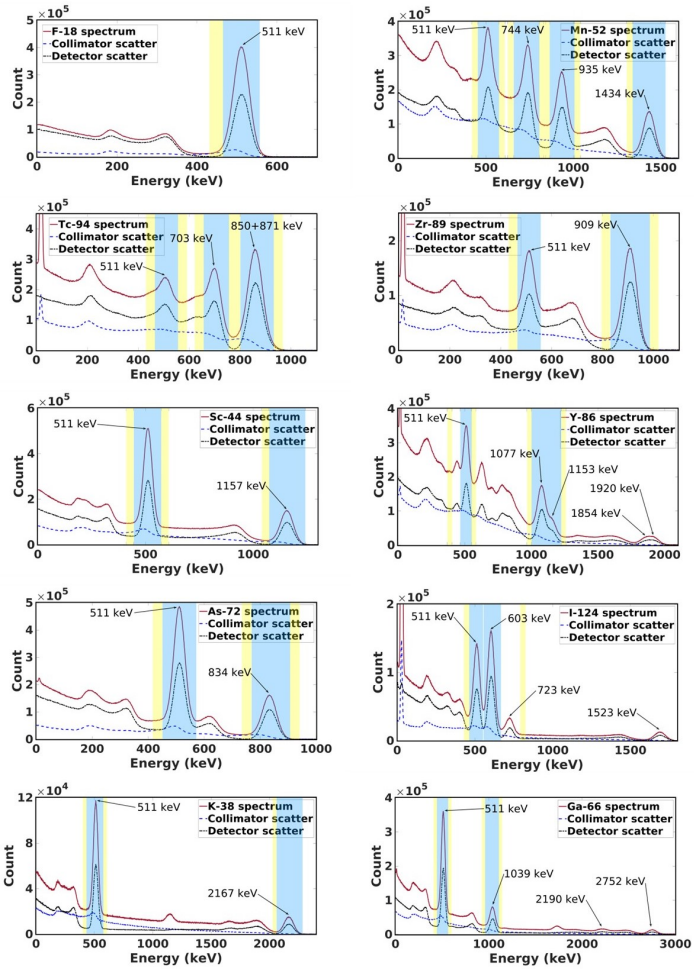

Figure 2.3: Energy spectra of PET isotopes used in this study: ^{18}F, ^{52}Mn, ^{94}Tc, ^{89}Zr, ^{44}Sc, ^{86}Y, ^{72}As, ^{124}I, ^{38}K and ^{66}Ga, including the photopeak and background energy windows in blue and yellow, respectively. The collimator and detector down scatter spectra are also presented.

Isotope	*Peak energy [keV]*	*Photopeak window [keV]*	*Background window-1 [keV]*	*Background window-2 [keV]*
^{18}F	511	465 – 557	430 – 465	n.a.
^{52}Mn	511	455 – 575	420 – 455	575 – 610
	744	660 – 805	625 – 660	805 – 840
	936	865 – 1005	830 – 865	1005 – 1040
	1434	1340 – 1525	1305 – 1340	n.a.
^{94}Tc	511	465 – 557	430 – 465	557 – 592
	703	657 – 766	622 – 657	766 – 801
	850+871	791 – 933	756 – 791	933 – 968
^{89}Zr	511	465 – 557	430 – 465	n.a.
	909	831 – 986	796 – 831	986 – 1021
^{44}Sc	511	445 – 573	410 – 445	573 – 608
	1157	1074 – 1242	1039 – 1074	n.a.
^{86}Y	511	467 – 550	369 – 404	550 – 585
	1077+1153	1000 – 1225	965 – 1000	1225 – 1260
^{72}As	511	445 – 570	410 – 445	907 – 942
	834	757 – 907	722 – 757	907 – 942
^{124}I	511	463 – 551	428 – 463	790 – 825
	603	554 – 667	790 – 825	n.a.
^{38}K	511	433 – 575	398 – 433	575 – 610
	2167	2064 – 2284	2029 – 2064	n.a.
^{66}Ga	511	445 – 566	410 – 445	566 – 601
	1039	960 – 1107	925 – 960	1107 – 1142

Table 2.3: Photopeak and background energy windows used.

Our simulations revealed a negligible contribution from phantom scatter. As an example, for ^{72}As, approximately 1.42% of counts within the photopeak window (table 2.3) for 511 keV and approximately 0.26% within the photopeak window for 834 keV originate from phantom scatter. Scattering of higher energy gamma rays from the collimator pinhole edges can also significantly contribute to the signal in the photopeak of lower energy gamma rays as is clear from figure 2.3. For example, down scatter from 2190 keV and 2752 keV gamma rays can contribute to the photopeak of the 1039 keV gamma ray of ^{66}Ga (figure 2.3). Depending on the relative distance between the higher energy gamma and photopeak of interest, this may result in severely misplaced counts on the detector plane due to the selective contribution from higher angle scatter. Consequently, this effect may

degrade image quality (more in section 2.3.4).

For all isotopes, photopeak and background windows were selected through visual inspection of spectra (figure 2.3 and reported in table 2.3). Many of the isotopes studied in our paper exhibit small to medium intensity gamma emissions near 511 keV, such as 443 keV (17%) for ^{86}Y, 603 keV (63%) for ^{124}I, and 630 keV (8%) for ^{72}As. To avoid including counts from these additional gamma emissions and to maximize the counts within the 511 keV photopeak window, the selected 511 keV photopeak windows for some isotopes are slightly different. For isotopes such as ^{94}Tc and ^{86}Y, adjacent unresolved gamma emissions were reconstructed using a single photopeak window.

2.3.3. Positron range

Line profiles of the generated positron range kernels for all isotopes are presented in the appendix (figure A.3). The positron range for various PET isotopes has been extensively studied, both experimentally [96, 97] and through simulations [98–101]. However, most reported results are two-dimensional projections of the original three-dimensional distribution of annihilation points, making them unsuitable for direct use in our study. To validate our simulation, we compared our results with values reported in the literature (see appendix).

2.3.4. Resolution studies

Resolution phantom images obtained from both the 511 keV and all prompt gamma emissions of sufficient intensity for all isotopes under study are shown in figures 2.4 and 2.5. Images were presented at three different iteration numbers: the 50th, 100th, and 180th iteration. Based on visual assessment, a resolution of ~0.65 mm is achievable for imaging ^{124}I utilizing its 603 keV prompt gamma emission. Similarly, resolutions of ~0.70 mm are attainable for ^{94}Tc, ^{52}Mn, ^{72}As, and ^{89}Zr using their respective prompt gamma emissions at 703 keV, 744 keV, 834 keV, and 909 keV. Furthermore, prompt gamma emissions at ultra-high energies of 1.2 MeV and 1.4 MeV from ^{44}Sc and ^{52}Mn isotopes yield resolutions of ~0.75 mm and ~0.80 mm, respectively. As expected, image resolution generally degrades with increasing gamma energy. On the contrary, the resolution achieved for ^{44}Sc using the 1.2 MeV prompt emission is superior to that obtained with the 1.0 MeV gamma emission from ^{66}Ga. This is likely due to significant collimator and detector down scatter from higher energy gammas of 2.2 MeV and 2.8 MeV emitted by ^{66}Ga (figure 2.3) contributing to the photopeak of low intensity (37% in table 2.1). PRC enhanced the image quality of 511 keV reconstructed images across all isotopes.

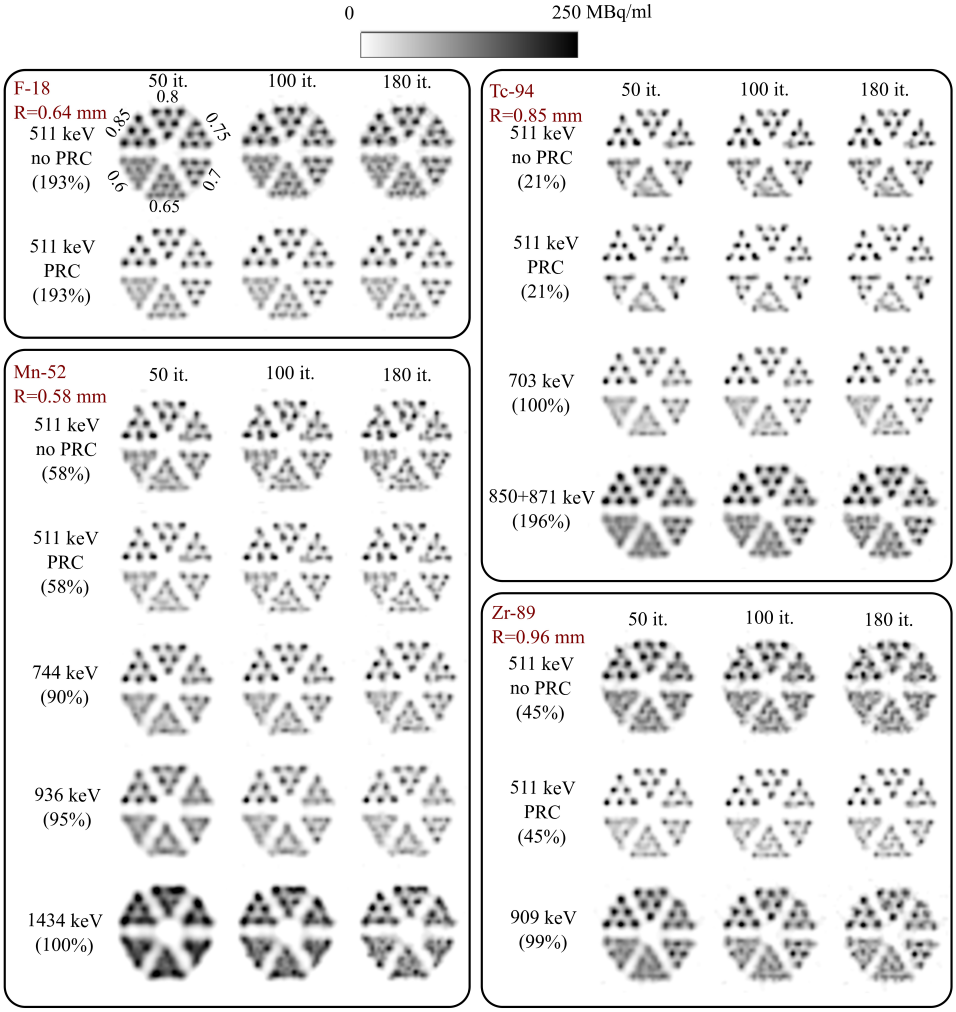

Figure 2.4: Derenzo resolution images after the 50th, 100th, and 180th iterations are shown for ^{18}F, ^{52}Mn, ^{94}Tc, and ^{89}Zr. With prompt gamma images, positron range-corrected and uncorrected 511 keV images are also presented. Abbreviation: PRC, Positron Range Correction; R, positron mean range.

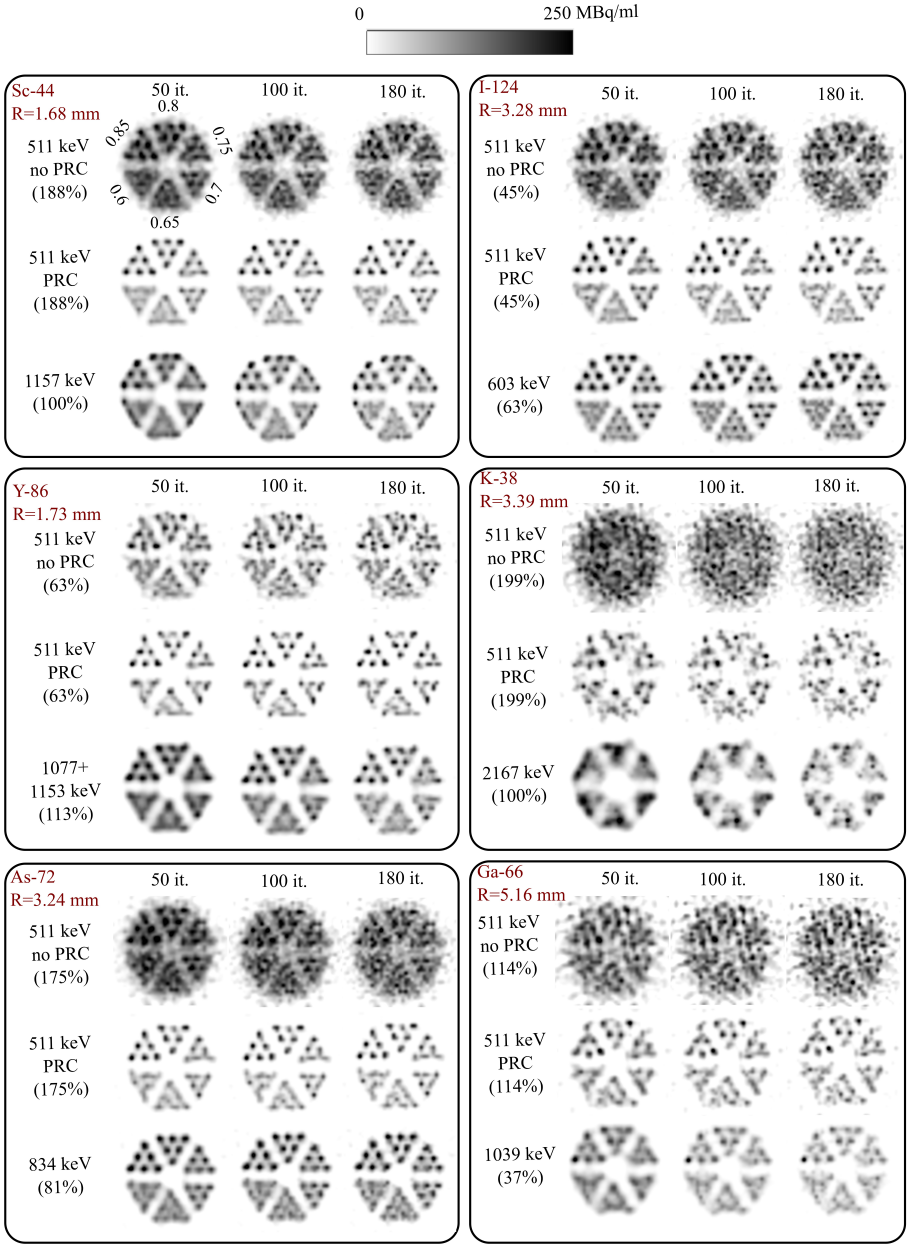

Figure 2.5: Derenzo resolution phantom images after 50th, 100th, and 180th iterations are shown for ^{44}Sc, ^{124}I, ^{86}Y, ^{38}K, ^{72}As and ^{66}Ga. Abbreviation: PRC, Positron Range Correction; R, positron mean range.

Isotope	*Gamma energy [keV]*	*Resolution [mm]*
^{52}Mn	744	0.70
^{94}Tc	703	0.70
^{89}Zr	909	0.70
^{44}Sc	511	0.70
^{86}Y	1077+1153	0.75
^{72}As	834	0.70
^{124}I	603	0.65
^{38}K	2167	1.20
^{66}Ga	1039	0.80

Table 2.4: Highest achievable resolutions for nine isotopes under study.

Note that the PRC applied in this study was conducted under ideal conditions as positron range in an infinite water medium was used which corresponds well to that in the phantom simulations, given the similar attenuation characteristics of water and PMMA, the two materials used in the digital phantom definition. In contrast, PRC in small animal scans is a nontrivial task due to the presence of different types of tissues within a relatively complex three-dimensional distribution [102]. Nonetheless, for all isotopes, prompt emissions, which don't suffer from positron range, produced images of better resolutions than the 511 keV with PRC, except for ^{44}Sc. The maximum achievable resolutions for the examined isotopes are listed in table 2.4. For 2.2 MeV prompt gamma emission of ^{38}K, PSFs were too broad to resolve the largest diameter rods (0.85 mm). Images obtained from a second Derenzo resolution phantom containing larger rod diameters demonstrate a supra-mm resolution of 1.2 mm when using 2.2 MeV gamma radiation from this isotope (see figure A.1 in Appendix).

2.3.5. Uniformity studies

Uniformity phantom images reconstructed using both 511 keV and the available prompt gamma emissions for all isotopes under study are presented in figures 2.6 and 2.7. The images correspond to the 50th iteration and include both positron range-uncorrected and corrected 511 keV images. Additional uniformity phantom images at the 100th iteration are provided in the supplementary material (figure A.4, A.5). The percentage uniformity (equation 2.1) is plotted against the iteration number for each isotope in figure 2.8.

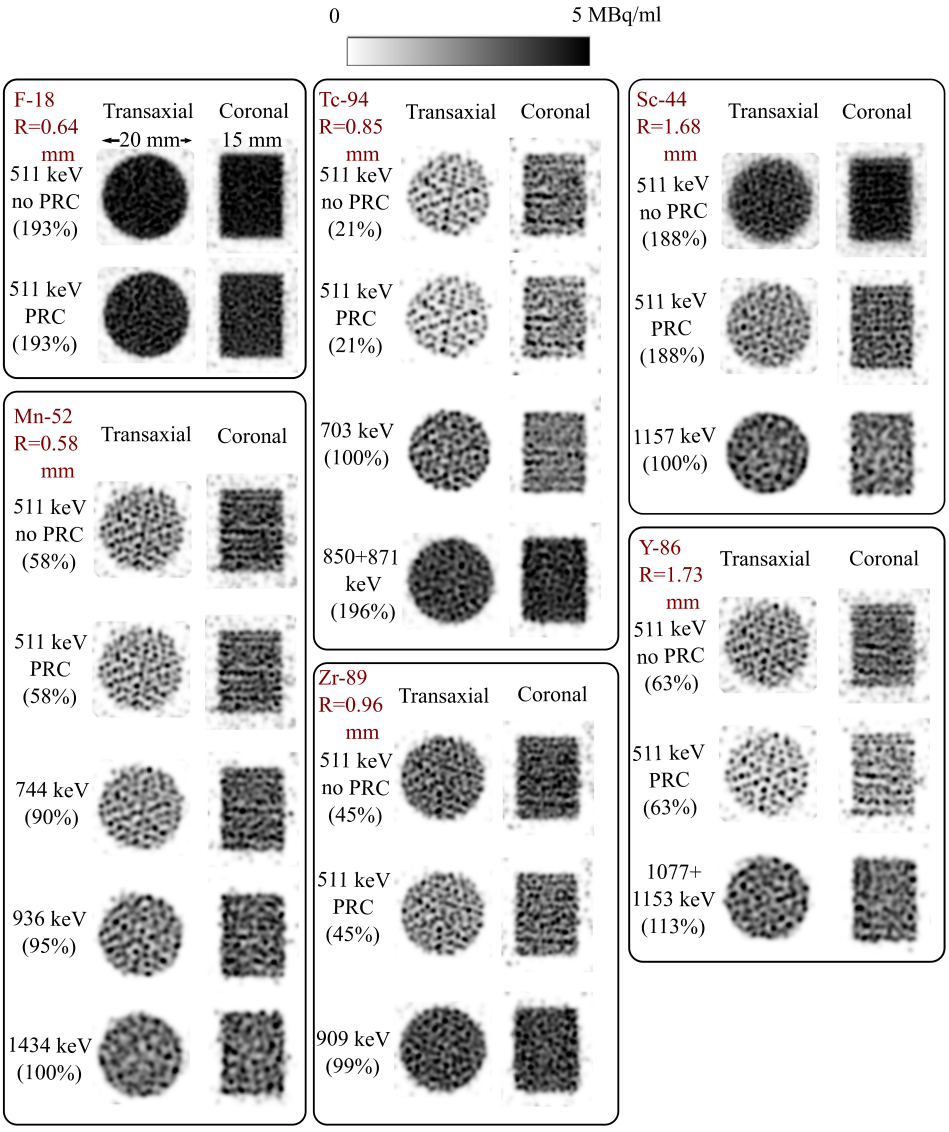

Figure 2.6: Uniformity phantom images at the 50th iteration are presented for isotopes ^{18}F, ^{52}Mn, ^{94}Tc, ^{89}Zr, ^{44}Sc, and ^{86}Y. Both transaxial and coronal views are displayed. Abbreviation: PRC, positron range correction; R, positron mean range.

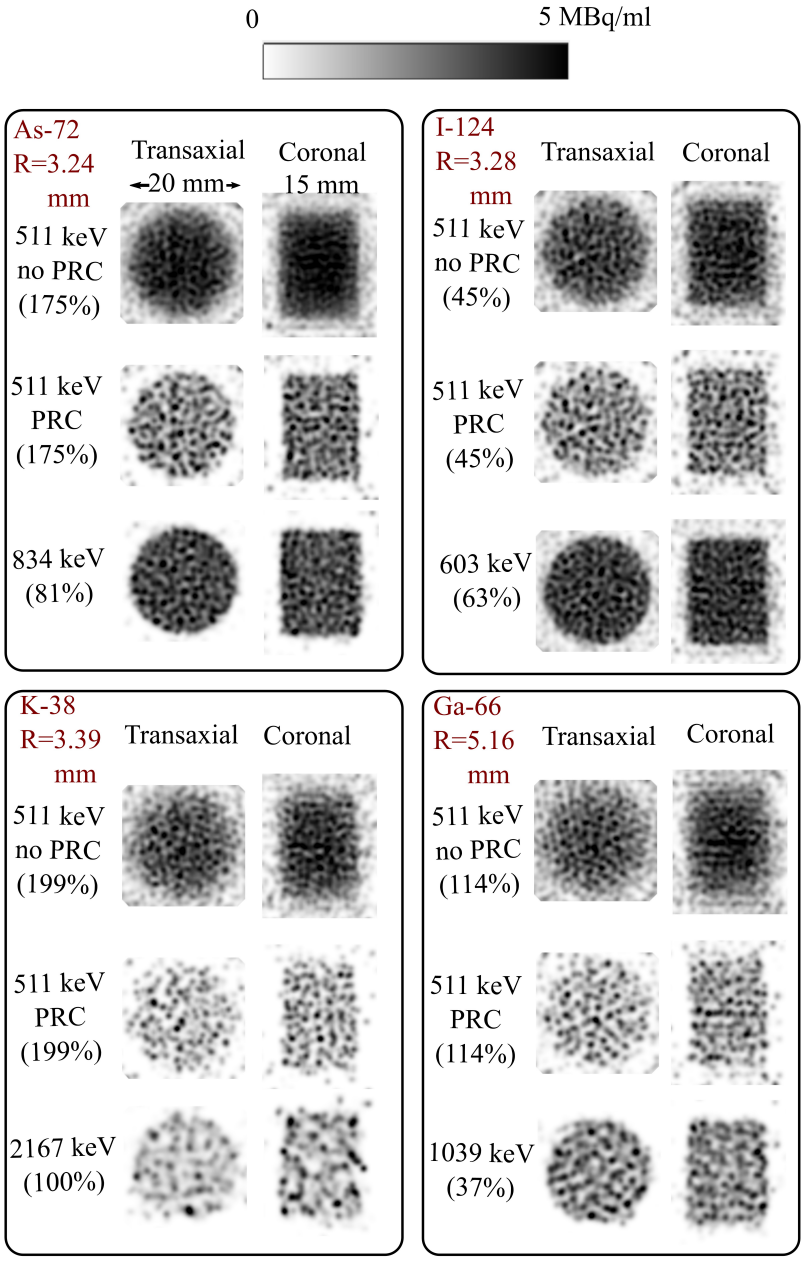

Figure 2.7: Uniformity phantom images at the 50th iteration are presented for isotopes ^{72}As, ^{38}K, ^{124}I, and ^{66}Ga. Both transaxial and coronal views are displayed. Abbreviation: PRC, positron range correction; R, positron mean range.

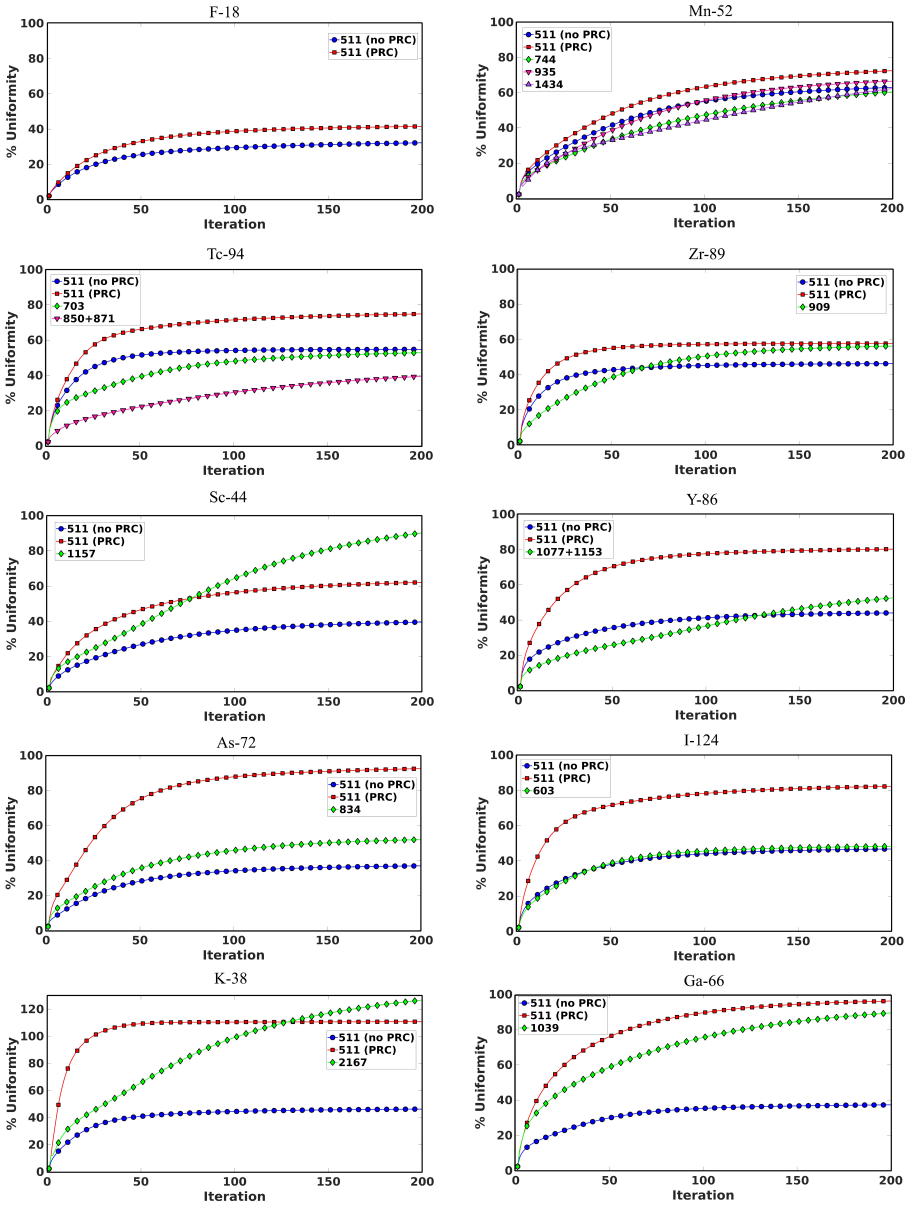

Figure 2.8: Percentage uniformity plotted against iteration number for all isotopes under study. Abbreviation: PRC, positron range correction.

The granular-like texture visible in the uniformity images arises from statistical noise inherent in the projection data combined with the used post-filter (1 mm). This is illustrated in figure A.7, where we show that as the FWHM of the Gaussian filter increases, the noise spikes progressively transform into a granular texture. Besides, the transaxial views of the 511 keV images of ^{52}Mn, ^{94}Tc, and ^{86}Y reveal a pattern consisting of three lines of dots intersecting at equal angles, slightly offset from the center of the cylindrical phantom while the coronal views of the same three isotopes exhibit a parallel, tubular-like arrangement of dots along the axis of the phantom, rather than a uniform distribution. We used GATE's '*comptonPhantom*' and '*comptonCrystal*' flags to reject collimator and detector down scatter from projection data respectively and we found that the artifact in the transaxial view is due to the detector down scatter contribution from high and ultra-high energy prompt gammas (figure A.8). The artifact in the coronal view, however, could not be attributed specifically to detector or collimator down scatter (figure A.8); it appeared when both types of down scatter were present in the projection data.

2.3.6. Ultra-high energy imaging

The 1.4 MeV prompt gamma emissions of ^{52}Mn are reconstructed using forward matrices with 1%, 3%, 5%, and 7% cutoffs and images are displayed in figure 2.9. Images with 1% cutoff exhibit ring artifacts [103], characterized by a visible dip at the center of phantoms due to enhanced edges. Such ring artifacts have been observed in PSF-based PET reconstruction also, when PSFs are broad [104, 105]. In fact, in the 1.2 MeV image of ^{44}Sc (figure 2.5), a slight ring artifact is also noticeable, but it becomes distinctively recognizable at 1.4 MeV. Conversely, at 2.2 MeV, no rods were visible (figure 2.5), and therefore, we did not perform a similar analysis.

These ring artifacts cannot be eliminated even with a large number of iterations (1000 it. in figure 2.9) for a 1% cutoff. It can however be mitigated by using higher cutoffs in matrix generation (e.g., 3%, 5%, 7%), as using higher cutoffs effectively sharpens the PSFs by truncating the tails. Also, resolution phantom images reconstructed using the 1% cutoff matrix exhibit rounding at the outer edges, resulting in a reduction in the size of the phantom compared to its original dimension.

Line profiles through six hot rods further support this observation (figure 2.10). A similar artifact of size reduction was observed in the uniformity phantom images at ultra-high energies (see Appendix). This effect may be attributed to the inability of broad PSFs to reconstruct high-frequency information at the periphery. The use of higher cutoffs allows for a more realistic reconstruction of the phantom's outer edges.

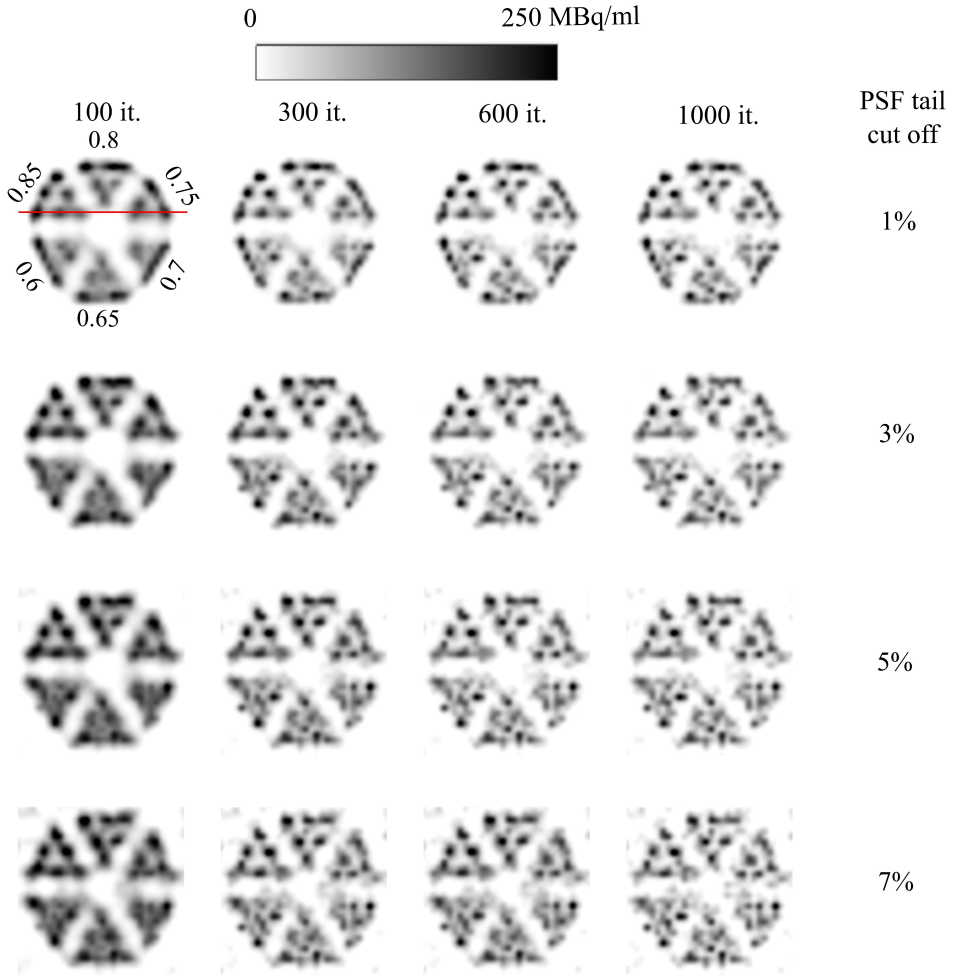

Figure 2.9: The 1.4 MeV prompt gamma emissions from ^{52}Mn are reconstructed using matrices with different tail cut offs (1%, 3%, 5%, 7%). Images at 100th, 300th, 600th and 1000th iteration are shown.

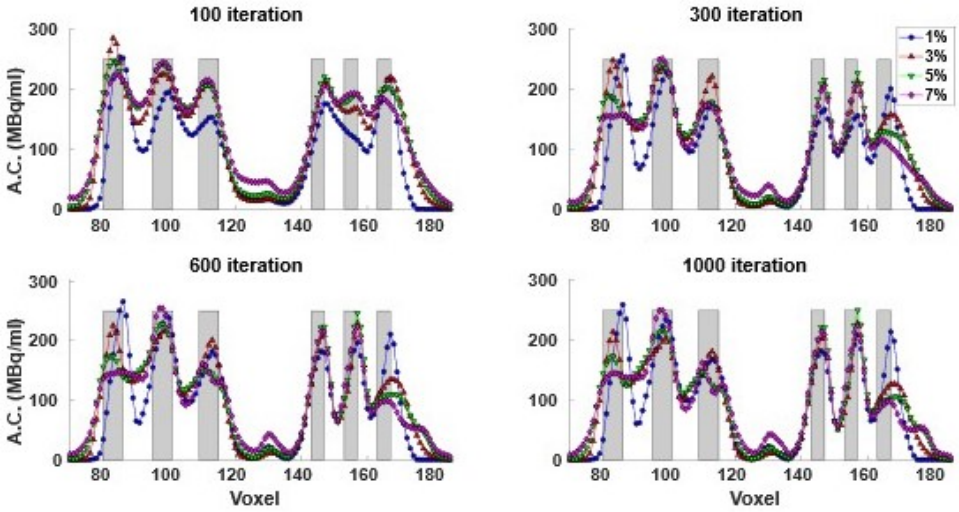

Figure 2.10: Line profiles through 0.85 mm and 0.75 mm rods of Derenzo resolution phantom at 100th, 300th, 600th and 1000th iterations are shown. For each iteration, profiles obtained from images reconstructed with different tail cut offs are shown. Rectangular bars denote the original positron of Derenzo rods. Abbreviation: A.C. – activity concentration.

2.4. Discussion

In this study, we assessed the resolutions that can be obtained for challenging PET isotopes when imaged with a high energy multi-pinhole scanner. Achieving a high resolution for these isotopes using conventional coincidence preclinical PET is challenging due to their long positron ranges or the down scatter of the prompt gammas into the 511 keV photopeak [106]. To circumvent these issues, VECTor utilizes prompt gamma emissions to image these isotopes instead of the 511 keV annihilation photons [45]. The resolutions obtained for the tested isotopes were in the sub-mm range (table 2.4), except for ^{38}K, for which 1.2 mm resolution can be realized by using the 2.2 MeV prompt emission (figure A.1). To the best of our knowledge, this capability is unique to PET with cluster pinhole collimation.

In this simulation, we modelled the VECTor system with a thin scintillator crystal (9.5 mm). This choice was motivated by the imaging study in [45], where ^{124}I and ^{89}Zr were imaged using a VECTor scanner with a 9.5 mm crystal, providing us with experimental data to see how well they match our simulations. A thicker crystal, such as the 19 mm XT crystal offered by MILabs, may prove advantageous for imaging low-intensity ultra-high energy gamma emissions, such as the 1039 keV (37%) gamma of ^{66}Ga. The 19 mm crystal demonstrates a sensitivity approximately 2.8 times greater than the 9.5 mm crystal at this energy. However, an effective depth-of-interaction (DOI) correction algorithm will be required to optimize performance [107]. Notably, the resolutions achieved in this work for

^{124}I and ^{89}Zr were 0.65 mm and 0.70 mm, respectively. In the previous experimental study [45], 0.75 mm rods of ^{124}I could be distinguished in the resolution phantom. However, since the phantom used did not contain smaller 0.65 mm or 0.70 mm rods, a direct comparison of image resolution is not possible. For ^{89}Zr the experiments indicated a 0.75 mm image resolution which is close to the 0.70 mm resolution reported in this work. The small difference may be explained by the higher activity concentration used in the simulation, the limited ability to include all image degrading effects of the detector in the simulation and perfect modelling of the system matrix that is not possible in an experimental situation. Overall, this work specifically demonstrates that the cluster collimation technology [49] used in the VECTor scanner can achieve sub-mm resolution even at ultra-high energies, as high as 1.4 MeV. Based on our results, we attribute the degradation of images at very high energies primarily to the following factors: (i) pinhole edge and collimator wall penetration, and (ii) down scatter from higher energy emissions within the photopeak, which is isotope-dependent.

In this simulation study, we modelled the detector response by assuming a simple Gaussian model for the energy-dependent energy resolution instead of detailed simulations of the scintillator light transport or electronics. This is certainly an over-simplification for ultra-high energies. Currently, the VECTor scanner detector electronics is optimized for energies up to 1.2 MeV and it would need to be upgraded to a wider energy range to perform imaging studies at higher energies. Upgrading the detector for a wide energy range, e.g., from 20 keV to 2.3 MeV, presents several technical challenges [108]. Non-linearity in PMT response and electronics can affect energy calibration, while maintaining uniformity across the field of view becomes increasingly difficult due to varying detection efficiencies at different energies. Additionally, count rate performance may degrade at higher energies due to pulse pile-up and extended dead time in the electronics. Thus, while we validated the current collimator for the investigated isotopes, the suitability of the detector in real experiments was not yet verified for energies >1.2 MeV.

Ring artifacts were observed in ultra-high energy images (figure 2.9). We found that using a higher cutoff forward matrix could mitigate these ring artifacts. This might seem contradictory to previous findings [55], where a lower cutoff of 1% (as opposed to 20% used in 140 keV imaging) improved image resolution and uniformity at 511 keV. This contradiction can be explained by considering that, in the VECTor system, at ultra-high energies, PSFs become broad due to enhanced edge penetration and significant wall penetration (figure 2.2), rendering the reconstruction problem underdetermined and leading to ring artifacts. Wall penetration can be mitigated by using a thicker collimator or an additional independent outer casing on top of the collimator. However, edge penetration cannot be reduced in this manner, which is the primary reason for the gradual degradation of image resolution with increasing energy (figures 2.4 and 2.5). This effect can be reduced by reducing the opening angle of the pinholes, but that requires sophisticated cluster geometries to maintain FOV (e.g. twisted cluster pinholes [109] or superclusters [70, 110]. Furthermore, additional artifacts were present in the 511 keV uniformity images of isotopes exhibiting pronounced down scatter (^{52}Mn, ^{94}Tc and ^{86}Y) due to higher energy prompts. Our analysis revealed that these artifacts arise either due

to detector down scatter (transaxial view) or a combination of detector and collimator scatter (coronal view). Hence, implementing a scatter correction scheme which goes beyond the used triple energy window method similar to [111] may improve imaging performance for these challenging isotopes.

Many of the isotopes studied have more than one prompt gamma with sufficient intensity, such as ^{52}Mn, ^{94}Tc, and ^{86}Y. In subsequent studies, we will perform a feasibility study of the joint reconstruction of multiple prompt gamma energies simultaneously. This approach may enable achieving comparable image quality with reduced activity levels and/or shorter acquisition times, which is particularly relevant for dose quantification in alpha-particle radiotherapies. Additionally, for isotopes like ^{89}Zr, ^{52}Mn, and ^{94}Tc, which have relatively short positron ranges, it may be worthwhile to investigate joint reconstruction with the 511 keV annihilation photons. Lastly, the current design of the cluster multi-pinhole collimator is prone to ring artifacts at ultra-high energies specifically from 1.2 MeV. Therefore, developing a mitigation technique to eliminate these artifacts will be a priority in the future.

2.5. Conclusion

Our research indicates that cluster pinhole collimators are suitable for sub-mm resolution for 9 out of the 10 PET isotopes studied in this paper, including those with long positron ranges by utilizing prompt emissions of high intensity at one or multiple energies. For example impressive ~0.80 mm imaging resolutions at gamma energies as high as 1.4 MeV where attained. The unique capability of cluster pinhole collimation to enable sub-mm resolution for such a diverse set of challenging isotopes can enable a wide range of applications in development of new tracers and therapies.

Acknowledgments

This work was supported by the research grant QUARAT: Quantitative Universal Radiotracer Tomography (TTW16885), which is partially funded by the Dutch Research Council (NWO). The authors wish to express their gratitude to Dr. Chris Kamphuis of MILabs B.V., The Netherlands, for providing information on the detector energy resolutions of VECTor scanner at various energies.

Appendix

Positron range

We conducted a comparative analysis of positron range distributions obtained from GATEv9.0 against another software called PeneloPET [98], a track structure code

developed by [98–101] and semi-empirical formula. Most of the literature studied a particular one dimensional distribution:

$$aPSF_{sin} = \int_{-\infty}^{\infty} dz \int_{-\infty}^{\infty} aPSF(x,y,z)\, dy \tag{A.1}$$

where $aPSF$ (annihilation point spread function) is three dimensional distribution of annihilation points. Derenzo [112] showed that $aPSF_{sin}$ can be modelled by double exponential function:

$$P(x) = Ce^{-k_1 x} + (1-C)e^{-k_2 x} \tag{A.2}$$

We compared the fitting parameters (C, k_1, k_2) obtained from GATE data with those reported in [98] and [99–101], (table A.1), maintaining a consistent bin size of 10 micrometers. Additionally, we compared the mean positron range obtained from GATE with [98–101] (table A.2). The mean ranges reported in [98] and [99–101] were derived from two-dimensional projection distributions of the original three-dimensional distribution of annihilation points. Accordingly, we projected the original three-dimensional annihilation distribution obtained from GATE onto a two-dimensional plane to calculate the mean ranges. In literature, the mean range is estimated using a semi-empirical expression.

$$R_{\text{mean}}\ [\text{cm}] = \frac{0.108 \left[E_{\beta}^{\max}\ [\text{MeV}]\right]^{1.14}}{\rho\ [\text{g cm}^{-3}]} \tag{A.3}$$

Positron range values reported in the literature exhibit considerable variation. Upon reaching thermal velocity, a positron will either annihilate directly with an electron or form a hydrogen like positronium atom. Due to its neutral charge, positronium does not interact electromagnetically, allowing it to drift depending on its residual momentum and half life. The formation probability of positronium is influenced by the energy of the beta particle and the medium.

Most Monte Carlo codes, such as GATE, PeneloPET, and EGSnrc, utilize cross-sections from [113], which do not account for positronium formation. To the best of our knowledge, studies in [99–101] have incorporated positronium formation in their track structure code. This may explain why the positron ranges reported by them are systematically larger compared to those from GATE, PeneloPET [98], and the semi-empirical formula A.3 (table A.1). However, it is noteworthy that the positronium yield in water reported in [114] (83%) significantly deviates from the values reported in other sources, such as [115], and [116], which are approximately 30%.

Isotope	*C*		k_1 *[mm^{-1}]*		k_2 *[mm^{-1}]*		
	GATE (v9.0)	*Loirec et al.*	*GATE (v9.0)*	*Loirec et al.*	*GATE (v9.0)*	*PeneloPET*	*Loirec et al.*
^{18}F	0.68	–	76.48	–	4.81	3.27	–
^{11}C	0.66	0.61	58.95	30.91	2.46	1.79	1.49
^{13}N	0.65	0.58	53.45	22.12	1.75	1.30	1.07
^{15}O	0.63	0.56	41.37	16.84	0.98	0.77	0.60
^{68}Ga	0.71	0.34	50.54	13.81	0.94	0.67	0.49
^{82}Rb	0.65	–	36.59	–	0.41	0.31	–
^{52}Mn	0.73	0.39	97.69	19.92	6.13	6.13	2.79
^{89}Zr	0.75	0.29	79.84	17.68	3.22	–	1.42
^{44}Sc	0.69	0.33	53.76	10.74	1.34	–	0.71
^{86}Y	0.77	0.40	64.41	7.89	1.70	–	0.76
^{72}As	0.70	0.50	41.47	14.82	0.60	–	0.35
^{124}I	0.77	0.39	57.27	8.38	1.18	–	0.54
^{38}K	0.39	0.38	10.27	11.70	0.48	–	0.30
^{66}Ga	0.83	0.79	41.48	7.46	0.35	–	0.20

Table A.1: Comparison of fitted parameters C, k_1, and k_2 between GATE v9.0, Loirec et al. [99–101], and PeneloPET [98].

Isotope	R_{mean} *[mm] GATE (v9.0)*	R_{mean} *[mm] PeneloPET*	R_{mean} *[mm] Loirec et al.*	R_{mean} *[mm] Semi-Empirical*
^{18}F	0.38	0.57	0.66	0.64
^{11}C	0.77	1.02	1.27	1.03
^{13}N	1.08	1.40	1.73	1.33
^{15}O	1.88	2.34	2.97	2.02
^{68}Ga	2.03	2.69	3.56	2.23
^{82}Rb	4.37	5.33	7.49	4.18
^{52}Mn	0.67	–	0.63	0.58
^{89}Zr	0.63	–	1.27	0.96
^{44}Sc	1.44	–	2.46	1.68
^{86}Y	2.52	–	2.51	1.73
^{72}As	3.31	–	5.19	3.24
^{124}I	2.22	–	3.37	3.28
^{38}K	4.48	–	5.67	3.39
^{66}Ga	7.49	–	8.69	5.16

Table A.2: Positron mean range compared between GATE (v9.0), PeneloPET [98], Monte Carlo track structure code by [99–101] and semi-empirical formula A.3 for PET isotopes under study and other.

Determining resolution for ^{38}K

Figure A.1 presents the ^{38}K reconstructed images for the second Derenzo resolution phantom with larger diameter rods. Following the convention outlined in section 2.2.3, a 5% cutoff matrix was employed to reconstruct the 2167 keV gamma to avoid the ring artifact. Both the 511 keV gamma, with PRC, and the 2167 keV gamma are capable of resolving the 1.2 mm rods, with the 2167 keV reconstruction exhibiting lower noise compared to the 511 keV.

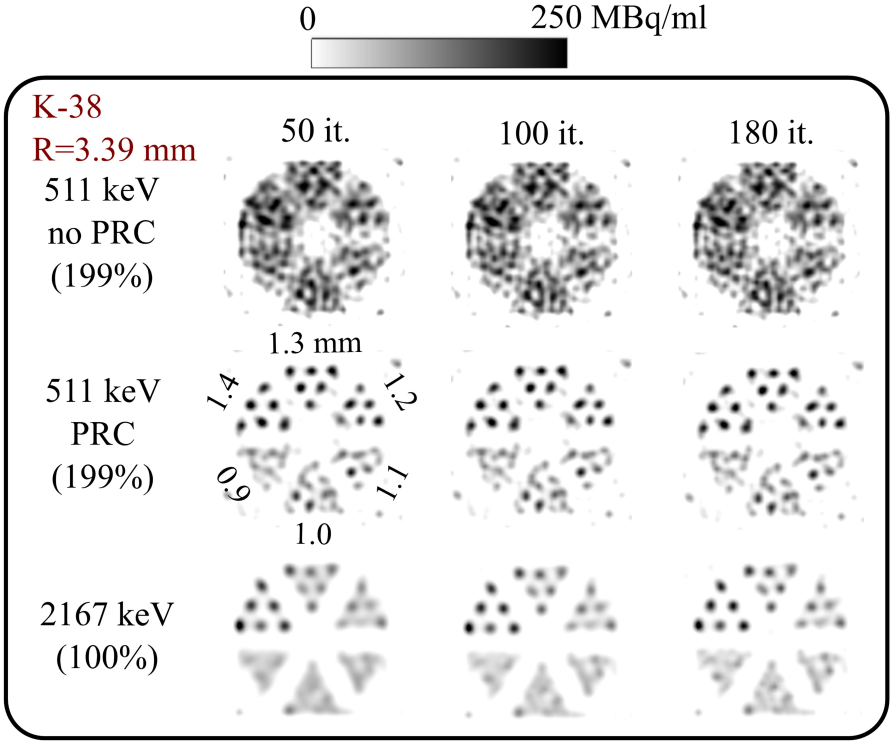

Figure A.1: Derenzo resolution phantom images after 50th, 100th and 180th iterations are shown for ^{38}K. Abbreviation: PRC, Positron Range Correction; R, positron mean range.

Ring artifact in uniformity phantom

At the ultra-high energy of 1.4 MeV for ^{52}Mn, a size reduction artifact appears in the transaxial view of the reconstructed uniformity phantom images when a 1% cutoff matrix is used (figure A.2). Similar to the resolution phantom case, a slightly larger cutoff matrix was employed to mitigate this artifact. Line profiles shown in figure A.6 confirm that using a higher cutoff matrix can effectively reduce the artifact.

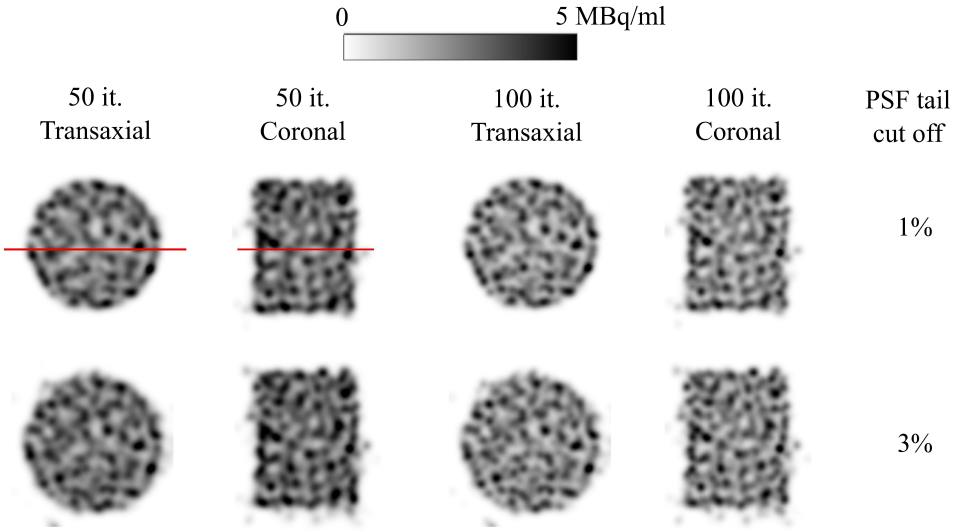

Figure A.2: Uniformity phantom reconstructed for 1.4 MeV of ^{52}Mn using matrices with tail cutoffs of 1% and 3%. Images at 50th and 100th iteration are shown. The significant size reduction observed in the transaxial view is attributed to the presence of a ring artifact.

Collimator penetration data

Gamma energy [keV]	*Escape probability*
140	~0.0%
511	0.003%
603	0.019%
703	0.071%
744	0.106%
834	0.214%
861	0.255%
909	0.336%
935	0.385%
1039	0.618%
1096	0.764%
1157	0.929%
1434	1.700%
2167	3.200%

Table A.3: Percentage of photons passing through 43 mm collimator wall without any interaction.

Line profiles of positron range kernels

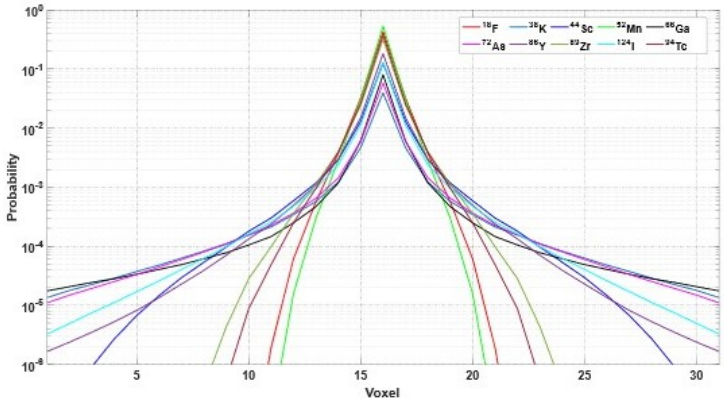

Figure A.3: Line profiles of positron range kernels of PET isotopes under study. One voxel equals to 0.4 mm.

Uniformity and resolution phantom

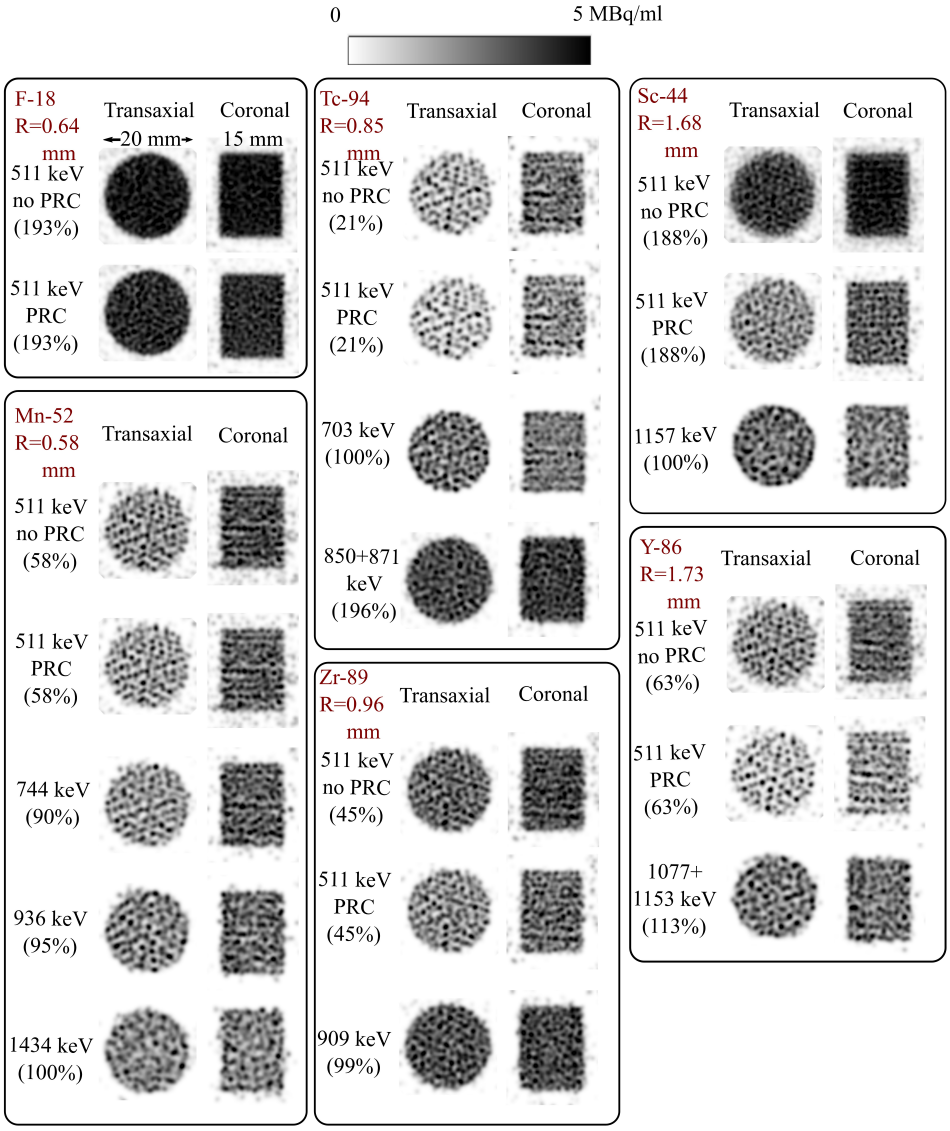

Figure A.4: Uniformity phantom images at the 100th iteration are presented for isotopes ^{18}F, ^{52}Mn, ^{94}Tc, ^{89}Zr, ^{44}Sc, and ^{86}Y. Both transaxial and coronal views are displayed. Abbreviation: PRC, positron range correction; R, positron mean range.

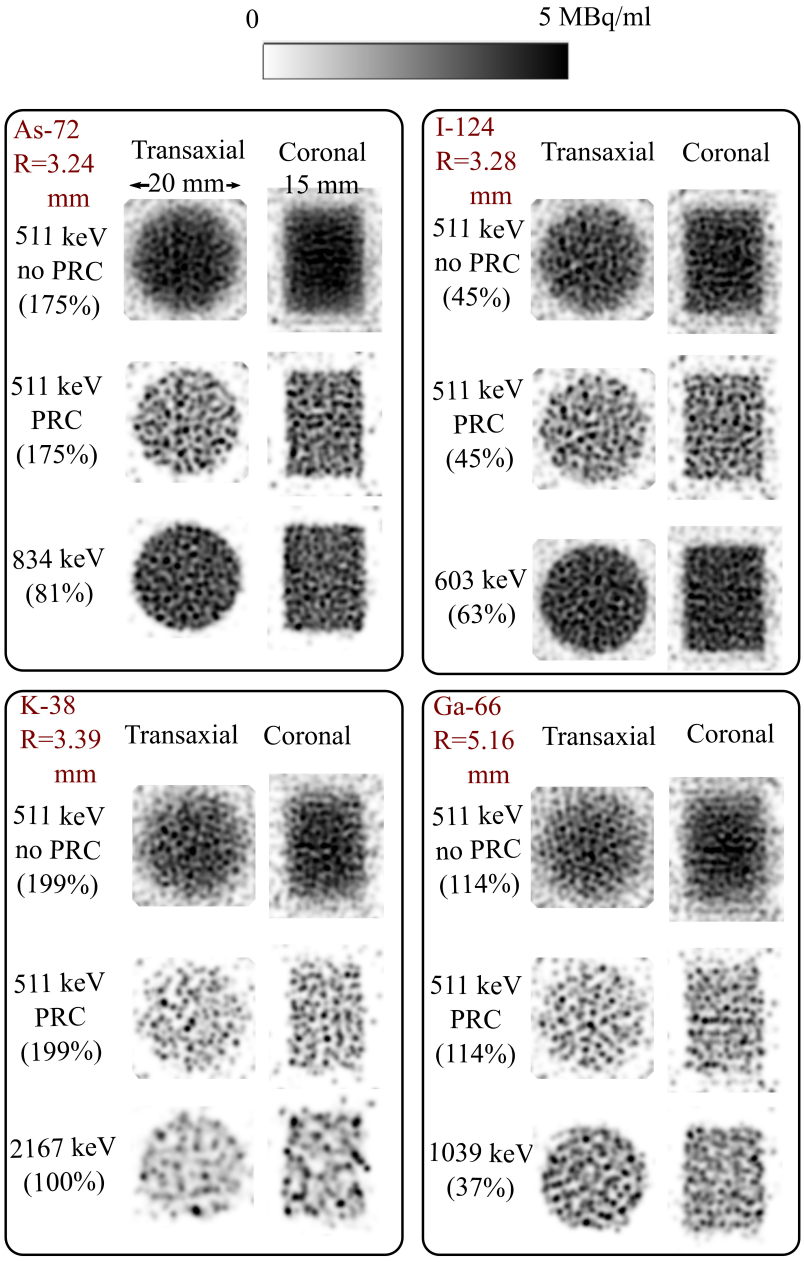

Figure A.5: Uniformity phantom images at the 100th iteration are presented for isotopes ^{72}As, ^{38}K, ^{124}I, and ^{66}Ga. Both transaxial and coronal views are displayed. Abbreviation: PRC, positron range correction; R, positron mean range.

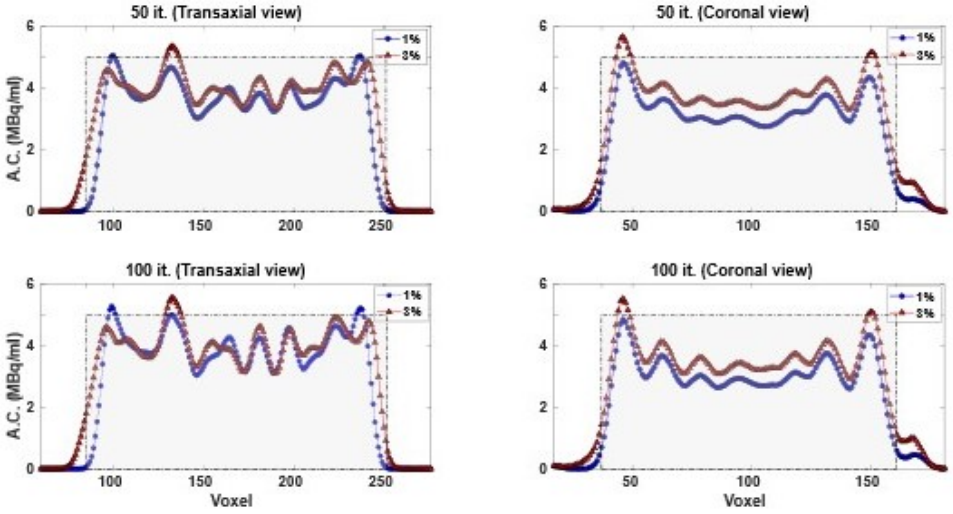

Figure A.6: Line profiles through the transaxial and coronal views of the uniformity phantom at the 50th and 100th iterations are presented. For each iteration, profiles obtained from images reconstructed with tail cut-offs of 1% and 3% are displayed. Rectangular areas denote the original position of the uniformity phantom. Abbreviation: A.C. – Activity Concentration.

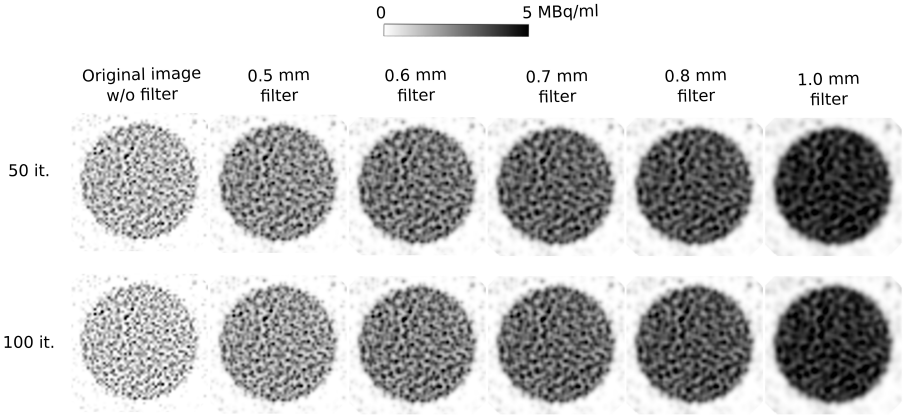

Figure A.7: Transaxial views of a uniformity phantom for 511 keV gamma emissions (with PRC) of ^{18}F isotope are shown at the 50th and 100th iterations. The images range from the original unfiltered image to post-processing with different widths of Gaussian filter.

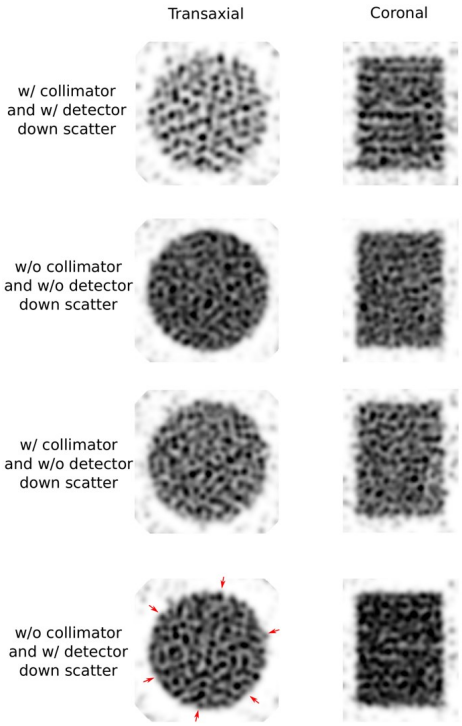

Figure A.8: Transaxial and coronal views of the 50th iteration of 511 keV reconstruction with positron range correction for ^{52}Mn isotope. Images are shown for projection data with and without collimator and detector down scatter contributions. All images were post-filtered using a 1 mm FWHM Gaussian filter.

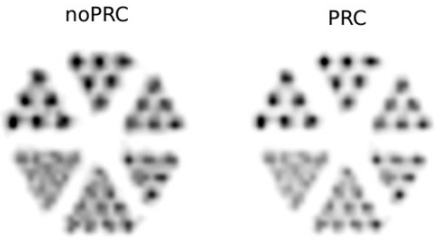

Figure A.9: Derenzo resolution phantom reconstructed from 511 keV emission of ^{52}Mn after rejecting down scatter from projection data. Rods are of diameters 0.85, 0.80, 0.75, 0.70, 0.65 and 0.60 mm. A Gaussian post-filter of 0.50 mm FWHM was applied on images. Abbreviation: PRC – Positron Range Correction.

3

Dual-photopeak joint image reconstruction for pinhole SPECT, PET and PET-SPECT

This chapter is adapted from: Satyajit Ghosh, Valerio Cosmi, Ruud M. Ramakers, Freek J. Beekman and Marlies C. Goorden, Dual-photopeak joint image reconstruction for pinhole SPECT, PET and PET-SPECT. *Physics in Medicine & Biology*, 2026. 71(1).

Many SPECT and PET radionuclides, along with radionuclides used in targeted alpha or beta therapy and their imaging surrogates have multiple gamma and/or positron emissions. Images of these radionuclides are usually obtained from the photopeak with the most convenient energy and/or highest intensity or by adding counts from different photopeaks. Smart utilization of multiple energy peaks may improve reconstructed images, especially in low-count scans.

We investigate and compare various multi-photopeak joint reconstruction approaches, namely (i) Single-Band Joint Reconstruction (SB-JR) – projections from multiple energy windows are summed and reconstructed with a system matrix at a single average energy, (ii) mixed Multi-Band Joint Reconstruction (mMB-JR) - like SB-JR but the system matrix incorporates the element-wise contributions from all photopeak energies, (iii) Multi-Band Joint Reconstruction (MB-JR) – separate projections for each window and separate system matrices at relevant gamma energies are utilized. We evaluate these methods for a multi-pinhole PET/SPECT system (VECTor, MILabs, The Netherlands) using Monte Carlo generated Derenzo phantom projections of ^{225}Ac (218 keV and 440 keV gammas), ^{226}Ac (158 keV and 230 keV gammas) and ^{89}Zr (511 keV annihilation gammas and 909 keV prompt gammas) at three different activity concentrations. A contrast-to-noise ratio (CNR) based quantitative performance analysis was done.

The MB-JR scheme of joint reconstruction showed superior visual image quality and highest CNRs in almost all cases, across all radionuclides and activity concentrations. The CNR improvement for the smallest visible rods in the Derenzo phantom ranged from 30% to 65% for ^{225}Ac, 20% to 54% for ^{226}Ac, and 25% to 47% for ^{89}Zr, respectively. CNR improvements/degradations for the other two joint reconstruction methods, mMB-JR and SB-JR, were as follows: for ^{225}Ac, −16% to 51% and −21% to 51%; for ^{226}Ac, 9% to 61% and 0.2% to 38%; and for ^{89}Zr, 19% to 52% and −3% to 16%, respectively.

We believe the proposed image reconstruction methods can enhance SPECT, PET, PET/SPECT imaging of a wide range of radionuclides that emit gammas with multiple energies.

3.1. Introduction

Many SPECT and PET radionuclides (e.g., ^{111}In, ^{67}Ga, ^{201}Tl, ^{89}Zr, ^{124}I), including radionuclides for targeted alpha therapy (TAT) and targeted beta therapy (TBT) (e.g., TAT: ^{225}Ac, ^{149}Tb, ^{223}Ra, ^{211}At; TBT: ^{177}Lu, ^{131}I, ^{161}Tb) and their imaging surrogates (e.g., TAT surrogates: ^{226}Ac, ^{155}Tb, ^{131}Ba, ^{209}At; TBT surrogates: ^{111}In, ^{124}I, ^{155}Tb) have multiple gamma and/or positron emissions that can be used for imaging (details provided in table 3.1). In most clinical and preclinical studies, either a single gamma emission (typically the one with the most convenient energy and/or highest intensity) is utilized for imaging, or peaks are added up and reconstructed with a single system matrix [117–120]. Leveraging all available gamma emissions jointly in an optimal way for imaging has the potential to further enhance imaging performance, especially in low-uptake and/or shorter time scans. A better reconstruction method may also enable to scan with a lower dose. Furthermore, the development of specialized low-count imaging methods is essential to facilitate image-based dosimetry for TAT radionuclides, given the often low

gamma-abundancies and/or limitations on the maximum injectable activity permissible [121–126] to prevent radiation damage to healthy organs. Preclinical imaging of TAT radionuclides and their surrogates can be conducted using SPECT [127, 128], PET [129], PET/SPECT [40, 45] or a Compton camera [130] depending on the type of emissions and resolution requirements.

Successful utilization of different emissions jointly has been attempted previously across a diverse range of imaging modalities: (i) joint reconstruction of ^{90}Y from the continuous bremsstrahlung spectrum in SPECT [131], (ii) projection-domain based dose quantification for ^{227}Th and ^{223}Ra in SPECT [132], (iii) joint utilization of 'PET events' and 'Compton events' in Compton-PET [133, 134], and (iv) joint reconstruction of different channels of information for a multi-layer Compton camera used in online beam range verification based on prompt gamma imaging [135].

In this work, we compare three joint reconstruction schemes to simultaneously use multiple photopeaks from radionuclides emitting multiple gammas and/or positrons. We tested these algorithms with simulations representing the preclinical PET/SPECT VECTor scanner [40] (MILabs B.V.). The VECTor scanner of which the initial version was introduced in 2013, equipped with clustered pinhole technology [49], experimentally demonstrates sub-mm resolutions at 140 keV of ^{99m}Tc [40], 364 keV of ^{131}I [46], 440 keV of ^{213}Bi [47], 511 keV of ^{18}F [40], 603 keV of ^{124}I and 909 keV of ^{89}Zr [45] and, according to simulations, can also achieve sub-mm resolution for ultra-high energy (>1 MeV) prompt gammas up till 1.4 MeV [30], making it a suitable modality for imaging all radionuclides listed in table 3.1, which emit gammas across a broad energy range. Additionally, the scanner is capable of performing positron range-free PET and multi-tracer PET imaging [45].

For this study, we performed Monte Carlo simulations for ^{225}Ac, ^{226}Ac and ^{89}Zr activity distributions to characterize the proposed methods for a wide energy range of 158 keV to 909 keV and, for simplicity, only two photopeaks were jointly reconstructed for each radionuclide. Derenzo resolution phantom images at different activity concentrations were assessed for each radionuclide and quantitatively compared via a contrast-to-noise (CNR) analysis.

Radionuclide	*Half-life*	*Imageable Emissions [keV] (% Int.)*	*Application*
^{111}In (SPECT)	2.8 days	X-rays: 23+26 (82%) γ: 171 (91%), 245 (94%)	pretherapeutic dosimetry, surrogate of ^{177}Lu [136]
^{89}Zr (PET)	3.3 days	X-rays: 14 (42%) γ: 511 (45%), 909 (99%)	immunoPET [74]
^{124}I (PET)	4.2 days	X-rays: 27+31 (54%) γ: 511 (45%), 603 (63%), 723 (10%), 1691 (11%)	thyroid cancer [78]
^{223}Ra (TAT)	11.4 days	X-rays: 81+84 (40%) γ: 154 (6%), 269 (14%)	prostate cancer [137]
^{131}Ba	11.5 days	X-rays: 31+35 (96%) γ: 124 (30%), 216 (20%), 373 (14%), 496 (48%)	surrogate of ^{223}Ra
^{225}Ac (TAT)	10.0 days	γ: 218* (11%), 440* (26%)	prostate [138], breast cancer [126]
^{226}Ac	1.2 days	γ: 158 (15%), 230 (22%)	surrogate of ^{225}Ac
^{211}At (TAT)	7.2 hours	X-rays: 73*+75* (57%), 77+79 (19%), 85* (8%) γ: 570* (98%), 1063* (75%), 1770* (7%)	ovarian cancer [139]
^{209}At	5.4 hours	X-rays: 77+79 (96%), 90+92 (19%) γ: 195 (24%), 239 (13%), 545 (91%), 781+790 (147%)	surrogate of ^{211}At
^{149}Tb (TAT)	4.1 hours	X-rays: 43+49 (58%), 41*+47* (100%) γ: 150* (48%), 165 (22%), 299* (28%), 346* (24%), 352 (25%), 389 (16%), 465 (5%), 511 (12%), 652 (14%), 789* (7%), 817 (10%), 853 (13%)	pancreatic cancer [140]
^{161}Tb (TBT)	6.9 days	X-rays: 45 (17%) γ: 26 (23%), 49 (17%), 75 (10%)	prostate cancer [141]
^{155}Tb	5.3 days	X-rays: 43+49 (106%) γ: 87 (32%), 105 (25%)	surrogate of ^{149}Tb and ^{161}Tb
^{177}Lu (TBT)	6.6 days	γ: 113 (6%), 208 (11%)	prostate cancer [142]

Table 3.1: Examples of radionuclides with multiple photopeaks that are of interest for (bio)medical applications. Half-lives, imageable emissions with corresponding energies and intensities, and applications are given for SPECT and PET radionuclides including TAT and TBT radionuclides (with their imaging surrogates), for which joint reconstruction can be used. All positrons yield 511 keV photons for imaging. Only >5% relative intensity emissions are presented; * indicates emission from daughters with intensity disregarding branching ratio.

3.2. Materials and methods

3.2.1. Scanner description

We simulated the VECTor PET/SPECT scanner [40] with standard crystal thickness to evaluate our algorithms. The detector component of this scanner consists of three, triangularly arranged, monolithic NaI(Tl) scintillator detectors (9.5 mm thick) with PMT-based light collection. Each individual planar detector has a surface area of 590×470 mm^2 [39]. The collimator employed in this study is designed based on proprietary cluster collimation technology [49] and consists of 48 clusters, each containing 2×2 pinholes, resulting in a total of 162 knife-edge pinholes. The cylindrical collimator has an inner diameter of 48 mm, and a wall thickness of 43 mm. The centers of all pinholes are positioned at a 64 mm diameter. The pinholes are organized into four adjacent rings in longitudinal direction, with those in the inner two rings having an opening angle of 18°, while the pinholes in the outer two rings have an opening angle of 16°. The collimator is made of a material mixture consisting of tungsten (97%), nickel (1.5%), and iron (1.5%).

The central field of view (CFOV) is the region sampled collectively by all pinholes. In the CFOV complete data sampling is thus achieved in accordance with Tuy's condition without any bed movement [81]. For imaging objects larger than the CFOV, data acquisition is performed using the scanning focus method [82], where the sample-holding bed is incrementally translated in a finite number of steps, and the data acquired from all bed positions is used simultaneously to reconstruct the 3D tracer distribution.

3.3. Monte Carlo simulations

3.3.1. Scanner simulation and data acquisition

Monte Carlo (MC) simulations were performed using GATE v9.0 [83–85], which is based on Geant4 v10.05 [86] and ran on a CentOS 7.0 cluster. The three NaI(Tl) planar detectors were modelled in the GATE environment as three rectangular boxes. The first detector was positioned perpendicular to the y-axis and translated to the coordinates (0, −215 mm, 0). The second and third detectors were rotated by ±120° around the z-axis and translated to the positions (−186 mm, −107 mm, 0) and (186 mm, −107 mm, 0), respectively, in order to precisely replicate the triangular configuration of the VECTor scanner. The clustered pinhole collimator was simulated according to the geometric parameters provided by the manufacturer, and its performance was validated on the VECTor scanner as reported in [40].

Three radionuclides, ^{225}Ac, ^{226}Ac and ^{89}Zr, were used in this study. GATE's "ion source" utility was used to simulate all types of emissions from these radionuclides. The selection of these radionuclides was motivated by their relevance to current applications and the opportunity to evaluate the proposed joint reconstruction methods using gamma

emissions across different energy ranges. The lower energy range includes 158 keV, 218 keV, 234 keV, and 440 keV emissions from ^{225}Ac and ^{226}Ac, while the higher energy range includes 511 keV and 909 keV emissions from ^{89}Zr. Additionally, these radionuclides offer varying degrees of proximity between gamma energies from individual radionuclides. For instance, ^{226}Ac provides closely spaced gamma emissions at 158 keV and 234 keV. ^{225}Ac exhibits more widely separated gamma lines at 218 keV and 440 keV, while ^{89}Zr results in a larger energy spacing with 909 keV gammas and 511 keV annihilation photons. Physics processes were built using the "*emstandard*" physics list builder (see GATE documentation [143]). Photomultipliers, light collection and back-end electronics of the scanner were not modelled. Rather, their aggregate effect is replicated by modelling 10% energy resolution (E_{res}) at 140 keV for ^{225}Ac and ^{226}Ac simulations and 9% E_{res} at 511 keV for ^{89}Zr, as per the manufacturer's specifications. For both cases, $\frac{1}{\sqrt{E}}$ scaling was considered individually from a 140 keV energy (model-A) for ^{225}Ac and ^{226}Ac and from a 511 keV energy (model-B) for ^{89}Zr to simulate the E_{res} at different gamma energies such that it matches well with experimentally determined E_{res} (table 3.2). Also, a 3.5 mm FWHM intrinsic spatial resolution of the detector was assumed, as per manufacturer's specifications. These resolutions were implemented by sampling from Gaussian distributions with respective FWHMs. Natural background (NB), corresponding to the detector counts present in the absence of activity, was also included to improve realism. A count rate of 1 keV-1sec-1 was assumed for each of the three planar detectors of the VECTor scanner, in accordance with the manufacturer's specifications. This count rate was used to generate Poisson distributed NB across all three detector planes. Finally, gamma detection positions on the detector surface were discretized in 1.072×1.072 mm^2 pixels to obtain projection data. All of these post processing tasks were implemented through MATLAB v2021b scripts.

Source	***Energy [keV]***	***Exp. E_{res}***	***Sim. E_{res}***
^{125}I	35	22.7% [108]	20.0%$^{(a)}$
^{99m}Tc	140	10.0% [108]	10.0%$^{(a)}$
^{22}Na	511	9.7% [108]	9.0%$^{(b)}$
^{124}I	603	8.3% [45, 144]	8.3%$^{(b)}$
^{89}Zr	909	7.2% [30, 45]	6.8%$^{(b)}$

Table 3.2: Comparing experimental energy resolution (E_{res}) values with simulated ones. Abbreviations: E_{res}(a) for model-A and E_{res}(b) for model-B.

3.3.2. Digital phantoms

For ^{225}Ac, two different Derenzo resolution phantoms and three different activity concentrations were utilized in the study. For a concentration of 20 MBq/ml, a Derenzo phantom with rod diameters of 0.75 mm, 0.70 mm, 0.65 mm, 0.60 mm, 0.55 mm, and 0.50 mm, each with a length of 10 mm, was employed (figure 3.1). These rods were positioned within a PMMA cylinder with a diameter of 12 mm and a height of 12 mm. We name this phantom DP-1. The activity concentration of 20 MBq/ml exceeds the values typically encountered in biological experiments for this radionuclide (appendix 3.9). Nevertheless, this concentration was investigated to characterize the proposed joint reconstruction methods in the SPECT energy range. For the other two activity concentrations of 0.5 MBq/ml and 0.2 MBq/ml, a different Derenzo phantom with rod diameters of 1.6 mm, 1.5 mm, 1.4 mm, 1.1 mm, 1.0 mm, and 0.90 mm and a rod length of 10 mm was used suitable for the changed reconstructed rod visibility. The hot rods were housed within a PMMA cylinder with a diameter of 20 mm and a height of 12 mm. We name this phantom DP-2.

For ^{226}Ac, the above described DP-1 phantom was used with activity concentrations kept at 10 MBq/ml, 2 MBq/ml, and 1 MBq/ml.

For ^{89}Zr, a Derenzo resolution phantom with rod diameters of 0.85 mm, 0.80 mm, 0.75 mm, 0.70 mm, 0.65 mm, and 0.60 mm and a rod length of 10 mm was employed, named DP-3 (figure 3.1). These rods were enclosed within a PMMA cylinder with a diameter of 14 mm and a height of 12 mm. Activity concentrations of 200 MBq/ml, 100 MBq/ml, and 50 MBq/ml were investigated.

For all three radionuclides, the selection of activity concentrations was motivated to show degradation of resolution as activity concentration decreases, and to investigate benefit of proposed joint reconstruction at these different levels of resolution degradation. For all cases, data acquisition was performed using a multiplanar trajectory (MPT) approach [88] across nine bed positions, with a total scan duration of one hour.

3.3.3. Positron range simulation

The positron annihilation point distribution was calculated for ^{89}Zr using a MC simulation of a point source placed at the center of a 20 cm water sphere. This simulation used the same electromagnetic physics list (*emstandard*) as that employed for the other radionuclides studied, in order to ensure consistency across all MC simulations. A total of five million positron annihilation events were simulated. The three-dimensional coordinates of the annihilation points were recorded on a $31 \times 31 \times 31$ voxel grid, where the central voxel corresponded to the position of the point source. The voxel size was the same as in the corresponding reconstructed images. The resulting positron range kernel was subsequently normalized.

3.4. Joint reconstruction schemes

Here we describe the proposed reconstruction schemes assuming that two photopeaks are being used as this simplifies the expressions. However, the extension to more photopeaks is in principle straightforward, though such schemes will have added computational complexity. Note that for the radionuclides considered in this paper, there are only two photopeaks with reasonable intensity.

Consider a radionuclide emitting gamma photons of two energies E_1 and E_2 of intensities I_1% and I_2% respectively. We assume that these two energies are sufficiently separated so that the different photopeaks can be resolved by the scanner. We define $\boldsymbol{a} \in \mathbb{R}^N$ as a vector representing the amount of activity in the N voxels in the object. Let $\boldsymbol{p}^{(1)} \in \mathbb{R}^V$ and $\boldsymbol{p}^{(2)} \in \mathbb{R}^V$ denote the noiseless projections from the two emissions corresponding to gamma photons of energy E_1 and E_2 respectively. Here, V is the total number of pixels of the detectors, multiplied by the number of bed positions utilized in the scan (see section 3.2.1). Also, let $\boldsymbol{s}^{(1)} \in \mathbb{R}^V$ and $\boldsymbol{s}^{(2)} \in \mathbb{R}^V$ be estimated noiseless scatter projections (for scattered gammas detected in the photopeak) which depend on the activity distribution. Furthermore, $\boldsymbol{M}^{(1)} \in \mathbb{R}^{V \times N}$ and $\boldsymbol{M}^{(2)} \in \mathbb{R}^{V \times N}$ are energy dependent system matrices describing photon transport for gamma energies E_1 and E_2 respectively. These matrices exclude scatter but include gamma photon penetration through collimator and in the detector.

In image reconstruction, we use an ordered-subset based maximum likelihood expectation maximization algorithm (see subsection 3.5 for specific implementation details). This algorithm includes forward projection/backprojection steps in each sub-iteration which are implemented in different ways for the different separate and joint reconstruction schemes that we compare. This is detailed below given the earlier defined quantities for the forward projection step in the algorithm. For the backprojection step, the same equation but without the scatter component is used.

3.4.1. Separate reconstruction of photopeaks

The conventional method for formulating the problem is to treat projections from different gamma energies independently which would result in separate images for each photopeak. Accordingly, the relation between noiseless projection and activity in the forward projection step of iterative image reconstruction can be written as:

$$\boldsymbol{p}^{(i)} = \boldsymbol{M}^{(i)}\boldsymbol{a} + \boldsymbol{s}^{(i)}$$

$$\begin{pmatrix} p_1^{(i)} \\ p_2^{(i)} \\ \vdots \\ p_V^{(i)} \end{pmatrix}_{V\times 1} = \tau_i \begin{pmatrix} m_{11}^{(i)} & m_{12}^{(i)} & \cdots & m_{1N}^{(i)} \\ m_{21}^{(i)} & m_{22}^{(i)} & \cdots & m_{2N}^{(i)} \\ \vdots & \vdots & \ddots & \vdots \\ m_{V1}^{(i)} & m_{V2}^{(i)} & \cdots & m_{VN}^{(i)} \end{pmatrix}_{V\times N} \begin{pmatrix} a_1 \\ a_2 \\ \vdots \\ a_N \end{pmatrix}_{N\times 1} + \begin{pmatrix} s_1^{(i)} \\ s_2^{(i)} \\ \vdots \\ s_V^{(i)} \end{pmatrix}_{V\times 1} \tag{3.1}$$

Where $\tau_i = (I_i T_{1/2})/(100 \ln 2)\left(1 - e^{-t(\ln 2/T_{1/2})}\right)$ factors convert activity into emitted counts for respective energies (here, $T_{1/2}$: half life of the radionuclide; t: scan time) and system matrix element $[m_{vn}^{(i)}]$ is defined as the probability of a gamma photon of energy E_i emitted from the n^{th} voxel to get detected in the v^{th} detector pixel.

3.4.2. Post combining images

Activity distribution estimates obtained from separate reconstructions of two gamma energies (section 3.4.1) can be combined (added) to generate an additional estimate.

3.4.3. Single-band joint reconstruction

One approach of combining the two projection equations in equation 3.1 is as follows:

$$\begin{pmatrix} p_1^{(1)} + p_1^{(2)} \\ p_2^{(1)} + p_2^{(2)} \\ \vdots \\ p_V^{(1)} + p_V^{(2)} \end{pmatrix}_{V\times 1} = \begin{pmatrix} m_{11}^{\text{ave}} & m_{12}^{\text{ave}} & \cdots & m_{1N}^{\text{ave}} \\ m_{21}^{\text{ave}} & m_{22}^{\text{ave}} & \cdots & m_{2N}^{\text{ave}} \\ \vdots & \vdots & \ddots & \vdots \\ m_{V1}^{\text{ave}} & m_{V2}^{\text{ave}} & \cdots & m_{VN}^{\text{ave}} \end{pmatrix}_{V\times N} \begin{pmatrix} a_1 \\ a_2 \\ \vdots \\ a_N \end{pmatrix}_{N\times 1} + \begin{pmatrix} s_1^{(1)} + s_1^{(2)} \\ s_2^{(1)} + s_2^{(2)} \\ \vdots \\ s_V^{(1)} + s_V^{(2)} \end{pmatrix}_{V\times 1} \tag{3.2}$$

where $[m_{ij}^{\text{ave}}]$ is a system matrix element at weighted average energy:

$$E_{\text{ave}} = \frac{I_1 E_1 + I_2 E_2}{I_1 + I_2} \tag{3.3}$$

The photon transport model for two gamma energies, when implemented in this manner in image reconstruction, is referred to as Single Band Joint Reconstruction (SB-JR).

3.4.4. Mixed multi-band modelling joint reconstruction

Another way to combine photon transport into a joint equation is to include photon transport in the system matrix by element-wise summation of the matrix elements for the two energies:

$$\begin{pmatrix} p_1^{(1)}+p_1^{(2)} \\ p_2^{(1)}+p_2^{(2)} \\ \vdots \\ p_V^{(1)}+p_V^{(2)} \end{pmatrix}_{V\times 1} = \begin{pmatrix} \tau_1 m_{11}^{(1)}+\tau_2 m_{11}^{(2)} & \tau_1 m_{12}^{(1)}+\tau_2 m_{12}^{(2)} & \cdots & \tau_1 m_{1N}^{(1)}+\tau_2 m_{1N}^{(2)} \\ \tau_1 m_{21}^{(1)}+\tau_2 m_{21}^{(2)} & \tau_1 m_{22}^{(1)}+\tau_2 m_{22}^{(2)} & \cdots & \tau_1 m_{2N}^{(1)}+\tau_2 m_{2N}^{(2)} \\ \vdots & \vdots & \ddots & \vdots \\ \tau_1 m_{V1}^{(1)}+\tau_2 m_{V1}^{(2)} & \tau_1 m_{V2}^{(1)}+\tau_2 m_{V2}^{(2)} & \cdots & \tau_1 m_{VN}^{(1)}+\tau_2 m_{VN}^{(2)} \end{pmatrix}_{V\times N} \begin{pmatrix} a_1 \\ a_2 \\ \vdots \\ a_N \end{pmatrix}_{N\times 1} + \begin{pmatrix} s_1^{(1)}+s_1^{(2)} \\ s_2^{(1)}+s_2^{(2)} \\ \vdots \\ s_V^{(1)}+s_V^{(2)} \end{pmatrix}_{V\times 1} \tag{3.4}$$

This approach for incorporating the photon transport model into image reconstruction is termed mixed Multi-Band Joint Reconstruction (mMB-JR).

3.4.5. Multi-band modelling joint reconstruction

In the above formulations we considered the total number of gammas detected in the two photopeak windows (projections were added). Simply adding projections means that information about the energy of the detected gamma is lost. We therefore consider a third formulation in which this information is retained:

$$\begin{pmatrix} \begin{pmatrix} p_1^{(1)} \\ p_2^{(1)} \\ \vdots \\ p_V^{(1)} \end{pmatrix}_{V\times 1} \\ \begin{pmatrix} p_1^{(2)} \\ p_2^{(2)} \\ \vdots \\ p_V^{(2)} \end{pmatrix}_{V\times 1} \end{pmatrix}_{2V\times 1} = \begin{pmatrix} \tau_1 \begin{pmatrix} m_{11}^{(1)} & m_{12}^{(1)} & \cdots & m_{1N}^{(1)} \\ m_{21}^{(1)} & m_{22}^{(1)} & \cdots & m_{2N}^{(1)} \\ \vdots & \vdots & \ddots & \vdots \\ m_{V1}^{(1)} & m_{V2}^{(1)} & \cdots & m_{VN}^{(1)} \end{pmatrix}_{V\times N} \\ \tau_2 \begin{pmatrix} m_{11}^{(2)} & m_{12}^{(2)} & \cdots & m_{1N}^{(2)} \\ m_{21}^{(2)} & m_{22}^{(2)} & \cdots & m_{2N}^{(2)} \\ \vdots & \vdots & \ddots & \vdots \\ m_{V1}^{(2)} & m_{V2}^{(2)} & \cdots & m_{VN}^{(2)} \end{pmatrix}_{V\times N} \end{pmatrix}_{2V\times N} \begin{pmatrix} a_1 \\ a_2 \\ \vdots \\ a_N \end{pmatrix}_{N\times 1} + \begin{pmatrix} \begin{pmatrix} s_1^{(1)} \\ s_2^{(1)} \\ \vdots \\ s_V^{(1)} \end{pmatrix}_{V\times 1} \\ \begin{pmatrix} s_1^{(2)} \\ s_2^{(2)} \\ \vdots \\ s_V^{(2)} \end{pmatrix}_{V\times 1} \end{pmatrix}_{2V\times 1} \tag{3.5}$$

We thus kept the two projections and their system matrices at the cost of doubling the computation time for reconstruction as the dimension of the equation doubled. Implementing this photon transport model into image reconstruction is denoted by Multi-Band Joint Reconstruction (MB-JR).

3.5. Image reconstruction

Image reconstructions were performed using the dual-matrix dual-voxel similarity-regulated ordered-subset expectation maximization (DM-DV-SROSEM) algorithm [92], with similarity threshold value set to 40%. Pixel-based ordered subsets were used for acceleration of reconstruction. For the DP-1 phantom (high-count ^{225}Ac and ^{226}Ac), a voxel size of 0.2 mm was used, due to the smallest rod diameter being 0.5 mm. A 3D Gaussian post-filter with FWHM values of 0.5 mm was applied. For DP-2 phantom (low-count ^{225}Ac), the voxel size was 0.4 mm, chosen because the smallest rod diameter is 0.9 mm. 3D Gaussian post-filters of 1.0 mm and 1.4 mm FWHM were used for the DP-2 phantom at activity concentrations 0.5 MBq/ml and 0.2 MBq/ml, respectively. For the DP-3 phantom (^{89}Zr), a voxel size of 0.4 mm was used in the reconstruction process. A 3D Gaussian filter with a FWHM of 0.5 mm was applied. The filter widths were selected to be approximately equal to the diameter of the smallest visible sector, except for ^{89}Zr, for which a value of 0.5 mm was chosen to enable comparison with the results reported in [30].

For improved visualization, the 20 central slices of the DP-1 phantom and 10 central slices of the DP-2 and the DP-3 phantom were summed, and the resulting images were resampled to a finer grid of 256×256 using MATLAB's "resize" function.

3.5.1. System matrices

Energy-dependent system matrices ($\boldsymbol{M}^{(1)}, \boldsymbol{M}^{(2)}$ of section 3.4) were generated using in-house developed ray-tracing software [55, 93]. This ray-tracer accounts for attenuation through the collimator and detector, but does not incorporate scatter. Instead, scatter projections ($\boldsymbol{s}^{(1)}, \boldsymbol{s}^{(2)}$ of section 3.4) were estimated from side energy windows using the triple-energy window (TEW) scatter correction method [94] and were then used as additive term only in forward projection. Attenuation and scatter within the small animal body were not modeled in the system matrix due to the relatively small size of mice.

In accordance with the dual-matrix (DM) method, cutoffs of 1% and 20% were applied to generate the forward and backprojection matrices, respectively, to accelerate the reconstruction process by using a smaller backprojection matrix. Here, 1% cutoff implies that gamma rays with less than a 1% chance of penetrating the collimator were excluded [55]. Furthermore, the forward matrix was divided into central and tail components. The PSF exhibits a rapidly varying central component and a slowly varying tail component on the detector plane. Since the tail component varies slowly, it was defined using coarser voxels; these were twice the size as those used for the central component. This dual voxel (DV) approach effectively reduces both storage requirements for the system matrix and computational load during reconstruction. Note that both the described matrix generation method as the reconstruction acceleration correspond to what is used in the experimental system.

For imaging single photopeaks from each radionuclide, system matrices at the respective energies with 128 subsets were used. For SB-JR, a system matrix at intensity weighted energy value (equation 3.2) was used where the total number of subsets was 128. The intensity weighted energy values are 374 keV, 207 keV, and 784 keV for ^{225}Ac, ^{226}Ac, and ^{89}Zr, respectively. In mMB-JR, a total of 128 subsets were used with matrix elements added (equation 3.4). For MB-JR, there are a total of 256 subsets, of which first 128 correspond to the lower gamma energy, while the remaining 128 correspond to the higher gamma energy (equation 3.5). A comparison of imaging performance due to different schemes of energy subsetting is presented in appendix 3.9.

Among the three radionuclides under investigation, ^{225}Ac exhibits gamma emissions at 218 keV (11%) and 440 keV (26%) that do not originate directly from the radionuclide itself; rather, these emissions are produced by its daughter nuclides, ^{221}Fr and ^{213}Bi, respectively. Nevertheless, the corresponding intensities of 11% and 26% are utilized for the $[\tau_i]$ calculation (section 3.4.1) without applying any correction. This is justified because of the shorter half-lives of ^{221}Fr (4.8 minutes) and ^{213}Bi (45.6 minutes) compared to ^{225}Ac (10 days), which allows the decay chain to reach transient equilibrium [145].

3.5.2. Positron range correction

For imaging 511 keV gammas resulting from positron decay of ^{89}Zr, the positron range was included in the system matrix. Consider $\boldsymbol{M}^{511} := [m_{ij}^{511}] \in \mathbb{R}^{V \times N}$ being the system

matrix for single gammas with an energy of 511 keV and $\boldsymbol{K}^{PR} := [h_j] \in \mathbb{R}^Q$ being the column matrix representation of the positron range kernel calculated as explained in section 3.3.3. Then, the corresponding system matrix, $\boldsymbol{M}^{511(\mathrm{PR})} := [m_{ij}^{511(\mathrm{PR})}] \in \mathbb{R}^{V \times N}$, including positron range can be written as:

$$m_{ij}^{\mathrm{PR}} = \sum_{r=1}^{Q} 2h_r \, m_{i\left(j+r-\frac{Q+1}{2}\right)} \tag{3.6}$$

Where the factor 2 is due the consideration that each positron emission results into approximately two annihilation photons.

3.6. Data analysis

A quantitative comparison of resolution phantom images generated from the different joint reconstruction methods and from individual photopeaks was conducted using CNR analysis. For the CNR analysis, circular regions-of-interests (ROIs) were drawn on the filtered and finer sampled images of the Derenzo phantom (section 3.5), with their placements aligned to the Derenzo rods and the spaces in between (figure 3.1). The diameters of these ROIs were set to 0.9 times those of the corresponding rod sectors. These ROIs were applied to 20 central layers (axial direction) of the DP-1 and 10 central layers (axial direction) of the DP-2 and DP-3 phantoms. If $\bar{h}$ is the average activity (over all axial layers) in ROIs corresponding to rods of diameter d and similarly $\bar{c}$ is the average activity for the in-between ROIs, then contrast for that rod sector is given by:

$$C_d = \frac{\bar{h} - \bar{c}}{\bar{c}} \tag{3.7}$$

Noise for that rod sector is then defined as:

$$N_d = \frac{\sqrt{\sigma_h^2 + \sigma_c^2}}{\bar{h} + \bar{c}} \tag{3.8}$$

where σ_h and σ_c are standard deviation for ROIs corresponding to Derenzo rods and in between ROIs respectively. CNR for a rod sector is defined as ratio between contrast and noise.

$$CNR_d = \frac{C_d}{N_d} \tag{3.9}$$

For statistical accuracy, CNR was calculated over three noise realisations.

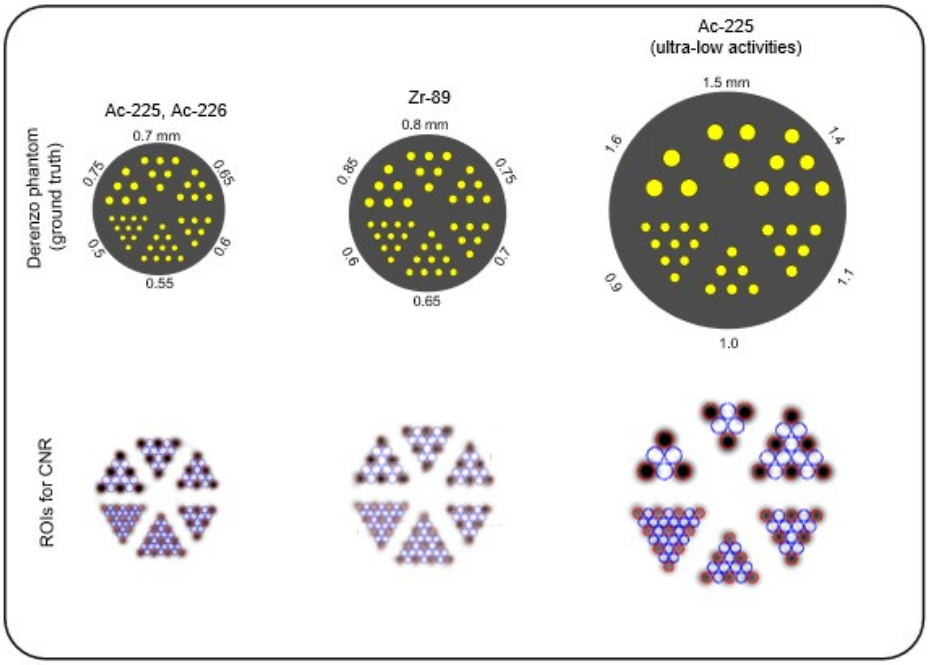

Figure 3.1: Ground truth representation of Derenzo resolution phantoms embedded within a PMMA cylinders (in gray) having diameters of 12 mm, 14 mm, and 20 mm (left to right), with rod diameters indicated in the top row. Respective ROI placements for CNR calculation are shown in the second row.

3.7. Results

3.7.1. Phantom simulation

The energy spectra for radionuclides ^{225}Ac and ^{226}Ac were generated using the first 5 minutes of the GATE simulations of the highest activity concentrations used in this work (20 MBq/ml for ^{225}Ac and 10 MBq/ml for ^{226}Ac). Similarly, the energy spectrum for ^{89}Zr was produced using the first minute of the simulated acquisition for the activity concentration of 200 MBq/ml. These spectra are presented in figure 3.2, where the photopeak and background energy windows are indicated in blue and yellow, respectively. The exact values of these energy windows are provided in table 3.3.

The photopeak energy windows were selected “by hand” to include nearby gamma emissions where feasible. For instance, the 230 keV and 254 keV gamma emissions of ^{226}Ac were combined within a single photopeak window, and the center of the peak was defined as the intensity-weighted mean energy of 231 keV, which was used for system matrix calculation. The widths of the background energy windows were maximized while

excluding nearby low intensity gamma emissions. This approach aimed to minimize noise propagation from side windows in the TEW scatter correction [146], which was particularly important when working with low and ultra-low activity levels.

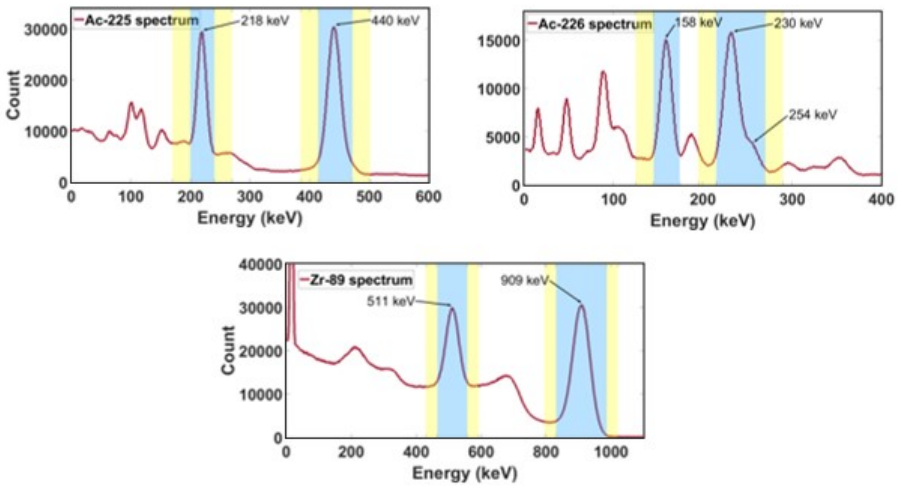

Figure 3.2: Energy spectra of the three radionuclides under study: ^{225}Ac, ^{226}Ac and ^{89}Zr, including the photopeak and background energy windows in blue and yellow, respectively.

Radionuclide	*Peak energy [keV]*	*Photopeak window [keV]*	*Background window-1 [keV]*	*Background window-2 [keV]*
^{225}Ac	218	200 – 240	170 – 200	240 – 270
	440	415 – 472	385 – 415	472 – 502
^{226}Ac	158	145 – 174	125 – 145	195 – 215
	230+254	215 – 270	195 – 215	270 – 290
^{89}Zr	511	465 – 557	430 – 465	557 – 592
	909	831 – 986	796 – 831	986 – 1021

Table 3.3: Photopeak and background windows used for three radionuclides under study.

3.7.2. Derenzo phantom studies

The 30th and 90th iterations of the ^{225}Ac resolution phantom images generated by using individual gamma emissions, by post-combining these after reconstruction, and by the proposed three joint reconstruction methods are presented in figure 3.3 for all studied activity concentrations.

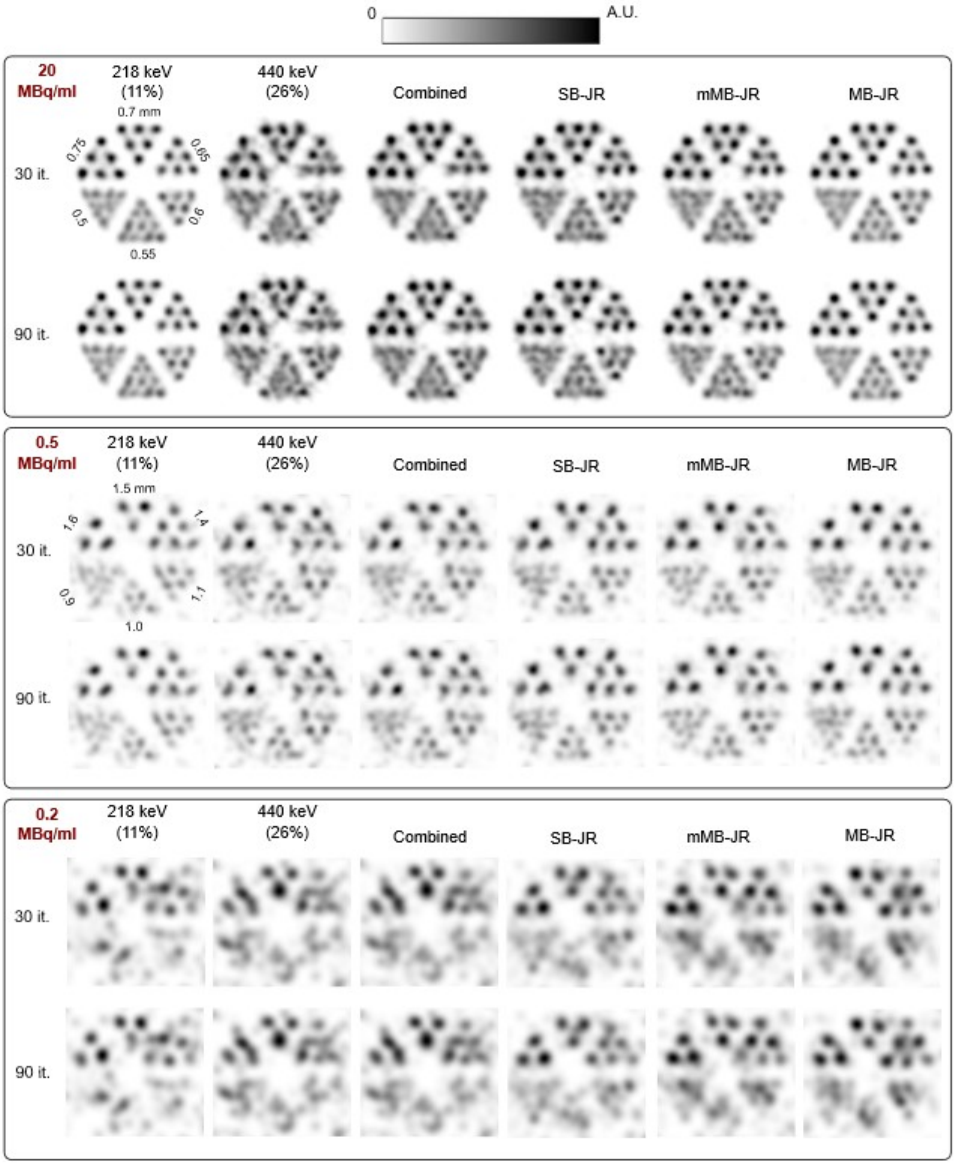

Figure 3.3: Derenzo resolution phantom images of ^{225}Ac after 30th and 90th iterations are shown for individual photopeaks (218 keV and 440 keV), two photopeak images combined after reconstruction, and three joint reconstruction schemes at three activity concentrations: 20 MBq/ml, 0.5 MBq/ml and 0.2 MBq/ml. Abbreviation: A.U., arbitrary unit.

Images obtained from the 440 keV photopeak exhibit lower quality compared to all other five methods. At an activity concentration of 20 MBq/ml, MB-JR produces slightly superior images compared to the 218 keV photopeak images, and markedly superior

images relative to the 440 keV photopeak images, the post-combined images and the images obtained by the two other joint reconstruction methods (mMB-JR and SB-JR). This improvement is evidenced by the enhanced peak-to-valley ratio observed in the line profiles (figure A.3) and is further confirmed by the CNR-based quantitative analysis presented in section 3.7.3. In contrast, no improvement was observed for mMB-JR and SB-JR relative to 218 keV images. At lower activity concentrations of 0.5 MBq/ml and 0.2 MBq/ml, images reconstructed using MB-JR are both visually and quantitatively superior to those from individual photopeaks and slightly outperform images from the other two joint reconstructions. For mMB-JR and SB-JR, minor improvements were observed in the smallest visible sectors, while slight degradations occurred in larger rod sectors compared to the 218 keV photopeak images (see CNR plot in figure 3.6 and percentage improvements in figure 3.9). Line profiles through rods from the last visible rod sector, 0.55 mm for 20 MBq/ml, 1.0 mm for 0.5 MBq/ml, and 1.4 mm for 0.2 MBq/ml, are shown in figure A.3.

Notably, the benefit of independently including the two projections and their system matrices as done in the MB-JR scheme results into improved imaging performance compared to images obtained using lower energy gammas, across all activity concentrations (see section 3.7.3). In contrast, other joint reconstruction methods (SB-JR, mMB-JR) involve adding projection data and using an average gamma energy for the system matrix to reduce computational load which resulted in both improvements and slight degradations (only in larger rod sectors) in comparison to images obtained from lower energy gamma emissions.

Furthermore, it is evident that the strategy of adding images generated from two gamma emissions after individual reconstructions does not yield optimal images for none of the activity concentrations studied, highlighting the importance of utilizing joint reconstruction methods.

Figure 3.4 presents ^{226}Ac images at activity concentrations of 10 MBq/ml, 2 MBq/ml, and 1 MBq/ml. Similar to observations for ^{225}Ac, the imaging performance achieved with the higher energy gamma emissions (230+254 keV) is inferior across all activity concentrations. For all activity concentrations examined, the joint reconstruction methods produced images of superior quality compared to those obtained from the lower energy gamma emission, with the exception of 0.75 mm rod sector in SB-JR for 1 MBq/ml case; as confirmed by line profiles (figure A.4), CNR analysis in section 3.7.3 and percentage improvements shown in figure 3.9. In the line profiles, rods from the outer edges of the respective last visible rod sector, 0.55 mm for 10 MBq/ml, 0.60 mm for 2 MBq/ml, 0.70 mm for 1 MBq/ml, were shown for all cases (figure A.3).

Similar to the ^{225}Ac case, the MB-JR method outperforms SB-JR and mMB-JR in almost all cases (see figure 3.7). However, for ^{226}Ac, the performance differences among the three joint reconstruction schemes are relatively small, as confirmed by the CNR analysis. One possible contributing factor to this may be the smaller separation between the gamma energies jointly reconstructed in this case (158 keV and 230+254 keV) compared to the more widely separated photopeaks of 218 keV and 440 keV in the ^{225}Ac case.

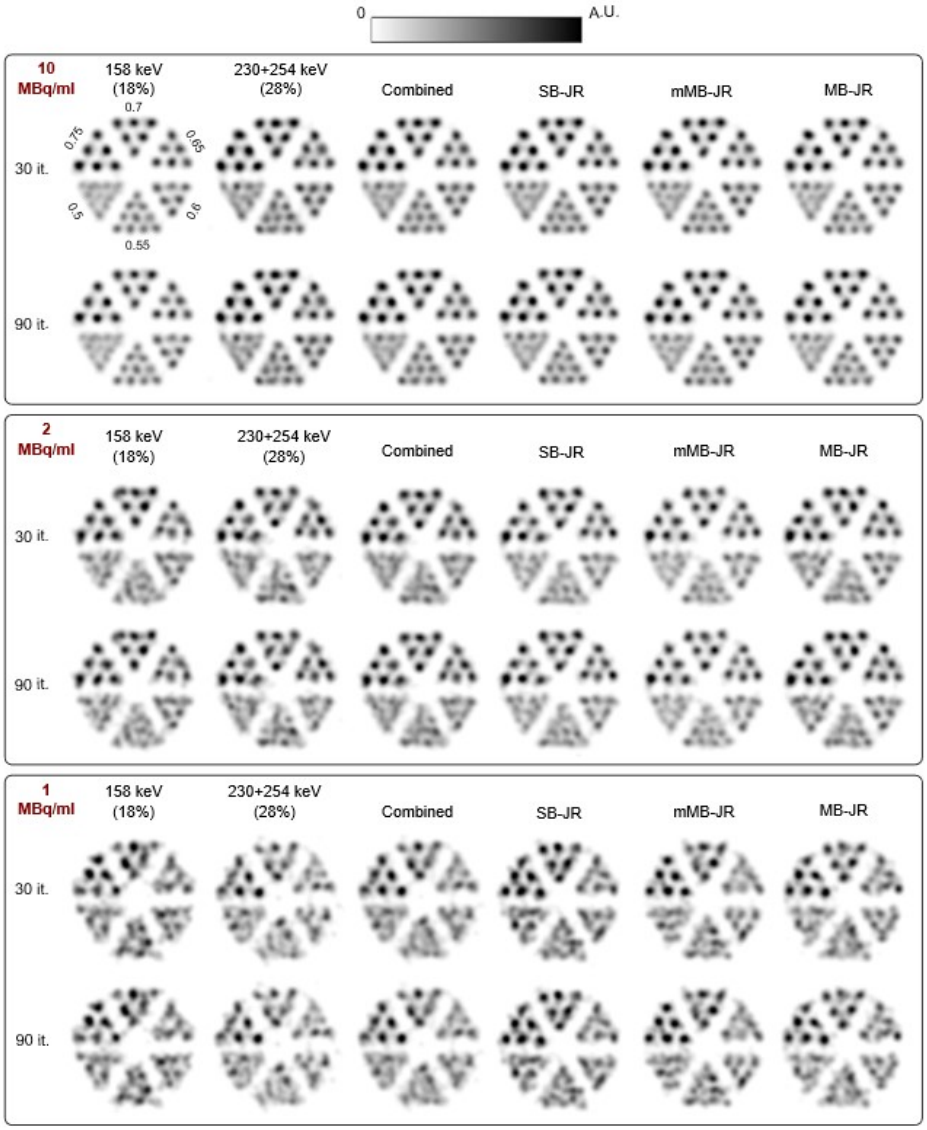

Figure 3.4: Derenzo resolution phantom images of ^{226}Ac after 30th and 90th iterations are shown for individual photopeaks (158 keV and 230 keV), two photopeak images combined after reconstructions, and three joint reconstruction schemes at three activity concentrations: 10 MBq/ml, 2 MBq/ml and 1 MBq/ml. Abbreviation: A.U., arbitrary unit.

Figure 3.5 shows the 50th and 100th iterations of resolution phantom images, reconstructed using individual photopeaks, combining images after reconstruction and for three schemes of joint reconstructions for ^{89}Zr at 200 MBq/ml, 100 MBq/ml and 50 MBq/ml activity concentrations.

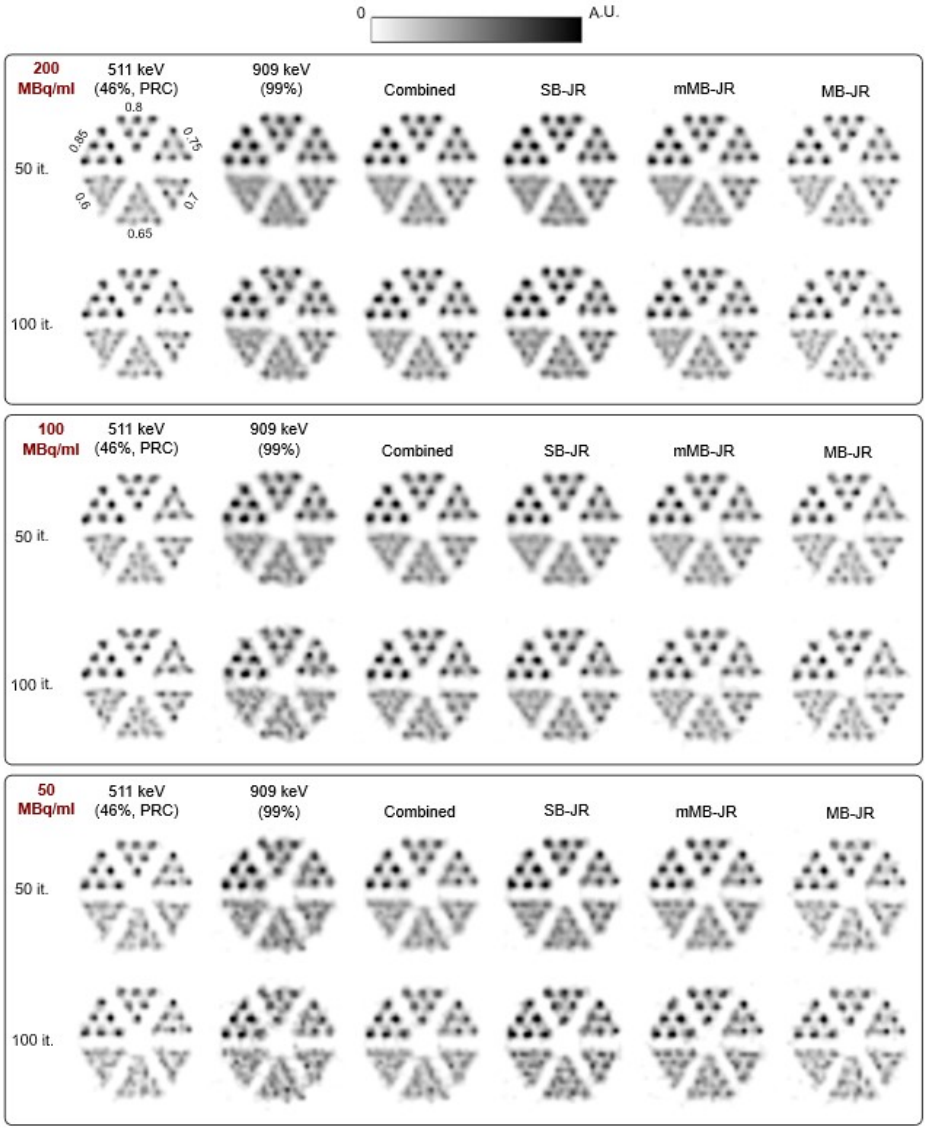

Figure 3.5: Derenzo resolution phantom images of ^{89}Zr after 50th and 100th iterations are shown for individual photopeaks (511 keV with PRC and 909 keV), two photopeak images combined after reconstructions, and three joint reconstruction schemes at three activity concentrations, 200 MBq/ml, 100 MBq/ml and 50 MBq/ml. Abbreviation: PRC, positron range correction; A.U., arbitrary unit.

As observed with other radionuclides, reconstructions based on the higher energy gamma emission (909 keV) exhibit inferior image quality compared to all other images. Across all activity concentrations, the smallest discernible rod sectors demonstrate noticeable

improvement when reconstructed using the proposed joint reconstruction methods, as also confirmed by CNR analysis in section 3.7.3 and line profiles (figure A.5). For larger rod sectors, the joint reconstruction methods yield image quality comparable to that obtained from the lower energy gamma (511 keV).

Unlike the results observed in the lower energy range (158 keV - 440 keV) for other two radionuclides where MB-JR consistently outperformed mMB-JR, in the higher energy range (511 keV – 909 keV) we see comparable or even improved performance with mMB-JR relative to MB-JR. Notably, at 100 MBq/ml, the smallest rod sector (0.65 mm) is clearly visible using mMB-JR, whereas its visibility is compromised in the MB-JR reconstruction. This observation is supported by the CNR plots shown in figure 3.8c and the line profile (figure A.5).

Finally, these results further confirm that post-combining images from two photopeak after reconstructions is not an effective approach, thereby additionally highlighting the advantages of joint reconstruction methods for the higher energy range.

Furthermore, to investigate the runtime differences between the 128-subset and 256-subset reconstructions (section 3.5.1), we performed ^{226}Ac reconstructions on a computing node with 12 CPU cores and 32 GB of memory of the same linux cluster used in this work (section 3.3.1). The jobs were executed with SINGLEJOB access policy to ensure exclusive node access and eliminate computational interference. The corresponding runtimes are presented in table 3.4.

Act. Conc. [MBq/ml]	*158 keV*	*230 keV*	*SB-JR*	*mMB-JR*	*MB-JR*
10	7134	7438	7379	7955	15612
2	6086	6533	6606	7266	13463
1	5880	6397	6263	6928	13126

Table 3.4: Runtimes (in seconds) for 30 iterations of reconstructions using 128 subsets (158 keV, 230 keV, SB-JR, and mMB-JR) and 256 subsets (MB-JR).

3.7.3. CNR analysis

In addition to visual assessment of images and inspection of line profiles, a quantitative CNR analysis was conducted for all radionuclides under investigation, utilizing three noise realizations (figures 3.6, 3.7, and 3.8). For each case, CNRs were calculated for the smallest discernible rod sectors (left column), and the mean CNRs of the remaining visible rod sectors were also provided (right column). It is noteworthy that the CNR improvements achieved by the MB-JR and mMB-JR schemes, relative to the respective lower-energy gamma emissions, are more pronounced for the smallest visible rod sectors than for the larger diameter rods, as reflected in the mean CNR values.

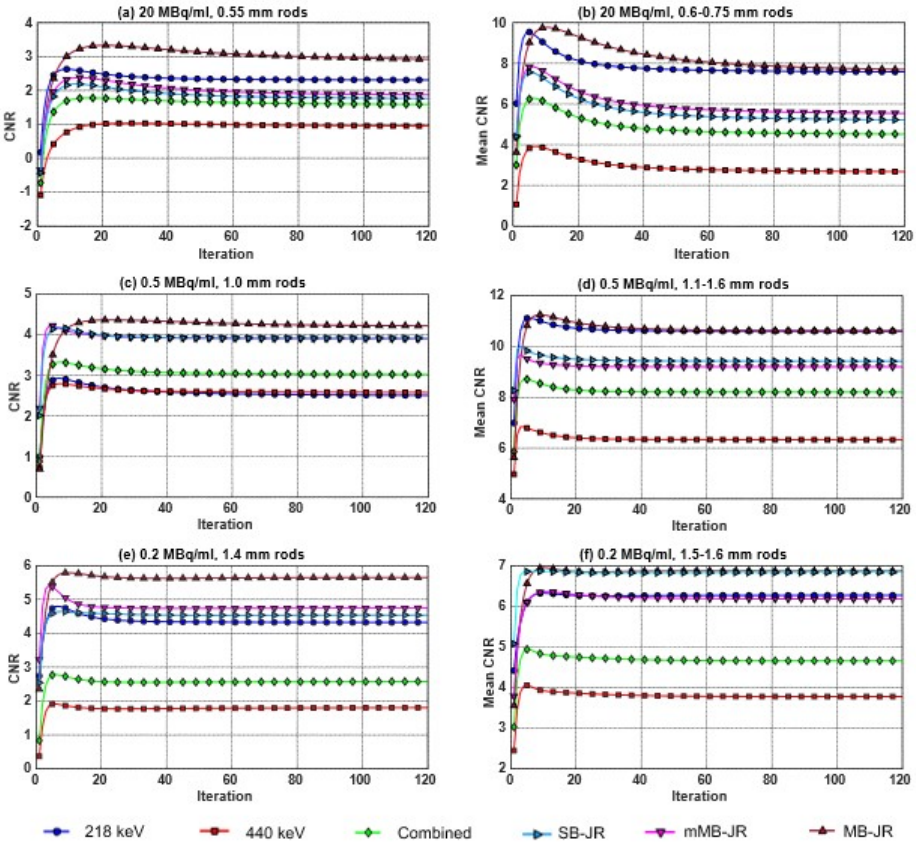

Figure 3.6: CNRs and mean CNRs of last visible sectors and rest of the visible sectors respectively (detailed in y-axis) are plotted against iteration number for all three different activity concentrations studied for ^{225}Ac. Abbreviation: SB-JR, Single-Band Joint Reconstruction; mMB-JR, mixed Multi-Band Joint Reconstruction; MB-JR, Multi-Band Joint Reconstruction.

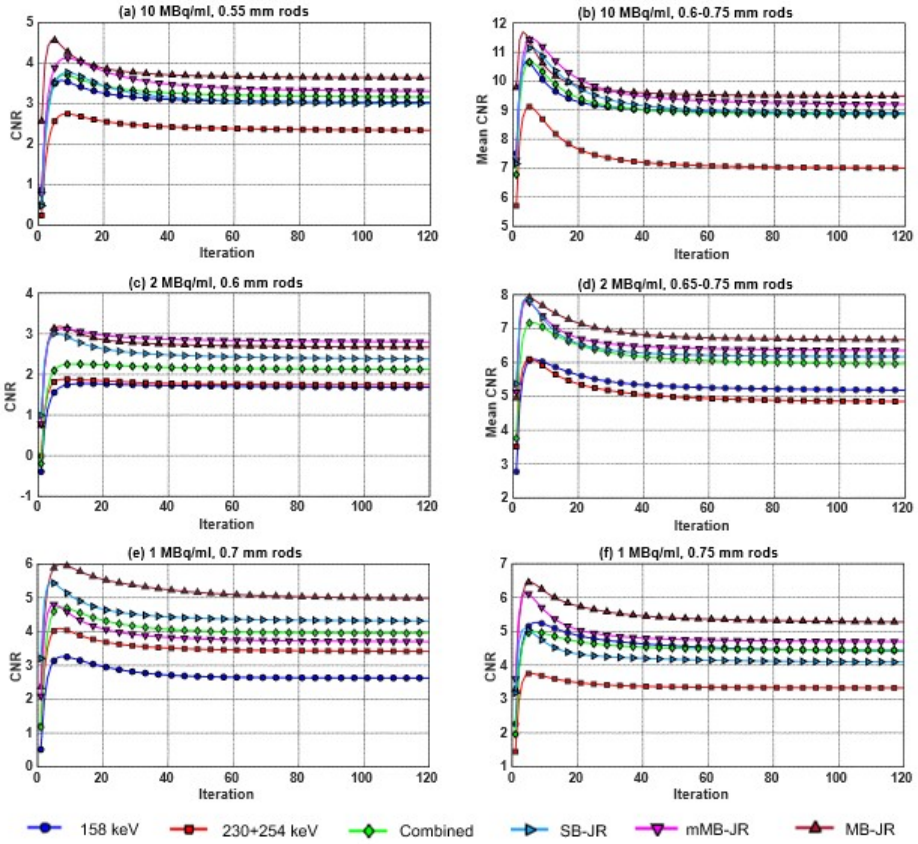

Figure 3.7: CNRs and mean CNRs of last visible sectors and rest of the visible sectors respectively (detailed in y-axis) are plotted against iteration number for all three different activity concentrations studied for ^{226}Ac. Abbreviation: SB-JR, Single-Band Joint Reconstruction; mMB-JR, mixed Multi-Band Joint Reconstruction; MB-JR, Multi-Band Joint Reconstruction.

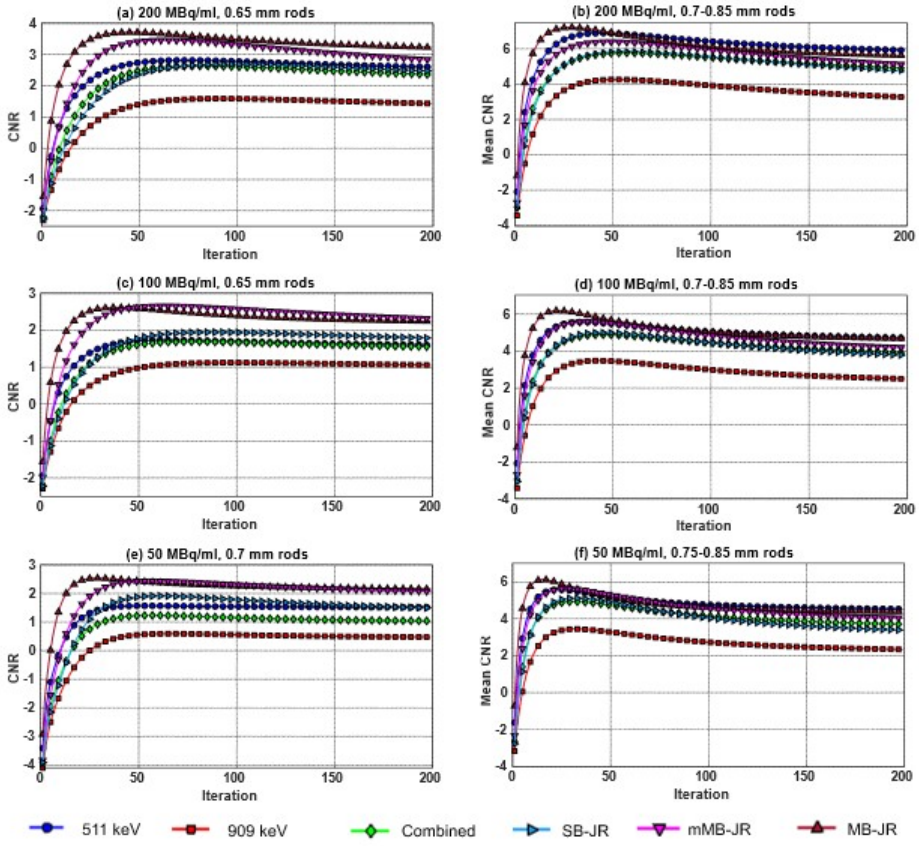

Figure 3.8: CNRs and mean CNRs of last visible sectors and rest of the visible sectors respectively (detailed in y-axis) are plotted against iteration number for all three different activity concentrations studied for ^{89}Zr. Abbreviation: SB-JR, Single-Band Joint Reconstruction; mMB-JR, mixed Multi-Band Joint Reconstruction; MB-JR, Multi-Band Joint Reconstruction.

Percentage improvement of CNR and mean CNR at the 60th (^{225}Ac, ^{226}Ac) and 100th (^{89}Zr) iterations for the three joint reconstruction schemes over the best performing image for the individual photopeaks are reported in figure 3.9 with detailed data in tables A.1, A.2 and A.3.

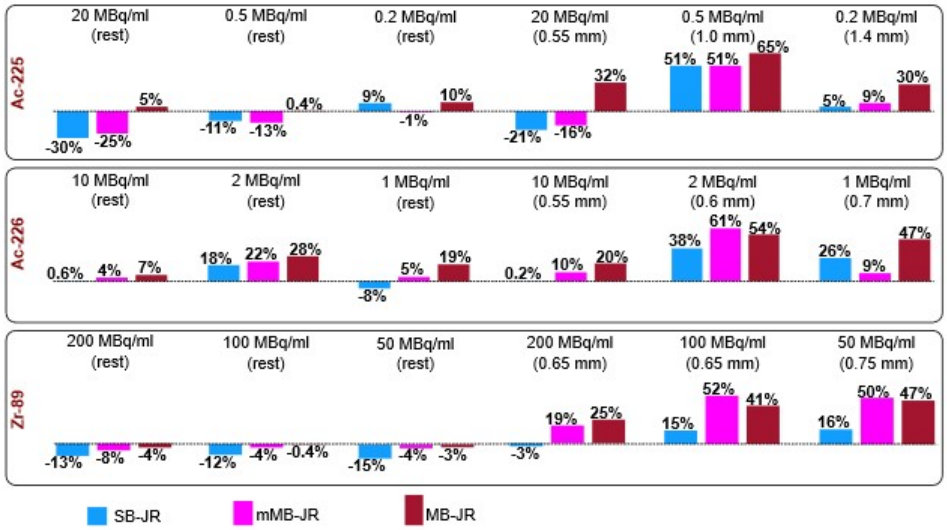

Figure 3.9: Percentage improvement (or degradation) of CNR of smallest visible sector and mean CNR (over rest of the visible sectors) at 60th (^{225}Ac, ^{226}Ac) and 100th (^{89}Zr) iterations due to three proposed joint reconstruction schemes over images from the best performing photopeak.

3.8. Discussion

Many SPECT and PET radionuclides have multiple detectable emissions with varying relative intensities and energies, sometimes affected by physical effects like positron range. Excluding certain emissions from the image-based diagnostics and therapies is not optimal especially in low-count scans. In this work, we proposed three types of joint reconstruction methods producing better image quality compared to using single photopeaks. In general, this improvement is more enhanced as activity concentration is lowered. This may be attributed to the fact that increasing the signal-to-noise ratio, as joint reconstruction incorporates information from both photopeaks, is most beneficial in low-count situations. Also, the enhancement from joint reconstruction schemes is more pronounced for the smallest diameter visible sectors over larger rod sectors. This evidence suggests that in mouse scans, proposed joint reconstruction methods may significantly enhance visibility and detectability of small and/or low-uptake lesions. Among the three joint reconstruction methods MB-JR outperforms the other two, mMB-JR and SB-JR, in almost all cases at the cost of higher computational load. In mMB-JR and SB-JR, we added the counts from different photopeaks, as done in earlier

studies [117–120], and, in contrast to previous works, we modeled the system matrix to include contributions from both gamma energies element-wise in mMB-JR and using an average energy matrix in SB-JR.

Proposed methods can become beneficial for image-based dosimetry for TAT or TBT radionuclides considering the limit on total allowed injected activity [121–126]. Many therapeutic radionuclides exhibit complex emission spectra (table 3.1), which can be imaged jointly using the proposed methods. As the focus on this work was on introducing the methodology rather than on optimizing imaging for a specific isotope, there are some limitations to our work. We did not consider the effects of alpha-recoil migration, meaning that the presented results for ^{225}Ac may overestimate the experimental outcome if this effect is not mitigated. The chemical detachment of alpha-emitting radionuclides from their carrier molecules because of alpha-recoil remains one of the major obstacles to the clinical application of TAT, as it can lead to unintended radiation dose to healthy tissues [147]. Recently, encapsulation of alpha-emitters within nanocarriers has emerged as a promising strategy to mitigate the recoil problem, as such systems can retain daughter nuclides and thereby reduce off-target toxicity while preserving therapeutic efficacy [148–150]. The choice of ^{225}Ac was specifically motivated by the opportunity to evaluate the proposed joint reconstruction approach using photopeaks at two widely separated energies (218 keV and 440 keV).

The lowest activity concentration of ^{225}Ac investigated in this study exceeds the currently available practical concentration range (estimated at 1–118 kBq/ml; see appendix). To evaluate the applicability of the proposed joint reconstruction methods under lower activity levels, additional studies were conducted at activity concentrations of 100 kBq/ml and 50 kBq/ml (figure A.1). At these lower activity concentrations, image quality deteriorated, though joint reconstruction methods still produced visually superior images. The primary cause of degradation was due to natural background, which becomes increasingly dominant at low activities, when excluded from simulations, all rod sectors became visible at both concentrations. This occurs because, with the clustered pinhole collimator employed in this study, photopeak counts from the Derenzo phantom become substantially smaller than the constant natural background contribution at these activity levels. Hence, we suggest that high sensitivity collimators and/or thicker detectors would be more suitable for achieving practical activity concentration levels with this isotope. This work focuses on developing a joint reconstruction method, and optimizing the scanner hardware for a specific isotope lies outside the scope of this study.

Besides, to apply the proposed multi-photopeak joint reconstruction methods in case of PET radionuclides with prompt emissions, we have modelled the positron range effect in the system matrix and applied joint reconstruction to ^{89}Zr imaging. In the future, we would like to test these methods for similar PET radionuclides, such as ^{124}I, ^{52}Mn. The relative intensities of annihilation photons and prompt gammas can vary substantially for different isotopes and benefits of joint reconstruction may be dependent on these relative intensities. Note that in the proposed MB-JR and mMB-JR joint reconstruction frameworks, these differences in emission yields were explicitly modeled through the factor τ_i (section 3.4.1), while in the SB-JR approach, yield variations are indirectly

accounted for by incorporating the constituent gamma energies and intensities to compute a weighted average energy (equation 3.3).

The use of more than two photopeaks in joint reconstruction represents a promising direction for future research, as the inclusion of additional photopeaks, depending on the isotope, may further enhance image quality. For each isotope, however, it is essential to evaluate which energy peaks are appropriate for incorporation into the joint reconstruction. In this study, we provide a general methodology and illustrate its applicability through several representative examples.

The ^{89}Zr spectrum exhibits a substantial down scatter contribution to the 511 keV photopeak due to 909 keV prompt gammas (figure 3.2). In this study, the TEW scatter correction method was employed. The TEW approach estimates the scatter component under the photopeak through linear interpolation between adjacent energy windows, which represents a simplification relative to the actual scatter distribution. Nonetheless, the TEW method was successfully applied for experimental ^{89}Zr imaging [45], achieving high quantitative accuracy.

Our study demonstrated that the proposed joint reconstruction methods, particularly the MB-JR approach, achieve improved imaging performance compared to reconstructions based on individual photopeaks in a multi-pinhole SPECT system. Although most clinical SPECT scanners employ parallel-hole collimators, we anticipate that similar benefits may be observed, especially in low-count scans, due to improved statistics. It is worth noting that the incorporation of both the 171 keV (91%) and 245 keV (94%) photopeaks of ^{111}In for imaging has been reported in certain clinical studies [117, 118]. However, in contrast to preclinical imaging, accurate attenuation correction for both photopeaks becomes essential in clinical applications.

Finally, we believe one of the major challenges in extracting larger improvements through joint reconstruction methods across diverse modalities [131–135] was that, based on the scanner system design, different emissions have varying levels of purity (retrievable information from individual emission, on average) and sensitivity. Indeed various subsystems of a scanner are designed synergistically to extract out the best imaging performance from a specific or narrow band of emissions. A more bottom-up design approach, which balances the levels of purity and sensitivity extracted from these different emissions, can enhance the performance of these software solutions. For example, in multi-pinhole SPECT, we suggest a hybrid collimator design incorporating pinholes with varying opening angles, including some smaller than those optimal for 511 keV, to improve the purity of 909 keV gamma detection through reduced edge penetration, may enhance joint reconstruction performance.

3.9. Conclusion

This study demonstrates that joint reconstruction methods leveraging multiple photopeak emissions can enhance image quality of preclinical systems for both SPECT

and PET radionuclides, especially in low-count scans. Among the proposed approaches, the MB-JR joint reconstruction scheme consistently yielded the best performance in almost all cases, albeit with increased computational demand. These methods may become promising for improved small and/or low-uptake lesion detectability in preclinical imaging but possibly also in clinical SPECT. Furthermore, the results indicate that their applicability can enable improved quantitative accuracy which e.g. is important for diagnostics and image-based dosimetry protocols for therapeutic radionuclides.

Acknowledgments

This work was supported by the research grant QUARAT: Quantitative Universal Radiotracer Tomography (TTW16885), which is partially funded by the Dutch Research Council (NWO).

Appendix

^{225}Ac imaging

The total activity of ^{225}Ac that can be administered to a typical mouse without inducing radiotoxic effects ranges from 20 to 40 kBq/mouse [121–125]. Recent advances using pre-targeted radioimmunotherapy (PRIT) methods have increased this limit to 296 kBq/mouse [126]. Based on these total injected activity values and typical tumor uptake of 5-40% (in %IA/ml) for this radionuclide [122–124, 126, 151], we tried to guess a rough estimate of realistic activity concentration range to be 1−118 kBq/ml in typical mouse scan.

It is noteworthy that the lowest activity concentration studied for this radionuclide in this work is 200 kBq/ml, just above the upper limit of estimated realistic activity concentration range. To further evaluate the applicability of the proposed joint reconstruction methods under realistic conditions, we conducted additional studies using a Derenzo resolution phantom (rod diameters 3.1–1.6 mm) filled with activity concentrations of 100 and 50 kBq/ml, both within the practical range. The corresponding reconstructed images, with and without natural background included in the projections, are provided in figure A.1.

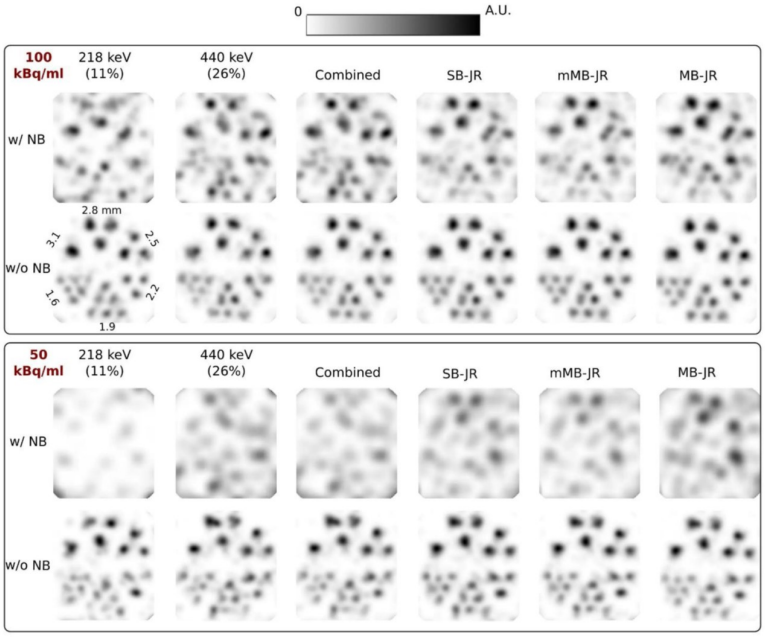

Figure A.1: Derenzo resolution phantom images of ^{225}Ac after 30th iterations are shown for individual photopeaks (218 keV and 440 keV), two photopeak images combined after reconstruction, and three joint reconstruction schemes at two activity concentrations, 100 and 50 kBq/ml. Post-filters FWHM 2.1/1.5 mm for w/ and w/o NB at 100 kBq/ml, 2.2/1.7 mm at 50 kBq/ml. Abbreviation: A.U., arbitrary unit; NB, natural background.

In the absence of NB, resolution of the reconstructed phantoms improved markedly. This observation is consistent with expectations, as for the cluster pinhole collimator employed in this study, the contribution of photopeak counts from the Derenzo phantom becomes relatively minor compared to NB at low activity concentrations. Specifically, at 100 kBq/ml, NB counts in the 218 keV and 440 keV photopeak windows were approximately 3.8 and 4.0 times higher than the phantom counts, respectively, while at 50 kBq/ml these ratios increased to 7.7 and 8.1.

Energy subsetting

We investigated the impact of different energy subsetting strategies within the MB-JR framework for all radionuclides and their respective activity levels (figure A.2). In the first approach (MB-JR in figure A.2), a total of 256 subsets were used, with the first 128 subsets corresponding to the lower energy gamma emissions and the remaining 128 subsets to the higher energy gamma emissions. In the alternative approach (MB-JR-mES), a total of 128 subsets were employed, each containing an equal mix from both the lower and higher energy gamma emissions. Visual inspection revealed that the reconstructed images produced by MB-JR and MB-JR-mES were largely similar across all radionuclides. Consequently, a CNR analysis, similar to section 3.7.3, was performed using three noise realizations. In nearly all cases, MB-JR demonstrated marginally superior performance compared to MB-JR-mES.

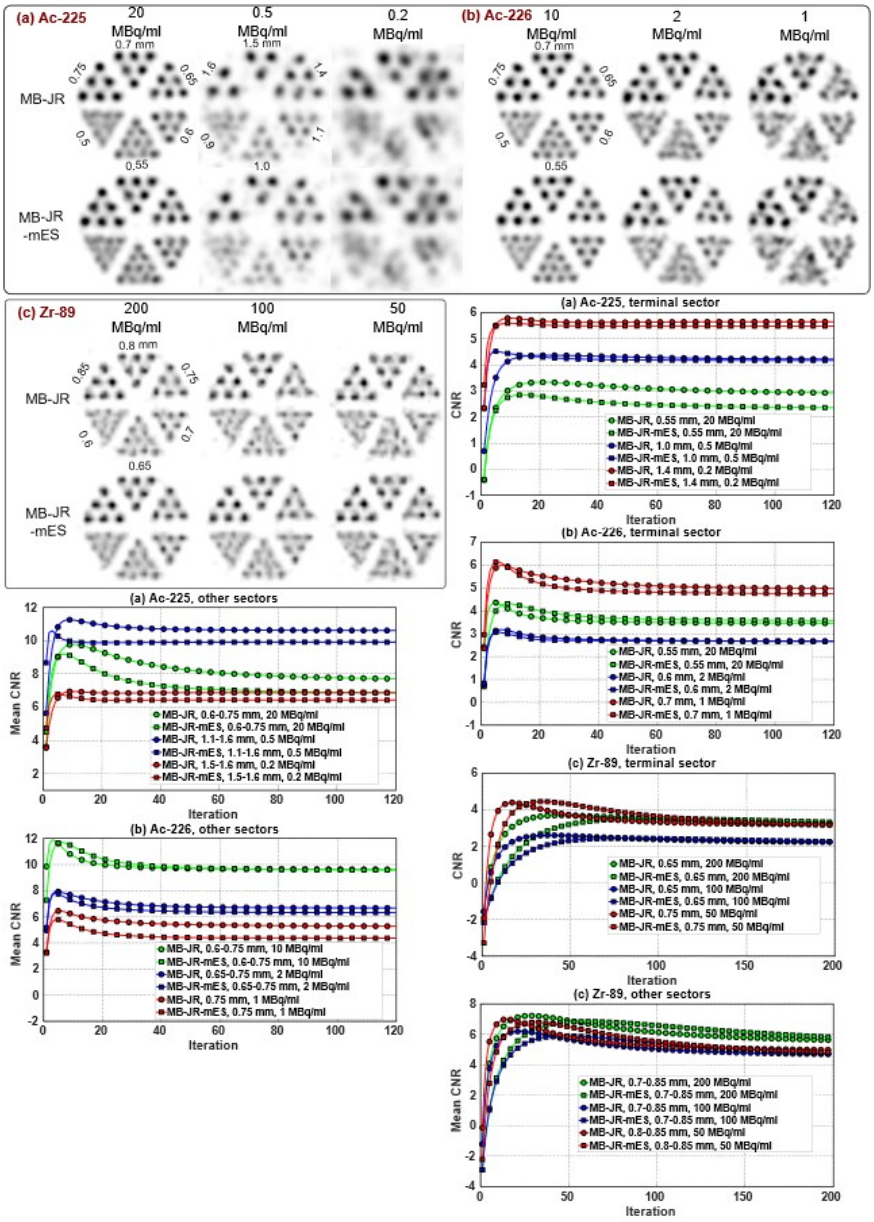

Figure A.2: The 30th iteration resolution phantom images are shown for MB-JR and MB-JR-mES reconstruction for radionuclides: (a) ^{225}Ac, (b) ^{226}Ac, and similarly 100th iteration images for (c) ^{89}Zr; along with similar CNR analysis as in section 3.7.3.

Line profiles

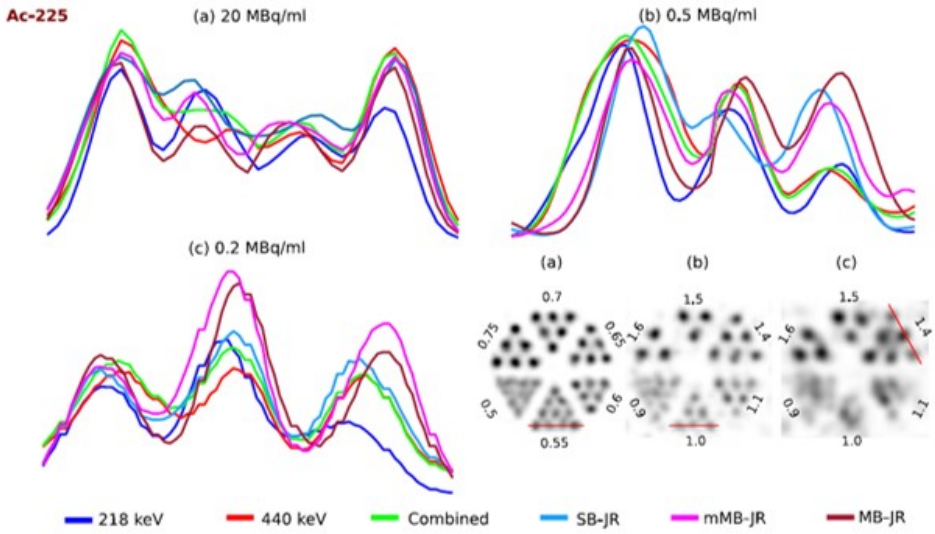

Figure A.3: Line profiles for 30th iteration of ^{225}Ac resolution images at activity concentrations of (a) 20 MBq/ml, (b) 0.5 MBq/ml, and (c) 0.2 MBq/ml are shown for rods at the outer edges of the respective smallest discernible rod sectors. MB-JR images are displayed alongside, with the corresponding line placement for each profile.

Activity Conc., size	*218 keV*	*440 keV*	*Comb.*	*SB-JR*	*mMB-JR*	*MB-JR*	*Impr. SB-JR*	*Impr. mMB-JR*	*Impr. MB-JR*
20 MBq/ml, 0.55 mm	2.33	0.99	1.64	1.83	1.96	3.08	-21%	-16%	+32%
0.5 MBq/ml, 1.0 mm	2.55	2.60	3.05	3.91	3.91	4.28	+51%	+51%	+65%
0.2 MBq/ml, 1.4 mm	4.33	1.79	2.56	4.53	4.74	5.63	+5%	+9%	+30%
20 MBq/ml, rest	7.66	2.77	4.64	5.38	5.71	8.06	-30%	-25%	+5%
0.5 MBq/ml, rest	10.61	6.33	8.21	9.43	9.20	10.65	-11%	-13%	+0.4%
0.2 MBq/ml, rest	6.27	3.78	4.66	6.83	6.19	6.87	+9%	-1%	+10%

Table A.1: CNR and mean CNR of the last visible sectors and remaining (rest) sectors respectively at the 60th iteration for ^{225}Ac, with percentage improvement (Impr.) of joint reconstruction schemes over the best performing individual photopeak images.

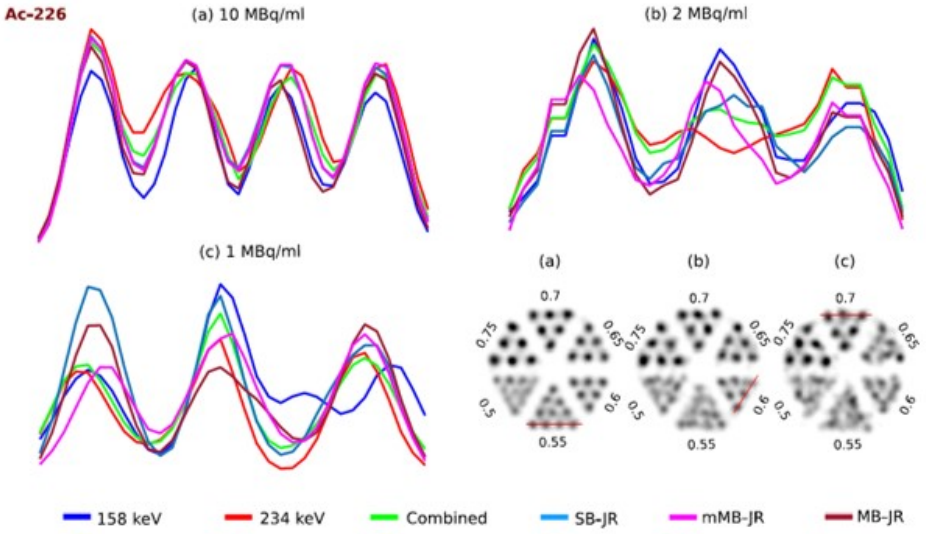

Figure A.4: Line profiles for 30th iterations of ^{226}Ac resolution images at activity concentrations of (a) 10 MBq/ml, (b) 2 MBq/ml, and (c) 1 MBq/ml are shown for rods at the outer edges of the respective smallest discernible rod sectors. The MB-JR images are displayed alongside, with the corresponding line placement for each profile.

Activity Conc., size	*158 keV*	*230 keV*	*Comb.*	*SB-JR*	*mMB-JR*	*MB-JR*	*Impr. SB-JR*	*Impr. mMB-JR*	*Impr. MB-JR*
10 MBq/ml, 0.55 mm	3.06	2.38	3.21	3.07	3.37	3.67	+0.2%	+10%	+20%
2 MBq/ml, 0.6 mm	1.71	1.76	2.15	2.43	2.84	2.71	+38%	+61%	+54%
1 MBq/ml, 0.7 mm	2.65	3.46	3.99	4.37	3.75	5.09	+26%	+9%	+47%
10 MBq/ml, rest	8.95	7.08	8.92	9.00	9.32	9.53	+0.6%	+4%	+7%
2 MBq/ml, rest	5.26	4.93	6.05	6.21	6.41	6.73	+18%	+22%	+28%
1 MBq/ml, rest	4.52	3.35	4.48	4.15	4.74	5.36	-8%	+5%	+19%

Table A.2: CNR and mean CNR of the last visible sectors and remaining (rest) sectors respectively at the 60th iteration for ^{226}Ac, with percentage improvement (Impr.) of joint reconstruction schemes over the best performing individual photopeak images.

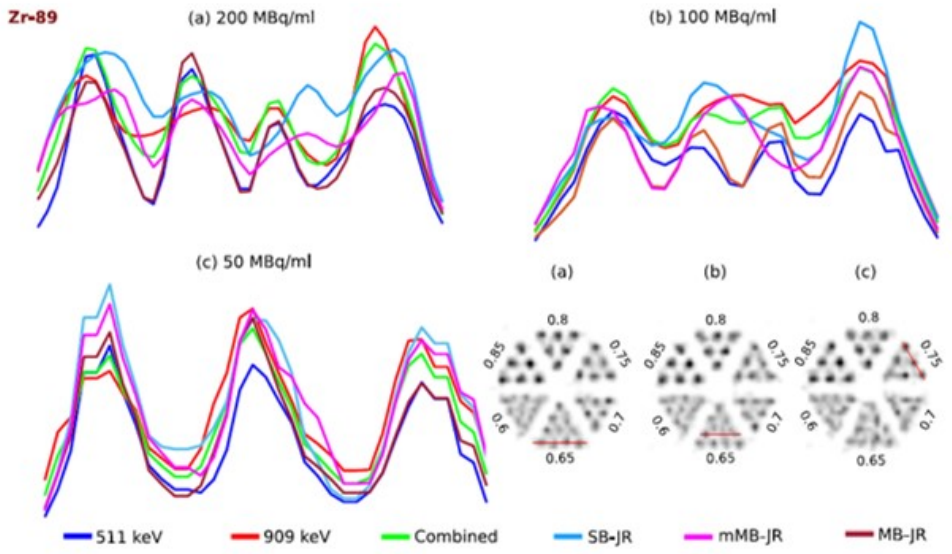

Figure A.5: Line profiles for 100th iteration of ^{89}Zr resolution images at activity concentrations of (a) 200 MBq/ml, (b) 100 MBq/ml, and (c) 50 MBq/ml are shown for rods at the outer edges of the respective smallest discernible rod sectors. The MB-JR images are displayed alongside, with the corresponding line placement for each profile.

Activity Conc., size	*511 keV*	*909 keV*	*Comb.*	*SB-JR*	*mMB-JR*	*MB-JR*	*Impr. SB-JR*	*Impr. mMB-JR*	*Impr. MB-JR*
200 MBq/ml, 0.65 mm	2.78	1.58	2.61	2.69	3.31	3.49	-3%	+19%	+25%
100 MBq/ml, 0.65 mm	1.69	1.12	1.67	1.94	2.58	2.39	+14%	+52%	+41%
50 MBq/ml, 0.7 mm	1.54	0.56	1.15	1.78	2.31	2.26	+16%	+50%	+47%
200 MBq/ml, rest	6.42	3.92	5.51	5.57	5.93	6.13	-13%	-8%	-4%
100 MBq/ml, rest	5.05	2.99	4.45	4.45	4.84	5.03	-12%	-4%	-0.4%
50 MBq/ml, rest	4.76	2.73	4.05	4.05	4.56	4.61	-15%	-4%	-3%

Table A.3: CNR and mean CNR of the last visible sectors and remaining (rest) sectors respectively at the 100th iteration for ^{89}Zr, with percentage improvement (Impr.) of joint reconstruction schemes over the best performing individual photopeak images.

4

NaI gamma camera performance for high energies: effects of crystal thickness, photomultiplier tube geometry and light guide thickness

This chapter is adapted from:
Valerio Cosmi, Beien Wang, Marlies C. Goorden, Freek J. Beekman, NaI gamma camera performance for high energies: effects of crystal thickness, photomultiplier tube geometry and light guide thickness. *Medical Physics*, 2024;51:4696–4708.

Gamma camera imaging, including Single Photon Emission Computed Tomography (SPECT), is crucial for research, diagnostics, and radionuclide therapy. Gamma cameras are predominantly based on arrays of Photon Multipliers Tubes (PMTs) that read out NaI(Tl) scintillation crystals. In this way, standard gamma cameras can localize gamma rays with energies typically ranging from 30 keV to 350 keV. In the last decade there has been an increasing interest towards gamma imaging outside this conventional clinical energy range, e.g. for theranostic applications and preclinical multi-isotope PET and PET/SPECT. However, standard gamma cameras are typically equipped with 9.5 mm thick NaI(Tl) crystals which can result in limited sensitivity for these higher energies.
Here we investigate to what extent thicker scintillators can improve the photopeak sensitivity for higher energy isotopes while attempting to maintain spatial resolution.
Using Monte Carlo simulations, we analyzed multiple PMT-based configurations of gamma detectors with monolithic NaI(Tl) crystals of 20 mm and 40 mm thickness. Optimized light guide thickness together with 2-inch round, 3-inch round, 60x60 mm^2 square and 76x76 mm^2 square PMTs were tested. For each set-up, we assessed photopeak sensitivity, energy resolution, spatial and depth-of-interaction (DOI) resolution for conventional (140 keV) and high (511 keV) energy gammas using a Maximum-Likelihood algorithm. These metrics were compared to those of a "standard" 9.5 mm thick crystal detector with 3-inch round PMTs.
Estimated photopeak sensitivities for 511 keV were 27% and 53% for 20 mm and 40 mm thick scintillators, which is respectively 2.2 and 4.4 times higher than for 9.5 mm thickness. In most cases, energy resolution benefits from using square PMTs instead of round ones, regardless of their size. Lateral and DOI spatial resolution are best for smaller PMTs (2-inch round and 60x60 mm^2 square) which outperform the more cost-effective larger PMT setups (3-inch round and 76x76 mm^2 square), while PMT layout and shape have negligible (<10%) effect on resolution. Best spatial resolution was obtained with 60x60 mm^2 PMTs; for 140 keV, lateral resolution was 3.5 mm irrespective of scintillator thickness, improving to 2.8 mm and 2.9 mm for 511 keV with 20 mm and 40 mm thick crystals respectively. Using the 3-inch round PMTs, lateral resolutions of 4.5 mm and 3.9 mm for 140 keV and of 3.5 mm and 3.7 mm for 511 keV were obtained with 20 mm and 40 mm thick crystals respectively, indicating a moderate performance degradation compared to the 3.5 mm and 2.9 mm resolution obtained by the standard detector for 140 and 511 keV. Additionally, DOI resolution for 511 keV was 7.0 mm and 5.6 mm with 20 mm and 40 mm crystals using 60x60 mm^2 square PMTs, while with 3-inch round PMTs 12.1 mm and 5.9 mm were obtained.
Depending on PMT size and shape the use of thicker scintillator crystals can substantially improve detector sensitivity at high gamma energies, while spatial resolution is slightly improved or mildly degraded compared to standard crystals.

4.1. Introduction

Planar gamma cameras and Single Photon Emission Computed Tomography (SPECT) are key for research, diagnostics and radionuclide therapy [33, 152]. Although solid state gamma cameras are gaining popularity, today's planar and SPECT imaging systems are

still predominantly based on gamma detectors employing continuous NaI scintillation crystals coupled to an array of Photomultiplier Tubes (PMTs). These components, together with a collimator, define the basic structure of the so-called Anger camera, a nuclear-imaging instrument first developed in 1953 [153]. More than seven decades later, this reliable camera technology is still very widely used as it grants an excellent balance between image quality and cost-effectiveness [154].

Clinical gamma cameras typically operate within a gamma energy range of 30−350 keV [155]. These cameras usually employ ~9.5 mm thick NaI scintillation crystals which provide an excellent sensitivity, e.g. ~90% photopeak efficiency for ^{99m}Tc that emits 140 keV photons. Additionally, these detectors are characterized by a good energy resolution for the most often used isotopes (~10% for ^{99m}Tc [28, 29]) and a moderate intrinsic spatial resolution of ~3.5 mm. The intrinsic resolution of a detector, together with the collimator's geometrical resolution, are among the main factors defining the whole system spatial resolution. In clinical SPECT, image resolution is usually 7-10 mm for general purpose systems and is mainly limited by the collimator. In preclinical SPECT instead, reconstructed image resolutions much better than the 3.5 mm intrinsic detector resolution are required. To achieve such high 3D image resolution, modern preclinical SPECT scanners often are equipped with multi-pinhole collimators. This gives the opportunity to exploit pinhole magnification, allowing these systems to attain a spatial resolution of 0.25 mm in vivo in mice [28], which further improves to 0.12 mm [29] for ex vivo mouse organ imaging.

Interest in imaging isotopes with energies outside the conventional SPECT range is increasing as it can be valuable in multiple fields [43, 156]. For instance, high energy gamma imaging is important for cancer therapy with e.g. the combined gamma - beta emitter ^{131}I (364 keV gammas from its decay) [157]. Interesting implementations also reside in cardiac imaging, where it was already demonstrated decades ago that injured but viable myocardium's regions can be evaluated with a SPECT camera using ^{99m}Tc-MIBI/^{18}FDG (requiring combined 140 keV-511 keV gamma imaging), improving patient convenience and cost-effectiveness [158]. New promising opportunities for high energy radionuclide therapy with alpha-particle emitters that also emit gammas, such as ^{225}Ac and ^{213}Bi, are being investigated as well. Here imaging of high-energy (440 keV from ^{213}Bi decay) gammas is required for adequate biodistribution and dosimetry studies [47]. Additionally, in a recent preclinical study [45] it was shown that it is possible to image PET radioisotopes, such as ^{124}I and ^{89}Zr, without positron range blurring via their large amounts of high-energy prompt gamma (603 and 909 keV gammas respectively) emissions. This approach invalidates strong image blurring effects due to positron range while also enabling simultaneous imaging of multiple PET isotopes.

For the high energy isotopes mentioned above, the sensitivity of 9.5 mm thick NaI crystals is limited (e.g. ~12% of 511 keV gammas end up in the photopeak [48]). Therefore, it is highly important to improve detector sensitivity for high-energy gammas, particularly when spatial resolution can be preserved. Considering the significance of cost-effectiveness for SPECT, it is desirable that such an improvement in sensitivity would be achieved in a cost-effective and straightforward way. In that regard, a possible solution

consists in increasing the scintillator's thickness. Research and development of gamma detectors already explored designs with thicker scintillation crystals than standard 9.5 mm in the late 90s (ADAC Forte, 16 mm thick crystal gamma detector). Today, numerous systems with thicker crystals are available on the market with applications in both the clinical (Siemens Pro.SPECT, 9.5 mm or 15.9 mm thick crystal; Mediso Anyscan Trio SPECT/CT, 9.5 mm or 15.9 mm thick crystal) and preclinical (MILabs VECTor, 9.5 mm or 19 mm thick crystal) field of nuclear medicine.

The use of thicker crystals in these systems helped increasing the sensitivity for high energy isotopes, but the possibility of further improving this result remains compelling. Therefore, it would be interesting to study even thicker crystals and evaluate their performance. However, further increasing the scintillator's thickness can negatively impact spatial resolution. This is due to the increased light spread within the crystal and the large variation in the depth-of-interaction (DOI) of the gamma radiation [159]. Such DOI is not estimated in conventional gamma detectors which only provide a 2D interaction position. This may lead to parallax errors for scanner geometries where the gammas enters the detector under an angle, e.g. for diverging, converging or pinhole collimators. Different techniques have been studied to alleviate the DOI limitations affecting pinhole SPECT including software-based modeling and corrections, the use of curved fiber bundles to collimate light from a curved scintillator, and the application of a laser processed scintillator with converging pixels [160–163]. Another possible solution to mitigate this issue and preserve spatial resolution consists in estimating the 3D interaction position. This estimation would be useful for crystals thicker than what is currently available on the market, but it could also be beneficial for already existing gamma cameras.

An example high-energy preclinical SPECT system that could benefit from above-mentioned detector developments is VECTor (Versatile Emission Computed Tomography, MILabs B.V. [40]) that was partly developed in our group and that was used for several of the preclinical imaging studies with high-energy gamma emitters described earlier (e.g. [45, 47]). VECTor uses high energy clustered multi-pinhole collimation [48, 49] suitable for gamma rays over a wide energy range (30-1000 keV). This system allows for sub-mm simultaneous PET/SPECT, sub-mm imaging of high-energy theranostic isotopes and positron-range free and multi-isotope PET. VECTor is characterized by large-area PMT-based gamma detectors in a triangular set-up, meaning that the aforementioned DOI estimation is particularly relevant as gammas can enter the detector under a large angle.

The goal of this work is to explore how much increasing the thickness of a scintillator would improve the photopeak sensitivity of a detector, while at the same time quantifying its effect on the detector's intrinsic spatial resolution. For this purpose, we conducted a Monte Carlo simulation study of multiple setups applying different NaI(Tl) scintillator thicknesses, several light guide thicknesses and various PMT configurations. A Maximum Likelihood (ML) algorithm was used to estimate the 3D interaction position. This methodology was applied to gammas of 140 keV and 511 keV, as these are the energies of frequently used SPECT radiotracers and of PET annihilation photons.

4.2. Materials and Methods

4.2.1. Detector description

In the present extensive simulation study, we designed gamma detectors based upon the geometry of the ones used in VECTor systems. We compared detectors equipped with large-area 590×470 mm monolithic NaI(Tl) scintillation crystals, with thicknesses of 9.5 mm, 20 mm and 40 mm. The 9.5 mm thick crystal was selected as a benchmark since it is widely used in conventional detectors. The 20 mm was chosen as it is comparable to the crystal thickness (19 mm) used by few systems available on the market. Finally, the 40 mm thick crystal was selected since it can greatly improve sensitivity for high energy gammas compared to standard crystals.

In our simulation model built using GATE v9.0 [83], scintillators were assumed to be placed inside an aluminum frame. Their sides and entrance surface were coated with Teflon tape (Lambertian reflector) to maximize light collection. The surface of such tape was assumed to be optically polished, with surface roughness set to 0.1 as indicated by GATE documentation. Furthermore, the finishes ("*groundbackpainted*") of such tape were selected to reflect the presence of airgaps between the tape and the structure coated with it. A box-shaped light guide made of glass was placed in front of the scintillator to optimize light collection. Its height and length were adapted to the different configurations of PMTs used. We tested light guide thicknesses of 2 mm, 6 mm, and 10 mm to analyze how this parameter would affect detector's performance. Such light guide values were selected as the results of a preliminary study with a larger range indicated that the chosen interval would be sufficient to convey the system performance trend. Like the scintillator crystal, the sides of the light guide were wrapped in a polished Teflon tape and protected by an aluminum frame. The interface between the scintillator and the light guide was treated as a specular surface which was modelled to consists of small micro-facets. The orientation of these micro-facets is characterized by the parameter σ_α, standardly set to 1.2°, which defines the standard deviation of the Gaussian distribution of the orientations of the micro-facets around the average surface normal. Moreover, this interface was assumed to be without any optical couplant. Such decision was based on the results of a preliminary study where the impact of the optical gel on the detector's performance was assessed. This was done by placing a thin (~0.4 mm) layer of Silicone Epoxy with refractive index (R_{index}) 1.5 between the scintillator and light guide, reproducing the characteristics of an actual detector system available in our lab which will be discussed later. Results with and without this optical couplant have shown a difference within the interval defined by the simulation uncertainty. This was thanks to the matching R_{index} of the couplant and the glass light guide which prevented additional refractions as photons traverse these two media. Therefore, while desirable in practical use, optical gel was left out of the simulation model as it would significantly increase computational load without providing relevant benefits.

For the readout, we analyzed four different configurations of PMTs with different geometries and layout. The PMTs were assumed to be equipped with bialkali photocatodes and are based on existing models produced by Hamamatsu Photonics. The

choice of the PMTs' sizes and placement was deeply influenced by the need of using large-area crystals and by the desire to build a cost-effective system. When selecting PMTs we tried to avoid an excessive deterioration of the spatial resolution compared to what is achieved with a 9.5 mm thick scintillator. In that regard, it is worth remarking that decreasing the sizes of the PMTs while increasing their total number generally grants better performance in terms of spatial resolution, because it allows to sample the light distribution at higher spatial frequency, improving the detector's response to small variations in the interaction position of the incident radiation [164–166]. However, this improvement in spatial resolution comes at an overall dramatically increased cost due to the higher number of light sensors and corresponding electronic channels required to cover the same detector area. For these reasons, we decided to use PMTs of similar or slightly smaller size compared to the light sensors commonly used in clinical gamma cameras. This allowed us to study detectors with costs comparable to the ones currently available on the market, as this is often required for practical use.

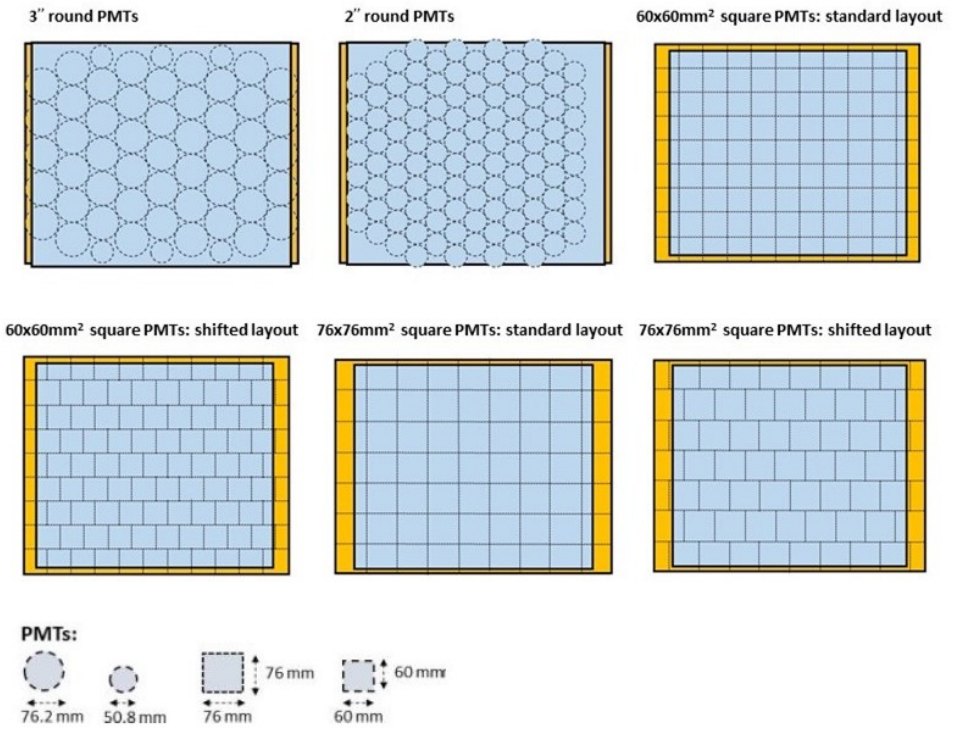

Figure 4.1: Schematic representation of the different PMT configurations studied. The yellow rectangle represents the light guide while the light blue indicates the scintillator. In each figure the outlines of the PMTs are shown to highlight the layout used.

The PMTs' placement was defined to guarantee coverage of the detector's central area, while their positioning at the edges was not optimized as in this study we decided to not

focus on edge effects. The four PMTs configurations tested are illustrated in Fig. 4.1 and they consist of: 49 3-inch (76.2 mm) diameter round PMTs combined with 6 2-inch (50.8 mm) diameter round PMTs, which represents the standard configuration currently used for VECTor's detectors; 108 2-inch (50.8 mm) diameter round PMTs, 99 60×60 mm^2 (~2-inch) square PMTs and 63 76×76 mm^2 (~3-inch) square PMTs. For square PMTs we tested two different layouts to evaluate their impact on the spatial resolution. In the first one, called "standard", the centres of PMTs belonging to different rows are aligned. In the second one, called "shifted", the centres of PMTs belonging to different rows are shifted by half the size of the PMT. For round PMTs, the light guide surface between the light sensors was assumed to be coated with an absorptive black painting according to the characteristics of the detector module used for validation that will be discussed later. Such coating was replicated in the simulation by counting only photons that ended within the surface covered by the PMTs when reaching the interface between the light guide and the PMTs.

In a cost analysis of the configurations presented, it is important to remark that the price of PMTs is approximately independent of their size. Since the variation of the number of light sensors is the main element differentiating the configurations tested, it was used as an indicator of the cost variation between the different setups.

4.2.2. Simulation setup and data acquisition process

Monte Carlo (MC) simulations were executed using GATE v9.0 [83–85] which is based on Geant4 version 10.05. To describe gammas and optical photon behavior we included the following GATE electromagnetic and optical physics processes: photoelectric effect, Compton scattering, Rayleigh scattering, electron ionization, Bremsstrahlung, scintillation, bulk absorption, and optical processes at boundaries (e.g. total internal reflection, refraction or reflection) depending on the surface properties. Photon interactions with all the scintillator crystal surfaces were modelled using the GATE UNIFIED model [143]. In this model the user must set four probabilities to control the reflectance due to the following kind of reflections: Specular lobe, Specular spike, Backscatter spike, and Lambertian. These probabilities were kept with the original values provided by the simulation model guide.

In our work we simulated the detector response to a perfectly collimated line source of 70 mm or 86 mm length depending on whether the smaller PMTs (2-inch round and 60×60 mm^2 square) or the larger PMTs (3-inch round and 76×76 mm^2 square) configurations were under analysis. This line source was set to emit, based on the scintillator's thickness, 30000 or 40000 perpendicular monoenergetic gamma radiation of 140 keV and 511 keV. These values were selected to grant at least 20000 events within the photopeak window in each configuration tested. The line source was positioned, along both x and y axis, above the centre of a PMT and near the PMT's edge by applying a 30 mm shift. These positions were chosen based upon the NEMA suggested procedure [167] to evaluate a gamma camera intrinsic spatial resolution and we denote them by "PMT centre" and "PMT edge" respectively. The former location represents a low-spatial-resolution region, while in the

latter position high spatial resolution can be achieved [168]. Data from these line source simulations were used to estimate the 3D interaction positions of emitted gammas via ML and to evaluate the detector's performance. We expect that the performance for sources placed above the PMT's centre and the PMT's edge will describe the behavior over the entire detector's central area thanks to the geometrical symmetry of the PMT placement.

4.2.3. Validation of simulation model

Prior to testing the thick scintillator designs we present, the simulation model was validated by comparing its results with experimental data previously collected [108]. Accordingly, we reproduced the same detector geometry consisting of a 9.5 mm thick crystal, a 16 mm thick light guide and the 3-inch round PMT configuration described earlier. Such a setup was exclusively used for validation purposes. The data acquisition followed the same procedure as reported in the previous section.

For validation purposes, the detector performance was evaluated by using the same offline processing that was also applied to the experimental data [108], consisting of a centroid estimation algorithm based on thresholding. The gammas interaction positions were reconstructed via Anger Logic estimation and the Line Response Functions (LRFs) were fitted with a Gaussian function. The Full Width at Half Maximum (FWHM) and Full Width at Tenth Maximum (FWTM) extracted from this fit were used to estimate the spatial resolution. This procedure was replicated for multiple sources within the 25-511 keV energy range.

4.2.4. Maximum likelihood estimation and system matrix

While for validation purposes Anger logic was used, we intend to apply an ML algorithm to estimate the 3D interaction positions in the thicker scintillators. The ML algorithm takes advantage of the assumption that for gammas with specified position of interaction and energy, the number of optical photons detected (n_m) by each PMT (m = 0, 1, ..., M) is Poisson distributed [168]. By calculating the mean value of such signal for every possible gamma interaction location ($\bar{n}_m(x,y,z)$), we can define the log-likelihood that an interaction observed at the coordinate (x, y, z) results in output $n = \{n_1, n_2, \ldots, n_M\}$ with the following equation, where constant terms were left out:

$$L(n \mid x,y,z) = \sum_{m=0}^{M} \{\ln\left(\left[\bar{n}_m(x,y,z)\right]^{n_m}\right) - \bar{n}_m(x,y,z)\} \tag{4.1}$$

The gamma interaction position $(\hat{x},\hat{y},\hat{z})$ that most likely generated n is obtained by maximizing Equation 4.1. No accelerated search algorithm for the maximum was implemented as we utilized only a small portion of the detector's area.

To calculate $(\bar{n}_m(x,y,z))$ we built a system matrix for each combination of PMT

configuration and light guide thickness tested. This gave us the required information to relate the gamma position of interaction to mean PMT signal. To generate these system matrices, a calibration measurement was simulated by placing the source at different positions in a grid configuration. The sizes of the grid were adjusted depending on the PMT setup under analysis: for the 2-inch round and 60×60 mm^2 square PMT configurations a 11×11 grid was used, whereas for the 3-inch round and 76x76 mm^2 square PMT configurations the grid was 13×13. In both grids each node is 8 mm away from the adjacent ones. To produce almost noiseless system matrices, the total number of emissions simulated was such that a total of 121000 (11×11 matrix) or 169000 (13×13 matrix) gammas were counted within the photopeak window, 1000 gammas for each position. From each scintillation event generated by these gammas we extracted its signal distribution, consisting of M PMT outputs where M refers to the total number of PMTs used. To improve the system matrix accuracy, we post-processed the simulated signals. We started by rejecting events resulting from large-angle Compton scatter using a preliminary Anger Logic position estimation. To this end, the 2D distribution of the coordinates estimated via Anger Logic was fitted with a 2D Gaussian and the FWHM along x and y axis was extracted. These FWHMs were then used to discard all events outside $0.9 \cdot \text{FWHM}$ along both axes. The described filtering process was applied to all grid positions, rejecting ~38% and ~32% of events respectively when working with 20 mm and 40 mm thick scintillators. Additionally, we identified and discarded PMTs that carried non-useful information. To do that, we calculated the mean PMT signals across all events generated from a specific grid position and compared it to a threshold value. This threshold was set to 1% of the sum of all PMT mean signals for the same grid position. As a result of the filtering process, we obtained for each event M'-dimensional data, with $M' < M$, containing information about the number of useful PMTs and the signal they detected.

In this simulation study, we decided to assess DOI in a realistic way as its ground truth value would not be known in an experimental calibration. To achieve that, we used the events' signal distribution and extracted the DOI information by applying a Factor Analysis (FA) statistical method to the filtered M'-dimensional data. Via the FA, we exploited the correlation between the DOI of an event and the width of its light distribution. In the FA algorithm, we decided to set the dimensionality of the latent space responsible for the variability among the correlated M'-dimensional simulation data to one. The obtained one-dimensional latent variable approximately indicates the DOI of each scintillation event analyzed. We then divided the scintillator in sections of 2 mm thickness and used the DOI estimated via FA to sort events in ascending DOI order. Each event was then placed accordingly into the corresponding section. Thanks to this process, we were able to model the mean detector response for scintillation events that happened at different depths within the scintillator crystal. This response was calculated for the events generated by placing the source in all the defined grid positions.

The obtained mean values were used to build a preliminary $11\times11\times S$ system matrix with voxel size of $8\times8\times2$ mm^3, where S refers to the number of sections in which the scintillator was divided. We further improved our matrix by interpolating the detector's response at intermediate steps using a smooth bivariate spline approximation, achieving a final $121\times121\times S$ system matrix with voxel size of $1\times1\times2$ mm^3.

4.2.5. Data analysis

Data acquired from system matrix and line source simulations were used in a MATLAB script to evaluate the detector's performance. To calculate energy resolution (E_{res}), we used the system matrix data as they are generated by irradiating the central part of the detector. This allowed to evaluate the detector's mean response in that area which was then used to calculate the distribution of the sum of PMTs' outputs. The E_{res} was defined as the FWHM of this distribution as indicated by NEMA [167].

To estimate the detector's lateral resolution, we first determined the 3D coordinates for each detected event. These coordinates were calculated by feeding energy filtered data into the ML algorithm to partially reject scatter events as it would be done in an experimental environment. The energy filtering consisted in applying an acceptance energy window of 20% and 15% respectively around the detected photopeak of 140 keV and 511 keV. From the algorithm's output we generated the XY planar distribution of the estimated positions of interactions and we projected these on either the x or y axis. Both projections were fitted with a two-term univariate Gaussian to extract their parameters, as a simple univariate Gaussian wasn't capable to accurately fit them. The resulting FWHMs were used to calculate the lateral resolution, defined as the Root Mean Square (RMS) average of the x and y projections' FWHM.

To determine the DOI resolution, first we compared the estimated DOI values to the ground truth values extracted from the simulation model. From these graphs, we extracted profiles at a simulated depth of 10 mm and fitted them with a three-term univariate Gaussian. The FWHMs extracted from these fits were then used to determine the DOI resolution. This resolution was only estimated for 511 keV data as for 140 keV gammas interactions happen mostly at the top of the crystal and DOI information is not useful.

For both DOI and lateral resolution, uncertainty associated to the estimated values was calculated using the Root Mean Square Error (RMSE).

To calculate the photopeak sensitivity, the same energy acceptance windows defined for filtering the input ML data were used. The photopeak sensitivity was then calculated as the ratio of the gammas that fell within these windows and the total number of emitted gammas.

4.3. Results

The validation study confirmed the accuracy of the simulation model as we compared the measured and simulated FWHM, FWTM and E_{res} at 25 keV, 140 keV and 511 keV gamma energy. Results for the 9.5 mm scintillator (scinti.) and 16 mm light guide (lg) are shown in Fig. 4.2 and Table 4.1.

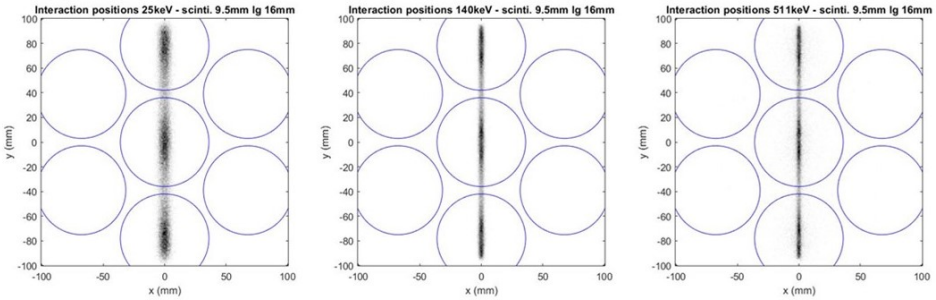

Figure 4.2: Line source images used for validation purposes. These images were acquired using a 9.5 mm thick scintillator (scinti.) and 16 mm thick light guide (lg) read out by the 3-inch round PMTs setup [108]. Equivalent images (not shown) were obtained with a horizontal line source.

Source	*Exp. FWHM [mm]*	*Exp. FWTM [mm]*	*Sim. FWHM [mm]*	*Sim. FWTM [mm]*	*Exp. E_{res} [%]*	*Sim. E_{res} [%]*
^{125}I	7.1	13.4	7.0	13.1	22.7	22.5
^{99}Tc	3.6	7.0	3.5	6.3	10.0	9.8
^{22}Na	3.0	–	2.9	–	9.7	8.8

Table 4.1: Experimental and simulated results for FWHM, FWTM, and energy resolution.

For the FWTM, experimental data for 511 keV is not available due to the strong background present in the images produced, therefore a comparison was not possible.

Fig. 4.3 illustrates the detector performance for the 511 keV line source for a few configurations. In these examples, we show results for the 40 mm scintillator equipped with 6 mm light guide readout for all tested PMT setups.

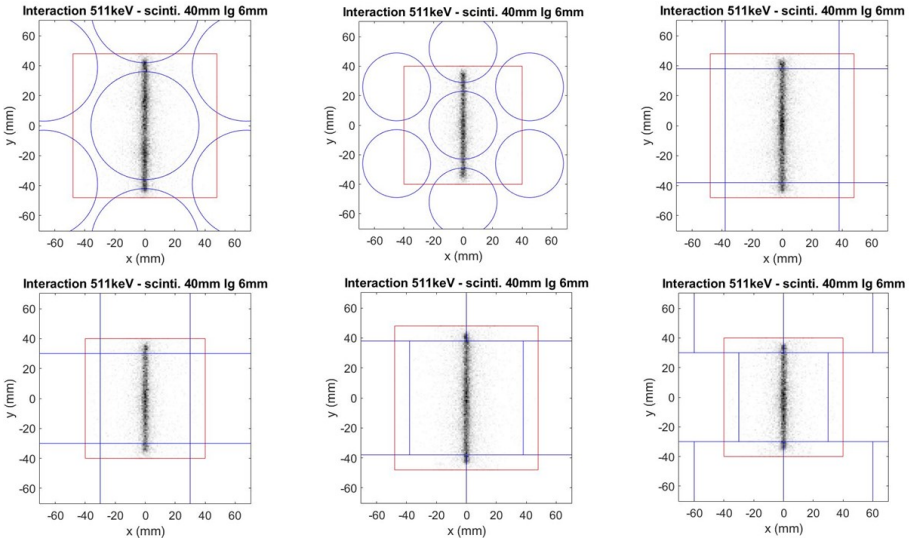

Figure 4.3: Line source images for a selected number of detector geometries. These images were acquired using a 40 mm thick scintillator (scinti.) and 6 mm thick light guide (lg) for all considered PMTs setup. These images were produced by placing the source at (0,0) mm, at the centre of the PMT's photocathode area.

Fig. 4.4 shows estimated DOI vs. true DOI for the same setups as in Fig. 4.3.

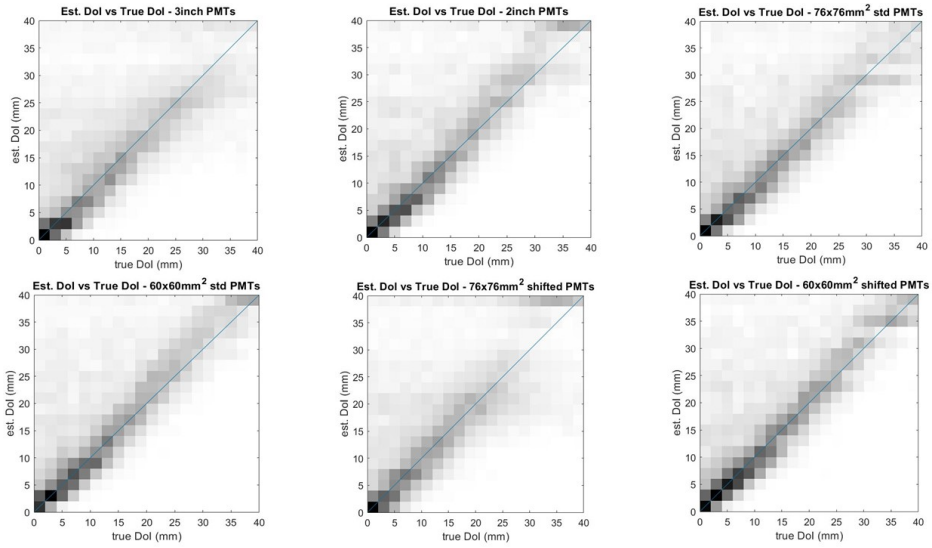

Figure 4.4: Comparison of estimated (Est.) vs. true DOI for multiple detector geometries consisting of a 40 mm thick scintillator with 6 mm thick light guide for all considered PMTs setups.

Figs. 4.5 and 4.6 provide an overview of E_{res}, lateral resolution as well as DOI resolution for all configurations with 20 mm thick crystals for 140 keV and 511 keV gammas respectively.

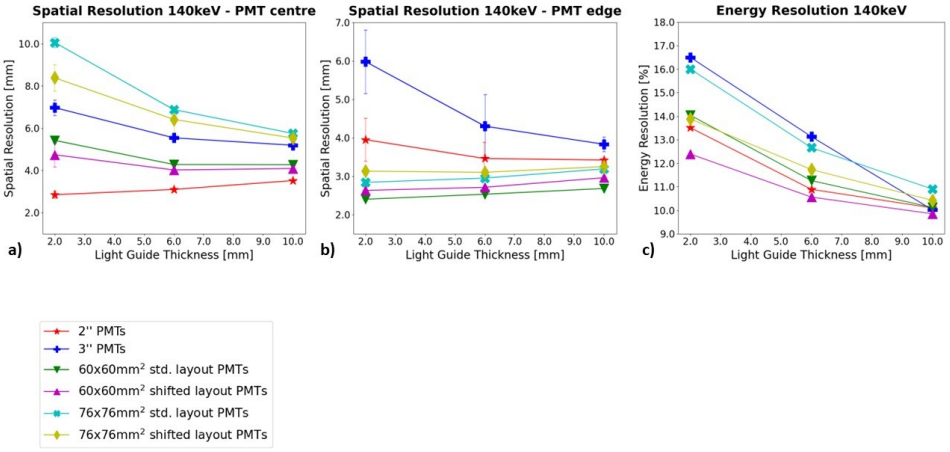

Figure 4.5: Comparison of spatial and energy resolution for all configurations with 20 mm thick crystal irradiated by 140 keV gammas; PMT centre (a) and PMT edge (b) results are presented in a separate set of graphs. To limit overlap the placement of error bars in the graphs was slightly shifted.

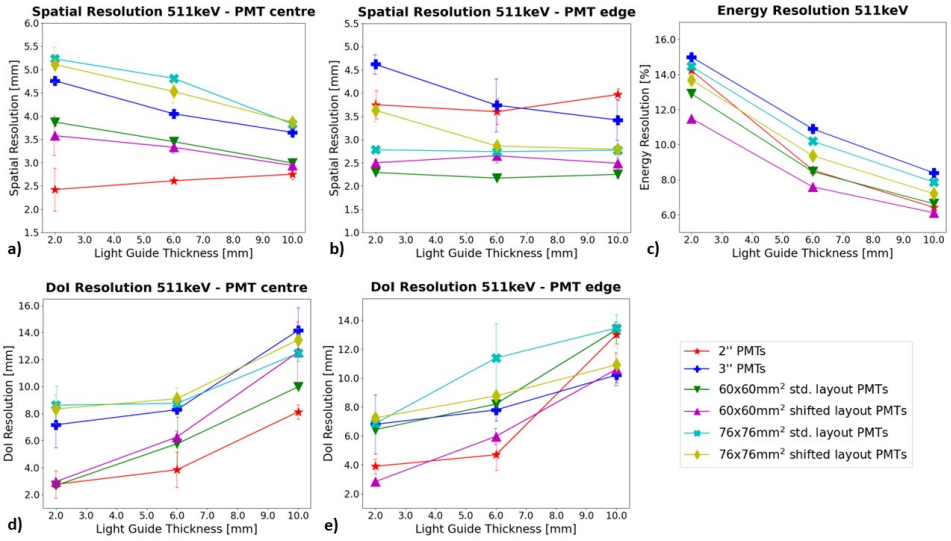

Figure 4.6: Comparison of spatial, DOI and energy resolution for all configurations with 20 mm thick crystal irradiated by 511 keV gammas; PMT centre (a, d) and PMT edge (b, e) results are presented in a separate set of graphs. To limit overlap the placement of error bars in the graphs was slightly shifted.

In Figs. 4.7 and 4.8, the same performance metrics shown for the 20 mm thick scintillator in Figs. 4.5 and 4.6 are presented for the 40 mm thick crystal when it is irradiated by 140 keV and 511 keV gammas respectively.

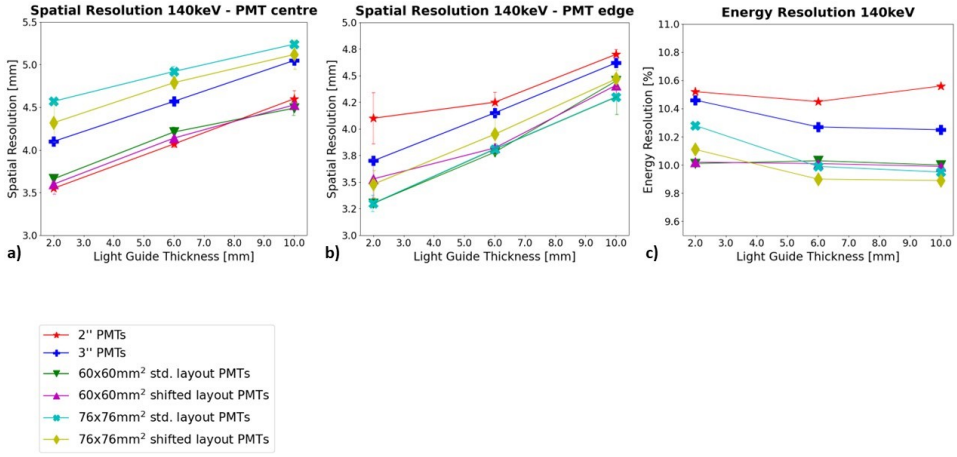

Figure 4.7: Comparison of spatial and energy resolution for all configurations with 40 mm thick crystal irradiated by 140 keV energy gammas; PMT centre (a) and PMT edge (b) results are presented in a separate set of graphs. To limit overlap the placement of error bars in the graphs was slightly shifted.

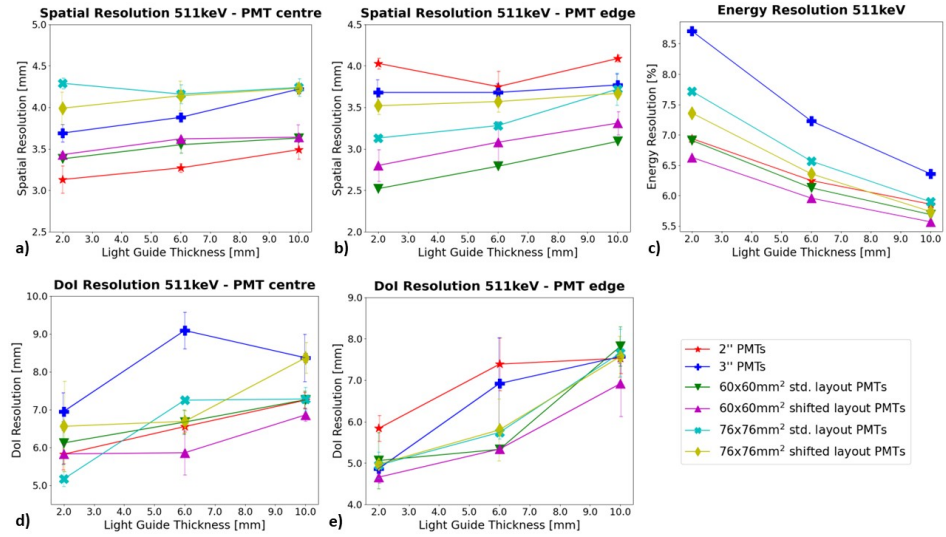

Figure 4.8: Comparison of spatial, DOI and energy resolution for all configurations with 40 mm thick crystal irradiated by 511 keV gammas; PMT centre (a, d) and PMT edge (b, e) results are presented in a separate set of graphs. To limit overlap the placement of error bars in the graphs was slightly shifted.

In Tables 4.2 and 4.3, we compare the performance of systems with 20 mm and 40 mm thick crystals to that of a standard detector with a 9.5 mm thick crystal. These results were calculated by averaging the performance both at the centre and at the edge of the PMT. The reported simulated results for 140 keV and 511 keV gammas were obtained using the 3-inch round PMTs combined with the light guide which granted the best performance.

Scintillator's thickness [mm]	*E_{res} @ 140 keV*	*Lateral resolution @ 140 keV [mm]*	*Photopeak sensitivity*
9.5	9.8%	3.5 ± 0.1	~88%
20	10.0%	4.5 ± 0.1	~97%
40	10.2%	3.9 ± 0.1	~97%

Table 4.2: Energy resolution, lateral resolution and photopeak sensitivity for 9.5 mm, 20 mm and 40 mm thick crystal detector for 140 keV gammas obtained with 3-inch round PMTs.

Scintillator's thickness [mm]	*E_{res} @ 511 keV*	*Lateral resolution @ 511 keV [mm]*	*DOI resolution @ 511 keV [mm]*	*Photopeak sensitivity*
9.5	8.8%	2.9 ± 0.2	N.A.	~12%
20	8.2%	3.5 ± 0.2	12.1 ± 0.9	~27%
40	6.4%	3.7 ± 0.1	5.9 ± 0.2	~53%

Table 4.3: Energy resolution, lateral and DOI resolution and photopeak sensitivity for 9.5 mm, 20 mm and 40 mm thick crystal detector for 511 keV gammas obtained with 3-inch round PMTs.

A further improvement of lateral and DOI resolution results compared to what can be obtained with 3-inch round PMTs is possible when using one of the smaller PMTs configurations tested, as can be seen in Figs. 4.5, 4.6, 4.7 and 4.8. In Table 4.4 the best results obtained with 60×60 mm^2 square PMTs are provided, calculated as the mean between PMT centre and PMT edge performance:

Scintillator's thickness [mm]	*Lateral resolution @ 140 keV [mm]*	*Lateral resolution @ 511 keV [mm]*	*DOI resolution @ 10 mm depth [mm]*
20	3.5 ± 0.3	2.8 ± 0.1	7.0 ± 1.0
40	3.5 ± 0.1	2.9 ± 0.1	5.6 ± 0.4

Table 4.4: Best lateral and DOI resolution for 20 mm and 40 mm thick crystal detector obtained with 60×60 mm^2 square PMTs.

4.4. Discussion

We presented the results of a MC simulation study in which we investigated to what extent a photopeak sensitivity improvement of a PMT-based NaI(Tl) gamma detector

for high energy gammas would be possible, without seriously deteriorating its intrinsic spatial resolution. To this end, we studied gamma detectors with increased scintillator thicknesses for a series of light guide thicknesses read out by various PMT configurations. To mitigate a possible reduction in performance due to the increased scintillator thickness, we estimated the 3D interaction position of each event using an ML algorithm. The obtained DOI information is not available in standard gamma detectors. The performance for gammas with energies of 140 keV and 511 keV was analyzed and the results were presented in Tables 4.2, 4.3 and 4.4. The obtained values show that it is possible to significantly improve photopeak sensitivity by increasing the scintillator's thickness while using the same PMT configuration. Depending on PMT size, this improvement comes with only a modest degradation or a slight improvement of the intrinsic detector resolution.

For both detector designs with thicker scintillators, intrinsic spatial performance depends on PMT configuration as well as source location and light guide thickness. In general, PMT layout and shape have a negligible effect (<10%) on spatial performance. Setups with smaller PMTs (2-inch round or 60×60 mm^2 square) perform best in terms of spatial and DOI resolution as can be seen from Figs. 4.5, 4.6, 4.7 and 4.8. However, the cost of these configurations is significantly higher than of the ones equipped with larger PMTs (3-inch round or 76×76 mm^2 square) due to the higher number of light sensors and electronic channels used. Making the rough assumption that costs scale linearly with number of required PMTs and channels, we estimate that compared to the current 3-inch round PMT configuration, the overall cost would increase by roughly ~15% if 76×76 mm^2 square PMTs were utilized, whereas if the 60×60 mm^2 square or the 2-inch round configurations were to be used the respective increments would be ~80% or ~97%. Regarding the source position, for a source placed above the PMT centre, round PMTs grant better spatial and DOI resolution than square PMTs. Moving towards locations above the PMTs' edges instead, square PMTs allow to gain a moderate performance improvement. Concerning the influence of light guide thickness on the spatial performance, the 20 mm and the 40 mm thick crystal show different behaviors. The performance of the 20 mm scintillator for most configurations tends to slightly improve as the light guide thickness increases. This is probably because, due to their size, the PMTs used require larger light spread to grant optimal performance. However, excessively increasing the light guide thickness would lead to unwanted spreading of the signal between different light sensors, with a low number of events in each of them and hence performance degradation. These considerations together with the results shown in Figs. 4.5 and 4.6 seems to suggest the existence of an optimal light guide thickness range for this crystal of around 10 mm. On the other hand, the majority of the 40 mm scintillator setups suffers from performance degradation when utilizing thicker light guides. This is probably due to the overall larger light spread of optical photons in a thicker crystal. It is important to remark that the improvement in spatial resolution observed for some configurations when increasing the light guide thickness is always compensated by a substantial degradation of the DOI resolution. Therefore, we believe that the overall spatial performance doesn't benefit from using thicker light guides.

Analyzing the 40 mm thick scintillator, the best results at the PMT centre were achieved

by the configuration with 2 mm light guide read out by 2-inch round PMTs. This setup obtained 3.5 mm spatial resolution for 140 keV photons (Fig. 4.7a), while for 511 keV it achieved 3.1 mm spatial resolution and 5.8 mm DOI resolution (Fig. 4.8a, d). Near the PMTs' edges, the best spatial performance was reached by the setup equipped with 60×60 mm^2 square PMTs (std layout) and 2 mm light guide. This configuration achieved 3.3 mm spatial resolution for 140 keV (Fig. 4.7b), while for 511 keV gammas the estimated spatial and DOI resolution were respectively 2.5 mm and 5.1 mm (Fig. 4.8b, e). Regarding the average spatial performance over the analyzed detector's central area, the best results for the 40 mm thick scintillator were reached using the 60×60 mm^2 square PMTs (std layout) combined with 2 mm light guide. This configuration obtained a spatial resolution of 3.5 mm for 140 keV, whereas for 511 keV results were 2.9 mm and 5.6 mm respectively for spatial and DOI resolution.

When discussing DOI results, it is important to emphasize that high DOI resolution is not necessarily required for our thick detectors' designs. For example, the VECTor system partly developed in our group can attain up to 0.6 mm resolution ^{18}F-PET using 9.5 mm thick crystal detectors without any DOI estimation. Such a system is characterized by a DOI uncertainty equal to the scintillator thickness, and we used that as a reference value. In most of the configurations tested, except the ones consisting of 20 mm thick crystal with 10 mm light guide, the estimated DOI resolution was below this 10 mm threshold. This represent an acceptable value as it would guarantee to be in a situation comparable to what conventional detectors have at best.

In terms of E_{res}, results for thick and conventional crystal detectors are comparable when working with 140 keV gammas, while for 511 keV gammas thick crystals allow to achieve improved E_{res}. These improvements could be related to the increased chance that gammas that Compton scatter in their first interaction in the detector do not escape the scintillator but lose all of their energy in subsequent interactions. An additional element that has an influence on the E_{res} is the shape of the PMTs used. Setups with square PMTs grant better performance compared to configurations with round PMTs. This is thanks to the increased percentage of the light sensors' active area covering the detector's surface, which improves detection of optical photons. Regarding the impact of the light guide thickness on this metric, both thicker crystals seem to benefit from the use of thicker light guides. This is likely due to the fact that part of the points source locations are directly above the dead area of a PMT. In this case, working with thicker light guides increases the spread of optical photons resulting in a higher probability of reaching the active area of a nearby PMT. However, such a trend won't extend indefinitely as with further increasing light spread optical photons will eventually reach the next dead area between PMTs. Moreover, as mentioned for the spatial performance, improvements in E_{res} achieved by further increasing the light guide thickness would be at the cost of the DOI resolution. Analyzing the 40 mm thick crystal, the best results were obtained using the 3-inch square PMTs (std layout) setup with 10 mm light guide. This configuration reached an average E_{res} of 9.6% and 5.9% respectively for 140 keV (Fig. 4.7c) and 511 keV gammas (Fig. 4.8c). On the other hand, the configuration consisting of 3-inch round PMTs combined with 10 mm light guide attained an average E_{res} of 9.9% for 140 keV gammas (Fig. 4.7c) and of 6.3% for 511 keV gammas (Fig. 4.8c).

Regarding the detector sensitivity, increasing the scintillator's thickness to 20 mm or 40 mm results in photopeak sensitivities respectively of ~27% or ~53% for 511 keV gammas. These values are 2.2 and 4.4 times better than what can be obtained with a standard 9.5 mm thick scintillator. Such a high improvement in sensitivity comes at modest deterioration in spatial resolution when using a cost-effective PMT setup, as shown in Tables 4.2 and 4.3. However, by choosing a different PMT configuration (e.g. 2-inch round or 60×60 mm^2 square) it is possible to maintain the same high sensitivity while also improving the spatial performance as indicated in Table 4.4.

By analyzing the presented results, it is clear that in terms of spatial and DOI resolution it would be highly beneficial to use smaller sized round or square PMTs. However, their overall higher cost is a relevant drawback in our study, as one of the goals of our work is to build a large-area cost-effective detector. Therefore, it is crucial to find the right balance between performance and cost. In this context, the 3-inch square PMTs could represent a valid option, as they offer moderately improved performance compared to the 3-inch round PMTs at a slightly higher cost.

A limitation of the present work is that a detailed performance analysis was executed for the central detector area while edge effects were not yet studied. Generally, the severeness of edge effects depends on crystal thickness and is therefore important when considering thick crystal detectors. However, for the large-area gamma detectors considered (590×470 mm^2), such dead edge effects are of lesser concern than when small crystals are used. Typically, for these large detectors a rather substantial area near the crystal edge is simply not used (~4.5 cm), a choice that can be made because this edge region is still relatively small compared to the whole crystal. Therefore, it is not expected that edge effects have a major influence within the FOV that is used in practice. To illustrate this, we conducted a small simulation study comparing the 9.5 mm and 40 mm thick crystals with the standard 3-inch PMT configuration (see Fig. A.1). The data reported in Table A.1 indicates that for a 40 mm thick crystal, spatial resolution near the edge only deteriorates moderately (<15%) while it remains constant for the 9.5 mm crystal. Although the illustrated results don't represent an in-depth analysis of the relation between crystal thickness and the extent of edge effects, they indicate that even for the worst-case scenario (thickest crystal and largest PMTs) edge effects are not severely influencing the overall detector performance.

4.5. Conclusion

We explored a possible cost-effective solution to improve sensitivity for high-energy gammas outside the conventional SPECT energy range. We have shown that increasing the scintillator's thickness can greatly improve the detector photopeak sensitivity for high-energy gammas. Moreover, we illustrated how the spatial resolution can be influenced by changes in light guide thickness and PMT geometry. Depending on PMT geometry, and thus on cost-effectiveness, spatial resolution of gamma detectors with thick scintillators can be slightly improved or moderately degraded compared to conventional gamma detectors.

Acknowledgement

This work was financed by the research grant QUARAT: Quantitative Universal Radiotracer Tomography (TTW16885) which is financed in part by the Dutch Research Council (NWO).

Appendix

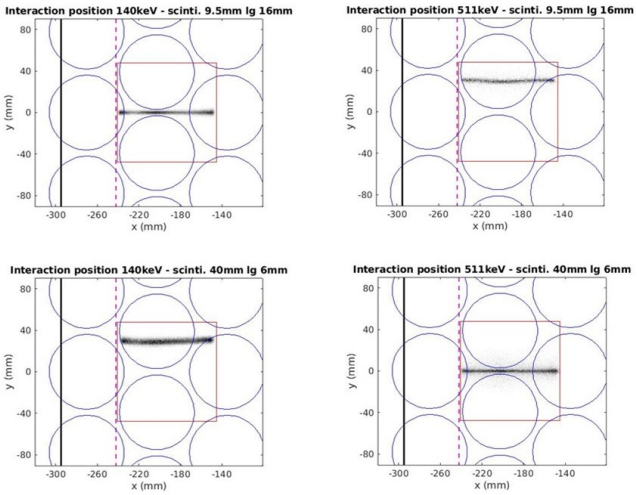

Figure A.1: Line source images for 140 and 511 keV gammas acquired near the detector edge (black). The edge of the detector used FOV is shown by the dashed purple line, and the system matrix by the red line. Data were acquired with 9.5-mm and 40-mm crystals read out by 3-inch round PMTs.

Scintillator thickness [mm]	*FWHM center 140 keV [mm]*	*FWHM edge 140 keV [mm]*	*FWHM center 511 keV [mm]*	*FWHM edge 511 keV [mm]*
9.5	3.8 ± 0.2	3.9 ± 0.6	2.6 ± 0.2	2.7 ± 0.5
40.0	4.4 ± 0.3	4.7 ± 0.3	3.7 ± 0.2	4.2 ± 0.7

Table A.1: Spatial performance for a 9.5 mm thick crystal with 16 mm light guide and a 40 mm thick crystal with 6 mm light guide, evaluated in the central region and at the detector edge.

5

Twisted clustered pinhole collimation for improved high-energy preclinical PET/SPECT

This chapter is adapted from:
Valerio Cosmi, Monika Kvassheim, Satyajit Ghosh, Freek J. Beekman and Marlies C. Goorden, Twisted clustered pinhole collimation for improved high-energy preclinical SPECT/PET. *Physics in Medicine & Biology*, 2024; 69 225016.

Advanced pinhole collimation geometries optimized for preclinical high-energy gamma imaging facilitate applications such as alpha and beta emitter imaging, simultaneous multi-isotope PET and PET/SPECT, and positron range-free PET. These geometries replace each pinhole with a group of clustered pinholes (CP) featuring smaller individual pinhole opening angles (POAs), enabling sub-mm resolution imaging up to ~1 MeV. Further narrowing POAs while retaining field-of-view (FOV) may enhance high-energy imaging but faces geometrical constraints. Here, we detail how the novel Twisted Clustered Pinholes (TCP) address this challenge.

We compared TCP and CP collimator sensitivity at equal system resolution and system resolution at matched sensitivity by tuning pinhole diameters for ^{18}F (511 keV) and ^{89}Zr (909 keV). Additionally, simulated Derenzo phantoms at low activity (LA: 12 MBq/ml) and high activity (HA: 190 MBq/ml) levels, along with uniformity images, were compared to assess image resolution and uniformity.

At equal system resolution, TCP increased average central FOV sensitivity by 15.6% for ^{18}F and 29.4% for ^{89}Zr compared to CP. Image resolution was comparable, except for ^{89}Zr at LA, where TCP resolved 0.80 mm diameter rods compared to 0.90 mm for CP. Image uniformity was equivalent for ^{18}F, while for ^{89}Zr TCP granted a 10.4% improvement. For collimators with matched sensitivity, TCP improved system resolution by 6.6% for ^{18}F and 17.7% for ^{89}Zr while also enhancing image resolution; for ^{18}F, rods distinguished were 0.65 mm (CP) and 0.60 mm (TCP) for HA, and 0.70 mm (CP and TCP) for LA. For ^{89}Zr, image resolutions were 0.75 mm (CP) and 0.65 mm (TCP) for HA, and 0.90 mm (CP) and 0.80 mm (TCP) for LA. Image uniformity with TCP decreased by 18.3% for ^{18}F but improved by 20.1% for ^{89}Zr. This study suggests that the TCP design has potential to improve high-energy gamma imaging.

5.1. Introduction

The continuous development of novel radiotracers and advanced imaging techniques is imperative for addressing unmet diagnostic and therapeutic requirements [62, 169]. This has notably augmented the significance of high-performance preclinical SPECT and PET, pivotal for evaluating radiotracer biodistribution and potential applications.

Recently, there has been a growing interest in radionuclides, such as alpha and beta emitters for therapeutic applications, which were previously overlooked due to the challenges in producing high-quality images of their distributions [69]. For instance, ^{124}I is a positron-emitter utilized in detecting residual thyroid tissue and/or metastases in differentiated thyroid cancer [170] despite its long mean positron range (3.4 mm) and several additional decay products that include high energy gammas (603 keV and 1691 keV). Similarly, ^{76}Br, although promising in tumor imaging via PET, faces implementation challenges due to its extended mean positron range (2.5 mm) and high-energy prompt gammas (559 keV) [171–173], which together result in blurred images and quantification errors [174]. Another emerging radionuclide is ^{89}Zr, which has been gaining popularity thanks to its role in immunoPET [175]. This positron emitter (23% abundance) co-emits 909 keV prompt gammas (99%), which generate a high scatter background. Other

radionuclides with promising applications for high-energy radionuclide therapy include the combined gamma - beta emitter ^{131}I and the gamma - alpha emitter ^{213}Bi. Their high energy gammas, respectively 364 keV and 440 keV, are extremely difficult to image with traditional SPECT.

In recent years, advanced high-energy pinhole technology has solved many of the challenges encountered when imaging such nonstandard radionuclides. This technology is integrated into the VECTor (Versatile Emission Computed Tomography) scanner currently marketed by MILabs which has been validated for sub-mm resolution SPECT and PET imaging from 30 keV up to 1 MeV gamma energies [40]. This system's capability to explore such an exceptionally wide energy range allows to image standard SPECT radionuclides as well as accurately capture tracer distributions using high-energy gammas. This has already been applied to several non-standard radionuclides mentioned above, by utilizing annihilation gammas (511 keV) resulting from positron emitters decay, or by detecting prompt gammas co-emitted by therapeutic radionuclides (alpha and beta emitters), as well as by positron emitting tracers. This capability enables new applications such as alpha and beta emitter imaging and simultaneous multi-isotope PET/SPECT. Imaging of high-energy gammas from ^{131}I and ^{213}Bi achieved image resolutions of 0.75 mm and 0.60 mm respectively [46, 47], while simultaneous imaging of ^{99m}Tc and ^{18}F resulted in image resolution of 0.50 mm and 0.80 mm [40]. The image resolutions for ^{131}I, ^{99m}Tc, and ^{18}F were obtained with a collimator achieving peak sensitivities of 0.16%, 0.24%, and 0.29%, respectively. Furthermore, recent studies have explored the use of prompt gammas emitted directly from the nuclei of positron emitters, thus unaffected by positron range effects. These prompt gammas enable high-resolution positron-range free PET as well as multi-isotope PET by exploiting their energy dependence. Prompt gamma imaging resulted in 0.75 mm image resolution for ^{89}Zr (909 keV prompts) and ^{124}I (603 keV prompts), while multi-isotope PET was demonstrated by simultaneously acquiring ^{18}F and ^{124}I images, achieving an image resolution of 0.75 mm [45].

The multi-pinhole system's ability to explore a wide energy range is supported by its advanced pinhole collimation geometry, which preserves resolution at higher energies. This is accomplished by replacing traditional pinholes with a group of clustered pinholes (CP), with each cluster designed to sample the same field-of-view (FOV) of a traditional pinhole while featuring narrower individual pinhole opening angles (POAs) [48, 49]. This approach addresses limitations encountered with conventional multi-pinhole collimators which suffer from pinhole edge penetration by high-energy gammas, resulting in reduced image resolution. Narrowing the pinhole opening angle alleviates this issue by increasing the path length that gammas travel through the pinhole edge material, making the edge a more effective barrier and reducing the likelihood of gammas penetrating it.

Further improving performance remains compelling and may demand even narrower POAs. In this work, we demonstrate that fitting such narrow POAs in a cluster comes with geometrical challenges as individual pinholes would begin to overlap. To enable clusters with narrower POAs, one can employ a "Super-Cluster" geometry [70, 110] or twist the pinholes around the cluster's central axis. The latter solution, denoted by

twisted clustered pinholes (TCP), is proposed and characterized in this study. The aim of this paper is to investigate the potential of TCP imaging with extremely narrow POAs and compare its performance to previous CP technology. For this purpose, we designed a TPC collimator and conducted a Monte Carlo (MC) simulation study where the sensitivity, image resolution, and uniformity of CP and TCP collimators with equal FOV were assessed by full system simulations of appropriately designed phantoms. This methodology was applied to low (12 MBq/mL) and high (190 MBq/mL) activity levels of ^{18}F and ^{89}Zr, two important tracers characterized by high-energy gamma emissions of 511 keV and 909 keV respectively.

5.2. Materials and Methods

5.2.1. Geometry of imaging system and collimators

In this simulation study, we compared the performance of a conventional CP collimator with a novel TCP collimator. Both collimators were assumed to be installed in the VECTor imaging system equipped with three PMT-based large-area monolithic NaI(Tl) scintillation detectors, measuring 590×470×9.5 mm^3 each, arranged in a triangular setup. Collimators compatible with the imaging system feature focusing pinhole geometries, meaning that all pinholes focus on a common volume, the central FOV (CFOV). Consequently, complete data acquisition for objects or organs that fit within the CFOV does not require any bed translation, while for larger objects up to whole body animal scans bed translation is done to ensure adequate sampling. Subsequently, images are reconstructed by using projection data from all the different bed positions simultaneously [82].

CP collimator design

The CP collimator, based on the design specified in a prior study [48], is composed of a tungsten alloy comprising 97.0% tungsten, 1.5% nickel, and 1.5% iron. It is characterized by a cylindrical geometry with inner and outer radii measuring 24 mm and 67 mm respectively. The collimator's wall thickness is optimized for stopping 511 keV gammas and ensures that for 909 keV gammas, the probability of passing through without interaction is 0.2% for perpendicular incidence. This probability decreases for gammas that enter at non-perpendicular angles, as they traverse a greater material thickness. Furthermore, the good performance of this wall thickness for 909 keV gammas has been experimentally demonstrated [45].

The pinhole centers are situated at a radius of 32 mm, placed asymmetrically within the collimator wall. This configuration facilitates substantial pinhole magnification factors while utilizing the thick collimator walls that are required for high-energy gamma imaging. A high pinhole magnification factor is key to high-resolution imaging since it compensates for the limited detector intrinsic resolution (~3.5 mm in this context). The

clustered pinholes of 0.7 mm diameter each are grouped into 48-2×2 clusters, with 162 of the 192 pinholes being used for image reconstruction. Each cluster sees the ellipsoidal CFOV with principal axes of 12×12×9 mm^3. These clusters are distributed across four rings, with pinholes in the outer rings exhibiting an opening angle of 16°, whereas those in the inner rings feature an opening angle of 18°. These angles ensure optimal detector coverage, resulting in a moderate projection overlap (multiplexing) of 16% at the detector's surface, which grants a reasonable fit of the elliptical pinhole projections onto the flat detector's surface [176]. Compared to conventional pinhole collimators (Fig. 5.1a) that can be accommodated on the same platform for traditional SPECT energies, the CP collimator (Fig. 5.1b) has reduced opening angles while maintaining an equivalent CFOV.

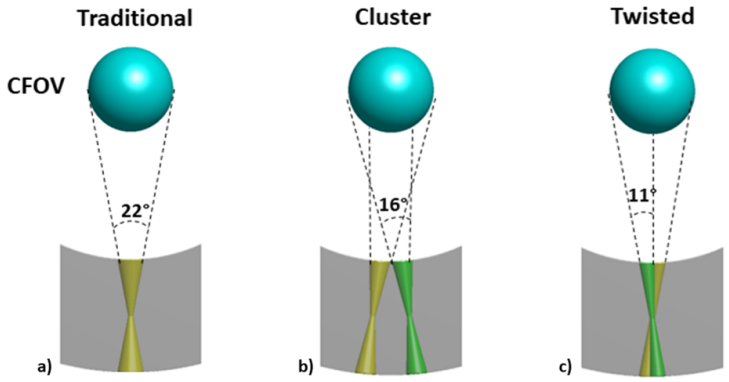

Figure 5.1: Illustration of various pinhole configurations. Images a), b), and c) display 2D views of traditional, clustered, and twisted clustered pinholes, respectively. Clustered and twisted cluster geometries retain the same CFOV as traditional pinholes while reducing the POA. Note that while POAs in this illustration are realistic for the collimator considered in this work, collimator thickness is reduced for improved visualization clarity.

Further reducing the POAs of the CP collimator could be a suitable solution to improve system performance. However, the current design constraints preclude such adjustments, as will be elaborated in the following section.

TCP collimator design

The TCP collimator we propose can be conceived as an evolution of the CP collimator, thus they share numerous characteristics. We kept consistency in parameters such as material composition, CFOV size, number of pinholes per cluster, degree of multiplexing, inner and outer radii of the collimator, and radius at which pinhole centers are placed. The only variable we altered was the placement of individual pinholes and their opening angles. This allows to perform identical imaging studies with both collimator types, while solely assessing the effect of the new TCP geometry.

The design concept of the TCP collimator can be visualized by describing the process for reducing POAs of CP and illustrating the constraints preventing this. For illustrative

purposes, we consider each pinhole as consisting of two cones without depicting the finite hole diameter (Fig. 5.2).

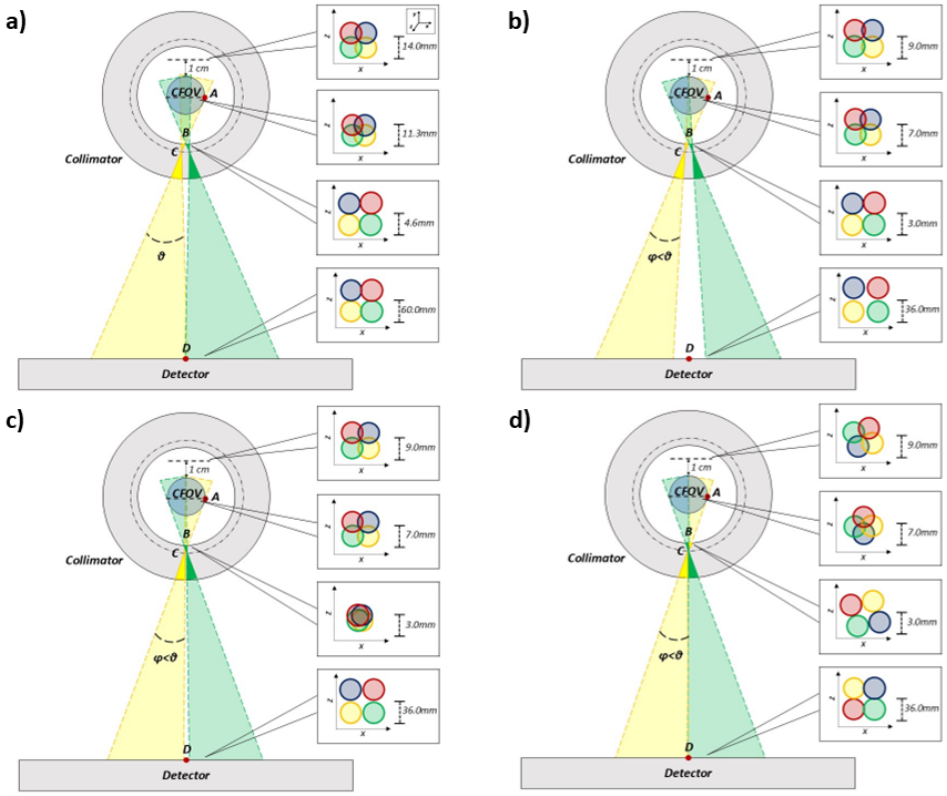

Figure 5.2: Schematic representation of challenges in narrowing POAs in CP technology and the solution in terms of TCP. The figure shows frontal views featuring two of four pinholes within a cluster and cross-sectional planes (xz-plane, with the z-axis pointing in the direction perpendicular to the page) showing all four pinholes. Image a) illustrates the current CP design with POAs θ, wherein the 'green' and 'yellow' pinholes are situated in the same plane. In b), reduced POAs ($\phi < \theta$) result in incomplete detector surface coverage. To address this limitation while retaining CFOV sampling, pinholes are inwardly rotated in c), causing pinhole overlap within the collimator as shown in the xz plane cross-section. Twisting pinholes around the cluster's central axis in d) overcomes these limitations, as pinholes lay in different planes. The image shown in d) closely resembles the final cluster design used for the TCP collimators. Note that for the twisted pinholes design in d), the relative position of all four pinholes in the xz-plane changes.

In the CP collimator, individual pinholes are defined by two lines: one tangent to the desired CFOV, and a second one determining the opening angle and projection size onto the detector. Assuming a design wherein pinholes in a cluster don't overlap (Fig. 5.2a), the line tangent to the CFOV (point A) is required to intersect point B (where the two pinholes touch without overlapping). The second line instead should cross the first line at the pinhole center (point C) and extend to point D on the detector to guarantee complete

coverage of the detector surface while avoiding projection overlap (Fig. 5.2a). These observations imply that, given the CFOV and the condition that individual pinholes don't overlap while utilizing the entire detector surface, the POA for a 2×2 cluster is determined (θ).

Expanding upon this concept, suppose that we reduce the POA ($\phi < \theta$) with such a design. In Fig. 5.2b it is shown that simply reducing the POA while preserving the tangential line to the CFOV (line AB) would result in a gap between pinhole projections on the detector near point D. One possible approach to reduce this involves inward rotation of pinholes around point A (Fig. 5.2c). However, this adjustment would lead to an overlap among individual pinholes in the collimator, as they are located in the same plane (Fig. 5.2c). This defies the intention of CP, whose aim is to minimize collimator penetration by increasing the amount of material traversed by photons when they don't go directly through the pinhole.

The new TCP collimator adopts the strategy illustrated in Fig. 5.2c of moving pinholes closer to each other to reduce their opening angles. Ideally, this would be possible if the two pinholes illustrated in Fig. 5.2 would not be in the same plane. However, merely shifting the pinhole in the direction perpendicular to the paper would lead to overlap with other pinholes within the 2×2 cluster. Instead, we accomplish this by twisting individual pinholes within a cluster around the cluster's central axis, ensuring that all four pinholes reside in distinct planes (Fig. 5.2d). This adjustment guarantees that, as with CP, every point within the CFOV is sampled by at least one pinhole. This was additionally checked by MC simulations. Furthermore, it allows to preserve collimator material separating the pinholes while reducing their opening angles.

The TCP design is expected to be more focused compared to CP, as evident from the differing extents of pinhole cone overlap in CP (Fig. 5.2a) and TCP (Fig. 5.2d). To comprehend the implications of such difference, sensitivity over the CFOV volume, as well as over larger volumes, will be examined.

As will be discussed later, a standard design for the TCP collimator was defined. Such collimator was used as a reference for different twisted designs, where pinhole diameter and amount of cluster's twisting were varied to grant a fair comparison between TCP and CP collimators.

Cluster arrangement in TCP collimator

As illustrated in Fig. 5.1, the TCP collimator allows for pinholes with half the POA of a traditional pinhole, while maintaining the same CFOV. As a result, the size of the projection of the whole cluster on the detector is comparable to that of traditional pinhole projections. Therefore, during the collimator design phase it is convenient to start with a traditional pinhole collimator housing pinholes that view the desired CFOV and then later replace them with a twisted cluster. The traditional POA α corresponding to the desired CFOV is given by the following equation:

$$\alpha = 2 \cdot \sin^{-1}\left(\frac{r_{\text{CFOV}}}{l}\right) \tag{5.1}$$

Here r_{CFOV} is the CFOV radius, set to 6 mm (Fig. 5.3b) to match that of the CP collimator; l is the distance of the pinhole center to the collimator's center (Fig. 5.3a). This distance is calculated by combining the pinhole center radius (32 mm) and the axial shift of the ring on which the pinhole is placed.

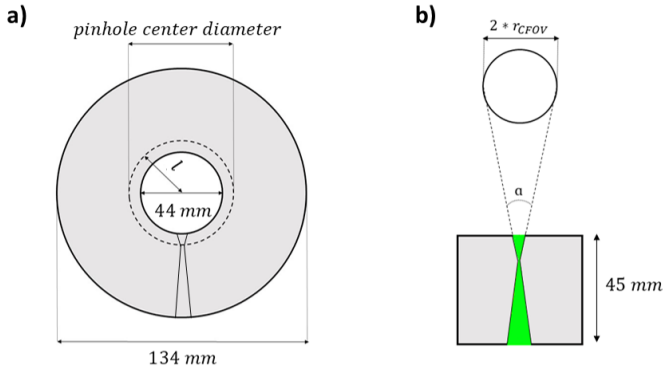

Figure 5.3: Schematic representation of the collimator geometry. a) Frontal view of the collimator with collimator radii provided that are valid for both TCP and CP designs, while l represents the distance from pinhole center to collimator center. The outline of a single traditional pinhole is visible. b) Illustration of a cross section of a traditional pinhole collimator, where rcfov indicates the CFOV radius and α the opening angle of an individual pinhole.

Using an AutoCAD script, we proceeded to design a collimator with traditional pinholes. These pinholes were characterized by opening angles of 22°, calculated via (5.1) to grant the desired CFOV ($12\times12\times9$ mm^3). A total of 108 traditional pinholes were distributed across six rings to achieve full detector coverage. The pinholes in each ring were evenly spaced, resulting in uniform angular separation between pinholes.

To evaluate detector coverage, the intersections of the extension of the pinhole cones with the detector surface were determined. Subsequently, these traditional pinholes were replaced with clusters of 2×2 twisted pinholes with the same FOV (Fig. 5.4).

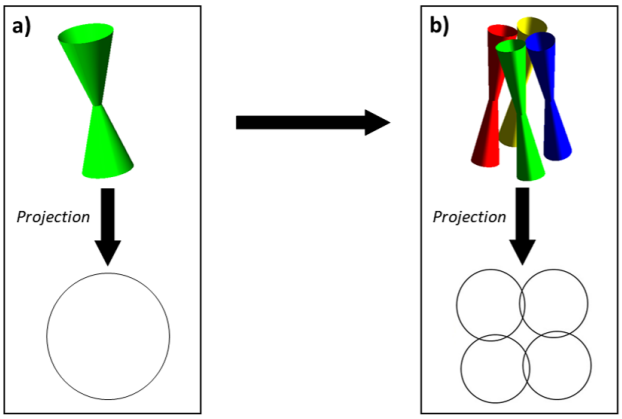

Figure 5.4: Visual representation of the procedure for placing the twisted clusters on the collimator's surface. For visualization purposes, symmetric pinholes with shorter lower cones than in the designed collimator are shown here. Image a) shows a single traditional pinhole, replaced in b) by a cluster of 2×2 pinholes twisted around their central axis. An iterative process defines the cluster's position and degree of twisting. Further adjustments to the amount of twisting and the placement of clusters are discussed in section 5.3.2

The centers of the TCPs, the shift between clusters within the same ring, and the amount of twisting, were all fine-tuned through an iterative process. The twisting angle, indicated by the angle between the pinhole's axis and the normal to the cluster's axis, was calculated via equation A.1. These parameters underwent gradual variation as we visually examined the geometric projection of the pinholes onto the detector and assessed the degree of multiplexing (Fig. 5.4b). The latter was calculated by verifying for each detector pixel center whether it was within the surface defined by a single or multiple pinhole projection cones.

$$Multiplexing\ [\%] = 100 \times \frac{\#\ pixels\ within\ multiple\ cones}{\#\ pixels\ with\ non\text{-}zero\ value} \tag{5.2}$$

This allowed to determine a TCP collimator with the same amount of multiplexing as the CP collimator (~16%).

5.2.2. Collimator comparison

The tradeoff between system resolution and sensitivity for the CP and TCP collimators placed in the imaging system was evaluated. To ensure a fair analysis, we compared: (i) sensitivity at equal system resolution, and (ii) system resolution at equal sensitivity. Meeting these criteria required iterative small adjustments of the TCP pinhole diameter and amount of cluster's twisting, resulting in the development of four distinct TCP designs, two for each radionuclide.

A detailed explanation of the equations used to establish equivalence between CP and

TCP theoretical system resolutions is provided in the Appendix. This equivalence was obtained by initially setting the same resolution equivalent diameter d_{re} (defined in A.5) for both collimators. The reference d_{re} values were calculated based on CP specifications, where d = 0.7 mm and α = 17°, the mean value of the opening angles in CP (16° and 18°). This calculation was performed both for ^{18}F (511 keV) and ^{89}Zr (909 keV), with the linear attenuation coefficient of the collimator material (μ) respectively 0.228 mm^{-1} and 0.135 mm^{-1}. The d_{re} values obtained, d_{re} (511keV) = 1.15 mm and d_{re} (909keV) = 1.46 mm, were then used to determine the TCP pinhole diameter by inverting (A.5). The TCP collimators thus characterized were denoted by "TwistResEq" and their sensitivity was calculated as explained in section 5.2.3.

To match CP and TCP sensitivity, the TCP pinhole diameters were systematically changed in steps of 0.001 mm. The final TCP designs for both radionuclides were those resulting in an average sensitivity over the entire CFOV closest to that of the CP collimator. The TCP designs obtained through this procedure were called "TwistSensEq", their system resolutions were subsequently calculated using (A.2).

5.2.3. Simulation setup and data acquisition process

The data used for the collimator comparison were generated via MC simulations using GATE v9.0, based on Geant4 version 10.05 [83–85]. The simulations modeled gamma photon interactions with the detector without tracking their optical transport (bulk and boundary processes). The behavior of gamma and optical photons was defined utilizing GATE's standard electromagnetic list of physical processes (*emstandard*). The imaging system and the phantoms used were modelled using GATE primitives.

The simulation setup consisted of the multi-pinhole imaging system equipped with either the CP or TCP collimator. The parameters of the system's triangular detector setup and of the cylindrical collimator were derived from the manufacturer's specifications. Accordingly, the detectors' intrinsic spatial resolution was set to 3.5 mm, while the energy resolution was 9.0% and 6.7% respectively for 511 keV and 909 keV photons. These values were implemented in our analysis as we randomized the interaction energy and position for each event using Gaussian probability distributions characterized by the standard deviation (σ) calculated from the provided resolutions.

These simulations served multiple purposes, including assessing sensitivity over the CFOV and larger volumes, as well as generating forward projections of a resolution and uniformity phantom, as described in the following subsections.

Sensitivity phantom scans

The sensitivity data were obtained through simulations involving two distinct phantoms: an ellipsoidal phantom matching the dimensions of the CFOV (12×12×9 mm^3 axes), and an elliptical tube phantom with sizes 24×16×50 mm^3. Additionally, an ellipsoidal volume

($24\times16\times9$ mm^3) was selected from the center of the elliptical tube phantom. Although the second phantom lacks internal structures resembling mouse anatomy, it was named the “whole-body mouse-sized phantom” because its shape and dimensions approximate those of an actual mouse. Consequently, the ellipsoidal volume selected from its center was referred to as the "mouse-sized phantom thick slice”.

The two phantoms were placed at the center of the collimator and were scanned for 1-hour after being uniformly filled with 2 MBq/mL of ^{18}F or ^{89}Zr. The percentage sensitivity was then calculated as the ratio between the number of detected photons per decay and the total number of emissions.

$$\textit{Sensitivity [\%]} = 100 \times \frac{\textit{\# detected photons per decay}}{\textit{\# emissions}} \tag{5.3}$$

In sensitivity analysis, it is important to acknowledge that not all detected photons provide equal information content regarding emission position. Typically, photons undergoing scattering events within the collimator or traversing the pinhole edges offer lower-quality information compared to those passing directly through pinholes. To address this, we distinguished sensitivity contributions from photons with different interaction behavior: those passing directly through the pinholes (direct), those penetrating the pinhole edges (attenuated), and those scattering within the collimator material (scattered). This differentiation was achieved by substituting the corresponding number of detected photons in (5.3). To determine these fractions, we conducted two sets of simulations, varying only the linear attenuation coefficient of the collimator material. In the first set, we used the standard tungsten alloy for the collimator. These simulations were employed to determine the overall sensitivity and the scattered fraction. Scattered events were identified based on their energies. In the second set, the linear attenuation coefficient of the collimator was increased by a factor of one thousand compared to the standard tungsten alloy such that only direct photons would be detected. These simulations were used to calculate the fraction of direct photons, with the remaining photons being categorized as attenuated.

The obtained data were used to calculate the average photopeak sensitivity of ^{18}F and ^{89}Zr by applying a 20% energy acceptance window around the 511 keV and 909 keV photopeak.

Resolution phantom scans

Image resolution was assessed by simulating a Derenzo phantom assuming a 1-hour total scan across nine bed positions. These positions were arranged in a 3×3 grid with adjacent points spaced 6 mm apart in the transaxial plane, while only one axial position was used [88]. Given the size of the CFOV and the phantom (a cylinder with 20 mm diameter and 8 mm length) this is a conservatively high number of bed positions. Such a decision was made to ensure adequate sampling of the object, with every part of the scan volume covered by the CFOV at least once. The phantom contained six sectors featuring

cylindrical rods with diameters of 0.90 mm, 0.80 mm, 0.75 mm, 0.70 mm, 0.65 mm, and 0.60 mm. Each rod had a height of 6 mm, and the distance between their centers within each sector was twice their diameter. The rods were filled with either low or high activity concentrations, respectively 12 MBq/mL and 190 MBq/mL, of ^{18}F or ^{89}Zr. This allowed to evaluate performance at different activity levels.

Uniformity phantom scans

To evaluate uniformity, we designed a cylindrical phantom with 14 mm diameter and 6 mm length filled uniformly with 2 MBq/mL of either ^{18}F or ^{89}Zr. The scan sequence comprised the same nine bed positions as for the Derenzo phantom, with a total scan duration of 1 hour.

5.2.4. Image reconstruction

Prior to reconstruction, we applied an energy acceptance window of 20% around the ^{18}F and ^{89}Zr photopeaks, centered respectively at 511 keV and 909 keV. Furthermore, a triple-energy window scatter correction method was implemented by defining two side windows adjacent to the photopeak, each having a width of 25% of the photopeak window's width [94].

We generated system matrices for each collimator and radionuclide analyzed. These energy dependent matrices were calculated with a ray-tracer which considers attenuation in the collimator and detector while it ignores scatter [55]. The system matrices for ^{18}F and ^{89}Zr were generated using the same tail cutoff (1% [55]) and differ solely due to the use of different attenuation coefficients in the ray-tracer software for the collimator and detector. Although the software and hardware were initially designed for 511 keV gammas, their effectiveness for higher energies, such as the 909 keV prompt gammas from ^{89}Zr, has been experimentally validated [45]. Images were reconstructed via the recently developed dual-matrix dual-voxel (DM-DV) pixel-based similarity-regulated ordered subsets expectation maximization (SROSEM) method [90, 92]. This algorithm employs two voxel sizes to accelerate reconstruction, with larger voxels used to model the slowly varying PSF tails and smaller voxels for the central parts of the PSFs. We defined the central part of the PSF as the part with values down to 20% of its peak value (modelled with 0.4 mm voxels), while the tails were defined as the part with smaller values (modelled with 0.8 mm voxels). During backprojection, only the central part of the PSFs was used. This accelerated photon transported modelling was integrated with SROSEM, an accelerated ordered subset algorithm that automatically and locally adapts the number of subsets, with a maximum of 128 subsets [90]. The images obtained underwent post-filtering using a series of 3D Gaussian filters with different FWHMs. For the resolution phantom, these FWHMs were the ones optimizing the CNR of selected rod sectors (the inspected sectors are indicated in the corresponding image captions, and the filter values are listed in Table A.2). For the uniformity phantom instead, a 1.0 mm filter was applied.

5.2.5. Data analysis

Data from the sensitivity, resolution and uniformity phantoms were used to quantitatively evaluate the TCP and CP collimators' performance.

A contrast-noise analysis was performed on the unfiltered reconstructed images of the resolution phantom [177]. To this end, these images were resampled to a fine grid and circular regions of interest (ROIs) were placed on and in between the rods. The ROIs had diameters equal to 0.9 times the rod size and were placed on 10 subsequent 0.4 mm slices of the reconstructed images. By determining the activity in each ROI, we calculated the contrast (C) in each sector (i) with the following equation:

$$C_{\text{rods},i} = \frac{\bar{h_i} - \bar{c_i}}{\bar{h_i}} \tag{5.4}$$

Here $\bar{h_i}$ and $\bar{c_i}$ are respectively the mean activity in all ROIs placed on and between the rods in sector i. Furthermore, the noise in each sector (N_i) was calculated:

$$N_{\text{rods},i} = \frac{\sqrt{\sigma^2_{h,i} + \sigma^2_{c,i}}}{\bar{h_i} + \bar{c_i}} \tag{5.5}$$

Here $\sigma_{h,i}$ and $\sigma_{c,i}$ are respectively the standard deviation of the activity in ROIs on and in between rods. Using (5.4) and (5.5), the contrast to noise ratio (CNR) was calculated and plotted against the iteration number.

Image uniformity was calculated by placing six circular ROIs with a diameter of 3.0 mm at five consecutive axial locations (evenly spaced at 0.8 mm intervals) on the reconstructed unfiltered uniformity phantom images [177]. The average value within the ROIs and the standard deviation between them, $\bar{U}$ and σ_U respectively, were measured to quantify the percentage uniformity.

$$\textit{Uniformity}\,[\%] = 100 \times \frac{\sigma_U}{\bar{U}} \tag{5.6}$$

For all the configurations analyzed, the average percentage uniformity calculated over multiple simulation runs of the same setup was plotted against the number of iterations.

5.2.6. Convergence speed

The number of iterations required for a reconstruction algorithm to converge to the desired image is influenced by the collimator characteristics. Therefore, to grant a fair comparison between the different collimators tested we quantified their convergence speed by calculating small detail contrast and defining an equivalent iteration number

[92]. This was done by comparing the number of iterations required by each design to achieve equal contrast for the smallest distinguishable rods filled with ^{18}F and ^{89}Zr, having diameters of 0.65 mm and 0.70 mm respectively. The contrast vs number of iterations plots of both collimators were then matched by multiplying the TCP collimator number of iterations by the constant factor that minimized the squared difference between the contrast curves.

5.3. Results

5.3.1. TCP collimator standard design

Through the design process previously described, we established a standard geometry for the TCP collimator, serving as a reference for the four different configurations examined in our analysis. These versions of the TCP collimator differ solely in terms of pinhole diameters and degree of clusters' twisting.

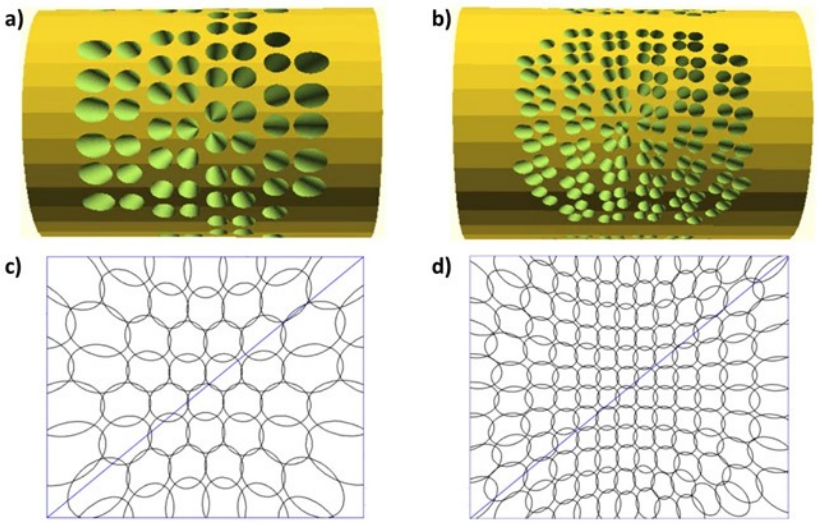

Figure 5.5: Visual comparison of the CP and the standard TCP collimator: a) and b) show the CP and the standard TCP collimators. The standard TCP collimator differs from those named TwistSensEq and TwistResEq solely in terms of pinhole diameter. Images c) and d) illustrate the pinhole projections on the detector surface of one of the three gamma detectors for each collimator.

The TCP collimator geometry (Fig. 5.5b) contains 108-2x2 twisted clusters of 0.7 mm diameter pinholes arranged in six rings. Adjacent rings were rotated 4° relative to one other as this allowed to sample the CFOV with a larger variation in angles. In each ring, clusters were placed 8° apart. The pinhole centers of the two innermost rings were at 32.3 mm from the collimator center. For the two central and two outermost rings, this

distance was 34.9 mm and 40.3 mm. After determining these distances, the pinholes placement on the inner surface was reviewed to prevent any overlap. The resulting POAs were 10.7°, 9.9° and 8.6° respectively for the two innermost, two central and two outermost rings. These opening angles appear to be narrower compared to the value initially indicated in Fig. 5.1 (11°). This is because the latter was calculated by considering a situation where the cluster was placed exactly at the central axial position of the cylindrical collimator. As clusters are positioned over several axial locations of the entire cylindrical collimator surface, their distances from the collimator's center increase and as expected from (eq. 5.1) their POAs diminish.

Thanks to these narrower angles, the average air volume of a single TCP cluster (~17.7 cm^3) decreased by ~64% compared to a CP cluster (~49.1 cm^3). Moreover, despite the increased total number of clusters (108 vs 48), the twisted design granted a ~19% reduction in the overall air volume within the collimator due to pinholes, indicating that more collimator material is present to stop gammas.

This standard TCP geometry resulted in an amount of multiplexing comparable to the one reached by CP (Fig. 5.5a) with the same pinhole diameter, respectively 16.0% (Fig. 5.5c) and 15.7% (Fig. 5.5d). Details about axial sampling are provided in the appendix.

5.3.2. Collimator performance comparison

To achieve a system resolution equivalent to that of the CP collimator, which has a 0.7 mm pinhole diameter and an average POA of 17°, the required pinhole diameters for the TCP design were calculated using equation A.5, assuming an average POA of 9.7°.The resulting diameters were 0.896 mm for 511 keV and 1.030 mm for 909 keV gammas, representing an increase from the 0.7 mm pinhole diameter in the previously described standard TCP design.

Adjusting the standard TCP collimator diameter to these new values affected the CFOV and the multiplexing, as both parameters increased compared to the values obtained with the reference twisted design employing 0.7 mm diameter. These issues were addressed by reducing the amount of twisting (eq A.1) until the CFOV and multiplexing returned to their original value. Additionally, for the 1.030 mm pinhole design, an overlap of two clusters on the outer ring was noticed. To prevent that, one of these clusters was rotated outward by 1° relative to its axis. The TCP designs achieving sensitivity equivalent to that of CP over the CFOV feature slightly larger pinhole diameters than the standard TCP design, with diameters of 0.788 mm and 0.725 mm, respectively for ^{18}F and ^{89}Zr. No additional adjustments were necessary for these designs since these values did not impact the CFOV and multiplexing.

The sensitivity performance of the TwistResEq and the TwistSensEq collimators compared to the CP collimator is summarized in Table 5.1 for the different-sized sensitivity phantoms.

	^{18}F				^{89}Zr			
Collimator	***Sens.***	***Direct***	***Atten.***	***Scatt.***	***Sens.***	***Direct***	***Atten.***	***Scatt.***
CFOV (12× 12× 9 mm^3)								
CP	0.32%	25.8%	65.5%	8.7%	0.17%	12.5%	83.0%	4.5%
TwistSensEq	0.32%	41.1%	50.0%	8.9%	0.17%	14.9%	80.9%	4.2%
TwistResEq	0.37%	46.0%	44.6%	9.4%	0.22%	24.2%	72.1%	3.7%
Mouse-sized phantom thick slice (24× 16× 9 mm^3)								
CP	0.23%	25.1%	63.7%	11.2%	0.14%	10.3%	84.7%	5.0%
TwistSensEq	0.22%	37.7%	50.4%	11.9%	0.13%	11.7%	83.5%	4.8%
TwistResEq	0.26%	42.8%	45.9%	11.3%	0.18%	19.3%	76.3%	4.4%
Mouse-sized phantom (24× 16× 50 mm^3)								
CP	0.096%	18.1%	61.4%	20.5%	0.097%	4.4%	89.0%	6.6%
TwistSensEq	0.087%	27.2%	51.9%	20.9%	0.091%	5.0%	88.0%	7.0%
TwistResEq	0.10%	31.5%	49.3%	19.2%	0.11%	8.9%	84.7%	6.4%

Table 5.1: Sensitivity (Sens.) and fraction of direct, attenuated (Atten.), and scattered (Scatt.) photons for the CP, TwistSensEq and TwistResEq collimators. Results were calculated over the CFOV, over a slice of the whole-body mouse-sized phantom, and over the whole-body mouse-sized phantom.

For the average sensitivity over the CFOV, the values achieved with the TwistResEq showed an increase of 15.6% and 29.4% for ^{18}F and ^{89}Zr respectively, compared to the CP collimator. Furthermore, results indicate that most of the photons detected within the photopeak traversed the pinhole edges (denoted by 'attenuated' in Table 5.1), rather than passing directly though the pinhole opening. Nonetheless, TCP demonstrated a higher relative number of photons going directly through the pinhole compared to CP; while for CP only 25.8% and 12.5% of the photons passed directly through the hole for ^{18}F and ^{89}Zr respectively, these percentages increased to 46.0% and 24.2% for the TwistResEq, and to 41.1% and 14.9% for the TwistSensEq. This increased fraction of direct photons came at the expense of attenuated photons, as the relative amount of pinhole scatter remained similar across different designs.

Evaluating the sensitivity over the larger mouse-sized phantom, the TwistResEq still granted noticeable improvement compared to the CP collimator. Specifically, within the selected confined region of this phantom, sensitivities increased by 13.0% for ^{18}F and by 28.6% for ^{89}Zr. When considering the entire mouse-sized phantom volume instead, smaller improvement of 4.2% and 13.4% were observed.

On the other hand, the TwistSensEq sensitivity results indicated a slight performance degradation compared to CP. Over the selected volume region, this sensitivity reduction was of 4.3% and 7.1% for ^{18}F and ^{89}Zr respectively, whereas over the entire phantom volume it was of 9.4% and 6.2%.

The trends observed for direct, attenuated, and scattered fractions of photons exhibited behaviors consistent with those described for the CFOV. The fractions of direct photons observed over a region of the whole-body phantom with the CP collimator were 25.1% and 10.3% respectively for ^{18}F and ^{89}Zr. These values increased to 42.8% and 19.3% with the TwistResEq, and to 37.7% and 11.7% with the TwistSensEq. Similarly, for the whole-body phantom CP achieved a relative number of direct photons of 18.1% for ^{18}F and 4.4% for ^{89}Zr, which improved to 31.5% and 8.9% with the TwistResEq, and to 27.2% and 5.0% with the TwistSensEq.

The system resolution (SR), pinhole diameter (d) and effective diameter (d_{re}) of the collimators tested are provided in Table 5.2.

	^{18}F			^{89}Zr		
Collimator	***SR [mm]***	***d [mm]***	***d_{re} [mm]***	***SR [mm]***	***d [mm]***	***d_{re} [mm]***
CP	1.52	0.70	1.15	1.86	0.70	1.46
TwistSensEq	1.42	0.79	1.05	1.53	0.73	1.16
TwistResEq	1.52	0.90	1.15	1.86	1.03	1.46

Table 5.2: System resolution, pinhole diameter and effective diameter for the CP, TwistSensEq and TwistResEq collimators.

The TwistSensEq designs improved system resolution by 6.6% and 17.7% for ^{18}F and ^{89}Zr, respectively, in comparison to the other analyzed collimators.

5.3.3. Equivalent iteration number

Contrast vs. iteration number curves for 0.65 mm (^{18}F) and 0.70 mm (^{89}Zr) rods in the Derenzo phantom were used to establish equivalent iteration numbers for different collimator types.

Our findings revealed that collimator designs with matched system resolutions converged at comparable speed. Therefore, images obtained with the TwistResEq and the CP collimators were compared at equal iteration number both for ^{18}F and ^{89}Zr.

On the other hand, when matching sensitivity, images obtained by the TCP collimator converged faster than those obtained with CP for both radionuclides analyzed. It was determined that 1 CP iteration is equivalent to 1.62 TwistSensEq iterations for ^{18}F, while for ^{89}Zr 1 CP iteration corresponds to 3.00 TwistSensEq iterations (Fig. A.1).

5.3.4. Resolution phantom simulations

Reconstructed images of the resolution phantom filled with 12 MBq/mL or 190 MBq/mL of ^{18}F are shown in Fig. 5.6 for different numbers of (equivalent) iterations.

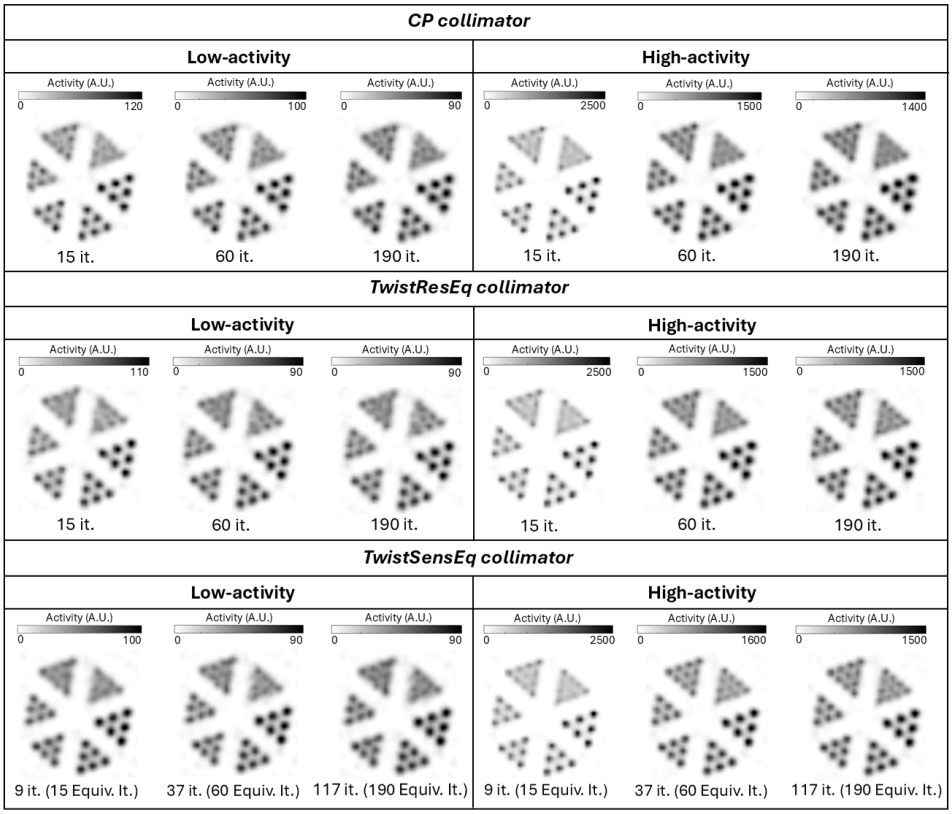

Figure 5.6: Resolution phantom images obtained with the CP and TCP collimators for ^{18}F. Rods with diameters of 0.90 mm, 0.80 mm, 0.75 mm, 0.70 mm, 0.65 mm, and 0.60 mm were filled with low (12 MBq/mL) or high (190 MBq/mL) activity. Based on the convergence speed analysis, images were compared at the same iteration number for collimators with matching system resolution, and at equivalent iteration numbers (Equiv. it.) for collimators with matching sensitivity. Images were post-filtered with the 3D Gaussian filters that optimized the CNR for 0.70 mm and 0.65 mm rods for both low and high activity results. The images shown were obtained by summing ten consecutive slices at the center of the phantom, resulting in a final image slice thickness of 4 mm.

A visual inspection of the results achieved with the TwistResEq and CP collimators indicates comparable performance, as for both configurations the smallest distinguishable rods have 0.70 mm diameter at low activity and 0.65 mm diameter at high activity. Images reconstructed with the TwistSensEq demonstrate equivalent performance to those obtained with other collimators at low activity levels. However, at higher activity levels, the TwistSensEq shows moderate improvement, with rods of 0.60

mm becoming more easily identifiable at 60 and 190 iterations. This can be seen in Fig. 5.8, which displays profiles of the smallest distinguishable rod sectors extracted from the resolution phantom images at the highest shown iteration number: 190 for CP and TwistResEq, and 117 for TwistSensEq.

Fig. 5.7 shows the images of the resolution phantom filled with 12 MBq/mL or 190 MBq/mL of ^{89}Zr for different numbers of (equivalent) iterations.

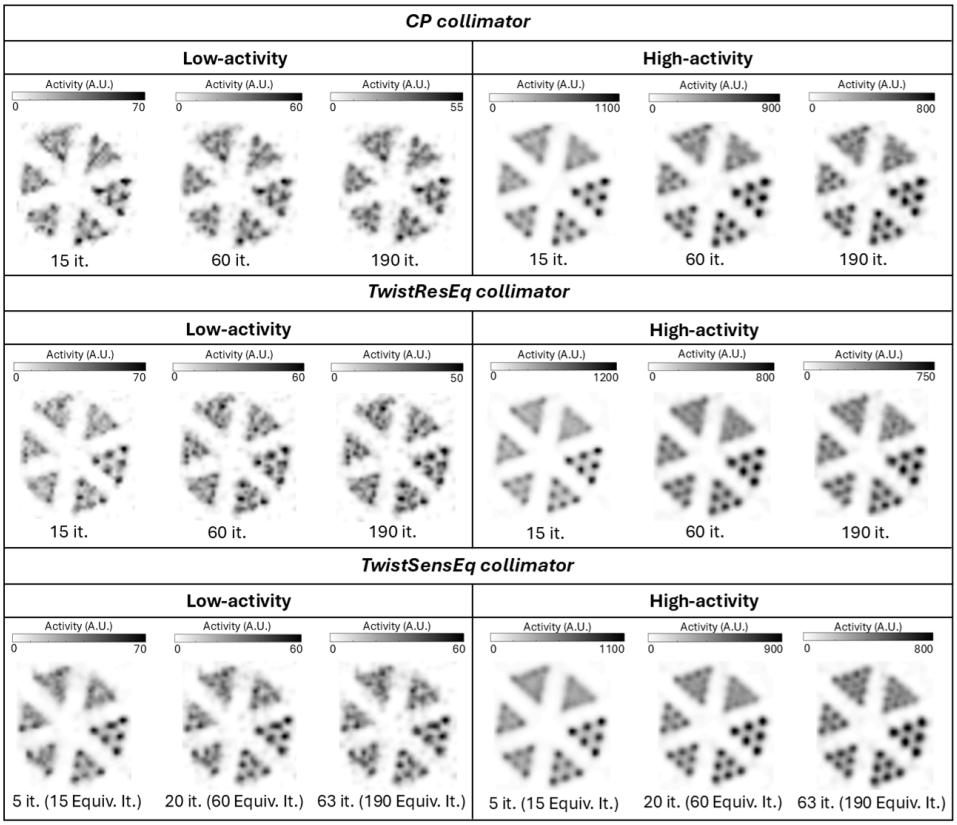

Figure 5.7: Resolution phantom images obtained with the CP and TCP collimators for ^{89}Zr. The rod diameters and activity levels are identical to those described in the caption of Fig. 5.6. Based on the convergence speed analysis, images were compared at the same iteration number for collimators with matching system resolution, and at equivalent iteration (Equiv. it.) numbers for collimators with matching sensitivity. Images were post-filtered with the 3D Gaussian filters that optimized the CNR for 0.75 mm and 0.70 mm rods for low and high activity results. The images shown were obtained by summing ten consecutive slices at the center of the phantom, resulting in a final image slice thickness of 4 mm.

At low activity, the TwistResEq shows superior performance compared to the CP design, as the former could resolve rods of 0.80 mm diameter, while the latter could discern rods of 0.90 mm. Performance of these two collimators is comparable at high activity,

with the 0.70 mm rods section being the smallest distinguishable for both collimators. Upon evaluation of images reconstructed with the TwistSensEq, an overall improvement in performance relative to the CP and TwistResEq collimators can be noticed. The TwistSensEq design could distinguish rods of 0.80 mm and 0.60 mm diameter respectively at low and high activity (Fig. 5.8).

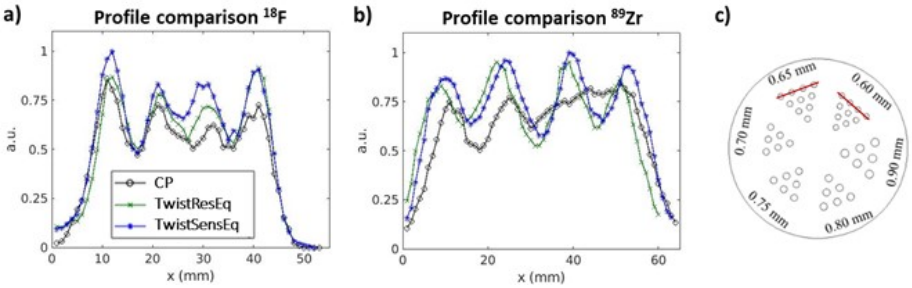

Figure 5.8: Profiles from resolution phantom images with high-activity levels of ^{18}F and ^{89}Zr, taken from Figures 5.6 and 5.7. Analysis used the highest iteration numbers: 190 for CP/TwistResEq and 117 (^{18}F) or 63 (^{89}Zr) for TwistSensEq. Profile positions (red lines in c) correspond to the 0.60 mm (^{18}F) and 0.65 mm (^{89}Zr) rod sectors.

5.3.5. Contrast and CNR analysis results

In addition to the visual comparison, a contrast-noise analysis was performed on the reconstructed resolution phantom images with results shown in Fig. 5.9 and tables A.3, A.4.

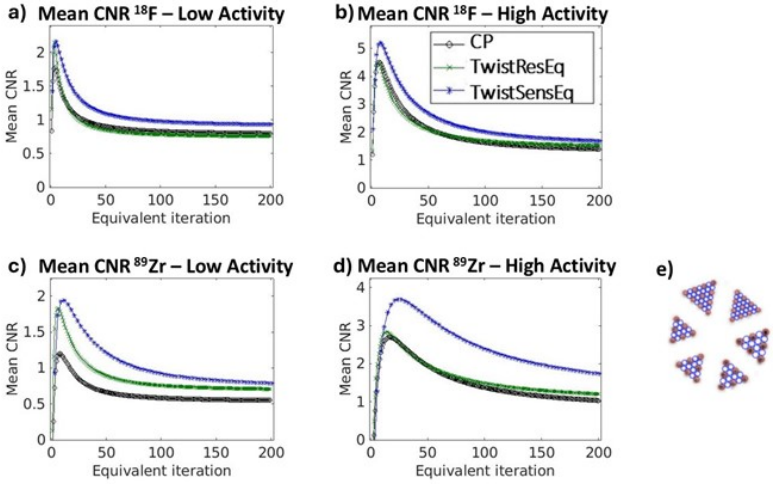

Figure 5.9: Mean CNRs of all collimators, averaged over visible rod sectors and selected hot/cold regions, plotted against the number of equivalent iterations.

Fig. 5.9 shows the average (over all visible rod sectors) CNR plotted against the equivalent number of iterations for all collimators, both for ^{18}F and ^{89}Zr. Overall, the TwistSensEq collimator granted a noticeable CNR improvement over the CP collimator for both ^{18}F and ^{89}Zr. On the other hand, the TwistResEq has shown only a moderate (negligible for ^{18}F) performance increase. Results per rod sector are provided in table A.3, A.4 in the appendix.

5.3.6. Image uniformity

Reconstructed images of the uniformity phantom filled with 2 MBq/mL of either ^{18}F or ^{89}Zr are shown in Fig. 5.10.

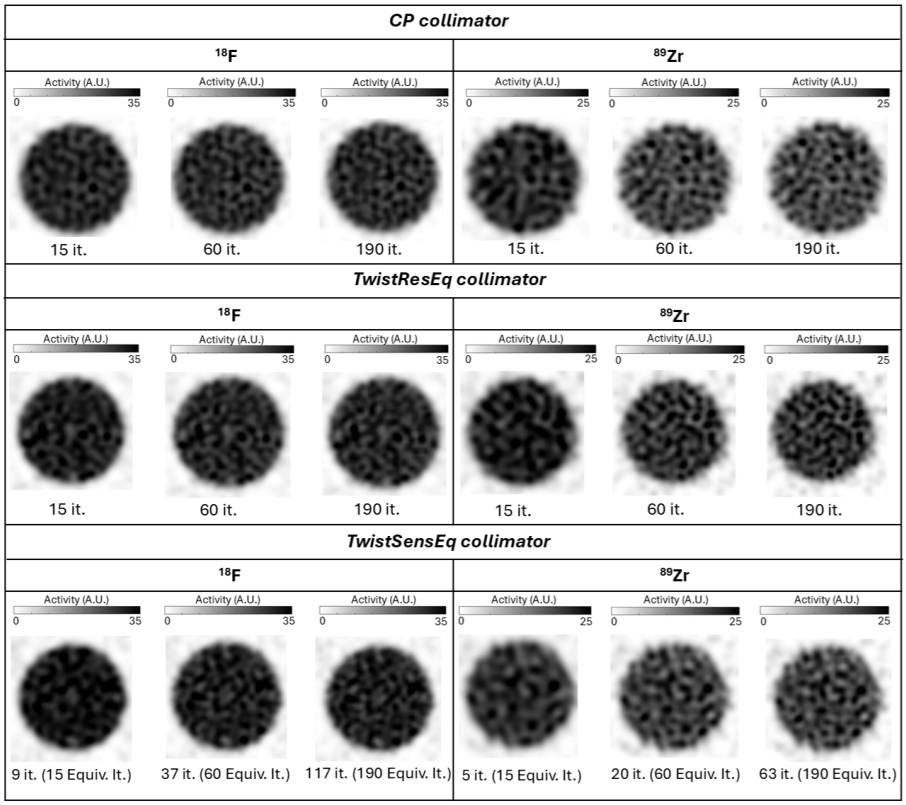

Figure 5.10: Images of the uniform phantom reconstructed using CP and TCP collimators. Based on the convergence speed analysis, images were compared at the same iteration number for collimators with matching system resolution, and at equivalent iteration numbers (Equiv. it.) for collimators with matching sensitivity. Images shown were post-filtered with a 3D Gaussian filter having a FWHM of 1 mm. The images shown were obtained by summing ten consecutive slices at the center of the phantom, resulting in a final image slice thickness of 4 mm.

These images were used to calculate the percentage image uniformity following the methodology described in the data analysis section. Results of this calculation were plotted against the equivalent number of iterations as illustrated in Fig. 5.11.

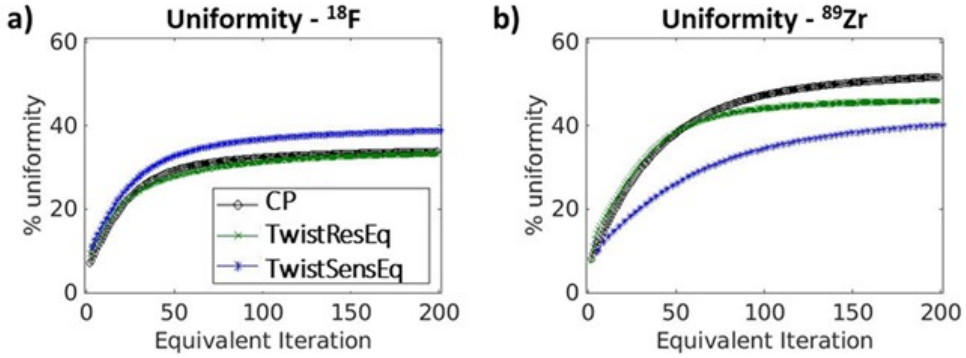

Figure 5.11: Average percentage uniformity of the collimators simulated for ^{18}F (left) and ^{89}Zr (right). Results were plotted against the equivalent number of iterations.

For ^{18}F, the TwistResEq and the CP collimator achieved similar results, while the TwistSensEq shows an 18.3% performance deficit compared to them. For ^{89}Zr, both twisted collimators converged to a more uniform result compared to the CP design, with an improvement of 10.4% for TwistResEq and of 20.1% for TwistSensEq.

5.4. Discussion

We presented the findings of a MC simulation study in which we investigated the implementation of narrower POA cones in a CP collimator with the aim to reduce pinhole edge penetration, a factor that degrades image resolution of multi-pinhole imaging systems for high-energy radionuclides. To this end, we introduced a novel pinhole arrangement for the CP collimator, wherein individual pinholes are twisted around their cluster central axis. This new design allows to reduce POAs compared to the current CP design while maintaining the same CFOV. Comparative assessments of sensitivity, image resolution and uniformity between the TCP and CP collimators were conducted for high-energy gamma imaging of ^{18}F and ^{89}Zr. Results are presented in Figs. 5.6 - 5.11 and tables 5.1 and 5.2.

The analysis of average sensitivity results over the CFOV showed that the TCP collimator achieved sensitivities of 0.37% and 0.22% respectively for ^{18}F and ^{89}Zr. These values indicate improvements of 15.6% and 29.4% over those attainable with the CP collimator at the same system resolution. For larger volumes, sensitivity at equal system resolution is still better for TCP compared to CP, but improvements are smaller. These results demonstrate that TCP designs are more focused towards the CFOV and thus have the largest benefit for focused organ or tumor imaging. Nevertheless, it should be stressed

that sensitivity alone does not determine image quality. Rather, it's the combination of sensitivity and the information content per detected photon that regulates the attainable level of image detail. In this context, the TwistResEq and TwistSensEq collimators significantly increase the fraction of direct photons reaching the detector compared to the CP collimator across all analyzed phantoms. Specifically, for the TwistResEq this fraction increased by 78.3% and 93.6% for ^{18}F and ^{89}Zr at the CFOV, by 70.7% and 87.4% when analyzing a portion of the whole-body phantom, and by 74.0% and 102.3% when considering the entire volume of the mouse-sized phantom (table 5.1). This may be advantageous since these direct photons are expected to carry more precise information about the emission locations compared to photons that penetrated the pinhole edges. However, quantitively estimating the impact of such improvement on image quality is complex. Regarding the sensitivity differences observed between the ^{18}F and ^{89}Zr simulations, these are influenced by two opposing factors. On one hand, the detector has lower sensitivity for ^{89}Zr high energy gammas. On the other hand, these gammas emitted by ^{89}Zr are more likely to penetrate the collimator material. This effect is amplified in larger phantoms, where regions outside the CFOV are covered by fewer clusters, or sometimes not covered at all. As a result, the sensitivity for ^{89}Zr in larger phantoms becomes closer to that of ^{18}F.

Results of the system resolution analysis indicate a moderate advantage for the TCP over the CP collimator (table 5.2). Matching the CP system resolution with the TwistResEq design yielded visually equal images for both activity levels of ^{18}F and ^{89}Zr except for the images obtained for the low activity ^{89}Zr distribution, where slightly better results were observed for the TwistResEq collimator, resolving 0.80 mm diameter rods compared to the 0.90 mm of CP (Fig. 5.7). Such improvement may be attributed to the increased fraction of direct photons detected by the twisted design (table 5.1). The TwistSensEq design instead outperformed the CP for both radionuclides analyzed, improving system resolution by 6.6% and 17.7% for ^{18}F and ^{89}Zr respectively. Regarding image resolution, for ^{18}F both collimators performed equally at low activity levels (Fig. 5.6) resolving 0.70 mm diameter rods, but at high activity the TwistSensEq distinguished 0.60 mm diameter rods compared to the 0.65 mm ones solved by the CP. For ^{89}Zr, the TwistSensEq discerned 0.80 mm and 0.65 mm rods at low and high activity levels, respectively, compared to the CP's 0.90 mm and 0.75 mm rods (Fig. 5.7). Resolving sectors containing small rods ($<$ 0.80 mm) filled with low activity of ^{89}Zr proved to be challenging for every collimator design tested. Overall, the TwistSensEq granted the best results for both radionuclides. Additionally, although a specific analysis of partial volume effect was not included in this work, we partially correct for it in the reconstruction through PSF modeling, and its influence can be observed in the reconstructed resolution phantom images (Figs. 5.6 and 5.7).

The CNR analysis indicated an increase in performance with the twisted designs (Fig. 5.9). For ^{18}F, CNR results obtained with the TwistSensEq design surpassed those of the CP and TwistResEq collimators at both low and high activity levels (Fig. 5.9a, 5.9b and tables A.3, A.4). Such an increase aligns with the expectations, considering the slightly improved system resolution achieved by the TwistSensEq design (table 5.2). For ^{89}Zr (Fig. 5.9c, 5.9d), the twisted designs granted moderately better CNR performance than CP across

both activity levels, with the TwistSensEq exhibiting the highest CNR values among the three collimators (tables A.3, A.4).

In the assessment of image uniformity, twisted collimators obtained slightly more uniform images for both radionuclides. Although visually inspecting the reconstructed uniform phantom images (Fig. 5.10) may not readily convey these differences, they become evident upon examination of the uniformity trend plots (Fig. 5.11). In this case the TwistResEq granted the best results, with comparable performance for ^{18}F and a 10.4% improvement for ^{89}Zr. For the TwistSensEq instead, performance resulted to be degraded of 18.3% for ^{18}F, while an improvement of 20.1% was observed for ^{89}Zr.

It is important to note that the imaging system simulated uses a 9.5 mm thick scintillator, which is not optimal for detecting the high-energy 511 keV or 909 keV prompt gammas. Previous research [107] indicated that increasing the scintillator's thickness to 19 mm or 40 mm roughly doubles or quadruples detection efficiency for 511 keV gammas (from ~12% to ~27% or ~53%). A similar improvement can be expected for 909 keV gammas. However, since our goal was to compare collimator performance, we used the most commonly available detector configuration, which typically employs 9.5 mm thick crystals, although 19 mm crystal thickness is also available.

In this work, we analyzed a 2×2 cluster, though larger clusters (e.g., 3×3) are theoretically possible. While these could provide more pinholes with narrower angles, they would increase system complexity. The higher number of pinhole projections would complicate calibration, and manufacturing may become more challenging due to the higher precision required for smaller pinholes. Therefore, in this work we focused on a 2×2 cluster, with the potential for exploring larger clusters in the future.

5.5. Conclusion

We introduced an improved arrangement of pinholes for the CP collimator, aimed at further mitigating the adverse effects of pinhole penetration in high-energy SPECT imaging. To this end, we presented a collimator characterized by clusters of 2×2 pinholes twisted around the cluster's axis, termed TCP collimator. Employing this novel collimator on a multi-pinhole preclinical scanner, we compared its performance to that of traditional CP collimators. Simulations indicate that the TCP collimator offers improved sensitivity and system resolution compared to the CP collimator. Image uniformity resulted to be equivalent for ^{18}F, while for ^{89}Zr TCP granted a noticeable improvement.

Acknowledgement

This work was financed by the research grant QUARAT: Quantitative Universal Radiotracer Tomography (TTW16885) which is financed in part by the Dutch Research Council (NWO).

Appendix

Twisting angle

$$Twisting\ angle = \frac{\delta \cdot \gamma}{\theta} \tag{A.1}$$

Here δ is the angle between the CFOV axis and the three-dimensional distance between the pinhole and the CFOV center; γ is an arbitrarily defined value expressed in degrees determining the rotation intensity, and θ is the angle between the CFOV axis and the pinhole center radius.

Matching system resolution

The system resolution was calculated as:

$$SR = \sqrt{\left(\frac{R_i}{M}\right)^2 + R_{\text{coll}}^2} \tag{A.2}$$

Here R_i indicates the detector's intrinsic spatial resolution, R_{coll} the collimator's geometric resolution, and M the magnification factor, defined as:

$$M = \frac{b}{l} \tag{A.3}$$

Here b is the average distance from the detector to the pinhole centers (~178 mm), and l the average distance from the object to the pinhole centers (~34 mm). Its value was calculated to be ~5.2 for all the designs analyzed. The term R_{coll} is dependent on the collimator's geometry according to the following equation:

$$R_{\text{coll}} = d_{\text{re}}\left(\frac{b+l}{b}\right) \tag{A.4}$$

where d_{re} is the resolution effective diameter. The parameter d_{re} can be calculated by [178, 179]:

$$d_{\text{re}} = d + \frac{\ln(2) \cdot \tan\left(\frac{\alpha}{2}\right)}{\mu} \tag{A.5}$$

Here d is the pinhole diameter and μ is the linear attenuation coefficient of the collimator material [180]. Since the collimators tested feature multiple POAs depending on their distance from the collimator's center, α used in the system resolution calculation was assumed to be their average.

Convergence speed

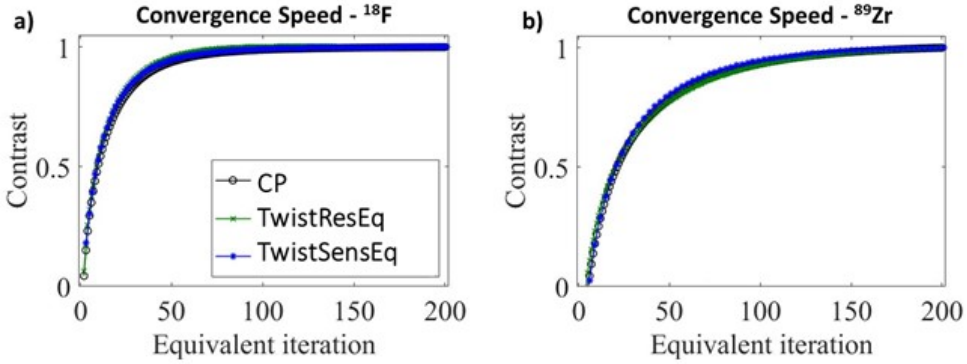

Figure A.1: Comparison of convergence speed of CP and TCP collimators. Contrast of both designs was plotted against the number of equivalent iterations. Rods of 0.65 mm and 0.70 mm diameter were considered respectively for ^{18}F (a) and ^{89}Zr (b). The equivalence factor indicates the relation between CP and TCP number of iterations. Collimator designs with equivalent system resolution converged at comparable speed, therefore no equivalence factor was required. For TwistSensEq instead, it was calculated that 1 CP iteration equates to 1.62 TwistSensEq iterations for ^{18}F (a), while for ^{89}Zr 1 CP iteration corresponds to 3.00 TwistSensEq iterations (b).

Simulation data

Phantom	^{18}***F emitted photons***	^{89}***Zr emitted photons***
Sensitivity CFOV	9.8×10^{9}	7.0×10^{9}
Sensitivity Mouse	2.2×10^{11}	1.6×10^{11}
Resolution LA	3.1×10^{12}	3.3×10^{12}
Resolution HA	4.9×10^{13}	5.2×10^{13}
Uniformity	1.3×10^{10}	9.5×10^{9}

Table A.1: Number of photons emitted from the phantoms used in our simulations.

Gaussian filtering

	^{18}F			^{89}Zr		
Collimator - Activity	***15 it. [mm]***	***60 it. [mm]***	***190 it. [mm]***	***15 it. [mm]***	***60 it. [mm]***	***190 it. [mm]***
CP - LA	0.60	0.70	0.75	0.15	0.60	0.65
CP - HA	0.45	0.70	0.75	0.15	0.55	0.65
TwistResEq - LA	0.65	0.75	0.75	0.20	0.55	0.60
TwistResEq - HA	0.45	0.70	0.70	0.15	0.65	0.70
	9 Eq. it. [mm]	***37 Eq. it. [mm]***	***117 Eq. it. [mm]***	***5 Eq. it. [mm]***	***20 Eq. it. [mm]***	***63 Eq. it. [mm]***
TwistSensEq - LA	0.70	0.75	0.80	0.15	0.60	0.65
TwistSensEq - HA	0.45	0.65	0.70	0.15	0.60	0.70

Table A.2: FWHMs in mm used for the 3D Gaussian post-filtering applied to the reconstructed images in Figures 5.6 and 5.7.

CNR data

	CNR ^{18}F			***CNR*** ^{89}Zr		
d [mm]	***CP***	***TwistResEq***	***TwistSensEq***	***CP***	***TwistResEq***	***TwistSensEq***
0.60	0.20 ± 0.13	0.48 ± 0.05	0.44 ± 0.12	0.03 ± 0.14	0.08 ± 0.10	0.04 ± 0.20
0.65	0.64 ± 0.02	0.58 ± 0.08	0.69 ± 0.08	0.06 ± 0.20	0.15 ± 0.09	0.27 ± 0.10
0.70	1.74 ± 0.16	1.55 ± 0.07	2.10 ± 0.14	0.50 ± 0.08	0.37 ± 0.13	0.69 ± 0.02
0.75	2.28 ± 0.21	2.20 ± 0.06	2.45 ± 0.22	0.48 ± 0.13	0.59 ± 0.11	0.75 ± 0.36
0.80	3.13 ± 0.21	3.63 ± 0.20	3.17 ± 0.05	0.80 ± 0.17	1.17 ± 0.19	1.36 ± 0.20
0.90	4.04 ± 0.40	4.93 ± 0.45	4.54 ± 0.54	1.69 ± 0.16	2.33 ± 0.04	2.31 ± 0.28

Table A.3: Highest CNR values and their standard deviation obtained at low activity (12 MBq/ml) by the collimator designs tested for each sector.

	CNR ^{18}F			***CNR*** ^{89}Zr		
d [mm]	***CP***	***TwistResEq***	***TwistSensEq***	***CP***	***TwistResEq***	***TwistSensEq***
0.60	1.42 ± 0.13	1.24 ± 0.07	1.62 ± 0.09	0.17 ± 0.16	0.55 ± 0.09	0.76 ± 0.13
0.65	1.82 ± 0.04	1.91 ± 0.06	2.46 ± 0.16	0.41 ± 0.04	0.77 ± 0.09	1.21 ± 0.16
0.70	4.79 ± 0.53	3.88 ± 0.10	5.14 ± 0.31	1.68 ± 0.37	1.54 ± 0.11	2.31 ± 0.24
0.75	5.48 ± 0.11	5.15 ± 0.23	5.64 ± 0.35	2.26 ± 0.78	2.30 ± 0.32	3.34 ± 0.36
0.80	6.66 ± 0.44	7.28 ± 0.18	8.23 ± 0.23	3.43 ± 0.24	4.13 ± 0.32	4.58 ± 0.25
0.90	8.89 ± 0.60	8.62 ± 0.35	9.05 ± 0.23	5.39 ± 0.61	6.26 ± 0.25	6.78 ± 0.68

Table A.4: Highest CNR values and their standard deviation obtained at high activity (190 MBq/ml) by the collimator designs tested for each sector.

6

Super-Cluster collimation for ultra-sensitive PET/SPECT: a simulation study

This chapter is adapted from: Valerio Cosmi, Satyajit Ghosh, Ruud M. Ramakers, Marlies C. Goorden, Freek J. Beekman, Super-Cluster collimation for ultra-sensitive SPECT-PET: a simulation study. *Physics in Medicine & Biology*, 2026. 71(1)

Clustered pinhole (CP) collimation currently supports sub-mm resolution imaging up to ~1 MeV, enabling SPECT of alpha and beta emitters with gamma emissions, simultaneous multi-isotope PET and PET/SPECT, and positron range-free PET. Nonetheless, increasing sensitivity in the original CP designs by enlarging pinhole diameters is limited, as the resulting pinhole opening cones would overlap.
To address this limitation, the use of Super-Cluster (SC) collimation was evaluated in a simulation study. Two SC designs were assessed: a standard configuration (SC-ST) offering a resolution-sensitivity trade-off similar to CP, and a high-sensitivity variant (SC-HS) with larger pinhole diameters to enhance sensitivity. Their performance was compared to CP collimation for ^{18}F at concentrations of 1.0 MBq/ml, 0.1 MBq/ml, 0.05 MBq/ml and ^{89}Zr at 2.0 MBq/ml, 0.2 MBq/ml, 0.1 MBq/ml, evaluating sensitivity, image resolution, recovery coefficients, and uniformity.
CP and SC-ST showed comparable sensitivity and image resolution. Both resolved ^{18}F rods of 0.9 mm, 1.4 mm, and 1.8 mm at 1.0 MBq/ml, 0.1 MBq/ml, and 0.05 MBq/ml, respectively. For ^{89}Zr, rods down to 1.0 mm and 1.6 mm were resolved at 2.0 MBq/ml and 0.2 MBq/ml, but none at 0.1 MBq/ml. Compared to CP and SC-ST, SC-HS increased sensitivity threefold for ^{18}F and twofold for ^{89}Zr. At the highest activity, SC-HS showed slightly reduced resolution for ^{18}F (1.0 mm) and similar for ^{89}Zr (1.0 mm). However, it clearly outperformed both other collimators at lower activities, resolving ^{18}F rods of 1.2 mm and 1.4 mm at 0.1 MBq/ml and 0.05 MBq/ml, respectively, and ^{89}Zr rods of 1.4 mm and 1.6 mm at 0.2 MBq/ml and 0.1 MBq/ml. Additionally, SC-HS showed superior contrast recovery. Image uniformity remained consistent across all collimators, confirming effective angular sampling.
The new SC geometry enables high-sensitivity collimation for high gamma energies, improving image quality at low activities. These results demonstrate SC collimation's strong potential for sensitivity-critical applications.

6.1. Introduction

State-of-the-art preclinical SPECT plays a pivotal role in advancing basic research and developing new diagnostic and therapeutic applications [15, 16, 181]. It provides invaluable insight into biological processes as it enables in vivo imaging and quantification of radiotracer biodistribution with spatial resolutions down to a quarter of a millimeter [28]. To achieve such high spatial resolution, these SPECT systems commonly use multi-pinhole collimators [36] combined with high image magnification to significantly reduce the impact of limited detector intrinsic resolution [35].

Although offering promising performance, earlier SPECT systems had limited applicability, as they were typically designed to operate within the gamma energy range of approximately 25–350 keV, which encompasses several commonly used radionuclides, such as ^{125}I (27–35 keV), ^{99m}Tc (140 keV), ^{111}In (171 and 245 keV), ^{201}Tl (69–83 and 167 keV), and ^{67}Ga (93–300 keV). While higher-energy emitters such as ^{131}I (364 keV) could in principle be imaged with conventional SPECT systems, the resulting image quality and resolution were generally suboptimal. In response to this limitation, over the past decade our group, in collaboration with the company MILabs B.V., has worked to

significantly extend the maximum gamma energy [48]. These efforts culminated in the development of the VECTor (Versatile Emission Computed Tomography) scanner [40], which has demonstrated sub-mm resolution for both SPECT and PET imaging at energies up to 1 MeV in experimental studies [45], and recently has been investigated through simulations for even higher energies [30]. This high-energy performance was enabled by the integration of Clustered Pinhole (CP) technology into the system [49].

The capabilities of CP collimation have sparked growing interest in imaging radionuclides with complex spectra and/or high-energy gamma emissions [42, 145, 182]. For instance, accurate determination of the biodistribution of ^{209}At, which together with ^{211}At forms a promising theranostic pair for targeted alpha therapy, has been demonstrated with high spatial and temporal resolution [43, 183]. For ^{213}Bi and ^{131}I, both important for existing and emerging therapeutic approaches, image resolutions of 0.75 mm and 0.60 mm have been achieved using their 440 keV and 364 keV gamma emissions, respectively [46, 47]. In addition to imaging therapeutic radionuclides, VECTor can also utilize prompt gamma emissions from positron-emitting nuclei, effectively eliminating blurring caused by positron range. The use of these prompt gammas resulted in image resolutions of 0.75 mm for ^{89}Zr and ^{124}I, based on their 909 keV and 603 keV emissions, respectively [45], and enabled the development of many new multi-isotope PET protocols.

While these high-resolution imaging results are promising, translating this performance to a broader range of theranostic isotopes remains challenging. Many of these isotopes are characterized by high-energy emissions and low administered activity, requiring collimators that combine effective high-energy performance with higher sensitivity than current CP designs provide to ensure high-quality images. Additionally, enhanced sensitivity reduces statistical noise and enables in vivo imaging at lower activity levels or at shorter scan times, which in turn facilitates the development of new tracers, lowers isotope costs and allows for faster dynamic imaging, making it possible to capture rapid biological processes [184].

A straightforward approach to achieve higher sensitivity is to enlarge the size of the pinhole apertures, modulating the resolution-sensitivity trade-off. In a previous work we developed and validated an ultra-high-sensitivity collimator with 2.0 mm conical pinholes that achieved a 1.3% peak sensitivity for ^{99m}Tc while maintaining sub-mm resolution [185]. However, this design was optimized for standard SPECT isotopes with typical low energy gamma emissions (< 350 keV [186, 187]) and is not suitable for higher-energy applications for which CP technology is required. Nonetheless, as we demonstrate in this work, the clustered configuration of CP introduces geometrical constraints that limit design flexibility. In particular, enlarging the pinhole diameter in this design causes significant overlap between pinhole cones, increasing the chance of unwanted collimator penetration.

To overcome this challenge and enhance sensitivity for high-energy imaging, a Super-Cluster (SC) geometry was introduced [70]. Similar to CP collimation, the SC design uses small opening-angle pinholes to reduce edge penetration. However, it samples the same central area (central field-of-view, CFOV) through a fundamentally

different pinhole arrangement. In each ring, the pinholes are arranged in a fan-like pattern with offsets between them, forming what is known as a supercluster. This results in a more uniform pinhole distribution across the collimator surface compared to the CP approach. SC collimators currently offer a range of resolution-sensitivity trade-offs, with the ultra-high sensitivity version (ultra-HS) achieving up to 17.0% sensitivity for ^{18}F when paired with a 19 mm thick scintillation crystal [61, 110].

This paper for the first time presents the underlying principles of the SC geometry [70] in detail and evaluates its performance against conventional CP collimation. To this end, a simulation approach was chosen, as it enables a controlled comparison between the two designs. Accordingly, two SC-based collimators were designed and assessed using Monte Carlo (MC) simulations. The first design, termed "*Super-Cluster Standard*," maintains the same resolution-sensitivity trade-off as CP and was developed to confirm that the SC sampling approach does not introduce artifacts. The second design, "*Super-Cluster High-Sensitivity*", demonstrates how the SC geometry can easily achieve higher sensitivity through a simple increase in pinhole diameter. Sensitivity, image resolution, recovery coefficient (RC), and uniformity were evaluated for both collimator types using two commonly employed positron-emitting radiotracers in nuclear medicine, ^{18}F [188–190] and ^{89}Zr [191–193], at different activity concentrations.

6.2. Materials and Methods

6.2.1. Imaging system

Collimators in this MC simulation study were modeled as part of a VECTor imaging system [40], which features three PMT-based large-area monolithic NaI(Tl) scintillation detectors, each measuring 590×470×9.5 mm^3, arranged in a stationary triangular layout.

Existing collimators used on this PET/SPECT system feature focusing pinhole geometries, where the pinholes sample a common CFOV, ensuring that complete data can be obtained within this region. This design enables imaging of objects or organs within the CFOV without requiring movement of the object. For larger subjects, such as whole-body animal scans, bed translation is required to grant adequate sampling. Images are then reconstructed using projection data from all bed positions belonging to one time frame simultaneously [82].

For standard pinhole collimators, data completeness within the CFOV is achieved by ensuring that each pinhole in the cylindrical collimator covers a FOV that always includes the entire CFOV. For CP, each cluster of four pinholes rather than every individual pinhole views the CFOV, as will be discussed in more detail below. For the SC collimators, an alternative sampling strategy was adopted, which is likewise detailed in the subsequent sections.

CP collimator design and geometrical constraints

The CP collimator simulated is modelled closely after the existing experimental collimator. It is constructed from a rather easily machinable tungsten alloy containing 97.0% tungsten, 1.5% nickel, and 1.5% iron (alloy density 18.5 g/cm^3) with a cylindrical shape and inner and outer radii of 24 mm and 67 mm, respectively [48]. This design's wall thickness ensures that only 0.005% of 511 keV gammas and 0.3% of 909 keV gammas can pass through the solid wall perpendicularly, with the probability decreasing at oblique angles due to the increased material thickness encountered. The effectiveness of this wall thickness for both 511 keV and 909 keV gammas has also been experimentally demonstrated [40, 45].

The pinholes are asymmetrically located within the collimator wall, with their centers at a radius of 32 mm. This setup enables significant pinhole magnification factors while still employing the thick collimator walls necessary for high-energy gamma imaging. High pinhole magnification is crucial for achieving high-resolution imaging, as it offsets the limited intrinsic resolution of the gamma detector, which is ~3.5 mm in this case. The pinholes, each measuring 0.7 mm in diameter, are organized into 48 clusters of 2 by 2 individual pinholes distributed across four rings. Of the total 192 pinholes, 162 are used for image reconstruction, while the remaining are excluded because their projections fall into the gaps between the three detectors. Each cluster is designed to sample the same FOV as a traditional pinhole, while incorporating narrower individual pinhole opening angles (POA) of 18° in the inner rings and 16° in the outer rings to reduce edge penetration effects that degrade image resolution [39, 48, 49]. These angles also ensure a good fit of the elliptical pinhole projections over the detector surface [176].

For traditional pinholes, adjusting their diameter offers a straightforward way to modulate the resolution-sensitivity trade-off. In contrast, CP offers less flexibility in this regard, as the close spacing of pinholes within each cluster limits diameter increases, since larger sizes lead to overlapping pinhole cones (Fig. 6.1a, b).

Super-Cluster collimator design

To address this limitation, the SC collimator uses an alternative geometry which will be described here. In this design, each ring comprises two sub-rings of evenly spaced pinholes (Fig. 6.1).

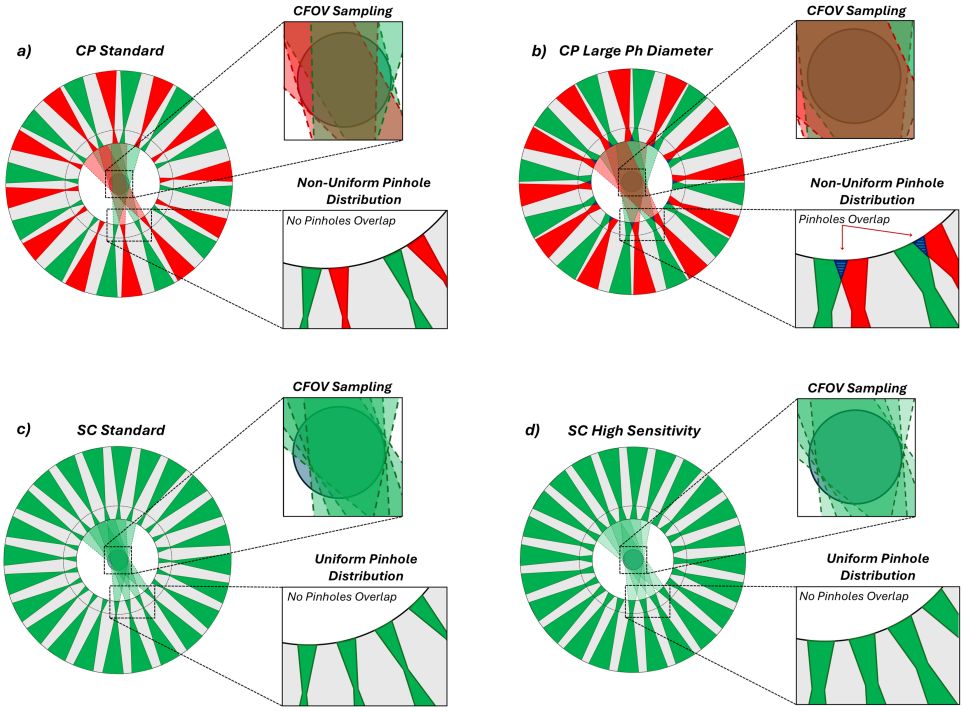

Figure 6.1: Illustration of CP (top) and SC (bottom) collimator ring geometries. Panels show the sampling of the CFOV (light blue circle) and the pinhole distributions. In CP configuration (a and b), within a ring pinholes are arranged less regularly due to the clustered design: pinholes within a cluster are closely spaced, while those from different clusters are more widely separated. This arrangement can lead to physical overlap when the pinhole diameter is increased, for example from 0.7 mm (a) to 2.0 mm (b). In contrast, the SC configuration (c and d) features a more uniform layout, with all pinholes evenly spaced. This regularity allows for an increase in pinhole diameter, in this case from 0.7 mm (c) to 2.0 mm (d), without encountering geometric constraints w.r.t. cone overlap.

As in CP design, a single pinhole cannot fully sample the CFOV due to the narrow POA. Instead, complete sampling of the elliptical CFOV is achieved by each full sub-ring, where pinholes are arranged in a fan-like pattern and collectively form a unified supercluster [70]. To enable this full coverage, each pinhole in a sub-ring is offset in the same direction and oriented to view a specific portion of the CFOV, with its sampled region illustrated by a projection cone shown as a shaded area in figure 6.1c and 6.1d. This offset configuration ensures that each projection covers a neighboring but distinct area of the CFOV. As a

result, moving counterclockwise along the sub-ring, the right-hand edge of each pinhole's coverage is progressively surpassed by that of the next, gradually expanding the overall sampled area of the CFOV. This systematic offset continues until the combined pinhole projections completely cover the CFOV. The second sub-ring follows the same principle, with its pinholes offset progressively expanding the sampled area of the CFOV when moving clockwise along the sub-ring (Fig. 6.2).

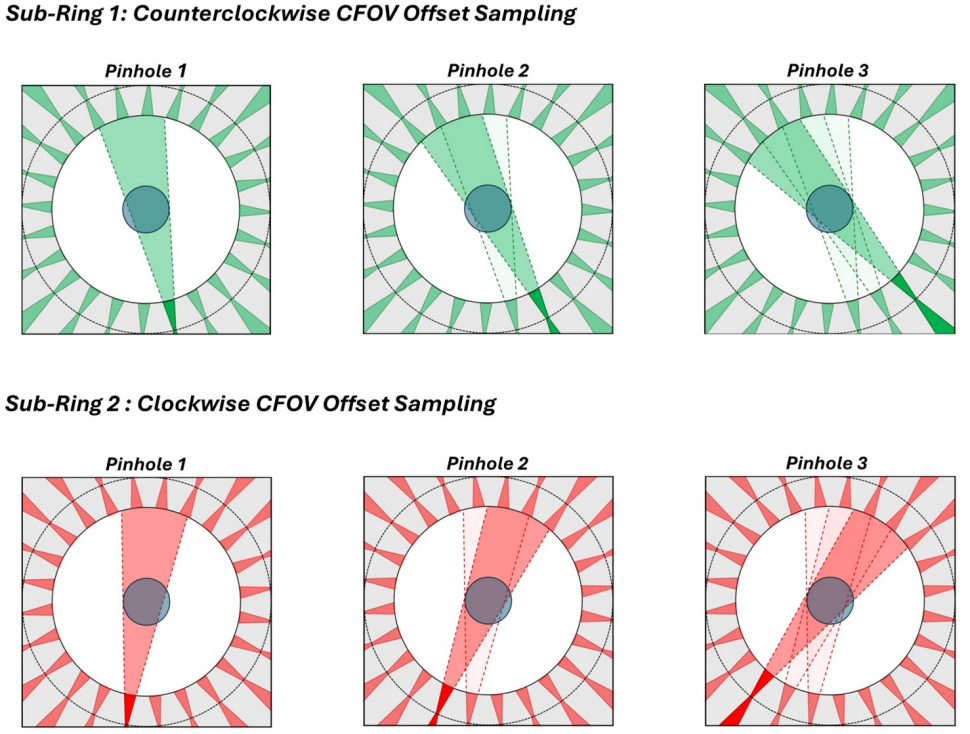

Figure 6.2: Illustration of the opposing orientation of pinholes in adjacent rings within the SC configuration. The sampling of the CFOV (light blue circle), both individually and collectively achieved by the pinholes, is shown through their shaded projection cones.

This design offers a straightforward solution to the limitations of CP collimator encountered when increasing pinhole diameter, providing a simpler and more flexible configuration with pinholes more evenly distributed across the collimator surface. Moreover, it is capable of maintaining narrow pinhole opening angles, such as those used in CP, which are necessary to minimize edge penetration effects.

Although the overall geometry differs substantially, several parameters were kept consistent with CP collimators to ensure a fair comparison and enable identical imaging studies that isolate the impact of the new design. Specifically, the material composition, CFOV size, degree of pinhole multiplexing on the detector, the inner and outer radii of the collimator, and the radius of the pinhole centers were maintained. Adjustments were

made to the number of pinholes, their opening angles and diameters, to achieve the desired performance.

Building on this controlled comparison, two distinct SC collimator designs were developed to explore different aspects of its performance. A first design, termed '*Super-Cluster Standard*' (SC-ST), was made using the same pinhole diameter and POAs as CP collimator, aiming for a similar resolution-sensitivity trade-off. This design was used to verify that the SC sampling method does not introduce artifacts compared to CP and to assess the impact of the new pinhole geometry on system performance. A second design, referred to as '*Super-Cluster High Sensitivity*' (SC-HS), was made to prioritize sensitivity by employing larger pinhole diameters than CP. To limit the associated resolution loss, the diameter was set to 2.0 mm, providing a balance between sensitivity improvement and modest degradation in resolution. This design also incorporates smaller POAs compared to CP, enabled by the larger pinhole diameter, which increases the sampled FOV. The POAs were set to the minimum values required to maintain the same sampled FOV as the CP while ensuring complete axial sampling and adequate coverage of the elliptical pinhole projections across the detector surface.

Pinhole arrangement in Super-Cluster collimator

The pinhole centers in each sub-ring were positioned midway between the centers of adjacent pinholes in neighboring sub-rings, ensuring an even distribution of pinholes both within each sub-ring and across the entire ring. The z-coordinates of the pinholes' centers were determined through an iterative process. This involved adjusting the distances between sub-rings and rings along the z-direction, while evaluating how the resulting geometric pinhole projections covered the detector surface and assessing the extent of multiplexing among them. The latter was calculated by verifying whether each detector pixel center was within a detector area covered by single or multiple pinholes projection cones.

$$\textit{Multiplexing [\%]} = 100 \times \frac{\textit{\# pixels within multiple cones}}{\textit{\# pixels with non-zero value}} \tag{6.1}$$

The values chosen for our final designs were those that, in combination with the selected POA, provided optimal detector coverage and a multiplexing as close as possible to that of the CP (29.3%).

6.2.2. Simulation setup and data acquisition process

In our study, we compared the two SC collimators to the traditional CP collimator. To perform this comparison, we generated data using MC simulations with GATE v9.0, based on Geant4 version 10.05 [83–86]. These simulations modeled gamma photon interactions with the detector while omitting the tracking of their optical transport,

including bulk and boundary processes. The behavior of gamma photons was defined through GATE's '*emstandard*' list of standard electromagnetic processes. The imaging system and phantoms were modeled using GATE primitives (i.e. cylinder, boxes and cones). An image of the resulting system model is provided in the Appendix (Fig. A.1).

The simulations were conducted assuming the imaging system was equipped with either the SC or CP collimator. The detector performance was based on manufacturer specifications, including an intrinsic spatial resolution of 3.5 mm and energy resolutions of 9.0% for 511 keV photons and 6.7% for 909 keV photons. Interaction events within the detector were simulated by introducing random variations in energy and position, sampled from Gaussian distributions with standard deviations (σ) calculated from the reported resolutions. Natural background was included in the simulation to better reflect real system behavior. A background factor per detector pixel was calculated using the manufacturer-provided background count rate (81 counts per second for ^{18}F and 63 counts per second for ^{89}Zr within the photopeak window), combined with the photopeak window width and scan duration defined in this study. This factor was used to generate Poisson-distributed natural background counts added to the data.

These simulations were utilized to measure sensitivity, as well as to generate forward projections for resolution, recovery, and uniformity phantoms which will be covered in the following sections.

Sensitivity phantom

Sensitivity was assessed by evaluating both the peak value and the CFOV-averaged value. The peak sensitivity was determined by simulating a spherical source in air (0.1 mm radius) positioned at the center of the collimator. The CFOV-averaged sensitivity was obtained using an ellipsoidal source in air matching the CFOV dimensions (12×12×9 mm^3 axes). The phantoms were filled with either ^{18}F or ^{89}Zr at concentrations of 2.0 MBq/ml and scanned for one hour.

Resolution phantom

Image resolution was evaluated using a Derenzo phantom made of PMMA, shaped as a cylinder with a diameter of 24 mm and a height of 12 mm. Given the wide range of activity concentrations analyzed and the six-sector design of a typical resolution phantom, we used two distinct versions. The first contained rods with diameters of 1.2 mm, 1.1 mm, 1.0 mm, 0.9 mm, 0.8 mm, and 0.7 mm, while the second had rods measuring 1.8 mm, 1.6 mm, 1.4 mm, 1.2 mm, 1.1 mm, and 1.0 mm (Fig. 6.3). Each rod was 8 mm in height, with a center-to-center spacing within each sector equal to twice the rod diameter. To account for the system's varying detection capabilities, the rods were filled with different concentrations of ^{18}F and ^{89}Zr. For ^{18}F, the resolution phantom with smaller rods was filled with 1.0 MBq/ml, while the phantom with larger rods used concentrations of 0.1 MBq/ml and 0.05 MBq/ml. For ^{89}Zr, the smaller-rod phantom was filled with 2.0 MBq/ml,

and the larger-rod phantom with 0.2 MBq/ml and 0.1 MBq/ml. These phantoms were scanned for one hour across nine bed positions. These positions were arranged in a 3×3 grid, with adjacent points spaced 6 mm apart in the transaxial plane, while only a single axial position was used. Considering the size of the CFOV and of the phantom, this represents a conservatively high number of bed positions. This approach was chosen to grant comprehensive sampling of the object (Fig. 6.3), ensuring that every part of the scan volume was covered by the CFOV at least once.

Calibration point source

The calibration factor is defined as the ratio of the activity concentration to the voxel value in reconstructed SPECT images [194]. For each collimator, these factors were determined by simulating a spherical point-like source with a 1.5 mm radius, filled with a known activity of ^{18}F or ^{89}Zr. The source was positioned at the collimator's center and scanned for one hour.

Recovery coefficient phantom

The recovery coefficient (RC) was evaluated using a cylindrical PMMA phantom (20 mm in diameter, 10 mm in height) containing five rods with diameters of 2.5 mm, 2.0 mm, 1.5 mm, 1.0 mm, and 0.5 mm, each 6.5 mm in height. The rods were uniformly filled with either ^{18}F at concentrations of 1.0 MBq/ml, 0.1 MBq/ml, or 0.05 MBq/ml, or with ^{89}Zr at concentrations of 2.0 MBq/ml, 0.2 MBq/ml, or 0.1 MBq/ml. This phantom design is based on the sector of the NEMA image quality phantom [195] used to assess RC. The size and activity concentration of the original NEMA phantom were adjusted to meet our goal of analyzing performance of a high-resolution preclinical SPECT system at low activity concentration levels [196]. The scan sequence comprised the same nine bed positions as for the Derenzo phantom, with a total scan duration of one hour.

Uniformity phantom

Uniformity was evaluated using a cylindrical PMMA phantom (18 mm in diameter, 10 mm in height) containing a cylindrical central cavity (14 mm in diameter, 6 mm in height) uniformly filled with either ^{18}F at concentrations of 10 MBq/ml, 1.0 MBq/ml, 0.1 MBq/ml, and 0.05 MBq/ml, or ^{89}Zr at 20 MBq/ml, 2.0 MBq/ml, 0.2 MBq/ml, and 0.1 MBq/ml. The highest activity concentrations (10 MBq/ml for ^{18}F and 20 MBq/ml for ^{89}Zr) were included to specifically assess the potential emergence of design-related artifacts under high-statistics conditions. The corresponding results are shown in the Appendix (Fig. A.3). The scan sequence included twenty-one bed position, following a spiral trajectory [88] along the phantom to ensure optimal axial sampling, with a total scan time of one hour.

6.2.3. Image reconstruction

The image reconstruction process started with defining energy acceptance windows for both the photopeak and the triple-energy window scatter correction technique [94]. A 20% energy window was centered on the 511 keV photopeak for ^{18}F and the 909 keV photopeak for ^{89}Zr. For scatter correction, two additional side windows were positioned adjacent to the photopeak, each set to 25% of the main photopeak window's width.

System matrices were created for every collimator and radionuclide evaluated in our study. We utilized a ray-tracing technique to calculate these matrices, which considers energy dependent attenuation within the collimator and detector while it ignores scatter [55]. Images were reconstructed via the dual-matrix dual-voxel (DM-DV) pixel-based similarity-regulated ordered subsets expectation maximization (SROSEM) method [92]. The DM-DV approach enhances computational efficiency by employing two voxel sizes: smaller voxels for the central region of the point spread function (PSF) and larger voxels for its slowly varying tails. The central PSF area, extending to 20% of its peak value, was modelled with 0.4 mm voxels, while the peripheral tails were modelled with 0.8 mm voxels. During backprojection, only the central portion of the PSFs was considered. This photon transport modeling was integrated with the SROSEM algorithm, which adapts the number of subsets automatically and locally, up to a maximum of 128 [90].

Post-processing consisted in applying 3D Gaussian filters with varying FWHMs, with specific values provided in the captions of the corresponding images.

6.2.4. Data analysis

Data from the sensitivity, resolution, recovery, and uniformity phantom studies were used to quantitatively evaluate the SC and CP collimators' performance.

Peak and average sensitivity were measured using data from the sensitivity phantoms and were defined as the ratio between the number of photons detected per decay and the total emissions:

$$\textit{Sensitivity [\%]} = 100 \times \frac{\textit{\# detected photons per decay}}{\textit{\# emissions}} \tag{6.2}$$

This calculation was performed by applying an energy acceptance window from 150 keV to 650 keV, based on the NEMA protocol [195]. For ^{89}Zr, a similar approach was applied, with an acceptance window ranging from 150 keV to 1100 keV. Sensitivity in cps/MBq was calculated using the emission branching ratios of ^{18}F and ^{89}Zr responsible for the detected photons (96.7% and 99.0%). A contrast-to-noise ratio (CNR) analysis was conducted on the unfiltered reconstructed images of the resolution phantom [177]. For this purpose, the images were resampled onto a fine grid, and circular regions of interest (ROIs) were positioned over the rods and the surrounding areas (Figs. 6.3 and 6.4). The ROIs had diameters equal to 90% of the corresponding rod size and were placed across

ten consecutive 0.4 mm slices of the reconstructed images. By determining the activity in each ROI, we calculated the contrast (C) in each sector (i) with the following equation:

$$C_{\text{rods},i} = \frac{\bar{h_i} - \bar{c_i}}{\bar{h_i}} \tag{6.3}$$

Here $\bar{h_i}$ and $\bar{c_i}$ are respectively the mean activity in all ROIs placed on and between the rods in sector i. Furthermore, the noise in each sector (N_i) was calculated:

$$N_{\text{rods},i} = \frac{\sqrt{\sigma_{h,i}^2 + \sigma_{c,i}^2}}{\bar{h_i} + \bar{c_i}} \tag{6.4}$$

Here $\sigma_{h,i}$ and $\sigma_{c,i}$ are respectively the standard deviation of the activity in ROIs on and in between rods. Using (6.3) and (6.4), the average CNR over five runs was calculated and plotted against the iteration number. To determine the RC values from the recovery phantom, the calibration factors (CF) for each collimator were first evaluated [197]:

$$CF\,[MBq/ml] = \frac{A}{V \cdot \sum R} \tag{6.5}$$

Here A represents the activity in MBq of the source used in the simulation, $\sum R$ is the summation of all voxel values in the reconstructed image, and V is the volume of a voxel in ml. These CFs were then applied to convert the reconstructed voxel values into activity concentrations. The RCs for the filled rods were calculated by defining ROIs with diameters equal to 90% of the corresponding rod sizes. The ratio of the estimated concentration from the reconstructed image (C_{SPECT}) within the selected ROI to the true concentration used in the simulation (C_{True}) for the corresponding rod was calculated:

$$RC\,[\%] = 100 \times \frac{C_{SPECT}}{C_{True}} \tag{6.6}$$

The average RCs for each rod was calculated over five runs for all the collimators. Image uniformity was quantitatively evaluated by calculating the percentage uniformity. Six circular ROIs with a diameter of 3.0 mm were placed at five consecutive axial positions, evenly spaced at 0.8 mm intervals, on the reconstructed unfiltered uniformity phantom images [177]. The average value within the ROIs and the standard deviation between them, $\bar{U}$ and σ_U respectively, were measured to quantify the percentage uniformity.

$$Uniformity\,[\%] = 100 \times \frac{\sigma_U}{\bar{U}} \tag{6.7}$$

For all the configurations analyzed, the average percentage uniformity was calculated over three simulation runs of the same setup.

6.3. Results

6.3.1. SC collimator designs

Two SC designs were obtained as described below.

The SC-ST features 192 0.7 mm diameter pinholes (165 used for reconstruction) arranged in four rings. The pinhole centers of the two innermost rings were at 32.2 mm for the first sub-ring and 33.7 mm for the second sub-ring from the collimator center, while for the two outermost rings they were at 36.8 mm for the first sub-ring and 41.1 mm for the second sub-ring. The POAs were 18° and 16° respectively for the two innermost, and two outermost rings.

The SC-HS design consists of 192 pinholes (159 used for reconstruction), each with a diameter of 2.0 mm, arranged in four rings. The POAs are 15° for the innermost rings and 13° for the outermost rings. In this design, the pinhole centers were positioned at 32.2 mm and 33.8 mm from the collimator center for the first and second sub-ring of the innermost rings, respectively, and at 36.6 mm and 41.7 mm for the first and second sub-ring of the outermost rings.

In terms of multiplexing, the SC-ST and SC-HS designs achieved values of 29.4% and 29.1%, respectively, which are comparable to the 29.3% achieved by the CP collimator.

6.3.2. Sensitivity comparison

Table 6.1 provides a summary of the sensitivity performance of the SC-ST and SC-HS collimators in comparison to the CP collimator.

	^{18}F		^{89}Zr	
Collimator	***Peak Sens. [cps/MBq] (%)***	***CFOV Sens. [cps/MBq] (%)***	***Peak Sens. [cps/MBq] (%)***	***CFOV Sens. [cps/MBq] (%)***
CP	$3.6*10^3$ (0.70%)	$2.8*10^3$ (0.55%)	$8.1*10^3$ (0.82%)	$7.3*10^3$ (0.74%)
SC-ST	$3.8*10^3$ (0.74%)	$3.0*10^3$ (0.58%)	$8.4*10^3$ (0.85%)	$7.5*10^3$ (0.76%)
SC-HS	$1.1*10^4$ (2.1%)	$8.8*10^3$ (1.7%)	$1.6*10^4$ (1.6%)	$1.4*10^4$ (1.4%)

Table 6.1: Peak and CFOV-averaged sensitivities for ^{18}F and ^{89}Zr using CP, SC standard (SC-ST), and SC high sensitivity (SC-HS) collimators with a thin (9.5mm) crystal. Results for ^{18}F were calculated for an energy window going from 150 keV to 650 keV, while for ^{89}Zr for an energy window going from 150 keV to 1100 keV.

For both isotopes, the results indicate comparable sensitivity between the CP and SC-ST collimators, while the SC-HS collimator provides approximately three times higher sensitivity for ^{18}F and two times higher for ^{89}Zr.

6.3.3. Image resolution comparison

Figure 6.3 shows reconstructed images of the resolution phantom with ^{18}F concentrations of 1.0 MBq/ml, 0.1 MBq/ml, and 0.05 MBq/ml, presented for various numbers of iterations.

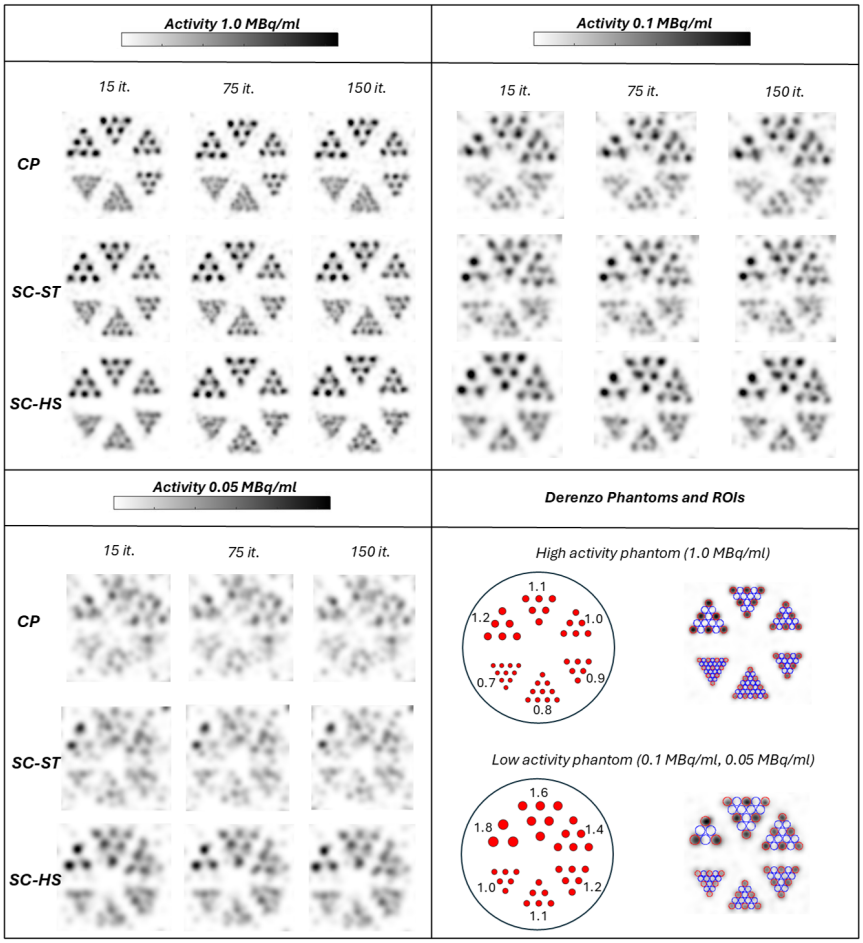

Figure 6.3: Resolution phantom images with CP and SC collimators for ^{18}F. At 1.0 MBq/ml, rods of 1.2–0.7 mm diameter were used; at lower concentrations (0.1 and 0.05 MBq/ml), rods of 1.8–1.0 mm were used. A 3D Gaussian filter was applied with FWHMs of 0.8 mm (1.0 MBq/ml), 1.2 mm (0.1 MBq/ml), and 1.4 mm (0.05 MBq/ml). Schematics of phantom designs and ROIs for CNR analysis are included. Images represent the sum of fifteen central slices, yielding a 6 mm slice thickness.

Visual inspection of the image shows that at the highest tested activity concentration (1.0 MBq/ml), both CP and SC-ST can resolve 0.9 mm rods, whereas SC-HS is limited to 1.0

mm rods. At 0.1 MBq/ml, CP and SC-ST resolve rods down to 1.4 mm, while the SC-HS reaches 1.2 mm. Finally, at 0.05 MBq/ml, CP and SC-ST struggle to resolve any sectors, whereas SC-HS can still resolve 1.6 mm rods.

Figure 6.4 shows reconstructed images of the resolution phantom with ^{89}Zr activity concentrations of 2.0 MBq/ml, 0.2 MBq/ml, and 0.1 MBq/ml, presented for various iteration numbers.

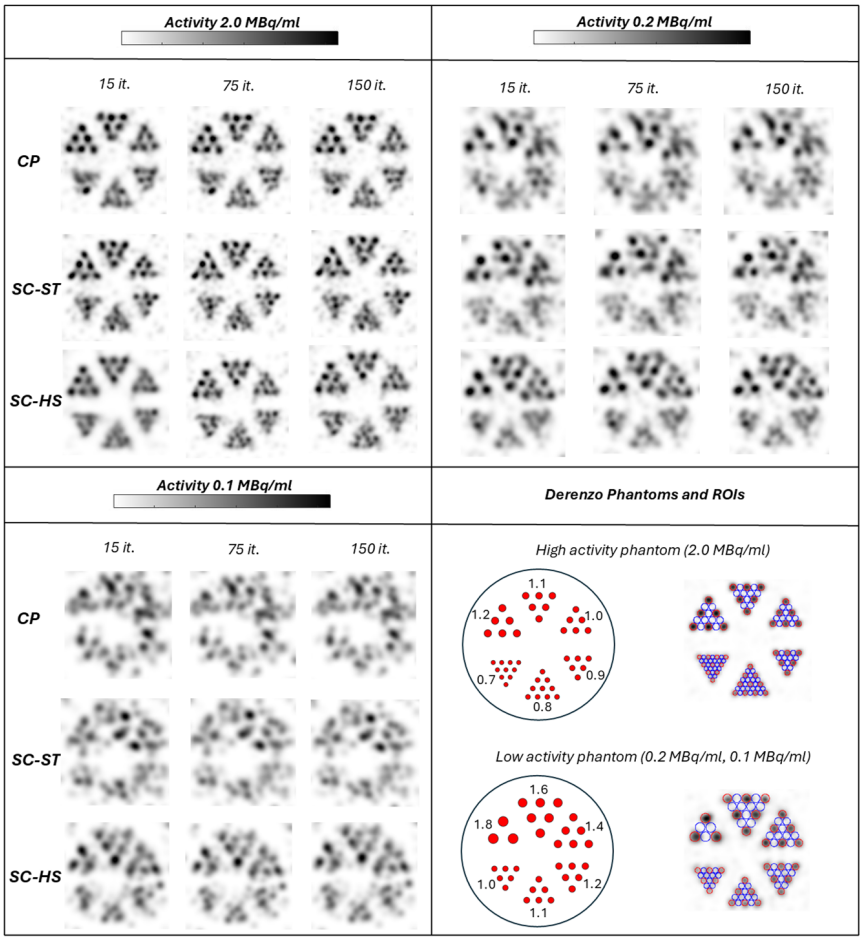

Figure 6.4: Resolution phantom images with CP and SC collimators for ^{89}Zr. At 2.0 MBq/ml, rods of 1.2–0.7 mm diameter were used; at lower concentrations (0.2 and 0.1 MBq/ml), rods of 1.8–1.0 mm were used. A 3D Gaussian filter was applied with FWHMs of 0.9 mm (2.0 MBq/ml), 1.4 mm (0.2 MBq/ml), and 1.6 mm (0.1 MBq/ml). Schematics of phantom designs and ROIs for CNR analysis are included. Images represent the sum of fifteen central slices, yielding a 6 mm slice thickness.

At the highest activity concentration tested (2.0 MBq/ml), the performance of the three collimators is comparable as all can resolve the 1.0 mm rod sector. At 0.2 MBq/ml, both the CP and SC-ST collimators can resolve the 1.8 mm rod sector, as the 1.6 mm sector exhibits missing rods. In contrast, SC-HS successfully distinguishes rods down to 1.4 mm. At 0.1 MBq/ml, all collimators encounter difficulties: no sectors are clearly discernible with CP and SC-ST, while SC-HS still allows for visible, though slightly misplaced, identification of rods in the 1.8 mm and 1.6 mm sectors.

For both isotopes and all activity concentrations, a line profile analysis through the smallest discernible rod sector is shown in the appendix (Fig. A.2).

6.3.4. CNR analysis

Beyond visual comparison, a CNR analysis was conducted on the reconstructed resolution phantom images. Figure 6.5 illustrates the average CNR values across all runs (considering all visible rod sectors), plotted against the number of iterations for each collimator.

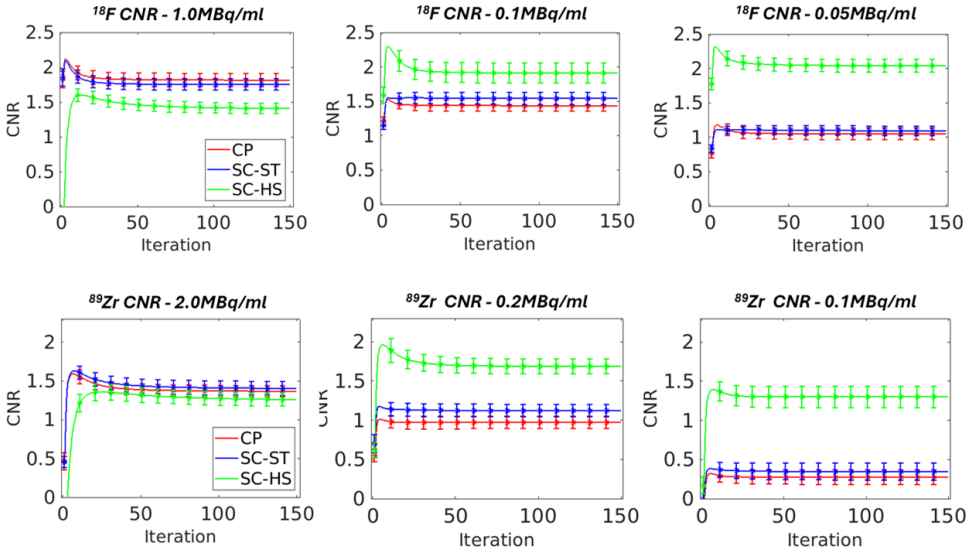

Figure 6.5: Mean CNR values for all tested collimators. Results, averaged across multiple runs and based on visible rod sectors and selected hot/cold regions, are plotted against the number of iterations. The images show CNR for rods filled with ^{18}F at activity concentrations of 1.0 MBq/ml, 0.1 MBq/ml, and 0.05 MBq/ml, as well as rods filled with ^{89}Zr at concentrations of 2.0 MBq/ml, 0.2 MBq/ml, and 0.1 MBq/ml.

For ^{18}F, at the highest activity concentration, both the CP and SC-ST collimators outperformed SC-HS by 22.1%. However, at lower activities, the SC-HS design demonstrated a significant improvement in CNR, exceeding the others by 24.0% at 0.1

MBq/ml and 85.6% at 0.05 MBq/ml. Similarly, for ^{89}Zr, the SC-HS collimator showed a moderate degradation of 10.0% at the highest activity compared to the other designs, but granted notable improvements of 33.7% at 0.2 MBq/ml and 73.1% at 0.1 MBq/ml.

6.3.5. Recovery coefficients

Images of the reconstructed recovery phantom filled with ^{18}F are shown in figure 6.6.

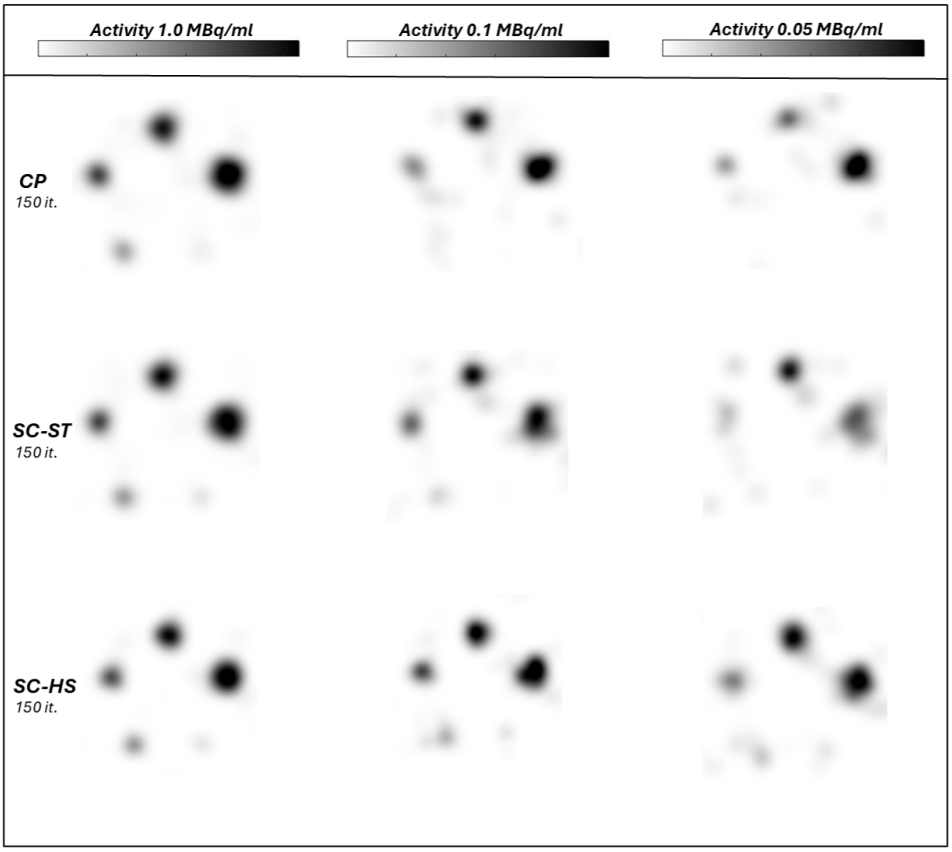

Figure 6.6: Images of the contrast recovery phantom imaged using CP, SC-ST, and SC-HS collimators. Rods were uniformly filled with 1.0 MBq/ml, 0.1 MBq/ml, and 0.05 MBq/ml of ^{18}F. Images shown were post-filtered with a 3D Gaussian filter having a FWHM of 1.25 mm. The displayed images were generated by summing fifteen consecutive slices at the phantom's center, resulting in a final slice thickness of 6 mm.

The ^{18}F RCs calculated for each rod are reported in table 6.2.

Collimator	*RC 2.5 mm*	*RC 2.0 mm*	*RC 1.5 mm*	*RC 1.0 mm*	*RC 0.5 mm*
			^{18}F — 1.0 MBq/ml		
CP	66.9 ± 4.1%	57.5 ± 2.5%	40.9 ± 1.4%	19.4 ± 0.9%	1.28 ± 0.3%
SC-ST	71.5 ± 4.0%	55.1 ± 1.5%	39.4 ± 0.4%	20.1 ± 0.7%	2.18 ± 0.4%
SC-HS	79.2 ± 1.1%	74.7 ± 2.3%	42.8 ± 1.2%	25.1 ± 0.1%	3.40 ± 0.3%
			^{18}F — 0.1 MBq/ml		
CP	67.6 ± 1.8%	46.9 ± 2.2%	25.8 ± 0.9%	3.64 ± 0.5%	$< 1.0 \times 10^{-6}$%
SC-ST	61.0 ± 0.5%	54.4 ± 2.9%	30.1 ± 0.5%	8.22 ± 0.4%	1.02 ± 0.2%
SC-HS	73.6 ± 1.6%	70.6 ± 4.6%	36.2 ± 1.8%	20.5 ± 1.6%	5.76 ± 0.5%
			^{18}F — 0.05 MBq/ml		
CP	54.3 ± 2.3%	25.5 ± 1.3%	14.9 ± 0.7%	0.121 ± 0.1%	$< 1.0 \times 10^{-36}$%
SC-ST	50.7 ± 1.1%	36.8 ± 1.1%	13.2 ± 0.7%	1.65 ± 0.6%	0.440 ± 0.2%
SC-HS	69.9 ± 2.9%	72.6 ± 2.2%	28.8 ± 1.5%	11.4 ± 1.0%	5.08 ± 0.3%

Table 6.2: Recovery coefficients (RCs), averaged over multiple runs, were calculated for all rods of the recovery phantom using both CP and SC collimators with ^{18}F. Errors represent the standard deviation across runs.

For ^{18}F, neither the CP nor the SC-ST design demonstrated clear overall superiority. Nonetheless, differences were observed at the lower activity concentrations (0.1 MBq/ml and 0.05 MBq/ml), where the CP design outperformed SC-ST for the largest rod (2.5 mm), while SC-ST yielded better results for the smaller rods. The SC-HS design consistently achieved the best overall performance, surpassing the other collimators across all rod sizes and activity concentrations. Improvements were particularly significant at the lowest activity level, where SC-HS yielded relative gains compared to CP of 28.7%, 184.7%, and 93.3% for rods between 2.5 mm and 1.5 mm. Furthermore, for the 1.0 mm and 0.5 mm rods, the SC-HS achieved RCs of 11.4% and 5.08%, whereas the CP design yielded negligible performance.

Images of the recovery phantom filled with ^{89}Zr are shown in figure 6.7.

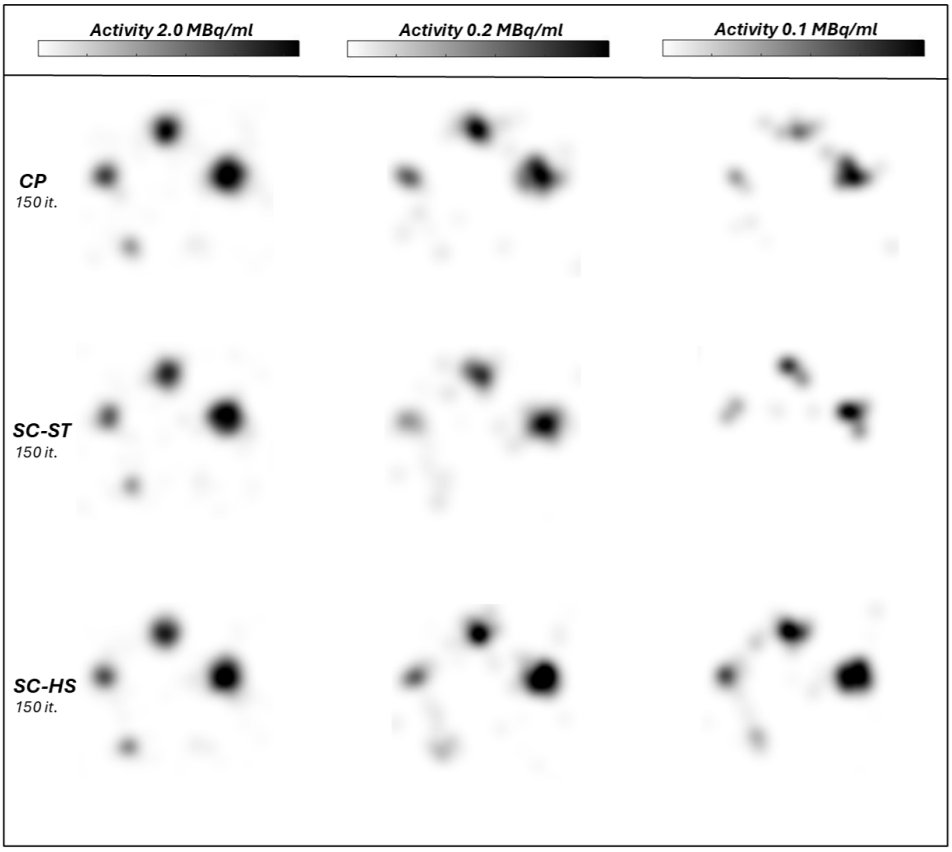

Figure 6.7: Images of the recovery phantom reconstructed using CP, SC-ST, and SC-HS collimators. Rods were uniformly filled with 2.0 MBq/ml, 0.2 MBq/ml, and 0.1 MBq/ml of ^{89}Zr. Images shown were post-filtered with a 3D Gaussian filter having a FWHM of 1.25 mm. The displayed images were generated by summing fifteen consecutive slices at the phantom's center, resulting in a final slice thickness of 6 mm.

The calculated RC coefficients for ^{89}Zr are indicated in table 6.3.

Collimator	*RC 2.5 mm*	*RC 2.0 mm*	*RC 1.5 mm*	*RC 1.0 mm*	*RC 0.5 mm*
			^{89}*Zr — 2.0 MBq/ml*		
CP	69.2 ± 3.5%	63.5 ± 2.3%	38.8 ± 1.8%	17.5 ± 0.9%	3.66 ± 0.5%
SC-ST	64.3 ± 3.5%	67.6 ± 3.0%	36.3 ± 1.3%	20.4 ± 0.7%	3.22 ± 0.4%
SC-HS	73.6 ± 0.8%	63.1 ± 1.6%	41.4 ± 1.8%	21.2 ± 0.7%	4.14 ± 0.5%
			^{89}*Zr — 0.2 MBq/ml*		
CP	61.3 ± 6.9%	49.0 ± 2.2%	28.7 ± 1.6%	3.42 ± 0.4%	$< 1.0 \times 10^{-6}$%
SC-ST	54.5 ± 3.6%	50.5 ± 3.9%	22.4 ± 0.9%	5.36 ± 0.5%	$< 1.0 \times 10^{-34}$%
SC-HS	69.4 ± 2.6%	54.9 ± 1.8%	32.0 ± 3.3%	12.5 ± 1.2%	$< 1.0 \times 10^{-10}$%
			^{89}*Zr — 0.1 MBq/ml*		
CP	37.4 ± 0.7%	22.1 ± 2.2%	13.3 ± 1.9%	$< 1.0 \times 10^{-10}$%	$< 1.0 \times 10^{-19}$%
SC-ST	46.5 ± 0.9%	28.7 ± 5.3%	10.8 ± 1.3%	$< 1.0 \times 10^{-4}$%	$< 1.0 \times 10^{-30}$%
SC-HS	63.7 ± 5.8%	46.6 ± 5.4%	26.3 ± 2.2%	8.46 ± 1.2%	$< 1.0 \times 10^{-15}$%

Table 6.3: Recovery coefficients (RC), averaged over multiple runs, were calculated for all rods of the recovery phantom using both CP and SC collimators for ^{89}Zr. Errors represent the standard deviation across runs.

For ^{89}Zr, performance at the highest activity concentration (2.0 MBq/ml) was comparable across all three collimators, with the SC-HS showing only a slight advantage over the CP design. As with ^{18}F, no clear preference could be established between the CP and SC-ST designs across the different activity concentrations. However, the SC-HS demonstrated superior overall results at lower activity concentrations. In particular, at the lowest tested activity (0.1 MBq/ml), SC-HS provided relative improvements over CP of 70.3%, 110.9%, and 100.0%. Additionally, SC-HS achieved a RC of 8.4% for the 1.0 mm rod while the other collimators could not recover any activity.

6.3.6. Image uniformity comparison

Reconstructed images of the uniformity phantom filled with ^{18}F, along with the corresponding line profile analysis, are shown in figure 6.8.

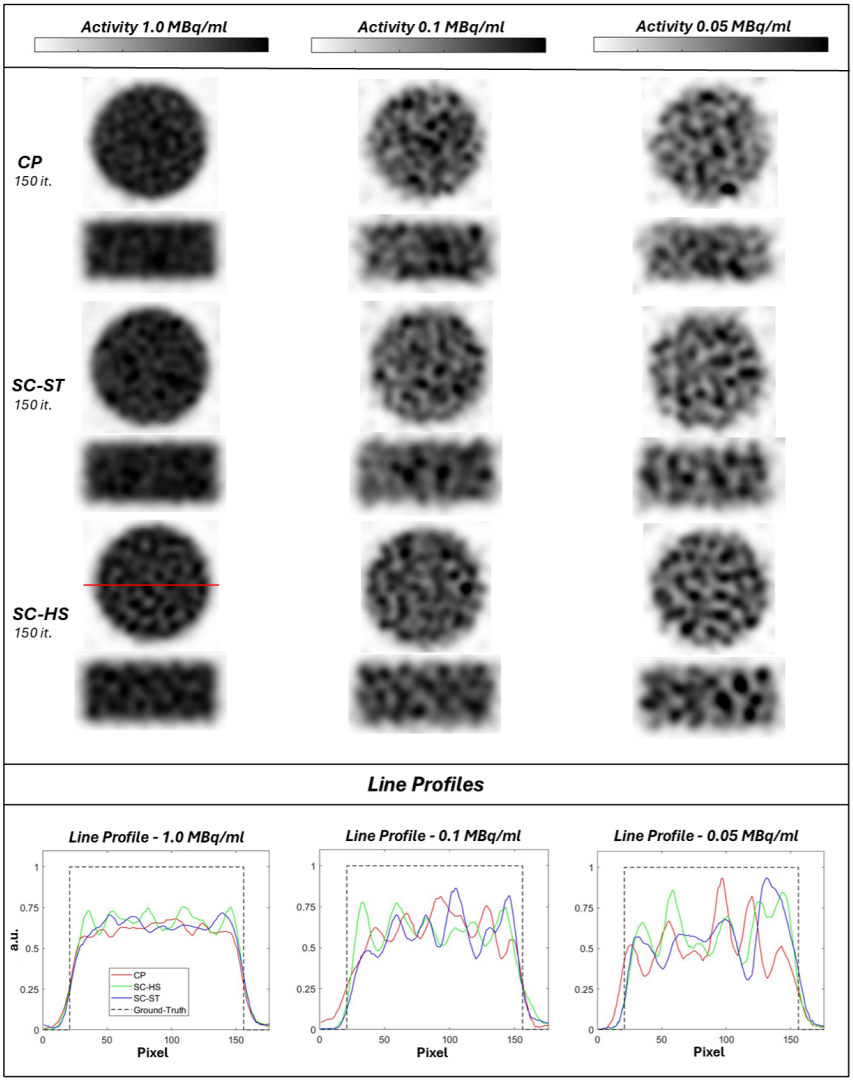

Figure 6.8: Images of the uniform phantom reconstructed using CP and SC collimators. The phantom was uniformly filled with 1.0 MBq/ml, 0.1 MBq/ml, and 0.05 MBq/ml of ^{18}F. A 3D Gaussian filter with a 1.25 mm FWHM was applied for post-filtering. The displayed images were generated by summing ten consecutive slices at the phantom's center, resulting in a final slice thickness of 4 mm. Line profiles were extracted for each configuration along the red line, which is shown only in one case for clarity.

Visual inspection of these images shows that all collimators produce comparable results, without distortions attributable to potential sampling issues.

Figure 6.9 shows the reconstructed images of the uniformity phantom filled with ^{89}Zr.

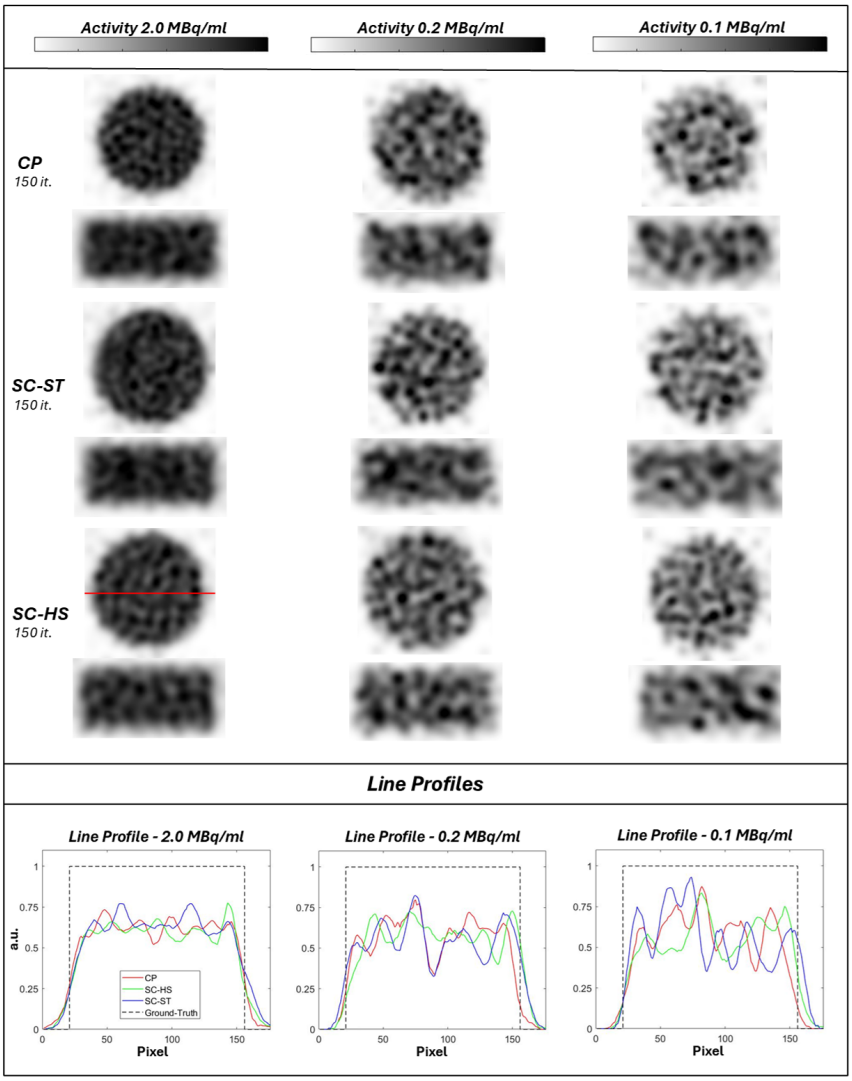

Figure 6.9: Images of the uniform phantom reconstructed using CP and SC collimators. The phantom was uniformly filled with 2.0 MBq/ml, 0.2 MBq/ml, and 0.1 MBq/ml of ^{89}Zr. A 3D Gaussian filter with a 1.25 mm FWHM was applied for post-filtering. The displayed images were generated by summing ten consecutive slices at the phantom's center, resulting in a final slice thickness of 4 mm. Line profiles were extracted for each configuration along the red line, which is shown only in one case for clarity.

All collimators demonstrate comparable performance for ^{89}Zr, with no visible artifacts suggesting sampling issues.

Results for the quantitative analysis of image uniformity are reported in the appendix, tables A.1 and A.2.

6.4. Discussion

We presented results from a MC simulation study investigating a novel supercluster geometry designed to enhance sensitivity in multi-pinhole imaging across a wide energy range (25−1000 keV). This approach aims to support SPECT and PET studies conducted at low activity concentrations and/or with short scan durations. As part of our broader investigation of collimator optimization, we previously introduced the Twisted Clustered Pinhole (TCP) design, showing that integrating narrower POAs into CP geometry could improve both spatial resolution and sensitivity [109]. However, compared to the original CP the sensitivity gains were modest (15.6% for ^{18}F and 29.4% for ^{89}Zr), and the overall complexity remained similar. Exploring a different approach, we here described the novel Super-Cluster design, featuring a simpler geometry with a more uniform distribution of pinholes across the collimator surface. This configuration provides greater flexibility in increasing pinhole diameter, reaching values not feasible with CP or TCP designs, while preserving the same CFOV. We performed comparative evaluations of sensitivity, image resolution, recovery coefficients, and uniformity between the SC and CP collimators using different activity concentrations of ^{18}F and ^{89}Zr. The results are summarized in figures 6.3–6.9 and tables 6.1–6.3.

The analysis of peak and CFOV-averaged sensitivity showed comparable sensitivities attained by the CP and SC-ST collimators (as expected by design), while the SC-HS design achieved improvements of approximately a factor of three for ^{18}F and a factor of two for ^{89}Zr compared to the CP collimator (Table 6.1) as a result of the larger pinhole diameter.

In terms of image resolution, the CP and SC-ST collimators performed similarly for both ^{18}F and ^{89}Zr (Figs. 6.3, 6.4), resolving the same rod sectors across all activity concentrations. These results indicate that the new geometry and sampling method of the SC design do not significantly affect the baseline performance of the collimator. Instead, image quality appears to be primarily governed by the resolution-sensitivity trade-off, which was identical for these two designs. By comparison, at the highest tested activity concentration, the SC-HS collimator showed slightly reduced performance with ^{18}F and comparable performance with ^{89}Zr. The reduced performance for ^{18}F is related to the expected resolution loss due to the larger pinhole diameter used in this configuration. The ^{89}Zr outcome presumably reflects a combination of two factors: lower intrinsic detector sensitivity and edge penetration effects both due to its high-energy prompt gammas. Because the SC-HS design combines the highest sensitivity with the smallest POAs among the tested designs, these effects were likely mitigated, resulting in performance comparable to that of the other collimators. At lower activity concentrations for both isotopes, the SC-HS outperformed the other collimators. These improvements

can be attributed to a favorable adjustment of the resolution-sensitivity trade-off. At these activity levels, the increased sensitivity offset the resolution loss caused by the wider pinhole opening, ultimately resulting in more accurate and detailed reconstructions.

CNR analysis (Fig. 6.5) confirmed the visual assessment from figures 6.3 and 6.4, showing mostly comparable results within the margin of error for the CP and SC-ST collimators, and highlighting the improvements achieved by the SC-HS at lower activity concentrations.

The RCs extracted from the recovery phantom (Figs. 6.6 and 6.7) demonstrate a clear performance advantage of the SC-HS collimator, which outperformed both the SC-ST and CP designs (Tables 6.2 and 6.3). This finding suggests that the increased sensitivity of the SC-HS enhances the system's ability to accurately localize the activity distribution. This improvement is likely due to the greater number of detected events, allowing the reconstruction algorithm to better differentiate between areas of true activity and regions dominated by background or noise. Such improvements are particularly relevant in quantitative studies conducted at low activity levels.

Finally, we investigated images of a uniform activity distribution with the purpose of analyzing the validity of the novel SC sampling strategy (Figs. 6.8 and 6.9). Visual inspection revealed no discernible differences among the three collimators, supporting the effectiveness of the new sampling strategy used in the SC designs. Significant data incompleteness would typically distort the shape of the uniform phantom, such as causing a convex appearance at its lateral edges, but these artifacts were not observed in the reconstructed images.

An important implication of the SC geometry is its flexibility, which permits the use of even larger pinhole diameters than those employed in the SC-HS configuration. Increasing the diameter further would enhance sensitivity and could therefore benefit studies conducted at lower activity concentrations than those presented in this work. However, such modifications may also increase multiplexing if the distance between pinholes is not increased. Higher multiplexing has been associated with reconstruction artifacts in highly multiplexed multi-pinhole systems [198]. In future work, the combination of larger pinholes with advanced de-multiplexing strategies, including approaches based on alternative pinholes with shutter devices as shown in [199] where de-multiplexing with pinholes was first presented, or more recently proposed alternative methods [200, 201], could be explored to balance these effects, allowing SC geometries to exploit higher sensitivity while mitigating the risk of image degradation. Another promising direction is the investigation of keel-edge pinholes within the SC framework. The current study focused on knife-edge pinholes to maintain consistency with the experimental imaging system. This choice was further supported by previous work comparing knife- and keel-edge geometries [202]. Nevertheless, keel-edge designs could be particularly interesting for applications where penetration is the dominant concern.

It is worth highlighting that the simulated imaging system employs a 9.5 mm thick scintillator, which is not ideal for detecting high-energy prompt gammas such as the 511 keV or 909 keV emissions. Prior studies have shown that increasing the scintillator

thickness to 19 mm or even 40 mm can approximately double or quadruple the detection efficiency for 511 keV gammas, improving it from around 12% to approximately 27% or 53%, respectively [107]. A similar enhancement is expected for 909 keV gammas. Nonetheless, to focus on comparing collimator performance, we chose MILabs' standard detector configuration, which is more commonly used in practice and typically features 9.5 mm crystals, although 19 mm options are also available from this vendor.

More broadly, this work contributes to ongoing efforts to enhance image quality. We pursued this goal by introducing a new collimator design with improved sensitivity. It is worth noting, however, that various strategies targeting different system components can be implemented to improve image quality [56–60]. Furthermore, similar improvements can be achieved by focusing on optimizing image reconstruction techniques [51–54, 203].

6.5. Conclusion

We described the SC collimator, a novel design featuring pinholes more evenly distributed across the collimator surface to enable both high-energy and high-sensitivity PET and SPECT imaging. Its performance was evaluated against that of a conventional CP collimator for which increasing the pinhole diameter is not possible due to geometric constraints. Results showed that the SC geometry introduced no imaging artifacts and enabled straightforward tuning of the resolution-sensitivity trade-off by increasing the pinhole diameter. This proved particularly advantageous at low activity concentrations of ^{18}F and ^{89}Zr, resulting in improved image quality and greater quantitative accuracy.

Acknowledgement

This work was financed by the research grant QUARAT: Quantitative Universal Radiotracer Tomography (TTW16885) which is financed in part by the Dutch Research Council (NWO).

Appendix

Simulation setup

Figure A.1 shows the system geometry as modeled in GATE.

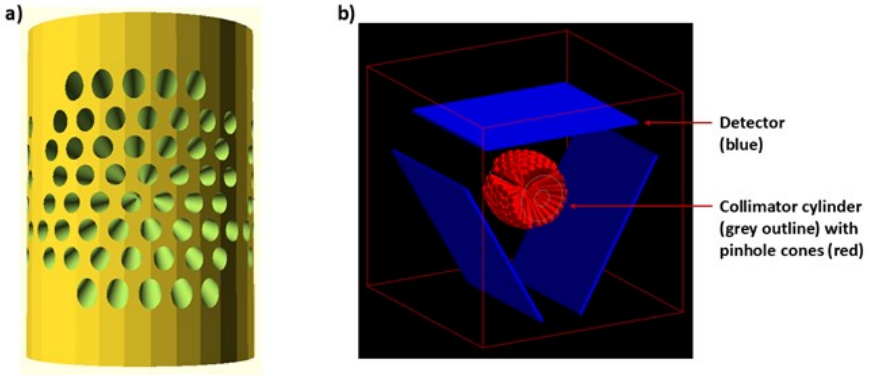

Figure A.1: Visual representation of the collimator in 3D (a) and of the system geometry as modeled in GATE (b). The blue rectangles represent the three detectors arranged in a triangular setup. The grey outlines indicate the cylindrical collimator, while the red cones depict the pinhole cones. Light guides and PMTs were not explicitly simulated; instead, their effects were incorporated by assuming an intrinsic spatial resolution and energy resolutions consistent with the manufacturer's specifications.

Profile analysis

An analysis of the profiles through the smallest distinguishable sector was conducted. The results, presented in figure A.2, support the observations from the visual inspection of figures 6.3 and 6.4 and are consistent with the CNR analysis shown in figure 6.5.

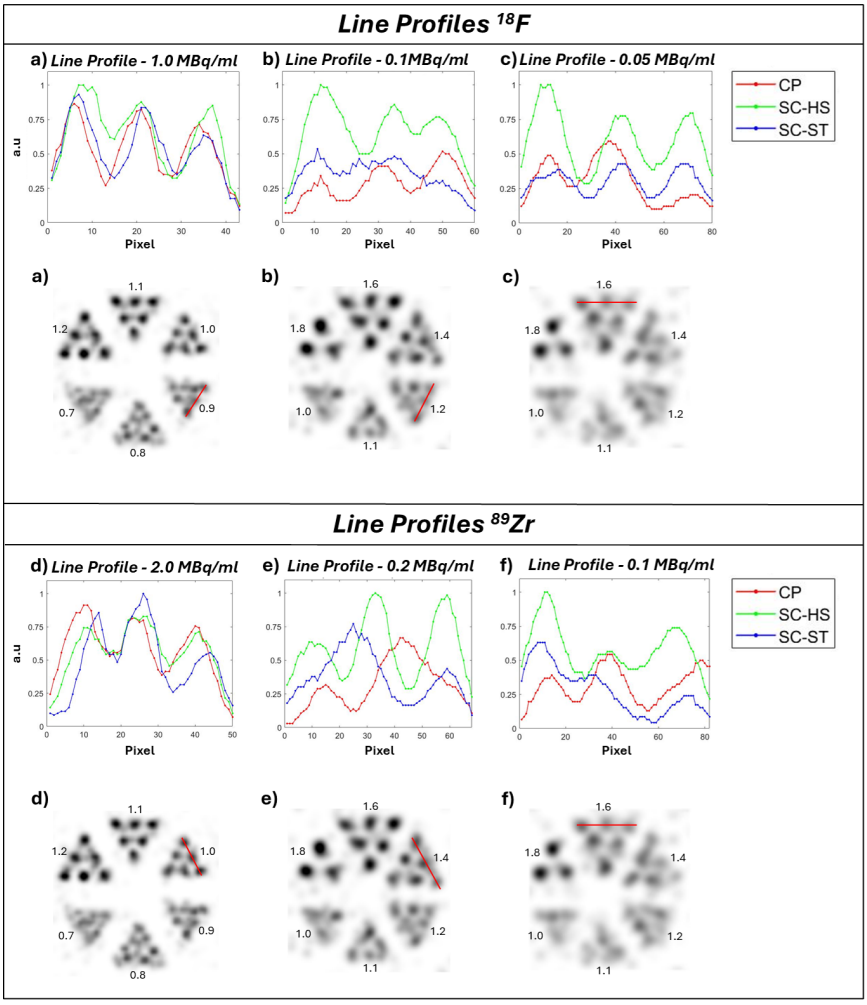

Figure A.2: Profiles obtained from resolution phantom images. The analysis was performed on images from figures 6.3 and 6.4 using the highest number of iterations. For each profile plot, the investigated rod sector corresponds to the sector marked with a red line in the resolution phantom, indicated by the same panel letter. The resolution phantom images shown were acquired using the SC-HS collimator.

Quantitative uniformity analysis

Results of the quantitative analysis of reconstructed uniformity images are reported in table A.1 for ^{18}F and A.2 for ^{89}Zr.

Collimator	*Uni. 1.0 MBq/ml [%]*	*Uni. 0.1 MBq/ml [%]*	*Uni. 0.05 MBq/ml [%]*
CP	43.2 ± 2.8	61.9 ± 6.2	86.8 ± 5.5
SC-ST	46.2 ± 4.9	68.8 ± 5.5	79.6 ± 6.7
SC-HS	43.6 ± 1.9	60.3 ± 5.8	96.6 ± 4.4

Table A.1: Results for average percentage uniformity obtained from multiple runs using CP and SC collimators for ^{18}F are presented. Reported values correspond to the final iteration (150) and include the standard deviations.

For ^{18}F, the CP and SC-ST collimators demonstrated similar performance across all three activity concentrations, with differences remaining within the margin of error. In contrast, the SC-HS collimator showed comparable performance at 1.0 MBq/ml and 0.1 MBq/ml, but exhibited a slight decline of 10.7% at 0.05 MBq/ml.

Collimator	*Uni. 2.0 MBq/ml [%]*	*Uni. 0.2 MBq/ml [%]*	*Uni. 0.1 MBq/ml [%]*
CP	56.2 ± 6.0	87.5 ± 9.2	99.2 ± 3.8
SC-ST	41.2 ± 1.8	77.4 ± 11.2	98.1 ± 6.3
SC-HS	34.4 ± 0.9	70.1 ± 5.9	87.7 ± 4.6

Table A.2: Results for average percentage uniformity obtained from multiple runs using CP and SC collimators for ^{89}Zr are presented. Reported values correspond to the final iteration (150) and include the standard deviations.

For ^{89}Zr, at the highest activity concentration, both SC-ST and SC-HS outperformed CP, with SC-HS providing an improvement of 48.1% compared to CP. At 0.2 MBq/ml, SC-HS again achieved the best performance, showing a 22.1% improvement over CP. Finally, at 0.1 MBq/ml, CP and SC-ST delivered comparable results, while SC-HS offered a moderate improvement of 12.3%.

Uniformity at high activity concentration

Image uniformity at high activity concentrations (10 MBq/ml for ^{18}F and 20 MBq/ml for ^{89}Zr) was evaluated to assess whether design-dependent artifacts emerge under such conditions. The results are presented in figure A.3.

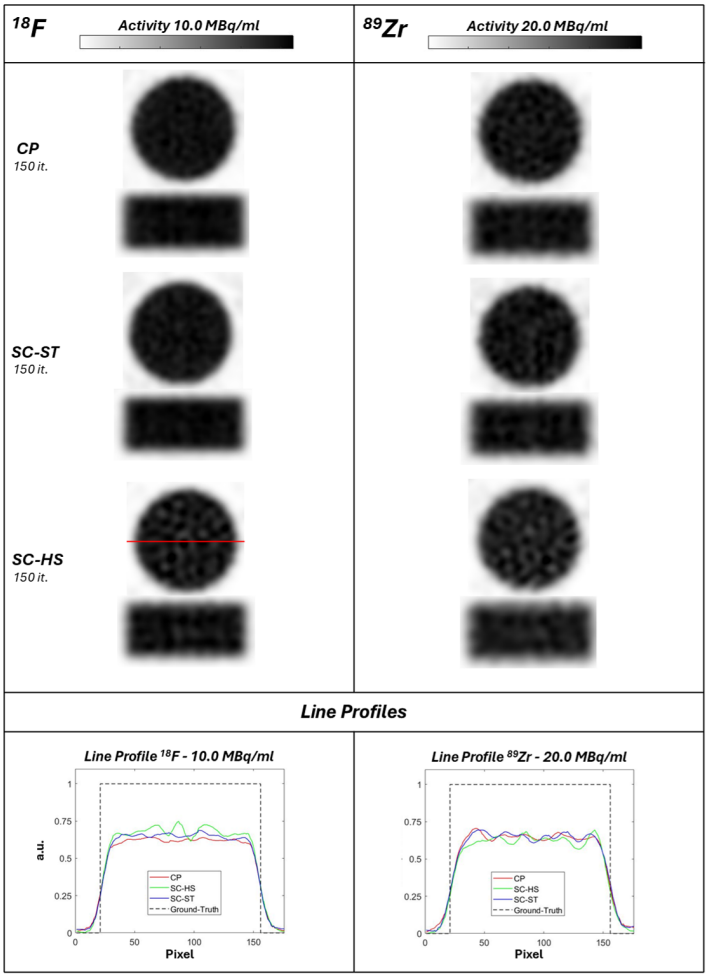

Figure A.3: Images of the uniform phantom reconstructed using CP and SC collimators. The phantom was uniformly filled with 10.0 MBq/ml of ^{18}F or 20.0 MBq/ml of ^{89}Zr, respectively. A 3D Gaussian filter with a 1.25 mm FWHM was applied for post-filtering. The displayed images were generated by summing ten consecutive slices at the phantom's center, resulting in a final slice thickness of 4 mm. Line profiles were extracted for each configuration along the red line.

The novel collimator shows no visible design-dependent artifacts under high-statistics conditions.

7

Conclusions

The optimization of an imaging system can significantly enhance its performance, particularly when tailored to a specific application. Achieving such improvements requires a comprehensive evaluation of the system, since performance depends on the complex interaction of multiple parameters rather than any single factor. To address this complexity, both software- and hardware-level strategies must be considered in concert. This thesis aims to explore such strategies to enhance the image quality of the preclinical PET/SPECT system VECTor (MILabs, B.V.), with a particular focus on high-energy imaging applications.

The image resolution and uniformity of the current system were first assessed using Monte Carlo simulations across a broad set of isotopes, featuring diverse emission spectra with extremely high gamma energies. Subsequently, within the system's existing image reconstruction workflow, various joint reconstruction techniques were applied to a selected group of isotopes to evaluate the potential of these methods to enhance image quality. Alongside this, the structure of the gamma camera constituting the system's detectors was investigated by analyzing how variations in crystal thickness, photomultiplier tube geometry, and light guide thickness influence the system's imaging performance at high energies. Finally, two distinct collimator geometries designed for high-energy imaging were introduced and their performance evaluated. The first, the Twisted Clustered Pinhole (TCP) collimator, preserves the cluster configuration of the current clustered pinhole (CP) design while incorporating narrower pinhole opening angles. The second, the Super-Cluster (SC) collimator, features a simpler layout where pinholes with large diameters and narrow opening angles are uniformly distributed across the collimator surface.

In **Chapter 2**, the feasibility of sub-mm resolution with the VECTor system using a CP collimator was evaluated across a broad set of PET isotopes, including those with high-energy prompt gammas (>1 MeV) or complex emission spectra. The study spanned prompt gamma energies from 603 keV to 2.2 MeV and included the following isotopes: ^{52}Mn (744 keV and 1.4 MeV), ^{94}Tc (703 keV), ^{89}Zr (909 keV), ^{44}Sc (1.2 MeV), ^{86}Y (1.1 MeV), ^{72}As (834 keV), ^{124}I (603 keV), ^{38}K (2.2 MeV), and ^{66}Ga (1 MeV). Conventional

preclinical PET systems struggle to image these isotopes due to long positron ranges and down scatter of prompt gammas into the 511 keV photopeak. To address this, prompt gamma emissions were used instead of annihilation photons, leveraging the capabilities of CP collimation. Resolution and uniformity phantom studies results were assessed both visually and quantitatively. Simulations demonstrated that sub-mm resolution is achievable for nearly all isotopes studied, up to an energy of 1.4 MeV. Notably, a resolution of 1.2 mm was also achieved for the highest tested energy of 2.2 MeV. These results highlight the unique potential of CP collimation for high-resolution imaging across a wide range of challenging isotopes.

Chapter 3 analyzes different joint reconstruction methods integrated into the system's current image reconstruction workflow. These techniques leverage multiple gamma emissions from the same isotope, captured in different photopeaks, to improve image quality. Three approaches were tested and compared. Single-Band Joint Reconstruction (SB-JR) sums projections from multiple energy windows and reconstructs the image using a system matrix at the average energy. Mixed Multi-Band Joint Reconstruction (mMB-JR) also sums projections but uses a system matrix that models photon transport across all photopeak energies. Multi-Band Joint Reconstruction (MB-JR) reconstructs each energy window separately, employing system matrices tailored to their specific gamma energies. The methods were evaluated through simulations using resolution phantoms filled with ^{225}Ac, ^{226}Ac, or ^{89}Zr. MB-JR consistently produced the best image quality and highest contrast-to-noise ratio (CNR) across all isotopes and activity levels. CNR gains for the smallest visible rods ranged from 30% to 65% for ^{225}Ac, 20% to 54% for ^{226}Ac, and 25% to 47% for ^{89}Zr. These results highlight the significant potential of multi-photopeak reconstruction, particularly MB-JR, to enhance image quality and quantification in SPECT, PET, and PET/SPECT of a wide range of isotopes that emit gammas with multiple energies.

Although joint reconstruction techniques have led to valuable improvements in image quality, further enhancements are still possible by optimizing specific components of the imaging system. **Chapter 4** specifically investigates how thicker scintillators can enhance photopeak sensitivity at higher energies and how this affects spatial resolution. The impact of light guide thickness, PMT geometry, and layout was examined, with all configurations benchmarked against a reference detector consisting of a 9.5 mm NaI(Tl) thick crystal and 3-inch round PMTs. Monte Carlo simulations were used to evaluate combinations of 20 mm and 40 mm NaI(Tl) thick crystals with optimized light guides and four types of PMTs: 2-inch round, 3-inch round, 2-inch square, and 3-inch square. Each configuration was assessed at 140 keV and 511 keV, representing conventional and high energies, respectively, for SPECT systems. Results showed that increasing crystal thickness can significantly enhance sensitivity (by 27% and 57% for the 20 mm and 40 mm crystals, respectively), with only modest losses in spatial resolution when using cost-effective PMTs. In contrast, smaller PMTs offer better spatial resolution but increase system cost, as more units are needed to cover a large-area detector. This study demonstrates a viable, cost-effective approach to improving sensitivity for high-energy gamma detection outside the conventional SPECT range. Additionally, it highlights how spatial resolution is influenced by variations in light guide thickness and PMT geometry.

Chapter 5 presents a new collimation technology, the twisted clustered pinhole (TCP) collimator, developed to enhance the performance of conventional CP designs through the use of narrower pinhole opening angles (POAs). To enable this, individual pinholes are rotated around the cluster's central axis, allowing the TCP to accommodate narrower POAs while preserving the same FOV coverage as the CP. In a simulation study, TCP and CP collimators were compared by adjusting TCP pinhole diameters to match either sensitivity or system resolution achieved with CP. Image resolution and uniformity were evaluated at low (12 MBq/mL) and high (190 MBq/mL) activity concentrations for both ^{18}F (511 keV) and ^{89}Zr (909 keV). At matched system resolution, the TCP collimator increased central FOV (CFOV) sensitivity by 15.6% for ^{18}F and 29.4% for ^{89}Zr compared to the CP collimator, while maintaining similar image resolution and uniformity for ^{18}F and providing moderate improvements for ^{89}Zr. When sensitivity was matched, TCP improved theoretical system resolution by 6.6% for ^{18}F and 17.7% for ^{89}Zr, resulting in better image resolution as smaller rods sector of the resolution phantom could be distinguished. These results indicate that the TCP collimator offers enhancements in both sensitivity and resolution relative to CP, suggesting its potential for improved high-energy gamma imaging.

The TCP design described in **Chapter 5**, showed that this new geometry could improve both spatial resolution and sensitivity. However, compared to the original CP the sensitivity gains were modest (15.6% for ^{18}F and 29.4% for ^{89}Zr), and the overall design complexity remained similar. Exploring a different approach, **Chapter 6** describes the Super-Cluster (SC) collimator, which offers a more straightforward design than CP and TCP while retaining their excellent performance for high-energy imaging. Its simplified geometry features a uniform pinhole distribution across the collimator surface, enabling greater design flexibility. This flexibility allows easy adjustment of the pinhole diameter to fine-tune the resolution-sensitivity trade-off, enabling diameter sizes not achievable with CP or TCP. The SC's performance was evaluated against CP using Monte Carlo simulations with ^{18}F at 1.0 MBq/mL, 0.1 MBq/mL, and 0.05 MBq/mL, and ^{89}Zr at 2.0 MBq/mL, 0.2 MBq/mL, and 0.1 MBq/mL. Results confirmed the feasibility of the SC design without introducing artifacts and demonstrated significant sensitivity improvements, by a factor three for ^{18}F and two for ^{89}Zr compared to CP. Image resolution at the highest activity was slightly reduced for ^{18}F and similar for ^{89}Zr. Importantly, the increased sensitivity was beneficial at lower activities, as the SC consistently resolved sectors with smaller-diameter rods more effectively than the CP for both ^{18}F and ^{89}Zr. The SC also achieved superior contrast recovery, with gains up to 184.7% for ^{18}F and 110.9% for ^{89}Zr at the lowest activity. Uniformity remained consistent across both designs, confirming effective angular sampling. This study highlights the SC geometry as a promising high-sensitivity collimation solution with strong potential for sensitivity-critical imaging applications, such as those associated to theranostic isotopes.

The results presented in this thesis not only provide important insights into the current capabilities of the preclinical PET/SPECT scanner VECTor, but also contribute to expanding its range of applications through the development of targeted strategies for performance improvement. In particular, we more precisely defined the upper energy limit at which the system can maintain sub-mm spatial resolution, demonstrating that

this level of performance is achievable even at photon energies up to 1.4 MeV. This highlights the system's versatility and its potential to support imaging tasks traditionally considered beyond the reach of standard preclinical SPECT systems. Alongside the characterization of system limits, software and hardware strategies were also proposed to enhance performance under challenging conditions, such as high-energy gamma emissions and low activity concentrations. These strategies proved effective and resulted in improved outcomes compared to the unmodified system. These advancements are especially valuable as they expand the range of isotopes that can be imaged with high resolution, paving the way for broader applications of PET/SPECT technologies in fundamental research and in the development of novel radiopharmaceuticals. Ultimately, these contributions support continued progress in biomedical science and translational medicine.

Future research could focus on experimentally validating the high-energy results (>1 MeV) presented in this thesis, particularly to assess whether the system's electronics can reliably handle such energy levels. Regarding the proposed collimator designs, one potential direction would be to optimize the geometry of the TCP collimator to support imaging of multiple isotopes simultaneously while maintaining high performance and ultimately manufacture and test it experimentally. For the SC collimator, it may be worthwhile to further explore its novel geometry to prioritize spatial resolution over sensitivity, for example by implementing a large number of pinholes with extremely narrow diameters. Lastly, combining the proposed hardware and software approaches, such as applying joint reconstruction techniques with the SC collimator, could reveal additional performance improvements worth investigating.

Scientific and technical contributions

- Contributed to quantifying the high-energy imaging capabilities of the preclinical PET/SPECT system VECTor, establishing the upper photon energy range over which sub-mm spatial resolution can be maintained, and demonstrating feasibility for gamma energies up to 1.4 MeV.
- Contributed to the development and evaluation of joint dual-photopeak reconstruction strategies within the existing image reconstruction framework, demonstrating their ability to improve image quality and contrast-to-noise ratio across a wide range of isotopes and activity levels.
- Investigated gamma detector optimization strategies for high-energy gamma imaging, quantifying the impact of scintillator thickness, light guide design, and photomultiplier tube geometry on sensitivity and spatial resolution, and identifying cost-effective configurations that enhance performance beyond the conventional SPECT energy range.
- Evaluated the Twisted Clustered Pinhole (TCP) collimator geometry, demonstrating how its design enables narrower opening angles while preserving field-of-view coverage, resulting in measurable improvements in sensitivity and/or spatial resolution compared to standard Clustered Pinhole designs.
- Investigated the Super-Cluster (SC) collimator concept, a simplified high-sensitivity collimation geometry that achieves substantial sensitivity gains while maintaining image quality, particularly relevant for sensitivity-limited and theranostic imaging applications.
- Provided, through simulation studies, an integrated software–hardware optimization framework for extending the applicability of preclinical pinhole PET/SPECT imaging systems to high-energy and low-count scenarios, thereby expanding the range of isotopes and applications that can be imaged with optimal performance.

Bibliography

[1] B. D. Ross and S. S. Gambhir. *Molecular Imaging: Principles and Practice*. Elsevier, 2021.

[2] M. E. Phelps, E. J. Hoffman, N. A. Mullani and M. M. Ter-Pogossian. 'Application of Annihilation Coincidence Detection to Transaxial Reconstruction Tomography'. In: *Journal of Nuclear Medicine* 16.3 (1975), pp. 210–24. URL: https://www.ncbi.nlm.nih.gov/pubmed/1113170.

[3] T. Jones and D. Townsend. 'History and Future Technical Innovation in Positron Emission Tomography'. In: *Journal of Medical Imaging* 4.1 (2017), p. 011013. DOI: 10.1117/1.JMI.4.1.011013. URL: https://www.ncbi.nlm.nih.gov/pubmed/28401173.

[4] D. E. Kuhl and R. Q. Edwards. 'Image Separation Radioisotope Scanning'. In: *Radiology* 80.4 (1963), pp. 653–662. ISSN: 0033-8419. DOI: Doi10.1148/80.4.653.

[5] R. J. Jaszczak. 'The Early Years of Single Photon Emission Computed Tomography (SPECT): an Anthology of Selected Reminiscences'. In: *Physics in Medicine and Biology* 51.13 (2006), R99–115. DOI: 10.1088/0031-9155/51/13/R07. URL: https://www.ncbi.nlm.nih.gov/pubmed/16790923.

[6] S. R. Cherry. 'Fundamentals of Positron Emission Tomography and Applications in Preclinical Drug Development'. In: *Journal of Clinical Pharmacology* 41.5 (2001), pp. 482–91. DOI: 10.1177/00912700122010357. URL: https://www.ncbi.nlm.nih.gov/pubmed/11361044.

[7] F. J. B. Brian F. Hutton Marlies C. Goorden. 'SPECT and SPECT/CT'. In: *Molecular Imaging (Second Edition)*, ed. by S. S. G. Brian D. Ross. Academic Press, 2021. Chap. 3, pp. 29–45. DOI: doi.org/10.1016/B978-0-12-816386-3.00008-9..

[8] S. P. Rowe and M. G. Pomper. 'Molecular imaging in oncology: Current impact and future directions'. In: *CA Cancer J Clin* 72.4 (2022), pp. 333–352. ISSN: 1542-4863 (Electronic) 0007-9235 (Print) 0007-9235 (Linking). DOI: 10.3322/caac.21713. URL: https://www.ncbi.nlm.nih.gov/pubmed/34902160.

[9] G. J. R. Cook and V. Goh. 'Molecular Imaging of Bone Metastases and Their Response to Therapy'. In: *Journal of Nuclear Medicine* 61.6 (2020), pp. 799–806. ISSN: 0161-5505. DOI: 10.2967/jnumed.119.234260.

[10] E. A. Osborn and F. A. Jaffer. 'The advancing clinical impact of molecular imaging in CVD'. In: *JACC Cardiovasc Imaging* 6.12 (2013), pp. 1327–41. ISSN: 1876-7591 (Electronic) 1936-878X (Print) 1876-7591 (Linking). DOI: 10.1016/j.jcmg.2013.09.014. URL: https://www.ncbi.nlm.nih.gov/pubmed/24332285.

[11] D. H. Yu, M. H. Liu, Q. H. Ding, Y. X. Wu, T. Q. Wang, L. T. Song, X. Y. Li, K. Qian, Z. Cheng, M. J. Gu and Z. Q. Li. 'Molecular Imaging-Guided Diagnosis and Treatment Integration for Brain Diseases'. In: *Biomaterials* 316 (2025). DOI: ARTN10.1016/j.biomaterials.2024.123021.

[12] J. Tan, G. Y. Zhang, J. Q. Hao, H. W. Cai, D. P. Wu, Z. X. Su, B. B. Liu and M. Wu. 'Progress in the Application of Molecular Imaging in Psychiatric Disorders'. In: *Psychoradiology* 3 (2023). DOI: ARTN10.1093/psyrad/kkad020.

[13] M. E. Thorsen, S. B. Singh, K. Rewers, T. J. Werner, A. Alavi and S. Hess. 'Molecular Imaging Techniques in the Diagnosis and Monitoring of Infectious Diseases'. In: *Current Treatment Options in Infectious Diseases* 16.3 (2024), pp. 73–88. DOI: 10.1007/s40506-024-00274-1.

[14] N. MacRitchie, M. Frleta-Gilchrist, A. Sugiyama, T. Lawton, I. B. McInnes and P. Maffia. 'Molecular Imaging of Inflammation - Current and Emerging Technologies for Diagnosis and Treatment'. In: *Pharmacology and Therapeutics* 211 (2020), p. 107550. DOI: 10.1016/j.pharmthera.2020.107550. URL: https://www.ncbi.nlm.nih.gov/pubmed/32325067.

[15] D. J. Rowland and S. R. Cherry. 'Small-animal preclinical nuclear medicine instrumentation and methodology'. In: *Semin Nucl Med* 38.3 (2008), pp. 209–22. DOI: 10.1053/j.semnuclmed.2008.01.004. URL: https://www.ncbi.nlm.nih.gov/pubmed/18396180.

[16] B. L. Franc, P. D. Acton, C. Mari and B. H. Hasegawa. 'Small-Animal SPECT and SPECT/CT: Important Tools for Preclinical Investigation'. In: *Journal of Nuclear Medicine* 49.10 (2008), pp. 1651–63. DOI: 10.2967/jnumed.108.055442. URL: https://www.ncbi.nlm.nih.gov/pubmed/18794275.

[17] P. Mukherjee, S. Roy, D. Ghosh and S. K. Nandi. 'Role of Animal Models in Biomedical Research: a Review'. In: *Laboratory Animal Research* 38.1 (2022), p. 18. DOI: 10.1186/s42826-022-00128-1. URL: https://www.ncbi.nlm.nih.gov/pubmed/35778730.

[18] M. Nguyen. 'Development of High-Resolution Ex Vivo Single-Photon and Positron Emission Tomography'. Thesis. 2021. DOI: https://doi.org/10.4233/uuid:106952cc-6ac9-4c5c-9b2b-e0d07b3bd8df.

[19] S. D. Metzler, S. Matej and J. S. Karp. 'Resolution Enhancement in PET Reconstruction Using Collimation'. In: *IEEE Transactions on Nuclear Science* 60.1 (2013), pp. 65–75. DOI: 10.1109/tns.2012.2214444. URL: https://www.ncbi.nlm.nih.gov/pubmed/23493920.

[20] J. S. Reddin, J. S. Scheuermann, D. Bharkhada, A. M. Smith, M. E. Casey, M. Conti and J. S. Karp. 'Performance Evaluation of the SiPM-based Siemens Biograph Vision PET/CT System'. In: *2018 IEEE Nuclear Science Symposium and Medical Imaging Conference Proceedings (NSS/MIC)* (2018).

[21] S. G. Chen, P. C. Hu, Y. S. Gu, H. J. Yu and H. C. Shi. 'Performance Characteristics of the Digital uMI550 PET/CT System According to the NEMA NU2-2018 Standard'. In: *EJNMMI Physics* 7.1 (2020). DOI: ARTN4310.1186/s40658-020-00315-w.

[22] R. D. Badawi, H. Shi, P. Hu, S. Chen, T. Xu, P. M. Price, Y. Ding, B. A. Spencer, L. Nardo, W. Liu, J. Bao, T. Jones, H. Li and S. R. Cherry. 'First Human Imaging Studies with the EXPLORER Total-Body PET Scanner'. In: *Journal of Nuclear Medicine* 60.3 (2019), pp. 299–303. DOI: 10.2967/jnumed.119.226498. URL: https://www.ncbi.nlm.nih.gov/pubmed/30733314.

[23] M. Ljungberg and P. H. Pretorius. 'SPECT/CT: an Update on Technological Developments and Clinical Applications'. In: *The British Journal of Radiology* 91.1081 (2018), p. 20160402. DOI: 10.1259/bjr.20160402. URL: https://www.ncbi.nlm.nih.gov/pubmed/27845567.

[24] K. Erlandsson, K. Kacperski, D. van Gramberg and B. F. Hutton. 'Performance Evaluation of D-SPECT: a Novel SPECT System for Nuclear Cardiology'. In: *Physics in Medicine and Biology* 54.9 (2009), pp. 2635–49. DOI: 10.1088/0031-9155/54/9/003. URL: https://www.ncbi.nlm.nih.gov/pubmed/19351981.

[25] V. Nuttens, G. Schramm, Y. D'Asseler and M. Koole. 'Comparison of a 3D CZT and Conventional SPECT/CT System for Quantitative Lu-177 SPECT Imaging'. In: *EJNMMI Physics* 11.1 (2024), p. 29. DOI: 10.1186/s40658-024-00627-1. URL: https://www.ncbi.nlm.nih.gov/pubmed/38499797.

[26] M. M. Alqahtani, K. P. Willowson, C. Constable, R. Fulton and P. L. Kench. 'Optimization of Tc Whole-Body SPECT/CT Image Quality: A Phantom Study'. In: *Journal of Applied Clinical Medical Physics* 23.4 (2022). DOI: ARTNe1352810.1002/acm2.13528.

[27] M. Amirrashedi, H. Zaidi and M. R. Ay. 'Advances in Preclinical PET Instrumentation'. In: *PET Clinics* 15.4 (2020), pp. 403–426. DOI: 10.1016/j.cpet.2020.06.003. URL: https://www.ncbi.nlm.nih.gov/pubmed/32768368.

[28] O. Ivashchenko, F. van der Have, J. L. Villena, H. C. Groen, R. M. Ramakers, H. H. Weinans and F. J. Beekman. 'Quarter-Millimeter-Resolution Molecular Mouse Imaging with U-SPECT(+)'. In: *Molecular Imaging* 13 (2014). DOI: 10.2310/7290.2014.00053. URL: https://www.ncbi.nlm.nih.gov/pubmed/25429783.

[29] M. P. Nguyen, R. M. Ramakers, C. Kamphuis, S. Koustoulidou, M. C. Goorden and F. J. Beekman. 'EXIRAD-3D: Fast Automated Three-Dimensional Autoradiography'. In: *Nuclear Medicine and Biology* 86-87 (2020), pp. 59–65. DOI: 10.1016/j.nucmedbio.2020.06.001. URL: https://www.ncbi.nlm.nih.gov/pubmed/32534896.

[30] S. Ghosh, V. Cosmi, R. M. Ramakers, F. J. Beekman and M. C. Goorden. 'Ultra-high Energy Spectral Prompt PET'. In: *Physics in Medicine and Biology* 70.7 (2025). DOI: 10.1088/1361-6560/adbfd7. URL: https://www.ncbi.nlm.nih.gov/pubmed/40073503.

[31] H. O. Anger. 'Use of a Gamma-Ray Pinhole Camera For in Vivo Studies.' In: *Nature* (1952). DOI: 10.1038/170200b0.

[32] H. O. Anger. 'Scintillation Camera'. In: *Review of Scientific Instruments* 29.1 (1958), pp. 27–33. DOI: 10.1063/1.1715998. URL: https://doi.org/10.1063/1.1715998.

[33] S. R. Cherry. *Physics in Nuclear Medicine*. Elsevier Inc, 2012.

[34] K. Van Audenhaege, R. Van Holen, S. Vandenberghe, C. Vanhove, S. D. Metzler and S. C. Moore. 'Review of SPECT Collimator Selection, Optimization, and Fabrication for Clinical and Preclinical Imaging'. In: *Medical Physics* 42.8 (2015), pp. 4796–813. DOI: 10.1118/1.4927061. URL: https://www.ncbi.nlm.nih.gov/pubmed/26233207.

[35] F. Beekman and F. van der Have. 'The Pinhole: Gateway to Ultra-High-Resolution Three-Dimensional Radionuclide Imaging'. In: *European Journal of Nuclear Medicine and Molecular Imaging* 34.2 (2007), pp. 151–161. DOI: 10.1007/s00259-006-0248-6.

[36] A. Wouters, K. M. Simon and J. G. Hirschberg. 'Direct Method of Decoding Multiple Images'. In: *Applied Optics* 12.8 (1973), pp. 1871–3. DOI: 10.1364/AO.12.001871. URL: https://www.ncbi.nlm.nih.gov/pubmed/20125623.

[37] e. a. Patton D D. 'FASTSPECT: A Four-Dimensional Brain Imager.' In: *Journal of Nuclear Medicine* 35 (1994).

[38] L. R. Furenlid, D. W. Wilson, Y. C. Chen, H. Kim, P. J. Pietraski, M. J. Crawford and H. H. Barrett. 'FastSPECT II: A Second-Generation High-Resolution Dynamic SPECT Imager'. In: *IEEE Transactions on Nuclear Science* 51.3 (2004), pp. 631–635. DOI: 10.1109/TNS.2004.830975. URL: https://www.ncbi.nlm.nih.gov/pubmed/20877439.

[39] F. van der Have, B. Vastenhouw, R. M. Ramakers, W. Branderhorst, J. O. Krah, C. Ji, S. G. Staelens and F. J. Beekman. 'U-SPECT-II: An Ultra-High-Resolution Device for Molecular Small-Animal Imaging'. In: *Journal of Nuclear Medicine* 50.4 (2009), pp. 599–605. DOI: 10.2967/jnumed.108.056606. URL: https://www.ncbi.nlm.nih.gov/pubmed/19289425.

[40] M. C. Goorden, F. van der Have, R. Kreuger, R. M. Ramakers, B. Vastenhouw, J. P. Burbach, J. Booij, C. F. Molthoff and F. J. Beekman. 'VECTor: a Preclinical Imaging System for Simultaneous Submillimeter SPECT and PET'. In: *Journal of Nuclear Medicine* 54.2 (2013), pp. 306–12. DOI: 10.2967/jnumed.112.109538. URL: https://www.ncbi.nlm.nih.gov/pubmed/23077113.

[41] P. L. Esquinas, C. Rodriguez-Rodriguez, T. V. F. Esposito, J. Harboe, M. Bergamo, A. Celler, K. Saatchi, V. Sossi and U. O. Hafeli. 'Dual SPECT Imaging of (111)In and (67)Ga to Simultaneously Determine in Vivo the Pharmacokinetics of Different Radiopharmaceuticals: a Quantitative Tool in Pre-Clinical Research'. In: *Physics in Medicine and Biology* 63.23 (2018), p. 235029. DOI: 10.1088/1361-6560/aaef63. URL: https://www.ncbi.nlm.nih.gov/pubmed/30520418.

[42] P. L. Esquinas, C. Rodriguez-Rodriguez, J. Carlos De La Vega, M. Bokharaei, K. Saatchi, M. Shirmohammad, U. O. Hafeli, V. Sossi and A. Celler. '(188)Re Image Performance Assessment Using Small Animal Multi-Pinhole SPECT/PET/CT System'. In: *Physica Medica* 33 (2017), pp. 26–37. DOI: 10.1016/j.ejmp.2016.11.105. URL: https://www.ncbi.nlm.nih.gov/pubmed/28007432.

[43] J. R. Crawford, A. K. H. Robertson, H. Yang, C. Rodriguez-Rodriguez, P. L. Esquinas, P. Kunz, S. Blinder, V. Sossi, P. Schaffer and T. J. Ruth. 'Evaluation of (209)At as a Theranostic Isotope for (209)At-Radiopharmaceutical Development Using High-Energy SPECT'. In: *Physics in Medicine and Biology* 63.4 (2018), p. 045025. DOI: 10.1088/1361-6560/aaaa95. URL: https://www.ncbi.nlm.nih.gov/pubmed/29466250.

[44] A. K. H. Robertson, C. F. Ramogida, C. Rodriguez-Rodriguez, S. Blinder, P. Kunz, V. Sossi and P. Schaffer. 'Multi-Isotope SPECT Imaging of the (225)Ac Decay Chain: Feasibility Studies'. In: *Physics in Medicine and Biology* 62.11 (2017), pp. 4406–4420. DOI: 10.1088/1361-6560/aa6a99. URL: https://www.ncbi.nlm.nih.gov/pubmed/28362640.

[45] F. J. Beekman, C. Kamphuis, S. Koustoulidou, R. M. Ramakers and M. C. Goorden. 'Positron Range-Free and Multi-Isotope Tomography of Positron Emitters'. In: *Physics in Medicine and Biology* 66.6 (2021), p. 065011. DOI: 10.1088/1361-6560/abe5fc. URL: https://www.ncbi.nlm.nih.gov/pubmed/33578400.

[46] F. van der Have, O. Ivashchenko, M. C. Goorden, R. M. Ramakers and F. J. Beekman. 'High-Resolution Clustered Pinhole (131)Iodine SPECT Imaging in Mice'. In: *Nuclear Medicine and Biology* 43.8 (2016), pp. 506–11. DOI: 10.1016/j.nucmedbio.2016.05.015. URL: https://www.ncbi.nlm.nih.gov/pubmed/27289328.

[47] J. de Swart, H. S. Chan, M. C. Goorden, A. Morgenstern, F. Bruchertseifer, F. J. Beekman, M. de Jong and M. W. Konijnenberg. 'Utilizing High-Energy Gamma-Photons for High-Resolution 213Bi SPECT in Mice'. In: *Journal of Nuclear Medicine* 57.3 (2016), pp. 486–92. DOI: 10.2967/jnumed.115.157685. URL: https://www.ncbi.nlm.nih.gov/pubmed/26635343.

[48] M. C. Goorden and F. J. Beekman. 'High-Resolution Tomography of Positron Emitters with Clustered Pinhole SPECT'. In: *Physics in Medicine and Biology* 55.5 (2010), pp. 1265–77. DOI: 10.1088/0031-9155/55/5/001. URL: https://www.ncbi.nlm.nih.gov/pubmed/20134086.

[49] F. J. Beekman. 'Focused Pinhole Gamma Detection Device'. US Patent 8,067,741 B2. 2011.

[50] Z. Cheng, P. Chen and J. Yan. 'A Review of State-of-the-Art Resolution Improvement Techniques in SPECT Imaging'. In: *EJNMMI Physics* 12.1 (2025), p. 9. DOI: 10.1186/s40658-025-00724-9. URL: https://www.ncbi.nlm.nih.gov/pubmed/39883257.

[51] S. Y. Chun, J. A. Fessler and Y. K. Dewaraja. 'Correction for Collimator-Detector Response in SPECT Using Point Spread Function Template'. In: *IEEE Transactions on Medical Imaging* 32.2 (2013), pp. 295–305. DOI: 10.1109/TMI.2012.2225441. URL: https://www.ncbi.nlm.nih.gov/pubmed/23086521.

[52] H. Marquis, D. Deidda, A. Gillman, K. P. Willowson, Y. Gholami, T. Hioki, E. Eslick, K. Thielemans and D. L. Bailey. 'Theranostic SPECT Reconstruction for Improved Resolution: Application to Radionuclide Therapy Dosimetry'. In: *EJNMMI Physics* 8.1 (2021), p. 16. DOI: 10.1186/s40658-021-00362-x. URL: https://www.ncbi.nlm.nih.gov/pubmed/33598750.

[53] M. M. A. Dietze, W. Branderhorst, B. Kunnen, M. A. Viergever and H. de Jong. 'Accelerated SPECT Image Reconstruction with FBP and an Image Enhancement Convolutional Neural Network'. In: *EJNMMI Physics* 6.1 (2019), p. 14. DOI: 10.1186/s40658-019-0252-0. URL: https://www.ncbi.nlm.nih.gov/pubmed/31359208.

[54] W. Q. Ao, W. B. Li and J. L. Qian. 'A Data And Knowledge Driven Approach For SPECT Using Convolutional Neural Networks And Iterative Algorithms'. In: *Journal of Inverse and Ill-Posed Problems* 29.4 (2021), pp. 543–555. DOI: 10.1515/jiip-2020-0056.

[55] M. C. Goorden, J. van Roosmalen, F. van der Have and F. J. Beekman. 'Optimizing Modelling in Iterative Image Reconstruction for Preclinical Pinhole PET'. In: *Physics in Medicine and Biology* 61.10 (2016), pp. 3712–33. DOI: 10.1088/0031-9155/61/10/3712. URL: https://www.ncbi.nlm.nih.gov/pubmed/27082049.

[56] K. Deprez, R. Van Holen and S. Vandenberghe. 'A High Resolution SPECT Detector Based on Thin Continuous LYSO'. In: *Physics in Medicine and Biology* 59.1 (2014), pp. 153–71. DOI: 10.1088/0031-9155/59/1/153. URL: https://www.ncbi.nlm.nih.gov/pubmed/24334315.

[57] Q. Y. Wei, T. Y. Ma, N. M. Jiang, T. P. Xu, Z. L. Lyu, Y. L. Hu and Y. Q. Liu. 'A Side-by-Side LYSO/GAGG Phoswich Detector Aiming for SPECT Imaging'. In: *Nuclear Instruments and Methods in Physics Research Section a-Accelerators Spectrometers Detectors and Associated Equipment* 953 (2020). DOI: ARTN10.1016/j.nima.2019.163242.

[58] R. Massari, A. D'Elia and A. Soluri. 'A new High-Resolution Imaging System (HiRIS2) Detector for Preclinical SPECT Imaging'. In: *Nuclear Instruments and Methods in Physics Research Section a-Accelerators Spectrometers Detectors and Associated Equipment* 917 (2019), pp. 25–30. DOI: 10.1016/j.nima.2018.11.095.

[59] S. Abbaspour, B. Mahmoudian and J. P. Islamian. 'Cadmium Telluride Semiconductor Detector for Improved Spatial and Energy Resolution Radioisotopic Imaging'. In: *World Journal of Nuclear Medicine* 16.2 (2017), pp. 101–107. DOI: 10.4103/1450-1147.203079.

[60] T. Y. Ma, T. P. Xu, H. Liu, Q. Y. Wei, F. Peng, Z. Deng, G. H. Gong, H. Gong, S. Wang and Y. Q. Liu. 'Development of a SiPM Based Preclinical PET SPECT Imaging System'. In: *Journal of Nuclear Medicine* 58 (2017).

[61] MILabs. *VECTor Collimators Datasheet*. Report. MILabs B.V., 2024.

[62] G. Crisan, N. S. Moldovean-Cioroianu, D. G. Timaru, G. Andries, C. Cainap and V. Chis. 'Radiopharmaceuticals for PET and SPECT Imaging: A Literature Review over the Last Decade'. In: *International Journal of Molecular Sciences* 23.9 (2022). DOI: 10.3390/ijms23095023. URL: https://www.ncbi.nlm.nih.gov/pubmed/35563414.

[63] C. S. Levin and E. J. Hoffman. 'Calculation of Positron Range and its Effect on the Fundamental Limit of Positron Emission Tomography System Spatial Resolution'. In: *Physics in Medicine and Biology* 44.3 (1999), pp. 781–99. DOI: 10.1088/0031-9155/44/3/019. URL: https://www.ncbi.nlm.nih.gov/pubmed/10211810.

[64] M. Lubberink and H. Herzog. 'Quantitative Imaging of 124I and 86Y with PET'. In: *European Journal of Nuclear Medicine and Molecular Imaging* 38.1 (2011), S10–8. DOI: 10.1007/s00259-011-1768-2. URL: https://www.ncbi.nlm.nih.gov/pubmed/21484385.

[65] N. Anizan, T. Carlier, C. Hindorf, J. Barbet and M. Bardies. 'Acquisition Setting Optimization and Quantitative Imaging for 124I Studies with the Inveon MicroPET-CT System'. In: *EJNMMI Research* 2 (2012), p. 7. DOI: 10.1186/2191-219X-2-7. URL: https://www.ncbi.nlm.nih.gov/pubmed/22330760.

[66] F. Rosar, H. Bohnenberger, E. S. Moon, F. Rosch, A. Denig, D. Vincenz-Zorner, M. A. Hoffmann, F. Khreish, S. Ezziddin, M. Schreckenberger, H. G. Buchholz and A. Schaefer-Schuler. 'Impact of Prompt Gamma Emission of (44)Sc on Quantification in Preclinical and Clinical PET Systems'. In: *Applied Radiation and Isotopes* 170 (2021), p. 109599. DOI: 10.1016/j.apradiso.2021.109599. URL: https://www.ncbi.nlm.nih.gov/pubmed/33515928.

[67] M. Lubberink, H. Schneider, M. Bergstrom and H. Lundqvist. 'Quantitative Imaging and Correction for Cascade Gamma Radiation of 76Br with 2D and 3D PET'. In: *Physics in Medicine and Biology* 47.19 (2002), pp. 3519–34. DOI: 10.1088/0031-9155/47/19/306. URL: https://www.ncbi.nlm.nih.gov/pubmed/12408479.

[68] S. Walrand, F. Jamar, I. Mathieu, J. De Camps, M. Lonneux, M. Sibomana, D. Labar, C. Michel and S. Pauwels. 'Quantitation in PET Using Isotopes Emitting Prompt Single Gammas: Application to Yttrium-86'. In: *European Journal of Nuclear Medicine and Molecular Imaging* 30.3 (2003), pp. 354–61. DOI: 10.1007/s00259-002-1068-y. URL: https://www.ncbi.nlm.nih.gov/pubmed/12634962.

[69] M. Conti and L. Eriksson. 'Physics of Pure and Non-Pure Positron Emitters for PET: a Review and a Discussion'. In: *EJNMMI Physics* 3.1 (2016), p. 8. DOI: 10.1186/s40658-016-0144-5. URL: https://www.ncbi.nlm.nih.gov/pubmed/27271304.

[70] F. J. Beekman. 'A SPECT Scanner and Collimator'. US Patent 0133246 A1. 2022.

[71] A. W. J. M. Glaudemans, E. F. J. de Vries, F. Galli, R. A. J. O. Dierckx, R. H. J. A. Slart and A. Signore. 'The Use of F-FDG-PET/CT for Diagnosis and Treatment Monitoring of Inflammatory and Infectious Diseases'. In: *Clinical and Developmental Immunology* (2013). DOI: Artn10.1155/2013/623036.

[72] S. A. Graves, R. Hernandez, J. Fonslet, C. G. England, H. F. Valdovinos, P. A. Ellison, T. E. Barnhart, D. R. Elema, C. P. Theuer, W. Cai, R. J. Nickles and G. W. Severin. 'Novel Preparation Methods of (52)Mn for ImmunoPET Imaging'. In: *Bioconjugate Chemistry* 26.10 (2015), pp. 2118–24. DOI: 10.1021/acs.bioconjchem.5b00414. URL: https://www.ncbi.nlm.nih.gov/pubmed/26317429.

[73] G. J. Topping, P. Schaffer, C. Hoehr, T. J. Ruth and V. Sossi. 'Manganese-52 Positron Emission Tomography Tracer Characterization and Initial Results in Phantoms and in Vivo'. In: *Medical Physics* 40.4 (2013), p. 042502. DOI: 10.1118/1.4793756. URL: https://www.ncbi.nlm.nih.gov/pubmed/23556918.

[74] D. N. Pandya, N. B. Bhatt, F. Almaguel, S. Rideout-Danner, H. D. Gage, K. K. S. Sai and T. J. Wadas. 'Zr-Chloride Can Be Used for Immuno-PET Radiochemistry Without Loss of Antigen Reactivity In Vivo'. In: *Journal of Nuclear Medicine* 60.5 (2019), pp. 696–701. DOI: 10.2967/jnumed.118.216457.

[75] E. Eppard, A. de la Fuente, M. Benesova, A. Khawar, R. A. Bundschuh, F. C. Gartner, B. Kreppel, K. Kopka, M. Essler and F. Rosch. 'Clinical Translation and First In-Human Use of [(44)Sc]Sc-PSMA-617 for PET Imaging of Metastasized Castrate-Resistant Prostate Cancer'. In: *Theranostics* 7.18 (2017), pp. 4359–4369. DOI: 10.7150/thno.20586. URL: https://www.ncbi.nlm.nih.gov/pubmed/29158832.

[76] F. Rosch, H. Herzog, C. Plag, B. Neumaier, U. Braun, H. W. Muller-Gartner and G. Stocklin. 'Radiation Doses of Yttrium-90 Citrate and Yttrium-90 EDTMP as Determined via Analogous Yttrium-86 Complexes and Positron Emission Tomography'. In: *European Journal of Nuclear Medicine* 23.8 (1996), pp. 958–66. DOI: 10.1007/BF01084371. URL: https://www.ncbi.nlm.nih.gov/pubmed/8753686.

[77] M. Jennewein, M. A. Lewis, D. Zhao, E. Tsyganov, N. Slavine, J. He, L. Watkins, V. D. Kodibagkar, S. O'Kelly, P. Kulkarni, P. P. Antich, A. Hermanne, F. Rosch, R. P. Mason and P. E. Thorpe. 'Vascular Imaging of Solid Tumors in Rats with a Radioactive Arsenic-Labeled Antibody that Binds Exposed Phosphatidylserine'. In: *Clinical Cancer Research* 14.5 (2008), pp. 1377–85. DOI: 10.1158/1078-0432.CCR-07-1516. URL: https://www.ncbi.nlm.nih.gov/pubmed/18316558.

[78] W. Jentzen, L. Freudenberg, E. G. Eising, W. Sonnenschein, J. Knust and A. Bockisch. 'Optimized 124I PET Dosimetry Protocol for Radioiodine Therapy of Differentiated Thyroid Cancer'. In: *Journal of Nuclear Medicine* 49.6 (2008), pp. 1017–23. DOI: 10.2967/jnumed.107.047159. URL: https://www.ncbi.nlm.nih.gov/pubmed/18483099.

[79] D. Duboc, A. Kahan, B. Maziere, C. Loc'h, C. Crouzel, C. J. Menkes, B. Amor, G. Strauch, F. Guerin and A. Syrota. 'The Effect of Nifedipine on Myocardial Perfusion and Metabolism in Systemic Sclerosis. A Positron Emission Tomographic Study'. In: *Arthritis and Rheumatology* 34.2 (1991), pp. 198–203. DOI: 10.1002/art.1780340211. URL: https://www.ncbi.nlm.nih.gov/pubmed/1994918.

[80] S. S. Rinne, A. Abouzayed, K. Gagnon, V. Tolmachev and A. Orlova. '(66)Ga-PET-Imaging of GRPR-Expression in Prostate Cancer: Production and Characterization of [(66)Ga]Ga-NOTA-PEG(2)-RM26'. In: *Scientific Reports* 11.1 (2021), p. 3631. DOI: 10.1038/s41598-021-82995-7. URL: https://www.ncbi.nlm.nih.gov/pubmed/33574368.

[81] H. K. Tuy. 'An Inversion-Formula for Cone-Beam Reconstruction'. In: *SIAM Journal on Applied Mathematics* 43.3 (1983), pp. 546–552. ISSN: 0036-1399. DOI: Doi10.1137/0143035.

[82] B. Vastenhouw and F. Beekman. 'Submillimeter Total-Body Murine Imaging with U-SPECT-I'. In: *Journal of Nuclear Medicine* 48.3 (2007), pp. 487–93. URL: https://www.ncbi.nlm.nih.gov/pubmed/17332628.

[83] S. Jan, G. Santin, D. Strul, S. Staelens, K. Assie, D. Autret, S. Avner, R. Barbier, M. Bardies, P. M. Bloomfield, D. Brasse, V. Breton, P. Bruyndonckx, I. Buvat, A. F. Chatziioannou, Y. Choi, Y. H. Chung, C. Comtat, D. Donnarieix, L. Ferrer, S. J. Glick, C. J. Groiselle, D. Guez, P. F. Honore, S. Kerhoas-Cavata, A. S. Kirov, V. Kohli, M. Koole, M. Krieguer, D. J. van der Laan, F. Lamare, G. Largeron, C. Lartizien, D. Lazaro, M. C. Maas, L. Maigne, F. Mayet, F. Melot, C. Merheb, E. Pennacchio, J. Perez, U. Pietrzyk, F. R. Rannou, M. Rey, D. R. Schaart, C. R. Schmidtlein, L. Simon, T. Y. Song, J. M. Vieira, D. Visvikis, R. Van de Walle, E. Wieers and C. Morel. 'GATE: a Simulation Toolkit for PET and SPECT'. In: *Physics in Medicine and Biology* 49.19 (2004), pp. 4543–61. DOI: 10.1088/0031-9155/49/19/007. URL: https://www.ncbi.nlm.nih.gov/pubmed/15552416.

[84] D. Sarrut, N. Arbor, T. Baudier, D. Borys, A. Etxebeste, H. Fuchs, J. Gajewski, L. Grevillot, S. Jan, G. C. Kagadis, H. G. Kang, A. Kirov, O. Kochebina, W. Krzemien, A. Lomax, P. Papadimitroulas, C. Pommranz, E. Roncali, A. Rucinski, C. Winterhalter and L. Maigne. 'The OpenGATE Ecosystem for Monte Carlo Simulation in Medical Physics'. In: *Physics in Medicine and Biology* 67.18 (2022). DOI: 10.1088/1361-6560/ac8c83. URL: https://doi.org/10.1088/1361-6560/ac8c83.

[85] D. Sarrut, M. Bała, M. Bardiès, J. Bert, M. Chauvin, K. Chatzipapas, M. Dupont, A. Etxebeste, L. M Fanchon, S. Jan, G. Kayal, A. S Kirov, P. Kowalski, W. Krzemien, J. Labour, M. Lenz, G. Loudos, B. Mehadji, L. Ménard, C. Morel, P. Papadimitroulas, M. Rafecas, J. Salvadori, D. Seiter, M. Stockhoff, E. Testa, C. Trigila, U. Pietrzyk, S. Vandenberghe, M.-A. Verdier, D. Visvikis, K. Ziemons, M. Zvolský and E. Roncali. 'Advanced Monte Carlo Simulations of Emission Tomography Imaging Systems with GATE'. In: *Physics in Medicine and Biology* 66.10 (2021). DOI: 10.1088/1361-6560/abf276. URL: https://doi.org/10.1088/1361-6560/abf276.

[86] S. Agostinelli *et al.* 'GEANT4-a Simulation Toolkit'. In: *Nuclear Instruments and Methods in Physics Research Section a-Accelerators Spectrometers Detectors and Associated Equipment* 506.3 (2003), pp. 250–303. DOI: 10.1016/S0168-9002(03)01368-8.

[87] P. Sibczynski, A. Broslawski, A. Gojska, V. Kiptily, S. Korolczuk, R. Kwiatkowski, S. Mianowski, M. Moszynski, J. Rzadkiewicz, L. Swiderski, A. Szydlowski and I. Zychor. 'Characterization of Some Modern Scintillators Recommended for Use on Large Fusion Facilities in Gamma-Ray Spectroscopy and Tomographic Measurements of Gamma-Emission Profiles'. In: *Nukleonika* 62.3 (2017), pp. 223–228. DOI: 10.1515/nuka-2017-0032.

[88] P. E. Vaissier, M. C. Goorden, B. Vastenhouw, F. van der Have, R. M. Ramakers and F. J. Beekman. 'Fast Spiral SPECT with Stationary Gamma-Cameras and Focusing Pinholes'. In: *Journal of Nuclear Medicine* 53.8 (2012), pp. 1292–9. DOI: 10.2967/jnumed.111.101899. URL: https://www.ncbi.nlm.nih.gov/pubmed/22707346.

[89] C. Kamphuis, F. J. Beekman, P. P. van Rijk and M. A. Viergever. 'Dual Matrix Ordered Subsets Reconstruction for Accelerated 3D Scatter Compensation in Single-Photon Emission Tomography'. In: *European Journal of Nuclear Medicine* 25.1 (1998), pp. 8–18. DOI: 10.1007/s002590050188. URL: https://www.ncbi.nlm.nih.gov/pubmed/9396869.

[90] P. E. Vaissier, F. J. Beekman and M. C. Goorden. 'Similarity-Regulation of OS-EM for Accelerated SPECT Reconstruction'. In: *Physics in Medicine and Biology* 61.11 (2016), pp. 4300–15. DOI: 10.1088/0031-9155/61/11/4300. URL: https://www.ncbi.nlm.nih.gov/pubmed/27206135.

[91] W. Branderhorst, B. Vastenhouw and F. J. Beekman. 'Pixel-Based Subsets for Rapid Multi-Pinhole SPECT Reconstruction'. In: *Physics in Medicine and Biology* 55.7 (2010), pp. 2023–34. DOI: 10.1088/0031-9155/55/7/015. URL: https://www.ncbi.nlm.nih.gov/pubmed/20299722.

[92] M. C. Goorden, C. Kamphuis, R. M. Ramakers and F. J. Beekman. 'Accelerated Image Reconstruction by a Combined Dual-Matrix Dual-Voxel Approach'. In: *Physics in Medicine and Biology* 65.10 (2020), p. 105014. DOI: 10.1088/1361-6560/ab82e9. URL: https://www.ncbi.nlm.nih.gov/pubmed/32208374.

[93] M. C. Goorden, F. van der Have, R. Kreuger and F. J. Beekman. 'An Efficient Simulator for Pinhole Imaging of PET Isotopes'. In: *Physics in Medicine and Biology* 56.6 (2011), pp. 1617–34. DOI: 10.1088/0031-9155/56/6/007. URL: https://www.ncbi.nlm.nih.gov/pubmed/21335647.

[94] K. Ogawa, Y. Harata, T. Ichihara, A. Kubo and S. Hashimoto. 'A Practical Method for Position-Dependent Compton-Scatter Correction in Single Photon Emission CT'. In: *IEEE Transactions on Medical Imaging* 10.3 (1991), pp. 408–12. DOI: 10.1109/42.97591. URL: https://www.ncbi.nlm.nih.gov/pubmed/18222843.

[95] C. E. Metz. 'Radiological Imaging - the Theory of Image-Formation, Detection, and Processing, Vol 2 - Barrett,H, Swindell,W'. In: *Applied Optics* 22.12 (1983).

[96] Z. H. Cho, J. K. Chan, L. Ericksson, M. Singh, S. Graham, N. S. Macdonald and Y. Yano. 'Positron Ranges Obtained from Biomedically Important Positron-Emitting Radionuclides'. In: *Journal of Nuclear Medicine* 16.12 (1975), pp. 1174–1176.

[97] S. Derenzo. 'Precision Measurement of Annihilation Point Spread Distributions for Medically Important Positron Emitters'. In: *Conference on Positron Annihilation* (Jan. 1979).

[98] J. Cal-Gonzalez, J. L. Herraiz, S. Espana, P. M. Corzo, J. J. Vaquero, M. Desco and J. M. Udias. 'Positron Range Estimations with PeneloPET'. In: *Physics in Medicine and Biology* 58.15 (2013), pp. 5127–52. DOI: 10.1088/0031-9155/58/15/5127. URL: https://www.ncbi.nlm.nih.gov/pubmed/23835700.

[99] C. Le Loirec and C. Champion. 'Track Structure Simulation for Positron Emitters of Medical Interest. Part I: The Case of the Allowed Decay Isotopes'. In: *Nuclear Instruments and Methods in Physics Research Section a-Accelerators Spectrometers Detectors and Associated Equipment* 582.2 (2007), pp. 644–653. DOI: 10.1016/j.nima.2007.08.159.

[100] C. Le Loirec and C. Champion. 'Track Structure Simulation for Positron Emitters of Physical Interest. Part II: The Case of the Radiometals'. In: *Nuclear Instruments and Methods in Physics Research Section a-Accelerators Spectrometers Detectors and Associated Equipment* 582.2 (2007), pp. 654–664. DOI: 10.1016/j.nima.2007.08.179.

[101] C. Le Loirec and C. Champion. 'Track Structure Simulation for Positron Emitters of Physical Interest. Part III: The Case of the Non-Standard Radionuclides'. In: *Nuclear Instruments and Methods in Physics Research Section a-Accelerators Spectrometers Detectors and Associated Equipment* 582.2 (2007), pp. 665–672. DOI: 10.1016/j.nima.2007.08.234.

[102] J. Cal-González, M. Pérez-Liva, J. L. Herraiz, J. J. Vaquero, M. Desco and J. M. Udías. 'Tissue-Dependent and Spatially-Variant Positron Range Correction in 3D PET'. In: *IEEE Transactions on Medical Imaging* 34.11 (2015), pp. 2394–2403. DOI: 10.1109/Tmi.2015.2436711.

[103] J. Li and K. F. Koral. 'Nature of Ringing Artifacts in SPECT Reconstruction and Their Reduction by the Use of Side Information'. In: *2007 4th IEEE International Symposium on Biomedical Imaging : Macro to Nano, Vols 1-3* (2007), pp. 181–+. DOI: Doi10.1109/Isbi.2007.356818.

[104] A. Rahmim, J. Y. Qi and V. Sossi. 'Resolution Modeling in PET Imaging: Theory, Practice, Benefits, and Pitfalls'. In: *Medical Physics* 40.6 (2013). DOI: Artn06430110.1118/1.4800806.

[105] S. Tong, A. M. Alessio, K. Thielemans, C. Stearns, S. Ross and P. E. Kinahan. 'Properties and Mitigation of Edge Artifacts in PSF-Based PET Reconstruction'. In: *IEEE Transactions on Nuclear Science* 58.5 (2011), pp. 2264–2275. DOI: 10.1109/Tns.2011.2164579.

[106] R. Laforest, D. J. Rowland and M. J. Welch. 'MicroPET Imaging with Nonconventional Isotopes'. In: *IEEE Transactions on Nuclear Science* 49.5 (2002), pp. 2119–2126. DOI: 10.1109/Tns.2002.803685.

[107] V. Cosmi, B. Wang, M. C. Goorden and F. J. Beekman. 'NaI Gamma Camera Performance for High Energies: Effects of Crystal Thickness, Photomultiplier Tube Geometry and Light Guide Thickness'. In: *Medical Physics* 51.7 (2024), pp. 4696–4708. DOI: 10.1002/mp.17043. URL: https://www.ncbi.nlm.nih.gov/pubmed/38569052.

[108] J. L. Villena, G. Tapias, E. Lage, R. Kreuger and F. J. Beekman. 'Evaluation of a 25-511keV List Mode Readout System for a Large Field-of-View Gamma Camera'. In: *2010 IEEE Nuclear Science Symposium Conference Record (Nss/Mic)* (2010), pp. 2168–2173.

[109] V. Cosmi, M. Kvassheim, S. Ghosh, F. J. Beekman and M. C. Goorden. 'Twisted Clustered Pinhole Collimation for Improved High-Energy Preclinical SPECT/PET'. In: *Physics in Medicine and Biology* 69.22 (2024). DOI: 10.1088/1361-6560/ad8c97. URL: https://www.ncbi.nlm.nih.gov/pubmed/39533753.

[110] M. P. Nguyen, B. Oostenrijk, C. Kamphuis and F. J. Beekman. 'Ultra-High Sensitivity Simultaneous Small Animal PET-SPECT for MicroCi Range Imaging'. In: *Journal of Nuclear Medicine* 63 (2022), pp. 2344–2344.

[111] J. Ouyang, G. El Fakhri and S. C. Moore. 'Fast Monte Carlo Based Joint Iterative Reconstruction for Simultaneous Tc/I SPECT Imaging'. In: *Medical Physics* 34.8 (2007), pp. 3263–3272. DOI: 10.1118/1.2756601.

[112] S. E. Derenzo. 'Mathematical Removal of Positron Range Blurring in High-Resolution Tomography'. In: *IEEE Transactions on Nuclear Science* 33.1 (1986), pp. 565–569. DOI: Doi10.1109/Tns.1986.4337166.

[113] W. Heitler. *The Quantum Theory of Radiation*. Vol. 5. International Series of Monographs on Physics. Oxford: Oxford University Press, 1936.

[114] C. Champion and C. Le Loirec. 'Positron Follow-up in Liquid Water: II. Spatial and Energetic Study for the Most Important Radioisotopes Used in PET'. In: *Physics in Medicine and Biology* 52.22 (2007), pp. 6605–6625. DOI: 10.1088/0031-9155/52/22/004.

[115] P. Castellaz, A. Siegle and H. Stoll. 'Positron Age-Momentum-Correlation (AMOC) Measurements on Organic Liquids'. In: *Journal of Nuclear and Radiochemical Sciences* 3 (Jan. 2002). DOI: 10.14494/jnrs2000.3.2_R1.

[116] E. Abuelhia, K. Kacperski and N. M. Spyrou. 'Three-Photon Annihilation in PET: 2D Imaging Experiments'. In: *Journal of Radioanalytical and Nuclear Chemistry* 271.2 (2007), pp. 489–495. DOI: 10.1007/s10967-007-0235-9.

[117] G. Ravizzini, W. Erwin, L. De Palatis, L. Martiniova, V. Subbiah, V. Paolillo, J. Mitchell, A. P. McCoy, J. Gonzalez and O. Mawlawi. 'Dosimetry of a Novel Indium-Labeled Anti-P-Cadherin Monoclonal Antibody (FF-21101) in Non-Human Primates'. In: *Cancers* 15.18 (2023). DOI: ARTN10.3390/cancers15184532.

[118] S. P. Rowe, E. Vicente, N. Anizan, H. Wang, J. P. Leal, M. A. Lodge, E. C. Frey and R. L. Wahl. 'Repeatability of Radiotracer Uptake in Normal Abdominal Organs with In-Pentetreotide Quantitative SPECT/CT'. In: *Journal of Nuclear Medicine* 56.7 (2015), pp. 985–988. DOI: 10.2967/jnumed.115.155358.

[119] F. S. Liu, S. Y. Wang, Y. C. Shiau and Y. W. Wu. 'The Clinical Value and Safety of ECG-Gated Dipyridamole Myocardial Perfusion Imaging in Patients with Aortic Stenosis'. In: *Scientific Reports* 9 (2019). DOI: ARTN1244310.1038/s41598-019-48901-y.

[120] T. Dey, B. E. Backus, R. L. Romijn, H. Wieczorek and J. F. Verzijlbergen. 'Low-Dose Single Acquisition Rest Tc/Stress Tl Myocardial Perfusion SPECT Protocol: Phantom Studies and Clinical Validation'. In: *European Journal of Nuclear Medicine and Molecular Imaging* 41.3 (2014), pp. 536–547. DOI: 10.1007/s00259-013-2551-3.

[121] V. J. Kelly, S. T. Wu, V. Gottumukkala, R. Coelho, K. Palmer, S. Nair, T. Erick, R. Puri, O. Ilovich and P. Mukherjee. 'Preclinical Evaluation of an In/Ac Theranostic Targeting Transformed MUC1 for Triple Negative Breast Cancer'. In: *Theranostics* 10.15 (2020), pp. 6946–6958. DOI: 10.7150/thno.38236.

[122] A. Ingham, L. Wharton, H. Koniar, H. Merkens, S. Mcneil, S. Sekar, M. Osooly, C. Rodríguez-Rodríguez, F. Bénard, P. Schaffer and H. Yang. 'Preclinical evaluation of [Ac]Ac-crown-TATE - An Alpha-Emitting Radiopharmaceutical for Neuroendocrine Tumors'. In: *Nuclear Medicine and Biology* 138-139 (2024). DOI: ARTN10.1016/j.nucmedbio.2024.108944.

[123] J. R. Nedrow, A. Josefsson, S. Park, T. Bäck, R. F. Hobbs, C. Brayton, F. Bruchertseifer, A. Morgenstern and G. Sgouros. 'Pharmacokinetics, Microscale Distribution, and Dosimetry of Alpha-Emitter-Labeled Anti-PD-L1 Antibodies in an Immune Competent Transgenic Breast Cancer Model'. In: *EJNMMI Research* 7 (2017). DOI: ARTN5710.1186/s13550-017-0303-2.

[124] Y. Qin, S. Imobersteg, A. Blanc, S. Frank, R. Schibli, M. P. Béhé and M. Grzmil. 'Evaluation of Actinium-225 Labeled Minigastrin Analogue [Ac]Ac-DOTA-PP-F11N for Targeted Alpha Particle Therapy'. In: *Pharmaceutics* 12.11 (2020). DOI: ARTN108810.3390/pharmaceutics12111088.

[125] C. Meyer, V. Prasad, A. Stuparu, P. Kletting, G. Glatting, J. Miksch, C. Solbach, K. Lueckerath, L. Nyiranshuti, S. J. Zhu, J. Czernin, A. J. Beer, R. Slavik, J. Calais and M. Dahlbom. 'Comparison of PSMA-TO-1 and PSMA-617 Labeled with Gallium-68, Lutetium-177 and Actinium-225'. In: *EJNMMI Research* 12.1 (2022). DOI: ARTN6510.1186/s13550-022-00935-6.

[126] S. M. Cheal, M. R. McDevitt, B. H. Santich, M. Patel, G. B. Yang, E. K. Fung, D. R. Veach, M. Bell, A. Ahad, D. B. Vargas, B. Punzalan, N. V. K. Pillarsetty, H. Xu, H. F. Guo, S. Monette, A. O. Michel, A. Piersigilli, D. A. Scheinberg, O. Ouerfelli, N. K. V. Cheung and S. M. Larson. 'Alpha Radioimmunotherapy Using Ac-proteus-DOTA for Solid Tumors - Safety at Curative Doses'. In: *Theranostics* 10.25 (2020), pp. 11359–11375. DOI: 10.7150/thno.48810.

[127] H. Koniar, C. Rodríguez-Rodríguez, V. Radchenko, H. Yang, P. Kunz, A. Rahmim, C. Uribe and P. Schaffer. 'SPECT Imaging of Ac as a Theranostic Isotope for Ac Radiopharmaceutical Development'. In: *Physics in Medicine and Biology* 67.18 (2022). DOI: ARTN18500910.1088/1361-6560/ac8b5f.

[128] H. Koniar, S. McNeil, L. Wharton, A. Ingham, M. van de Voorde, M. Ooms, S. Sekar, C. Rodríguez-Rodríguez, P. Kunz, V. Radchenko, A. Rahmim, C. Uribe, H. Yang and P. Schaffer. 'Quantitative SPECT Imaging of Tb and Tb for Preclinical Theranostic Radiopharmaceutical Development'. In: *EJNMMI Physics* 11.1 (2024). DOI: ARTN7710.1186/s40658-024-00682-8.

[129] C. Müller, C. Vermeulen, U. Köster, K. Johnston, A. Türler, R. Schibli and N. P. van der Meulen. 'Alpha-PET with Terbium-149: Evidence and Perspectives for Radiotheragnostics'. In: *EJNMMI Radiopharmacy and Chemistry* 1.1 (2016). DOI: ARTN510.1186/s41181-016-0008-2.

[130] B. Das, B. Mehrdel, D. Goodman, M. Streicher, Y. Seo and J. Caravaca. 'Compton Imaging of Ac-225 In Pre-Clinical Phantoms With a 3D-Positioning CZT Camera'. In: *IEEE Transactions on Radiation and Plasma Medical Sciences* PP (June 2025), pp. 1–1. DOI: 10.1109/TRPMS.2025.3577212.

[131] S. Y. Chun, M. P. Nguyen, T. Q. Phan, H. Kim, J. A. Fessler and Y. K. Dewaraja. 'Algorithms and Analyses for Joint Spectral Image Reconstruction in Y-90 Bremsstrahlung SPECT'. In: *IEEE Transactions on Medical Imaging* 39.5 (2020), pp. 1369–1379. DOI: 10.1109/Tmi.2019.2949068.

[132] Z. K. Li, N. Benabdallah, R. Laforest, R. L. Wahl, D. L. J. Thorek and A. K. Jha. 'Joint Regional Uptake Quantification of Thorium-227 and Radium-223 Using a Multiple-Energy-Window Projection-Domain Quantitative SPECT Method'. In: *IEEE Transactions on Medical Imaging* 43.12 (2024), pp. 4281–4293. DOI: 10.1109/Tmi.2024.3420228.

[133] S. Takyu, H. Tashima, M. Takahashi, E. Yoshida, H. Wakizaka, F. Obata, G. Akamatsu, K. Nagatsu, A. Sugyo, H. Sudo, A. B. Tsuji, M. Ishibashi, Y. Imai, K. Parodi and T. Yamaya. 'A Whole Gamma Imaging Prototype for Higher Quantitative Imaging of Zr-Labeled Antibodies in a Tumor Mouse Model'. In: *Physics in Medicine and Biology* 70.2 (2025). DOI: ARTN02501210.1088/1361-6560/ada5a7.

[134] D. P. Ghosh S. 'Single-Cell Tracking with Compton-PET: An in Silico Feasibility Study'. In: *Nuclear Instruments and Methods in Physics Research Section a-Accelerators Spectrometers Detectors and Associated Equipment* 1053 (2023). DOI: ARTN10.1016/j.nima.2023.168373.

[135] J. Roser, L. Barrientos, J. Bernabéu, M. Borja-Lloret, E. Muñoz, A. Ros, R. Viegas and G. Llosá. 'Joint Image Reconstruction Algorithm in Compton Cameras'. In: *Physics in Medicine and Biology* 67.15 (2022). DOI: ARTN15500910.1088/1361-6560/ac7b08.

[136] J. Y. C. Wong, A. Raubitschek, D. Yamauchi, L. E. Williams, A. M. Wu, P. Yazaki, J. E. Shively, D. Colcher and G. Somlo. 'A Pretherapy Biodistribution and Dosimetry Study of Indium-111-Radiolabeled Trastuzumab in Patients with Human Epidermal Growth Factor Receptor 2-Overexpressing Breast Cancer'. In: *Cancer Biotherapy and Radiopharmaceuticals* 25.4 (2010), pp. 387–394. DOI: 10.1089/cbr.2010.0783.

[137] P. Jarvis, A. Ho and F. Sundram. 'Radium-223 Therapy for Metastatic Castration-Resistant Prostate Cancer: Survival Benefit When Used Earlier in the Treatment Pathway'. In: *Nuclear Medicine Communications* 42.3 (2021), pp. 332–336. DOI: 10.1097/Mnm.0000000000001325.

[138] A. P. Bidkar, L. Zerefa, S. Yadav, H. F. VanBrocklin and R. R. Flavell. 'Actinium-225 Targeted Alpha Particle Therapy for Prostate Cancer'. In: *Theranostics* 14.7 (2024), pp. 2969–2992. DOI: 10.7150/thno.96403.

[139] Y. Dekempeneer, T. Bäck, E. Aneheim, H. Jensen, J. Puttemans, C. Xavier, M. Keyaerts, S. Palm, P. Albertsson, T. Lahoutte, V. Caveliers, S. Lindegren and M. D'Huyvetter. 'Labeling of Anti-HER2 Nanobodies with Astatine-211: Optimization and the Effect of Different Coupling Reagents on Their in Vivo Behavior'. In: *Molecular Pharmaceutics* 16.8 (2019), pp. 3524–3533. DOI: 10.1021/acs.molpharmaceut.9b00354.

[140] A. K. Mapanao, S. D. Busslinger, A. Mehta, K. Kegler, C. Favaretto, P. V. Grundler, Z. Talip, U. Köster, K. Johnston, R. Schibli, N. P. van der Meulen and C. Müller. 'Preclinical Investigation of [Tb]Tb-DOTATATE and [Tb]Tb-DOTA-LM3 for Tumor-Targeted Alpha Therapy'. In: *European Journal of Nuclear Medicine and Molecular Imaging* 52.4 (2025), pp. 1383–1398. DOI: 10.1007/s00259-024-07035-8.

[141] V. J. Tschan, S. D. Busslinger, P. Bernhardt, P. V. Grundler, J. R. Zeevaart, U. Köster, N. P. van der Meulen, R. Schibli and C. Müller. 'Albumin-Binding and Conventional PSMA Ligands in Combination with 161Tb: Biodistribution, Dosimetry, and Preclinical Therapy'. In: *Journal of Nuclear Medicine* 64.10 (2023), pp. 1625–1631. DOI: 10.2967/jnumed.123.265524.

[142] C. Foxton, B. Waldron, R. V. Gronlund, J. Simón, B. Cornelissen, E. O'Neill and D. Stevens. 'Preclinical Evaluation of Lu-rhPSMA-10.1, a Radiopharmaceutical for Prostate Cancer: Biodistribution and Therapeutic Efficacy'. In: *Journal of Nuclear Medicine* 66.4 (2025), pp. 599–604. DOI: 10.2967/jnumed.124.268508.

[143] *GATE Users Guide*. Electronic Book. URL: www.opengatecollaboration.org.

[144] M. P. Nguyen, M. C. Goorden and F. J. Beekman. 'EXIRAD-HE: Multi-Pinhole High-Resolution Imaging of High-Energy Isotopes'. In: *Physics in Medicine and Biology* 65.22 (2020). DOI: ARTN22502910.1088/1361-6560/abbb77.

[145] A. K. H. Robertson, C. F. Ramogida, C. Rodríguez-Rodríguez, S. Blinder, P. Kunz, V. Sossi and P. Schaffer. 'Multi-Isotope SPECT Imaging of the Ac Decay Chain: Feasibility Studies'. In: *Physics in Medicine and Biology* 62.11 (2017), pp. 4406–4420. DOI: 10.1088/1361-6560/aa6a99.

[146] M. A. King, D. J. deVries, T. S. Pan, P. H. Pretorius and J. A. Case. 'An Investigation of the Filtering of TEW Scatter Estimates Used to Compensate for Scatter with Ordered Subset Reconstructions'. In: *IEEE Transactions on Nuclear Science* 44.3 (1997), pp. 1140–1145. DOI: Doi10.1109/23.596978.

[147] R. M. De Kruijff, H. T. Wolterbeek and A. G. Denkova. 'A Critical Review of Alpha Radionuclide Therapy-How to Deal with Recoiling Daughters?' In: *Pharmaceuticals* 8.2 (2015), pp. 321–336. ISSN: 1424-8247. DOI: 10.3390/ph8020321.

[148] A. Majkowska-Pilip, W. Gaweda, K. Zelechowska-Matysiak, K. Wawrowicz and A. Bilewicz. 'Nanoparticles in Targeted Alpha Therapy'. In: *Nanomaterials* 10.7 (2020). DOI: ARTN10.3390/nano10071366.

[149] U. Holzwarth, I. O. Jimenez and L. Calzolai. 'A Random Walk Approach to Estimate the Confinement of Alpha-Particle Emitters in Nanoparticles for Targeted Radionuclide therapy'. In: *EJNMMI Radiopharmacy and Chemistry* 3.1 (2018). DOI: ARTN910.1186/s41181-018-0042-3.

[150] A. R. Muslimov, D. O. Antuganov, Y. V. Tarakanchikova, M. V. Zhukov, M. A. Nadporojskii, M. V. Zyuzin and A. S. Timin. 'Calcium Carbonate Core-Shell Particles for Incorporation of Ac and Their Application in Local alpha-Radionuclide Therapy'. In: *Acs Applied Materials and Interfaces* 15.47 (2023), pp. 55193–55193. DOI: 10.1021/acsami.3c13857.

[151] S. R. Banerjee, A. Lisok, I. Minn, A. Josefsson, V. Kumar, M. Brummet, S. Boinapally, C. Brayton, R. C. Mease, G. Sgouros, R. F. Hobbs and M. G. Pomper. 'Preclinical Evaluation of Bi- and Ac-Labeled Low-Molecular-Weight Compounds for Radiopharmaceutical Therapy of Prostate Cancer'. In: *Journal of Nuclear Medicine* 62.7 (2021), pp. 980–988. DOI: 10.2967/jnumed.120.256388.

[152] R. Weissleder. *Molecular Imaging: Principles and Practice*. People's Medical Publishing House, 2010.

[153] H. O. Anger. *The Scintillation Camera : a New Instrument for Mapping the Distribution of Radioactive Isotopes*. University of California Radiation Laboratory, 1957. URL: http://hdl.handle.net/2027/mdp.39015077592759.

[154] T. E. Peterson and L. R. Furenlid. 'SPECT Detectors: the Anger Camera and Beyond'. In: *Physics in Medicine and Biology* 56.17 (2011), R145–82. DOI: 10.1088/0031-9155/56/17/R01. URL: https://www.ncbi.nlm.nih.gov/pubmed/21828904.

[155] Y. Chen. 'Image Acquisition and Attenuation Map Estimation for Multi-pinhole Clinical SPECT'. Thesis. 2021.

[156] F. J. Huizing, B. A. W. Hoeben, G. M. Franssen, O. C. Boerman, S. Heskamp and J. Bussink. 'Quantitative Imaging of the Hypoxia-Related Marker CAIX in Head and Neck Squamous Cell Carcinoma Xenograft Models'. In: *Molecular Pharmaceutics* 16.2 (2019), pp. 701–708. DOI: 10.1021/acs.molpharmaceut.8b00950. URL: https://www.ncbi.nlm.nih.gov/pubmed/30550290.

[157] A. M. Avram. 'Radioiodine Scintigraphy with SPECT/CT: An Important Diagnostic Tool for Thyroid Cancer Staging and Risk Stratification'. In: *Journal of Nuclear Medicine Technology* 42.3 (2014), pp. 170–180. DOI: 10.2967/jnumed.111.104133.

[158] D. Delbeke, S. Videlefsky, J. A. Patton, M. G. Campbell, W. H. Martin, I. Ohana and M. P. Sandler. 'Rest Myocardial Perfusion/Metabolism Imaging Using Simultaneous Dual-Isotope Acquisition SPECT with Technetium-99m-MIBI/Fluorine-18-FDG'. In: *Journal of Nuclear Medicine* 36.11 (1995), pp. 2110–9. URL: https://www.ncbi.nlm.nih.gov/pubmed/7472607.

[159] I. K. Hwang A B and H. B. H. 'Simulation of Depth of Interaction Effects for Pinhole SPECT'. In: *Nuclear Science Symposium Conference Record IEEE* vol 3 (2001), pp 1293–7.

[160] M. A. Korevaar, J. W. Heemskerk, M. C. Goorden and F. J. Beekman. 'Multi-Scale Algorithm for Improved Scintillation Detection in a CCD-Based Gamma Camera'. In: *Physics in Medicine and Biology* 54.4 (2009), pp. 831–42. DOI: 10.1088/0031-9155/54/4/001. URL: https://www.ncbi.nlm.nih.gov/pubmed/19141886.

[161] M. A. Korevaar, J. W. Heemskerk and F. J. Beekman. 'A Pinhole Gamma Camera with Optical Depth-of-Interaction Elimination'. In: *Physics in Medicine and Biology* 54.13 (2009), N267–72. DOI: 10.1088/0031-9155/54/13/N02. URL: https://www.ncbi.nlm.nih.gov/pubmed/19521006.

[162] S. B. Nagarkar VV Kudrolli H. 'Focused Scintillator Array for High Resolution Gamma Ray Imaging'. In: *IEEE Medical Imaging Conference* (2010), pp. M14–M98.

[163] F. Alhassen, H. Kudrolli, B. Singh, S. Kim, Y. Seo, R. G. Gould and V. V. Nagarkar. 'Depth-of-Interaction Compensation Using a Focused-Cut Scintillator for a Pinhole Gamma Camera'. In: *IEEE Transactions on Nuclear Science* 58.3 (2011), pp. 634–638. DOI: 10.1109/TNS.2011.2136386. URL: https://www.ncbi.nlm.nih.gov/pubmed/21731108.

[164] W. C. J. Hunter. *Modeling Stochastic Processes in Gamma-Ray Imaging Detectors and Evaluation of a Multi-Anode PMT Scintillation Camera for Use with Maximum-Likelihood Estimation Methods*. Electronic Book. 2007. URL: http://arizona.openrepository.com/arizona/handle/10150/196121.

[165] R. Haghshenas. *The Effect of Shape, Size and Arrangement of PMT's on the Intrinsic Spatial Resolution of Anger Camera*. Conference Paper. 2013.

[166] J. Xia, Q. Sen, W. Wang, Z. Ning, Y. Cheng, Z. Wang, X. Li, M. Qi, Y. Heng, S. Liu and X. Lei. 'A Performance Evaluation System for Photomultiplier Tubes'. In: *Journal of Instrumentation* 10 (2015). DOI: 10.1088/1748-0221/10/03/P03023.

[167] *NEMA Standards Publication NU 1-2007 Performance Measurements of Gamma Cameras*. Report.

[168] H. H. Barrett, W. C. Hunter, B. W. Miller, S. K. Moore, Y. Chen and L. R. Furenlid. 'Maximum-Likelihood Methods for Processing Signals From Gamma-Ray Detectors'. In: *IEEE Transactions on Nuclear Science* 56.3 (2009), p. 725. DOI: 10.1109/tns.2009.2015308. URL: https://www.ncbi.nlm.nih.gov/pubmed/20107527.

[169] S. Barrington, P. Blower and G. Cook. 'New Horizons in Multimodality Molecular Imaging and Novel Radiotracers'. In: *Clinical Medicine* 17.5 (2017), pp. 444–448. DOI: 10.7861/clinmedicine.17-5-444. URL: https://www.ncbi.nlm.nih.gov/pubmed/28974596.

[170] R. Kuker, M. Sztejnberg and S. Gulec. 'I-124 Imaging and Dosimetry'. In: *Molecular Imaging and Radionuclide Therapy* 26 (2017), pp. 66–73. DOI: 10.4274/2017.26.suppl.07. URL: https://www.ncbi.nlm.nih.gov/pubmed/28117290.

[171] Y. Zhou, K. E. Baidoo and M. W. Brechbiel. 'Mapping Biological Behaviors by Application of Longer-Lived Positron Emitting Radionuclides'. In: *Advanced Drug Delivery Reviews* 65.8 (2013), pp. 1098–111. DOI: 10.1016/j.addr.2012.10.012. URL: https://www.ncbi.nlm.nih.gov/pubmed/23123291.

[172] M. Bruehlmeier, U. Roelcke, P. Blauenstein, J. Missimer, P. A. Schubiger, J. T. Locher, R. Pellikka and S. M. Ametamey. 'Measurement of the Extracellular Space in Brain Tumors Using 76Br-bromide and PET'. In: *Journal of Nuclear Medicine* 44.8 (2003), pp. 1210–8. URL: https://www.ncbi.nlm.nih.gov/pubmed/12902409.

[173] A. Lovqvist, A. Sundin, A. Roberto, H. Ahlstrom, J. Carlsson and H. Lundqvist. 'Comparative PET Imaging of Experimental Tumors with Bromine-76-Labeled Antibodies, Fluorine-18-Fluorodeoxyglucose and Carbon-11-Methionine'. In: *Journal of Nuclear Medicine* 38.7 (1997), pp. 1029–35. URL: https://www.ncbi.nlm.nih.gov/pubmed/9225786.

[174] R. Laforest and X. Liu. 'Cascade Removal and MicroPET Imaging with 76Br'. In: *Physics in Medicine and Biology* 54.6 (2009), pp. 1503–31. DOI: 10.1088/0031-9155/54/6/008. URL: https://www.ncbi.nlm.nih.gov/pubmed/19229093.

[175] Y. W. Jauw, C. W. Menke-van der Houven van Oordt, O. S. Hoekstra, N. H. Hendrikse, D. J. Vugts, J. M. Zijlstra, M. C. Huisman and G. A. van Dongen. 'Immuno-Positron Emission Tomography with Zirconium-89-Labeled Monoclonal Antibodies in Oncology: What Can We Learn from Initial Clinical Trials?' In: *Frontiers in Pharmacology* 7 (2016), p. 131. DOI: 10.3389/fphar.2016.00131. URL: https://www.ncbi.nlm.nih.gov/pubmed/27252651.

[176] G. S. P. Mok, Y. C. Wang and B. M. W. Tsui. 'Quantification of the Multiplexing Effects in Multi-Pinhole Small Animal SPECT: A Simulation Study'. In: *IEEE Transactions on Nuclear Science* 56.5 (2009), pp. 2636–2643. DOI: 10.1109/Tns.2009.2023444.

[177] M. D. Walker, M. C. Goorden, K. Dinelle, R. M. Ramakers, S. Blinder, M. Shirmohammad, F. van der Have, F. J. Beekman and V. Sossi. 'Performance Assessment of a Preclinical PET Scanner with Pinhole Collimation by Comparison to a Coincidence-Based Small-Animal PET Scanner'. In: *Journal of Nuclear Medicine* 55.8 (2014), pp. 1368–74. DOI: 10.2967/jnumed.113.136663. URL: https://www.ncbi.nlm.nih.gov/pubmed/24904110.

[178] R. Accorsi and S. D. Metzler. 'Analytic Determination of the Resolution-Equivalent Effective Diameter of a Pinhole Collimator'. In: *IEEE Transactions on Medical Imaging* 23.6 (2004), pp. 750–63. DOI: 10.1109/tmi.2004.826951. URL: https://www.ncbi.nlm.nih.gov/pubmed/15191149.

[179] R. Accorsi and S. D. Metzler. 'Resolution-Effective Diameters for Asymmetric-Knife-Edge Pinhole Collimators'. In: *IEEE Transactions on Medical Imaging* 24.12 (2005), pp. 1637–46. DOI: 10.1109/TMI.2005.857229. URL: https://www.ncbi.nlm.nih.gov/pubmed/16353374.

[180] V. Bom, M. Goorden and F. Beekman. 'Comparison of Pinhole Collimator Materials Based on Sensitivity Equivalence'. In: *Physics in Medicine and Biology* 56.11 (2011), pp. 3199–214. DOI: 10.1088/0031-9155/56/11/003. URL: https://www.ncbi.nlm.nih.gov/pubmed/21540488.

[181] M. R. Bernsen, P. E. B. Vaissier, R. Van Holen, J. Booij, F. J. Beekman and M. de Jong. 'The Role of Preclinical SPECT in Oncological and Neurological Research in Combination with ither CT or MRI'. In: *European Journal of Nuclear Medicine and Molecular Imaging* 41 (2014), S36–S49. DOI: 10.1007/s00259-013-2685-3.

[182] H. Koniar, L. Wharton, A. Ingham, C. Rodríguez-Rodríguez, P. Kunz, V. Radchenko, H. Yang, A. Rahmim, C. Uribe and P. Schaffer. 'Quantitative SPECT Imaging of Actinium-226: Feasibility and Proof-of-Concept'. In: *Physics in Medicine and Biology* 69.15 (2024). DOI: ARTN15500310.1088/1361-6560/ad5c37.

[183] K. Ogawa, H. Echigo, K. Mishiro, S. Hirata, K. Washiyama, Y. Kitamura, K. Takahashi, K. Shiba and S. Kinuya. 'Ga- and At-Labeled RGD Peptides for Radiotheranostics with Multiradionuclides'. In: *Molecular Pharmaceutics* 18.9 (2021), pp. 3553–3562. DOI: 10.1021/acs.molpharmaceut.1c00460.

[184] B. Sigurdsson, N. L. Hauglund, T. O. Lilius, F. L. Mogensen, K. N. Mortensen, N. Beschorner, L. Klinger, S. L. Baerentzen, M. P. Rosenholm, V. Shalgunov, M. Herth, Y. Mori and M. Nedergaard. 'A SPECT-based method for dynamic imaging of the glymphatic system in rats'. In: *J Cereb Blood Flow Metab* 43.7 (2023), pp. 1153–1165. ISSN: 1559-7016 (Electronic) 0271-678X (Print) 0271-678X (Linking). DOI: 10.1177/0271678X231156982. URL: https://www.ncbi.nlm.nih.gov/pubmed/36809165.

[185] O. Ivashchenko, F. van der Have, M. C. Goorden, R. M. Ramakers and F. J. Beekman. 'Ultra-High-Sensitivity Submillimeter Mouse SPECT'. In: *Journal of Nuclear Medicine* 56.3 (2015), pp. 470–5. DOI: 10.2967/jnumed.114.147140. URL: https://www.ncbi.nlm.nih.gov/pubmed/25678487.

[186] B. Saeedi Saghez, C. Rodriguez-Rodriguez, P. L. Esquinas, H. Merkens, F. Benard, V. Radchenko and H. Yang. 'First Preclinical SPECT/CT Imaging and Biodistribution of [(165)Er]ErCl(3) and [(165)Er]Er-PSMA-617'. In: *EJNMMI Radiopharmacy and Chemestry* 9.1 (2024), p. 90. DOI: 10.1186/s41181-024-00312-9. URL: https://www.ncbi.nlm.nih.gov/pubmed/39692986.

[187] L. Wharton, S. W. McNeil, C. Zhang, G. Engudar, M. Van de Voorde, J. Zeisler, H. Koniar, S. Sekar, Z. Yuan, P. Schaffer, V. Radchenko, M. Ooms, P. Kunz, F. Benard and H. Yang. 'Preclinical Evaluation of MC1R Targeting Theranostic Pair [(155)Tb]Tb-Crown-AlphaMSH and [(161)Tb]Tb-Crown-AlphaMSH'. In: *Nuclear Medicine and Biology* 136-137 (2024), p. 108925. DOI: 10.1016/j.nucmedbio.2024.108925. URL: https://www.ncbi.nlm.nih.gov/pubmed/38796924.

[188] S. Vallabhajosula. 'F-Labeled Positron Emission Tomographic Radiopharmaceuticals in Oncology:: An Overview of Radiochemistry and Mechanisms of Tumor Localization'. In: *Seminars in Nuclear Medicine* 37.6 (2007), pp. 400–419. ISSN: 0001-2998. DOI: 10.1053/j.semnuclmed.2007.08.004.

[189] M. Reivich, D. Kuhl, A. Wolf, J. Greenberg, M. Phelps, T. Ido, V. Casella, J. Fowler, E. Hoffman, A. Alavi, P. Som and L. Sokoloff. 'The [18F]fluorodeoxyglucose method for the measurement of local cerebral glucose utilization in man'. In: *Circ Res* 44.1 (1979), pp. 127–37. ISSN: 0009-7330 (Print) 0009-7330 (Linking). DOI: 10.1161/01.res.44.1.127. URL: https://www.ncbi.nlm.nih.gov/pubmed/363301.

[190] M. M. Alauddin. 'Positron Emission Tomography (PET) Imaging with (18)F-based Radiotracers'. In: *American Journal of Nuclear Medicine and Molecular Imaging* 2.1 (2012), pp. 55–76. URL: https://www.ncbi.nlm.nih.gov/pubmed/23133802.

[191] P. K. Borjesson, Y. W. Jauw, R. Boellaard, R. de Bree, E. F. Comans, J. C. Roos, J. A. Castelijns, M. J. Vosjan, J. A. Kummer, C. R. Leemans, A. A. Lammertsma and G. A. van Dongen. 'Performance of Immuno-Positron Emission Tomography with Zirconium-89-Labeled Chimeric Monoclonal Antibody U36 in the Detection of Lymph Node Metastases in Head and Neck Cancer Patients'. In: *Clinical Cancer Research* 12 (2006), pp. 2133–40. DOI: 10.1158/1078-0432.CCR-05-2137. URL: https://www.ncbi.nlm.nih.gov/pubmed/16609026.

[192] M. S. De Feo, M. Pontico, V. Frantellizzi, F. Corica, F. De Cristofaro and G. De Vincentis. 'Zr-PET Imaging in Humans: a Systematic Review'. In: *Clinical and Translational Imaging* 10.1 (2022), pp. 23–36. DOI: 10.1007/s40336-021-00462-9.

[193] M. J. Vosjan, L. R. Perk, G. W. Visser, M. Budde, P. Jurek, G. E. Kiefer and G. A. van Dongen. 'Conjugation and Radiolabeling of Monoclonal Antibodies with Zirconium-89 for PET Imaging Using the Bifunctional Chelate P-Isothiocyanatobenzyl-Desferrioxamine'. In: *Nature Protocols* 5.4 (2010), pp. 739–43. DOI: 10.1038/nprot.2010.13. URL: https://www.ncbi.nlm.nih.gov/pubmed/20360768.

[194] C. Wu, F. van der Have, B. Vastenhouw, R. A. Dierckx, A. M. Paans and F. J. Beekman. 'Absolute Quantitative Total-Body Small-Animal SPECT with Focusing Pinholes'. In: *European Journal of Nuclear Medicine and Molecular Imaging* 37.11 (2010), pp. 2127–35. DOI: 10.1007/s00259-010-1519-9. URL: https://www.ncbi.nlm.nih.gov/pubmed/20577738.

[195] N. E. M. Association. 'NEMA Standards Publication NU 4-2008: Performance Measurements of Small Animal Positron Emission Tomographs'. In: (2008).

[196] E. P. Visser, A. A. Harteveld, A. P. W. Meeuwis, J. A. Disselhorst, W. J. G. Oyen and O. C. Boerman. 'Image Quality Phantom and Parameters for High Spatial Resolution Small-Animal SPECT'. In: *European Journal of Nuclear Medicine and Molecular Imaging* 38 (2011), S173–S173.

[197] C. Wu, J. R. de Jong, H. A. Gratama van Andel, F. van der Have, B. Vastenhouw, P. Laverman, O. C. Boerman, R. A. Dierckx and F. J. Beekman. 'Quantitative Multi-Pinhole Small-Animal SPECT: Uniform Versus Non-Uniform Chang Attenuation Correction'. In: *Physics in Medicine and Biology* 56.18 (2011), N183–93. DOI: 10.1088/0031-9155/56/18/N01. URL: https://www.ncbi.nlm.nih.gov/pubmed/21865622.

[198] G. Mok, B. Tsui, F. Beekman, Y. Wang and A. Ahuja. 'Effects of Object Activity Distribution on Multiplexing Multi-Pinhole SPECT'. In: *Journal of Nuclear Medicine* 51.supplement 2 (2010).

[199] F. J. Beekman. 'A focused Pinhole Gamma Detection Device'. Patent application NL 2006107 EP2482101. 2012.

[200] L. C. Johnson, S. Shokouhi and T. E. Peterson. 'Reducing Multiplexing Artifacts in Multi-Pinhole SPECT With a Stacked Silicon-Germanium System: A Simulation Study'. In: *IEEE Transactions on Medical Imaging* 33.12 (2014). DOI: 10.1109/TMI.2014.2340251.

[201] S. Pells, N. Zeraatkar, K. S. Kalluri, S. C. Moore, M. May, L. R. Furenlid, M. A. Kupinski, P. H. Kuo and M. A. King. 'Correction of Multiplexing Artefacts in Multi-Pinhole SPECT Through Temporal Shuttering, De-Multiplexing of Projections, and Alternating Reconstruction'. In: *Physics in Medicine and Biology* 69.12 (2024), p. 125004. DOI: 10.1088/1361-6560/ad4f47.

[202] F. Van Der Have and F. Beekman. 'Penetration, Scatter and Sensitivity in Channel Micro-Pinholes for SPECT: A Monte Carlo Investigation'. In: *IEEE Transactions on Nuclear Science* 53.5 (2006), pp. 2635–2645. DOI: 10.1109/TNS.2006.882739.

[203] S. Ghosh, V. Cosmi, R. M. Ramakers, F. J. Beekman and M. C. Goorden. 'Dual-photopeak joint image reconstruction for pinhole SPECT, PET and PET-SPECT'. In: *Physics in Medicine and Biology* 71.1 (2026). DOI: 10.1088/1361-6560/ae2ce0.

[204] V. Cosmi, S. Ghosh, R. M. Ramakers, M. C. Goorden and F. J. Beekman. 'Super-Cluster collimation for ultra-sensitive SPECT-PET: a simulation study'. In: *Physics in Medicine and Biology* 71.1 (2026). DOI: 10.1088/1361-6560/ae2e7a.

[205] Y. Zhang, V. Cosmi, S. Ghosh, R. M. Ramakers and F. J. Beekman. 'Ultra-Fine Sampling for Ultra-Sensitive Preclinical Supercluster Pinhole SPECT and PET'. In: *Physics in Medicine and Biology (Under revision)* (2025).

[206] V. Cosmi, M. Kvassheim, S. Ghosh, F. J. Beekman and M. C. Goorden. *High-Resolution Twisted Clustered Pinhole for High-Energy Preclinical SPECT*. Abstract presented at the IEEE Nuclear Science Symposium, Medical Imaging Conference and Room Temperature Semiconductor Detector Conference, Tampa, USA. 2024.

[207] V. Cosmi, M. Kvassheim, F. J. Beekman and M. C. Goorden. *Novel Arrangement of Pinhole Clusters for High-Energy Preclinical SPECT*. Abstract presented at the IEEE Nuclear Science Symposium, Medical Imaging Conference and Room Temperature Semiconductor Detector Conference, Vancouver, Canada. 2023.

[208] V. Cosmi, M. C. Goorden and F. J. Beekman. *Performance of Detectors with Thick NaI Scintillators for High-Energy Pinhole SPECT*. Abstract presented at the IEEE Nuclear Science Symposium, Medical Imaging Conference and Room Temperature Semiconductor Detector Conference, Milan, Italy. 2022.

[209] M. Capogni, E. Cisbani, V. Cosmi, M. Croia, F. Giuliani, G. Limiti, M. Lucentini, S. Murri, P. Musico, M. Pilade, F. Santavenere and A. Spurio. *Toward Quantitative Bremsstrahlung Medical Imaging by Custom Gamma Camera Device*. Abstract presented at the Advancements in Nuclear Instrumentation Measurement Methods and their Applications (ANIMMA) Conference, Valencia, Spain. 2025.

[210] Y. Zhang, V. Cosmi, S. Ghosh, R. M. Ramakers and F. J. Beekman. *Ultra-Fine Sampling for Ultra-Sensitive Preclinical SPECT-PET with High-Energy Super-Cluster Collimators*. Abstract presented at the IEEE Nuclear Science Symposium, Medical Imaging Conference and Room Temperature Semiconductor Detector Conference, Yokohama, Japan. 2025.

[211] S. Ghosh, V. Cosmi, F. J. Beekman and M. C. Goorden. *Sub-mm Resolution PET in Case of Long Positron Ranges Using High and Ultra-High Energy Prompts*. Abstract presented at the IEEE Nuclear Science Symposium, Medical Imaging Conference and Room Temperature Semiconductor Detector Conference, Tampa, USA. 2024.

Acknowledgements

This journey would not have been possible without the support of many people who, over the years, contributed to the completion of this thesis.

First, I would like to express my deepest gratitude to my promotor, Prof. em. dr. Freek Beekman. His expertise and passion for the field have been both inspiring and motivating. I greatly appreciated the balance he maintained between providing guidance and allowing me the independence to develop my own work. I wish him all the best for the future.

I am equally grateful to my co-promotor, Dr.ir. Marlies Goorden, for her invaluable daily supervision. Her support, insightful suggestions, and critical questions have been instrumental in shaping me as a scientist. Her dedication to the students she mentors is admirable, and I hope to carry that spirit forward should I ever find myself in a similar role. I wish her every success in the future.

I am thankful to have worked with my colleagues at the Biomedical Imaging section, part of the Department of Radiation Science and Technology in the Faculty of Applied Sciences at TU Delft. Satyajit, my colleague for nearly two years, was always the first person I would turn to when I faced challenges, and his thoughtful ideas and humility have been truly inspiring. Yirong, who joined the team more recently, made collaboration both enjoyable and enriching, I learned a great deal from her determination and technical expertise. I also thank Rob and Jan for always being ready to help when needed.

I am grateful as well for the collaboration with the team at MILabs B.V. In particular, I would like to thank Ruud for his continuous support and valuable insights, and Sofia for giving me the opportunity to participate in experimental work.

Beyond academia, I am fortunate to have friends and loved ones who provided balance and encouragement throughout this journey.

Finally, I owe my deepest gratitude to my family. Their constant support has been the foundation of everything I have accomplished, and I cannot thank them enough.

Valerio Cosmi

Curriculum Vitæ

Valerio COSMI

29-03-1992 Born in Anzio, Italy

2021/04–2025/06	Delft University of Technology, The Netherlands Ph.D. candidate Thesis: Design and Optimization of Next-Generation Broad Energy Pinhole PET/SPECT
2017/09–2020/01	Sapienza University, Rome, Italy Master of Science in Nuclear physics Thesis: Characterization of a beta imaging device for studies on animal models
2012/09–2016/12	Sapienza University, Rome, Italy Bachelor's degree in physics Thesis: PET physics

List of Publications

Peer-reviewed journal articles

- V. Cosmi, S. Ghosh, R. M. Ramakers, M. C. Goorden and F. J. Beekman. 'Super-Cluster collimation for ultra-sensitive SPECT-PET: a simulation study'. In: *Physics in Medicine and Biology* 71.1 (2026). DOI: 10.1088/1361-6560/ae2e7a

- V. Cosmi, M. Kvassheim, S. Ghosh, F. J. Beekman and M. C. Goorden. 'Twisted Clustered Pinhole Collimation for Improved High-Energy Preclinical SPECT/PET'. In: *Physics in Medicine and Biology* 69.22 (2024). DOI: 10.1088/1361-6560/ad8c97. URL: https://www.ncbi.nlm.nih.gov/pubmed/39533753

- V. Cosmi, B. Wang, M. C. Goorden and F. J. Beekman. 'NaI Gamma Camera Performance for High Energies: Effects of Crystal Thickness, Photomultiplier Tube Geometry and Light Guide Thickness'. In: *Medical Physics* 51.7 (2024), pp. 4696–4708. DOI: 10.1002/mp.17043. URL: https://www.ncbi.nlm.nih.gov/pubmed/38569052

- S. Ghosh, V. Cosmi, R. M. Ramakers, F. J. Beekman and M. C. Goorden. 'Dual-photopeak joint image reconstruction for pinhole SPECT, PET and PET-SPECT'. In: *Physics in Medicine and Biology* 71.1 (2026). DOI: 10.1088/1361-6560/ae2ce0

- Y. Zhang, V. Cosmi, S. Ghosh, R. M. Ramakers and F. J. Beekman. 'Ultra-Fine Sampling for Ultra-Sensitive Preclinical Supercluster Pinhole SPECT and PET'. In: *Physics in Medicine and Biology (Under revision)* (2025)

- S. Ghosh, V. Cosmi, R. M. Ramakers, F. J. Beekman and M. C. Goorden. 'Ultra-high Energy Spectral Prompt PET'. In: *Physics in Medicine and Biology* 70.7 (2025). DOI: 10.1088/1361-6560/adbfd7. URL: https://www.ncbi.nlm.nih.gov/pubmed/40073503

Conference abstracts and proceedings

- V. Cosmi, M. Kvassheim, S. Ghosh, F. J. Beekman and M. C. Goorden. *High-Resolution Twisted Clustered Pinhole for High-Energy Preclinical SPECT*. Abstract presented at the IEEE Nuclear Science Symposium, Medical Imaging Conference and Room Temperature Semiconductor Detector Conference, Tampa, USA. 2024

- V. Cosmi, M. Kvassheim, F. J. Beekman and M. C. Goorden. *Novel Arrangement of Pinhole Clusters for High-Energy Preclinical SPECT*. Abstract presented at the IEEE Nuclear Science Symposium, Medical Imaging Conference and Room Temperature Semiconductor Detector Conference, Vancouver, Canada. 2023

- V. Cosmi, M. C. Goorden and F. J. Beekman. *Performance of Detectors with Thick NaI Scintillators for High-Energy Pinhole SPECT*. Abstract presented at the IEEE Nuclear Science Symposium, Medical Imaging Conference and Room Temperature Semiconductor Detector Conference, Milan, Italy. 2022

- M. Capogni, E. Cisbani, V. Cosmi, M. Croia, F. Giuliani, G. Limiti, M. Lucentini, S. Murri, P. Musico, M. Pilade, F. Santavenere and A. Spurio. *Toward Quantitative Bremsstrahlung Medical Imaging by Custom Gamma Camera Device*. Abstract presented at the Advancements in Nuclear Instrumentation Measurement Methods and their Applications (ANIMMA) Conference, Valencia, Spain. 2025

- Y. Zhang, V. Cosmi, S. Ghosh, R. M. Ramakers and F. J. Beekman. *Ultra-Fine Sampling for Ultra-Sensitive Preclinical SPECT-PET with High-Energy Super-Cluster Collimators*. Abstract presented at the IEEE Nuclear Science Symposium, Medical Imaging Conference and Room Temperature Semiconductor Detector Conference, Yokohama, Japan. 2025

- S. Ghosh, V. Cosmi, F. J. Beekman and M. C. Goorden. *Sub-mm Resolution PET in Case of Long Positron Ranges Using High and Ultra-High Energy Prompts*. Abstract presented at the IEEE Nuclear Science Symposium, Medical Imaging Conference and Room Temperature Semiconductor Detector Conference, Tampa, USA. 2024